

## University of Southampton Research Repository

Copyright © and Moral Rights for this thesis and, where applicable, any accompanying data are retained by the author and/or other copyright owners. A copy can be downloaded for personal non-commercial research or study, without prior permission or charge. This thesis and the accompanying data cannot be reproduced or quoted extensively from without first obtaining permission in writing from the copyright holder/s. The content of the thesis and accompanying research data (where applicable) must not be changed in any way or sold commercially in any format or medium without the formal permission of the copyright holder/s.

When referring to this thesis and any accompanying data, full bibliographic details must be given, e.g.

Thesis: Author (Year of Submission) "Full thesis title", University of Southampton, name of the University Faculty or School or Department, PhD Thesis, pagination.

Data: Author (Year) Title. URI [dataset]



**University of Southampton**

Faculty of Environmental and Life Sciences

School of Biological Sciences

**Identification of Annexin A1 as a novel regulator of oriented cell divisions in  
mammary epithelial cells**

by

**Maria Fankhaenel**

BSc MSc

ORCID ID 0000-0003-1218-3820

Thesis for the degree of Doctor of Philosophy

August, 2021



# University of Southampton

## Abstract

Faculty of Environmental and Life Sciences

School of Biological Sciences

Identification of Annexin A1 as a novel regulator of oriented cell divisions in  
mammary epithelial cells

by

Maria Fankhaenel

Oriented cell divisions (OCDs) represent a fundamental mechanism for tissue morphogenesis, repair and differentiation where the mitotic spindle is oriented along a specific polarity axis. Early research identified the evolutionarily conserved Gai/LGN/NuMA ternary complex that mediates orientation of the mitotic spindle by being restricted to specific cortical regions. The mechanisms that control the recruitment of these proteins to the cortex remain unfolding, particularly in epithelial systems such as the mammary gland.

The mammary gland represents a unique organ that develops predominantly after birth where postnatal morphogenesis of the mammary gland drives dramatic tissue turnover and remodelling. Thus, differentiation and proliferation are constantly balanced to allow normal mammary gland development and homeostasis. How mammary epithelial cells regulate mitotic spindle orientation, hence OCDs, to accompany the rapid and constant tissue turnover is not well understood. This study aimed to identify novel factors that regulate the LGN-mediated spindle orientation machinery and determine how their dysregulation affects OCDs in mammary epithelial cells.

By combining co-immunoprecipitation with mass spectrometry, the LGN interactome at the cell cortex of mitotic mammary epithelial cells was characterised and the membrane-associated protein Annexin A1 (ANXA1) was identified as a novel partner of LGN. Confocal and time-lapse microscopy demonstrated a critical role of ANXA1 in regulating the position and planar orientation of the mitotic spindle by instructing the accumulation and restriction of the LGN complex at the lateral cortex. Moreover, loss of ANXA1 leads to mitotic spindle misassembly and chromosome segregation defects, affecting the dynamics and progression of mitosis.

Collectively the present study identified ANXA1 as a novel intrinsic cue of OCDs in mammary epithelial cells. Given increasing evidence of a link between OCD and tumorigenesis, this work is not only important for advancing our understanding of normal epithelial biology but also elucidating how imbalance of OCDs can contribute to the abnormal cell behaviour observed in cancer.





2.1	Microbial methods.....	39
2.1.1	Growth of bacteria.....	39
2.1.2	Transformation of <i>E. coli</i> with plasmid DNA.....	39
2.2	Cell culture methods.....	40
2.2.1	Cell culture of human cell lines.....	40
2.2.2	Cell counting .....	42
2.2.3	Cell cycle arrest at metaphase.....	42
2.2.4	Transfection using calcium phosphate .....	43
2.2.5	Gene knockdown using small interfering RNA .....	43
2.2.6	Retroviral production and transduction .....	44
2.2.7	Cell sorting using flow-cytometry .....	45
2.3	DNA methods.....	47
2.3.1	Purification of plasmid DNA from <i>E. coli</i> .....	47
2.3.2	Amplification of DNA by polymerase chain reaction.....	47
2.3.3	Purification of PCR products .....	48
2.3.4	Agarose gel electrophoresis.....	48
2.3.5	Purification of DNA from agarose gels.....	49
2.3.6	Restriction enzyme digestion.....	49
2.3.7	Ligation of vector and insert.....	49
2.3.8	Screening for positive clones .....	50
2.3.9	Spectrophotometric quantification of DNA.....	50
2.3.10	DNA sequencing.....	50
2.4	Generation of mammary cell lines.....	51
2.4.1	Plasmid construction .....	51
2.4.1.1	Cloning strategy GFP control .....	51
2.4.1.2	Cloning strategy ANXA1-mCherry .....	52
2.4.1.3	Cloning strategy mCherry control.....	53
2.4.2	Establishment of cell lines using retroviral transduction .....	54
2.5	Protein methods .....	54
2.5.1	Protein expression analysis.....	54

2.5.1.1	Protein extraction from mammalian cells.....	54
2.5.1.2	Quantification of total protein concentration .....	55
2.5.1.3	Sodium dodecyl sulphate polyacrylamide gel electrophoresis.....	56
2.5.1.4	Western blot.....	58
2.5.1.5	Quantitative Western blot analysis.....	60
2.5.2	Proteomic analysis .....	62
2.5.2.1	Immunoprecipitation using Nano-Traps .....	62
2.5.2.2	Sample preparation for mass spectrometry .....	63
2.5.2.3	Mass Spectrometry .....	64
2.6	Microscopy methods.....	65
2.6.1	Immunocytochemistry .....	65
2.6.2	Proximity ligation assay.....	70
2.6.3	Confocal imaging of fixed cell preparations.....	72
2.6.4	Live cell microscopy.....	72
2.6.5	Spindle orientation analysis .....	73
2.6.6	Spindle oscillation measurements .....	73
2.6.6.1	Spindle oscillation in the z-view .....	73
2.6.6.2	Spindle oscillation in the xy-view .....	74
2.6.6.3	Quantification of spindle oscillations .....	75
2.6.6.4	Quantification of the oscillation index .....	75
2.6.7	Metaphase plate tracking .....	75
2.6.8	Quantification of cortical fluorescence intensity.....	77
2.6.8.1	Cortical fluorescence intensities of metaphase cells .....	77
2.6.8.2	Cortical fluorescence intensities of prometaphase cells .....	78
2.6.9	Astral microtubule measurements .....	78
2.6.9.1	Quantification of astral microtubule intensity.....	78
2.6.9.2	Quantification of astral microtubule length and pole to cortex distance .....	79
2.6.10	Co- localisation analyses using line-scans .....	80
2.6.11	Quantification of mitotic index .....	80

2.7	Bioinformatics analyses of mass spectrometry data .....	81
2.7.1	Construction of protein- protein interaction networks.....	81
2.7.2	Gene Ontology and pathway enrichment analyses.....	81
2.8	Statistical analysis .....	82
<b>Chapter 3</b>	<b>Generation of a stable cell line expressing GFP-LGN to uncover mechanisms of oriented cell divisions in mammary epithelial cells .....</b>	<b>83</b>
3.1	Introduction .....	85
3.2	Results.....	86
3.2.1	Expression and dynamics of GFP-LGN does not alter cell dynamics.....	86
3.2.2	GFP-LGN co-localises with the spindle orientation machinery .....	91
3.3	Discussion.....	96
3.3.1	Expression of GFP-LGN does not alter mitotic dynamics in mammary epithelial cells .....	96
<b>Chapter 4</b>	<b>Characterisation of the LGN interactome in dividing mammary epithelial cells reveals ANXA1 as a novel partner .....</b>	<b>99</b>
4.1	Introduction .....	101
4.2	Results.....	103
4.2.1	Co-immunoprecipitation of GFP-LGN from interphase and mitotic cells .....	103
4.2.2	Protein-protein interaction network of LGN during mitosis .....	108
4.2.3	Functional enrichment analysis of the LGN interaction network.....	114
4.3	Discussion.....	116
4.3.1	Characterising the complete LGN interactome requires optimal conditions	117
4.3.2	Reproducibility of the proteomics approach.....	119
4.3.3	The mitotic LGN interactome in mammary epithelial cells comprises known and novel regulators of mitotic spindle dynamics.....	120
<b>Chapter 5</b>	<b>ANXA1 is a novel partner of LGN: Characterisation of the ANXA1 and LGN binding .....</b>	<b>127</b>
5.1	Introduction .....	129
5.2	Results.....	130

5.2.1	Validation of an association between ANXA1 and LGN .....	130
5.2.2	ANXA1 shows a cell-cycle dependent localisation .....	134
5.2.3	ANXA1 localises with LGN to the cell cortex during mitosis .....	136
5.3	Discussion .....	141
5.3.1	ANXA1 and LGN associate at the cell cortex during metaphase .....	141
5.3.2	ANXA1 displays a distinct subcellular localisation during the cell cycle .....	143
5.3.3	The distribution of ANXA1 and LGN at the cortex is spatiotemporally regulated .....	144
<b>Chapter 6 ANXA1 coordinates the polarised cortical localisation of LGN during mitosis .....</b>		<b>147</b>
6.1	Introduction .....	149
6.2	Results .....	150
6.2.1	siRNA targeting <i>ANXA1</i> results in knockdown of the protein .....	150
6.2.2	Loss of ANXA1 leads to misplacement of GFP-LGN during mitosis .....	152
6.2.3	Loss of ANXA1 affects the localisation of the core spindle orientation machinery .....	154
6.2.4	Loss of LGN does not alter ANXA1 dynamics .....	158
6.3	Discussion .....	162
6.3.1	ANXA1 is required to localise the LGN-NuMA-Dynein/Dynactin complex to the lateral cortex during mitosis .....	163
6.3.2	ANXA1 acts upstream of LGN .....	164
<b>Chapter 7 ANXA1 is required for correct spindle orientation and mitotic progression .....</b>		<b>167</b>
7.1	Introduction .....	169
7.2	Results .....	170
7.2.1	Loss of ANXA1 leads to mitotic defects and mitotic delay .....	170
7.2.2	Loss of ANXA1 increases spindle oscillation and metaphase plate movement .....	174
7.2.3	Loss of ANXA1 alters astral microtubule dynamics .....	183
7.3	Discussion .....	185

7.3.1 ANXA1 is required for accurate spindle assembly and mitotic progression .	185
7.3.2 ANXA1 enables proper mitotic spindle positioning and planar spindle orientation .....	187
<b>Chapter 8 General discussion and future directions .....</b>	<b>191</b>
8.1 Summary .....	193
8.2 Binding dynamics of ANXA1 and LGN in mitotic and interphase mammary epithelial cells .....	195
8.3 Regulation of ANXA1 function in oriented cell divisions .....	196
8.4 Regulators of mitotic spindle orientation in the mammary gland and as universal mechanisms in epithelial systems .....	197
8.5 ANXA1 mediates planar spindle orientation in an <i>in vitro</i> cell culture model .....	199
<b>Appendix A Plasmid maps of retroviral transfer vectors .....</b>	<b>202</b>
<b>Appendix B Additional proteomics data .....</b>	<b>211</b>
<b>Appendix C Fiji macro script .....</b>	<b>219</b>
<b>Bibliography .....</b>	<b>221</b>

## Table of Tables

<b>Table 2.1 Cell culture media and supplements for MCF-10A cells</b> .....	41
<b>Table 2.2 Cell culture media and supplements for HEK293 cells</b> .....	41
<b>Table 2.3 SiRNA sequences targeting human <i>ANXA1</i> and <i>LGN</i></b> .....	43
<b>Table 2.4 General thermal cycling conditions for amplification of plasmid DNA</b> .....	48
<b>Table 2.6 Primer sequences and thermal cycling condition to generate the pTk14-GFP plasmid</b> .....	52
<b>Table 2.7 Primer sequences and thermal cycling condition to generate the pTK93-mCherry plasmid</b> .....	53
<b>Table 2.8 Primers used to sequence cloned retroviral plasmids</b> .....	53
<b>Table 2.10 List of generated stable cell lines using retroviral transduction</b> .....	54
<b>Table 2.11 NP40 lysis buffer ingredients</b> .....	55
<b>Table 2.12 Components for SDS-PAGE gel preparation</b> .....	57
<b>Table 2.13 List of primary and secondary antibodies used for immunodetection via Western blot</b> .....	60
<b>Table 2.14 Lysis buffer ingredients to extract proteins for immunoprecipitation</b> .....	62
<b>Table 2.15 Ingredients of elution buffers for on-bead tryptic digestion</b> .....	64
<b>Table 2.16 List of primary antibodies used for immunocytochemistry</b> .....	66
<b>Table 2.17 List of secondary antibodies used for immunocytochemistry</b> .....	67
<b>Table 4.1 Members of the spindle orientation machinery identified by MS</b> .....	108
<b>Table 4.2 Number of protein hits before and after interaction network generation</b> .....	109
<b>Table 4.3 Comparison of members of the LGN subnetwork in two independent MS experiments</b> .....	112

## Table of Figures

Figure 1.1 Mammalian cell cycle and phases of mitosis.....	5
Figure 1.2 Regulation and checkpoints of the mammalian cell cycle .....	7
Figure 1.3 Dynamic instability of microtubules .....	8
Figure 1.4 Key components of the mitotic spindle .....	10
Figure 1.5 Localisation of cell polarity complexes in epithelial cells.....	12
Figure 1.6 Modes of oriented cell divisions .....	14
Figure 1.7 Hierarchy of the cortical spindle orientation machinery in oriented cell divisions	15
Figure 1.8 Binding domains and motifs in the LGN sequence .....	17
Figure 1.9 Binding domains and motifs in the NuMA sequence .....	18
Figure 1.10 Simplified model of the dynein/dynactin complex .....	19
Figure 1.11 Principle of cortical force generation to orientate the mitotic spindle .....	21
Figure 1.12 Developmental stages of the postnatal mammary gland .....	27
Figure 1.13 Structure and interaction dynamics of mammalian annexins .....	30
Figure 1.14 ANXA1 implication in cellular processes.....	34
Figure 2.1 Representative samples and controls for FACS .....	46
Figure 2.3 Representative Ponceau S staining of after protein transfer.....	59
Figure 2.4 Example of a quantification of relative protein bands sizes .....	61
Figure 2.5 Representative immunocytochemistry staining controls .....	69
Figure 2.6 Schematic of the principle of PLA technology .....	71
Figure 2.7 Schematic of spindle oscillation measurements in z-view.....	73
Figure 2.8 Schematic of spindle oscillation measurements in xy-view.....	74
Figure 2.9 Schematic of metaphase plate tracking.....	76
Figure 2.10 Schematic of determining the displacement length of the DNA plate during .....	76

Figure 2.11 Schematic of positions along the cortex .....	77
Figure 2.12 Schematic of the quantification of astral microtubule intensity .....	79
Figure 2.13 Schematic of quantification astral microtubule length and pole-to-cortex distance	80
Figure 3.1 Localisation and expression levels of LGN, GFP-LGN and GFP in interphase and metaphase .....	87
Figure 3.2 Expression of GFP-LGN or GFP does not influence mitotic dynamics of MCF-10A cells .....	89
Figure 3.3 Mitotic spindle characteristics are not affected by the expression of GFP-LGN or GFP in MCF-10A cells .....	90
Figure 3.4 Co-localisation of GFP-LGN or GFP with LGN during metaphase .....	91
Figure 3.5 Co-localisation of GFP-LGN or GFP with NuMA during metaphase .....	92
Figure 3.6 Co-localisation of GFP-LGN or GFP with p150 <sup>Glured</sup> during metaphase .....	94
Figure 3.7 Co-localisation of GFP-LGN or GFP with Gai1 during metaphase .....	95
Figure 4.1 Immunoprecipitation of GFP-LGN from MCF-10A cells using GFP-Trap .....	103
Figure 4.2 GFP-Trap specifically immunoprecipitates GFP and GFP-LGN .....	104
Figure 4.3 Cell cycle arrest of MCF-10A cells expressing GFP-LGN or GFP .....	105
Figure 4.4 Localisation of GFP-LGN or GFP in cell cycle arrested MCF-10A cells .....	106
Figure 4.5 Mitotic index in cells arrested at G2/M or metaphase .....	107
Figure 4.6 Number of enriched proteins and overlap between two independent MS experiments .....	110
Figure 4.7 Known and novel interaction partners of LGN identified in a STRING protein interaction network .....	111
Figure 4.8 Classification of identified proteins based on their biological function .....	114
Figure 4.9 Gene enrichment analysis of significantly enriched biological processes and pathways from proteins in the LGN subnetwork .....	115
Figure 5.1 Immunoprecipitation of ANXA1 via GFP-LGN pulldown .....	130

Figure 5.2 Localisation and expression levels of ANXA1, ANXA1-mCherry and mCherry in interphase and metaphase.....	131
Figure 5.3 Immunoprecipitation of LGN via ANXA1-mCherry pulldown .....	132
Figure 5.4 In situ detection of an LGN and ANXA1 interaction in metaphase and interphase cells .....	133
Figure 5.6 Distinct subcellular localisation of ANXA1 during the cell cycle .....	135
Figure 5.7 Co-localisation dynamics of GFP-LGN and .....	137
Figure 5.8 Co-localisation dynamics of ANXA1-mCherry and LGN during the cell cycle .....	139
Figure 5.9 Co-localisation of ANXA1 with endogenous LGN and NuMA.....	140
Figure 5.10 Schematic of ANXA1 and LGN cortical dynamics during mitosis .....	146
Figure 6.1 Protein levels after ANXA1 knockdown using siRNA .....	151
Figure 6.2 ANXA1 depletion induces defects in GFP-LGN cortical localisation during mitosis.....	153
Figure 6.3 ANXA1 depletion results in cortical misplacement of the spindle orientation machinery .....	155
Figure 6.4 ANXA1 depletion has no effect on cortical localisation of G <i>ai</i> 1 .....	157
Figure 6.5 Protein levels after LGN knockdown using siRNA .....	158
Figure 6.6 LGN depletion leads to spindle orientation defects.....	159
Figure 6.7 Cortical localisation of NUMA and LGN after LGN depletion LGN depletion leads to cortical misplacement of NuMA but has no effect on ANXA1 localisation .....	161
Figure 7.1 ANXA1 depletion results in aberrant mitotic timing.....	171
Figure 7.2 ANXA1 depletion induces mitotic defects .....	173
Figure 7.3 ANXA1 depletion leads to excessive z-rotations of the mitotic spindle.....	175
Figure 7.4 Spindle angle measurements during metaphase in ANXA1-depleted cells .....	177
Figure 7.5 ANXA1 depletion leads to spindle orientation defects .....	178
Figure 7.6 ANXA1 depletion leads to increased xy-rotations of the mitotic spindle .....	180
Figure 7.7 ANXA1 depletion leads to increased mitotic spindle displacement .....	182

**Figure 7.8 ANXA1 depletion leads to astral microtubule defects .....184**

**Figure 8.1 Proposed model for ANXA1 regulation of planar mitotic spindle orientation .....194**



# Research Thesis: Declaration of Authorship

Print name: Maria Fankhaenel

Title of thesis:

**Identification of Annexin A1 as a novel regulator of oriented cell divisions in mammary epithelial cells**

I declare that this thesis and the work presented in it are my own and has been generated by me as the result of my own original research.

I confirm that:

1. This work was done wholly or mainly while in candidature for a research degree at this University;
2. Where any part of this thesis has previously been submitted for a degree or any other qualification at this University or any other institution, this has been clearly stated;
3. Where I have consulted the published work of others, this is always clearly attributed;
4. Where I have quoted from the work of others, the source is always given. With the exception of such quotations, this thesis is entirely my own work;
5. I have acknowledged all main sources of help;
6. Where the thesis is based on work done by myself jointly with others, I have made clear exactly what was done by others and what I have contributed myself;
7. Parts of this work have been published before submission as a preprint:
  - Fankhaenel, M., et al. (2021) 'Annexin A1 is a polarity cue that directs planar mitotic spindle orientation during mammalian epithelial morphogenesis' bioRxiv 07.28.454117; DOI: <https://doi.org/10.1101/2021.07.28.454117>.

Signature: ..... Date: 14/08/2021



## Acknowledgements

The past four years have been a roller coaster of emotions. It was wonderful, challenging and truly memorable, and I am grateful for all the people who advised and supported me.

Firstly, I would like to thank the Gerald Kerkut Charitable Trust and the School of Biological Sciences, who funded my PhD and without which this thesis would not have been possible.

I gratefully acknowledge the guidance and support from my supervisor Dr Salah Elias. I am proud to be your first PhD student and I thank you for teaching me. I appreciate the time you have spent to help me to become the scientist that I am today.

I would like to thank the rest of the Elias lab, past and present. In particular, I want to thank Manal Hosawi. We have been best friends since the first day you joined the lab and I am grateful for your endless support in and out the lab. Thank you for listening to my complaints, for understanding and for being my partner in crime. Thank you Dr Farahnaz Sadat Golestan Hashemi and Dr Mohammed A. Mansour for supporting me with my project. Another thank you goes to Dr Joseph Pally. You truly brought a lot of fun to the lab and I am grateful for your help and support.

A lot of my daily lab work has been made easy by the amazing staff in B85. Especially, I would like to thank David Cook and Georgie Dawes for all your help in the daily lab madness. I am also very grateful for the technical support and advice from Dr Mark Willett from the imaging facility.

Another thank you goes to Dr Marcin Przewloka and Dr Bhav Sheth for helping with my project and advising me.

Big 'thank yous' go to all the other amazing scientists I met during my PhD. Especially, Jessica Bampton, who started the PhD with me and has become a true friend. I cannot believe we are at the end and I am glad that we went on this journey together.

I would like to thank my support cats – Zeus, Hermes and Purzi. It is very true that furry friends help relief stress and have healing powers with their endless purring.

## Acknowledgements

An enormous thank you goes to Jon. I am very grateful for the last 1.5 years. Thank you for listening to my complaints and worries. Thank you for your support, your understanding and for taking me to the beach when I needed to get away from everything.

Finally, the biggest 'thank yous' of all go to my friends and family in Germany who have always supported me from afar. Thank you to my best friends, Jenny Borchert, Aline Starzynski and Steffi Juergens. Although we cannot see each other very often, you have always been there for me and I am very lucky to call you my friends. Thank you to my parents and my little brother. You have always been there for me when I needed to talk. I am forever grateful for believing in me and for encouraging me to pursue my dreams and goals.

## Definitions and Abbreviations

ACD	Asymmetric cell division
ACTR1A	Alpha-centractin
AGS3	Activator of G-protein signalling 3
AJ	Adherens junctions
ANXA	Annexin
aPKC	Atypical protein kinase C
APS	Ammonium persulfate
BCA	Bicinchoninic acid
BRB80	Brinkley buffer 1980
BSA	Bovine serum albumin
CACNA1B	Voltage-dependent N-type calcium channel subunit alpha-1B
CAPZ	Actin-capping protein subunit
CASP	Caspase
CCNB1	G2/mitotic-specific cyclin-B1
CDC42	Cell division control protein 42
CDK	Cyclin- dependent kinase
CELSR	Cadherin EGF LAG seven-pass G-type receptor 1
CEP78	Centrosomal protein of 78 kDa
CMV	Cytomegalovirus
DHC	Dynein heavy chains
Clasp1	CLIP-associating protein 1
CO <sub>2</sub>	Carbon dioxide

DAPI	4',6-diamidino-2-phenylindole
DCTN	Dynactin subunit
Dlg1	Disks large homolog 1
DMEM	Dulbecco's Modified Eagle Medium
DMSO	Dimethyl sulfoxide
DNA	Deoxyribonucleic acid
dNTP	Deoxyribonucleotide triphosphate
DPBS	Dulbecco's phosphate-buffered saline
dsRNA	Double-stranded ribonucleic acid
DTT	Dithiothreitol
Dvl	Dishevelled
DYNC1/2	Cytoplasmic dynein 1 intermediate chain 2
DYNLRB1	Dynein light chain roadblock-type 1
ECL	Enhanced chemiluminescence
E. coli	Escherichia coli
EDTA	Ethylenediaminetetraacetic acid
EGF	Epidermal growth factor
eGFP	Enhanced green fluorescent protein
EGTA	Ethylene glycol-bis( $\beta$ -aminoethyl ether)-N,N,N',N'-tetraacetic acid
EIF3E	Eukaryotic translation initiation factor 3 subunit E
ERM	Ezrin/Radixin/Moesin
EXP	Experiment
FACS	Fluorescence-activated cell sorting
FDR	False discovery rate

FPR	Formyl peptide receptors
FZD	Frizzled
G-protein	Guanine nucleotide binding protein
G <sub>1/2</sub>	Gap phase ½
GDT	Guanosine diphosphate
GNAI3	Guanine nucleotide-binding protein G(i) subunit alpha-3
GO	Gene ontology
GPSM2	G-protein-signalling modulator 2, LGN
GTP	Guanosine triphosphate
GTSE	G2 and S phase-expressed protein 1
HAUS	Homologues of augmin subunits
HCl	Hydrochloric acid
HEK293	Human embryonic kidney 293 cells
HBS	HEPES Buffered Saline
HEPES	4-(2-hydroxyethyl)-1-piperazineethanesulfonic acid
IAA	Iodoacetamide
IC	Intermediate chain
ID	Identification
INSC	Inscuteable
IP	Immunoprecipitation
Kb	Kilobase
KLD	Kinase, Ligase and Dpnl
KPNA2	Importin subunit alpha-1
LB	Luria-Bertani

## Definitions and Abbreviations

LC-MS/MS	Liquid Chromatography with tandem mass spectrometry
LGN	Leucin, Glycine, Asparagine
Lis1	Lissencephaly-1 homologue
M	Mitosis
MaSC	Mammary stem cells
MAP	Microtubule- associated protein
MAPK3	Mitogen-activated protein kinase 3
MDCK	Madin-Darby Canine Kidney
MgCl <sub>2</sub>	Magnesium chloride
MISP	Mitotic Spindle Positioning
Mo-MLV	Moloney murine leukemia virus
mRNA	Messenger ribonucleic acid
MS	mass spectrometry
MT	Microtubules
MTOC	Microtubule-organising centre
Na <sub>3</sub> Vo <sub>4</sub>	Sodium orthovanadate
NaCl	Sodium chloride
NaF	Sodium fluoride
NEBD	Nuclear envelope breakdown
NuMA	Nuclear mitotic apparatus protein
OCD	Oriented cell division
PAGE	Polyacrylamide gel electrophoresis
Pals1	Protein associated with Lin-7 1
Par3	Partitioning defective 3

PCR	Polymerase chain reaction
PFA	Paraformaldehyde
pH3	Phospho- histone 3
PIPES	Piperazine-N,N'-bis(2-ethanesulfonic acid)
PK	Prickle
PLA	Proximity ligation assay
PLK	Polo-like kinase
PMSF	Phenylmethylsulfonyl fluoride
PPI	Protein-protein interaction
PTPN11	Tyrosine-protein phosphatase non-receptor type 11
Ran	Ras-related nuclear protein
RNAi	Ribonucleic acid interference
ROI	Region of interest
Rpm	Revolutions per minute
RT	Room temperature
S	Synthetic phase
SAA1	Serum amyloid A 1
SAC	Spindle assembly checkpoint
SAPCD2	Suppressor APC Domain Containing 2
SCD	Symmetric cell division
Scrib	Scribble
SDS	Sodium dodecyl sulfate
SEM	Standard error of the mean
siRNA	Small interfering ribonucleic acid

S.O.C	Super Optimal broth with Catabolite repression
STRING	Search Tool for the Retrieval of Interacting Genes/Proteins
TAE	Tris-acetate-EDTA
TAS T	Traceable Author Statement
TBS/T	Tris-buffered saline with Tween 20
TCA	Trichloroacetic acid
TEMED	Tetramethylethylenediamine
TJ	Tight junction
TPR	Tetratricopeptide repeat
TPX2	Targeting protein for Xklp2
TUBG1	Tubulin gamma-1
UV	Ultraviolet
Vangl	Van Gogh
WT	Wild type
$\gamma$ TuRC	$\gamma$ -tubulin ring complex
2D	Two-dimensional
3D	Three-dimensional

# Chapter 1 Introduction



Cell division has been studied since the early 1880s when Walther Flemming coined the term “mitosis” after observing and describing the behaviour of chromosomes during cell division (Flemming, 1882). In the following decades, the basic processes of mitosis were described. Cell imaging studies in the 1920s to 1950s and later work with advanced technologies led to a detailed, but still incomplete, summary of cell division including descriptions of spindle dynamics, regulatory mechanisms at the molecular level and an extensive list of involved proteins (Mitchison and Salmon, 2001). Although a large number of essential mitotic processes and often involved protein functions are now known, the number of new regulators and pathways is still growing and not all are completely understood mechanistically (Yanagida, 2014).

The basis of cellular diversity and tissue morphology is built on a balance of different cell divisions, called oriented cell divisions (OCDs). These divisions form the overall architecture of an organism and must be tightly regulated because disruption of this balance may result in premature depletion of cell pools or abnormal growth (Malumbres and Barbacid, 2001; Gómez-López, Lerner and Petritsch, 2014). One fundamental mechanism that controls OCDs involves the alignment of the mitotic spindle along a specific cell axis (Morin and Bellaiche, 2011). Our present challenge is to understand the molecular events that underlie the orientation of the mitotic spindle. For example, extrinsic factors such as cell-cell contacts and polarity cues or intrinsic factors including cues at the cell cortex regulate spindle orientation (Vorhagen and Niessen, 2014). It is not well understood how these factors define a framework that coordinates the direction of cell division. Furthermore, most knowledge derives from invertebrate systems and only recent work has proposed conserved mechanisms in vertebrates (Neumuller and Knoblich, 2009; Siller and Doe, 2009). Therefore, it is now determined that spindle orientation plays a crucial role in different mammalian tissues, including retina, brain, mammary tissue and hair follicles. Whether this process is universal for epithelial differentiation and architecture remains poorly understood (Williams and Fuchs, 2013; Santoro *et al.*, 2016).

Identifying novel factors that regulate spindle orientation and uncovering the molecular mechanisms of the tissue-specific signalling and regulation of spindle orientation is critical to provide new insights into normal tissue biology, but also enhance our understanding of how imbalance of OCDs contributes to diseases.

## 1.1 The mammalian cell cycle

The mammalian cell cycle is a highly ordered sequential process that culminates in the generation of two daughter cells. It consists of four phases including a round of chromosomal DNA replication (Synthetic or S phase) and division of cellular compounds between two daughter cells (Mitosis or M phase). Between those phases, two 'gap' periods ( $G_1$  and  $G_2$ ) assure cell growth and preparation for completion of S and M phases. The time between M phase is also called interphase. If cells cease division, they leave  $G_1$  phase and enter a senescent (irreversibly non-proliferative) or quiescent state ( $G_0$ ) where cells are metabolically active but non-proliferative (Figure 1.1) (Norbury and Nurse, 1992; Israels and Israels, 2000).

During mitosis, replicated DNA, condensed to chromosomes, equally distributes into two daughter cells which is followed by cytokinesis, the physical division of the two new cells (Flemming, 1882; Wilson, 1928). Mitosis consists of different stages starting with prophase where the chromatin condenses, and spindle poles begin building the mitotic spindle at opposite sides of the cell. Concomitantly, mitotic entry is accompanied by major cytoskeleton remodelling and change of the cell shape via reorganization of the cell cortex (Rizzelli *et al.*, 2020). The cortex is a network of actin filaments (F-actin) with myosin motors tethered to the plasma membrane<sup>1</sup>. F-actin is organized as a dense cross-linked meshwork which responds to stresses and intracellular signalling. During the first phase of mitosis, the cortex reorganizes into a contractile cortex that is thinner and stiffer. In order to maintain this cortex, a protein called vimentin accumulates as a thin layer beneath F-actin which controls cortical tension (Serres *et al.*, 2020). This tension is needed to promote cell rounding that maintains until the end of mitosis. This is important to generate enough intracellular space for spindle assembly and chromosome capture (Chugh and Paluch, 2018). In prometaphase, the nuclear envelope disassembles (also called nuclear envelope breakdown, NEBD) and growing microtubules (MTs) from the spindle poles attach to the kinetochores at the chromosomes which leads to movement of the chromosomes (Schrader, 1953; Bajer and Mole-Bajer, 1972; Karsenti and Vernos, 2001). Simultaneously, growing MTs extend towards and interact with the cell cortex to position the mitotic spindle in a central position within the cell (di Pietro, Echard and Morin, 2016).

---

<sup>1</sup> For simplicity, when the word "cortex" was used in this thesis, it was referred to the inner surface of the plasma membrane unless otherwise specified.

Chromosome movement continues in metaphase until they align in the metaphase plate (ÖSTERGREN, 1951; Rieder and Salmon, 1994). Once the chromosomes are positioned correctly, sister chromatids are segregated by pulling forces between the kinetochores and spindle poles during anaphase. Simultaneously, spindle poles separate from each other as the mitotic spindle elongates (Wilson, 1928; Goldstein, 1993). With the equal partitioning of genetic material, mitosis finishes with telophase where chromosomes reach the spindle poles and decondense as a nuclear envelope reforms around each set of chromosomes. Simultaneously, the mitotic spindle starts to break down (Gerace and Burke, 1988; Alberts, Johnson and Lewis, 2002).

From anaphase onwards until telophase, mitosis is accompanied by the final process of the cell cycle called cytokinesis. At this stage actomyosin contractility redistributes to the equatorial plane leading to formation of a contractile ring which shrinks and pinches the plasma membrane until two separate cells arise and new cell cycles begin (Figure 1.1) (Salmon, 1989).

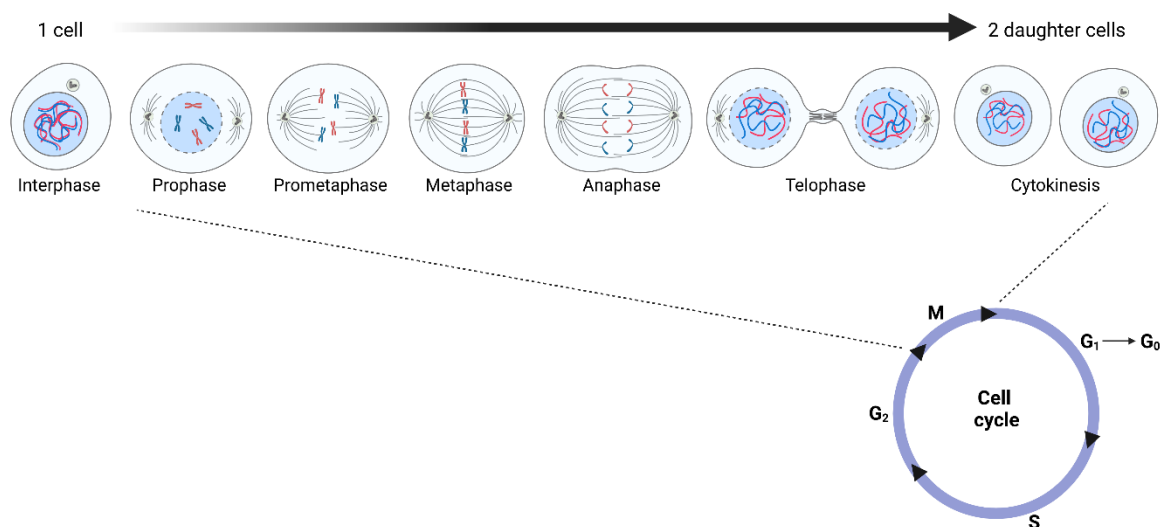


**Figure 1.1 Mammalian cell cycle and phases of mitosis**

*The cell cycle consists of two gap phases,  $G_1$ , and  $G_2$ , the S phase and mitosis (M). The time between M phase is called interphase. Cells can leave the cycle and enter a quiescent state ( $G_0$ ). During M phase, DNA is condensed into chromosomes (prophase) and becomes attached to the growing mitotic spindle after nuclear envelope breakdown (prometaphase). Chromosomes align along the equator of the cell (metaphase) and pulling forces generated from the mitotic spindle separate sister chromatids (anaphase). After pulling chromatids to opposite sides of the cell, a nuclear envelope forms around each set of chromosomes that start to decondense (telophase). Simultaneously, the cytoplasm of the parent cell is divided generating two daughter cells (cytokinesis) and a new cell cycle begins.*

Progression through the cell cycle is driven by the cyclin-dependent kinase (CDK) family and their regulatory partners called cyclins (Lim and Kaldis, 2013). Cyclins are proteins that accumulate and degrade during the cell cycle in a sequential manner to activate and inactivate CDKs (Johnson & Walker, 1999). Cyclin/CDK complexes phosphorylate specific proteins to initiate the next phase at distinct cell cycle stages. The first time point in the cell cycle where D cyclins form complexes with CDK4 and CDK6 to regulate progression is called restriction point. At this moment, cells commit to DNA synthesis and do not longer require growth factors that were necessary before to move through  $G_1$  towards S phase (Pardee, 1974; Blagosklonny and Pardee, 2002; Williams and Stoeber, 2012). To progress further from  $G_1$ , cyclin E/CDK2 drives entry into S phase and initiation of DNA replication. Soon after, cyclin A/CDK2 is present to control S phase progression. Lastly, cyclin B/CDK1 promote going forward through  $G_2$  and entry into mitosis (Figure 1.2) (Israels and Israels, 2000; Obaya and Sedivy, 2002).

In order to complete the cell cycle error-free, several regulatory mechanisms exist that ensure that all events in each phase are completed before entering the next stage. Thus, surveillance mechanisms, called checkpoints, monitor appropriate cell size, DNA replication, integrity of chromosomes and accurate chromosome segregation. When these mechanisms detect errors or incomplete cell cycle phases, such as DNA damage or inaccurate chromosome segregation, cell cycle delay is initiated until the problem is solved or complete cycle arrest is triggered (Kaufmann and Paules, 1996; Israels and Israels, 2000; Williams and Stoeber, 2012). DNA damage can be detected at checkpoints in  $G_1$ , S and at the  $G_2$ /M transition phase. The first checkpoint is critical to prevent cells with DNA double-strand breaks to initiate DNA replication. If the checkpoint is triggered, cyclin E/CDK2 is silenced and cells do not proceed to S phase. Another checkpoint detects DNA damage during S phase where further replication is prevented (Segurado and Tercero, 2009; Visconti, Della Monica and Grieco, 2016). If cells experience DNA damage or possess not fully replicated DNA during  $G_2$ , the  $G_2$ /M checkpoint prevents entry into mitosis by inhibiting cyclin B/CDK1 (Kastan and Bartek, 2004).

The final checkpoint of the cell cycle constitutes the spindle assembly checkpoint (SAC) that prevents chromosome segregation defects and thus incorrect partitioning of genomic material. The SAC prevents anaphase progression by delaying degradation of cyclin B until the mitotic spindle is completely assembled. Once the SAC is satisfied, cells can progress through mitosis which ensures maintenance of genome stability and generation of two new genetically identical daughter cells (Figure 1.2) (Lara-Gonzalez, Westhorpe and Taylor, 2012; Visconti, Della Monica and Grieco, 2016).

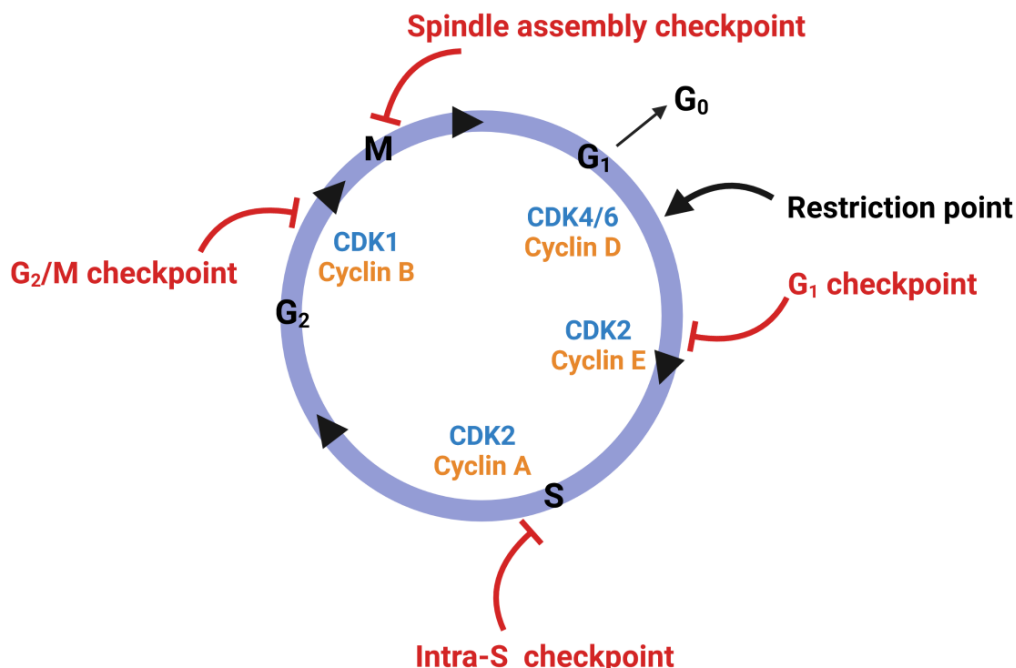


**Figure 1.2 Regulation and checkpoints of the mammalian cell cycle**

The mammalian cell cycle is regulated by protein complexes that consist of cyclin-dependent kinases (CDKs) that are bound to cyclins. These complexes are active at specific cell cycle phases. G<sub>1</sub> progression is controlled by CDK4 and CDK6 containing cyclin D types that control the restriction point. This is the point of no return in the cell cycle and cells commit to move towards S phase. The transition to S phase is initiated by a cyclin E/CDK2 complex and cyclin A/CDK2 regulate progression to G<sub>2</sub>. Cyclin B/CDK1 regulates the entry into M phase. Several checkpoint mechanisms (highlighted in red) can inhibit cycle progression at specific phases when it is not permitted to prevent progression of cells with defects.

### 1.1.1 Assembly and organisation of the mammalian mitotic spindle

The assembly and positioning of the mitotic spindle during mitosis are crucial for the correct segregation of chromosomes (Prosser and Pelletier, 2017). The mitotic spindle is a bipolar, self-organising macromolecular machine that is constructed from MT polymers, MT-associated proteins (MAPs) and motor proteins (Sharp, Rogers and Scholey, 2000; Walczak and Heald, 2008). MTs are long cylinders of 13 linear polymers (protofilaments) assembled from dimers of  $\alpha$ - and  $\beta$ -tubulin. MTs undergo very dynamic instabilities with sudden changes of growth and shrinkage, and switching back to growth (rescue). Shrinkage of MTs, called catastrophe, leads to disassembly of  $\alpha/\beta$ -dimers and thus shortening of MTs. The more dynamic end of MTs (plus-end) grows and shrinks

while the other end (minus end) does not change (Figure 1.3). This is important for the assembly and positioning of the mitotic spindle as well as for the aligning of the chromosomes (Amos, 2004; McIntosh *et al.*, 2010; Gardner, Zanic and Howard, 2013).

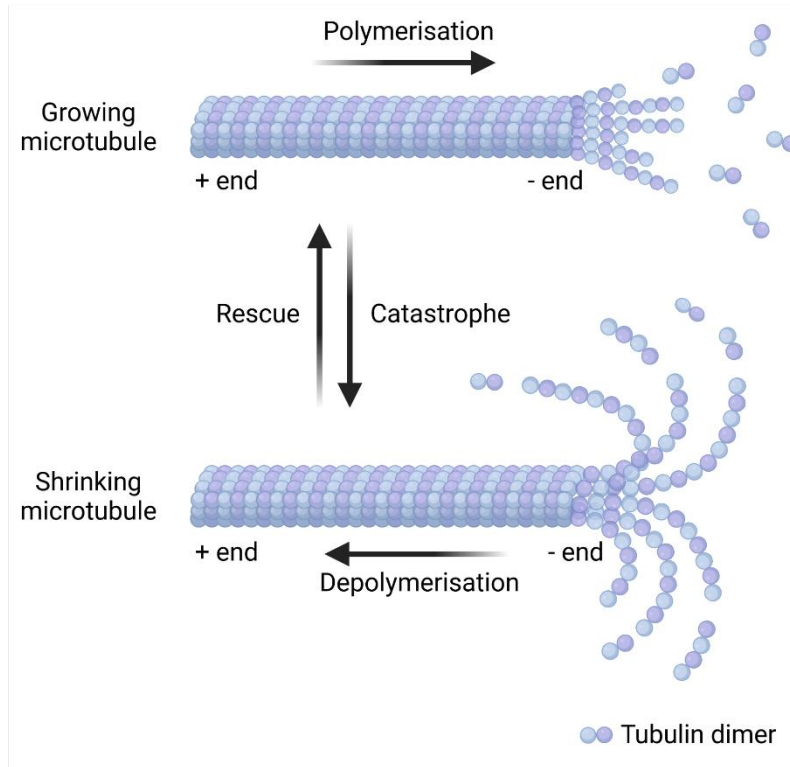


**Figure 1.3 Dynamic instability of microtubules**

*Microtubules are built of 13 protofilament cylindrical polymers which are assembled from  $\alpha$ - and  $\beta$ -tubulin dimers. The dynamic plus end (+ end) grow and shrink whereas the indynamic minus ends (- ends) remain unchanged. Microtubules switch between polymerisation and depolymerisation by incorporating tubulin dimers into growing or disassembling dimers from shrinking microtubules. Transition from growth to shrinkage is called catastrophe and returning to growth is known as rescue.*

To assemble the mitotic spindle at mitosis, cells already prepare for this event earlier in the cell cycle. Cells possess only one centrosome with two centrioles that is duplicated during early S phase. At G<sub>2</sub>/M transition, the duplicated centrosomes that are surrounded by pericentriolar material are located at the nuclear envelope and start to separate. This instructs the formation of the two spindle poles as the foundation of the bipolar spindle (Kellogg, Moritz and Alberts, 1994; Holland, Lan and Cleveland, 2010). After moving apart, centrosomes start nucleating MTs to form the spindle

structure (Petry, 2016). The nucleation of MTs is regulated by the  $\gamma$ -tubulin ring complex ( $\gamma$ TuRC) and related  $\gamma$ -tubulin complexes. Although it is not fully understood, it was suggested that  $\gamma$ -tubulin molecules within the complex interact with  $\alpha/\beta$ -tubulin dimers to assist the association between dimers during protofilament assembly. Thus,  $\gamma$ TuRC regulates MT growth in a spatial and temporal manner during mitosis (Tovey and Conduit, 2018; Zupa *et al.*, 2021). This allows that slow-growing minus-ends of MTs are focused into spindle poles, while fast-growing plus-ends switch between states of polymerization and depolymerisation during stretching into the cytoplasm (McIntosh and Euteneuer, 1984; Petry, 2016). In addition to MT nucleation from centrosomes as one MT-organizing centre (MTOC), additional pathways exist (Petry, 2016; Prosser and Pelletier, 2017). Another MTOC constitutes the spindle itself (Petry, 2016)., MTs within the spindle can branch off from various positions and converge towards the spindle poles. It was suggested that this is also regulated by the  $\gamma$ TuRC. In this context the protein complex Augmin was discovered which consists of 8 Homologues of augmin subunits (Haus) (Goshima *et al.*, 2008; Lawo *et al.*, 2009). This complex interacts with MTs to connect the  $\gamma$ TuRC with pre-existing MTs to nucleate more in a branched way (Goshima and Kimura, 2010; Lee and Liu, 2019). These MTOCs allow continuous MT nucleation that build and maintain the spindle.

Assembled mitotic spindles contain hundreds of MTs comprising several categories that support the shape by balancing forces that act on the spindle (Figure 1.4). These classes of MTs differ in their location and stability (Hoyt and Geiser, 1996; Petry, 2016). MTs that extend inwards to interact with the kinetochore structures of chromosomes are called kinetochore MTs or kinetochore fibers. Kinetochore fibers consists of about 20-25 parallel MTs. These bundles are the most stable but very dynamic MTs in the metaphase spindle. Kinetochore fibers undergo a process called biorientation with cycles of growth and shrinkage, randomly searching the cytoplasm until finding kinetochores resulting in capture of chromosomes near the spindle equator. The stability of these MTs is finely regulated to allow stable attachment to chromosomes and release of MT plus-ends from kinetochores to promote correct attachment of the chromosomes to the correct spindle pole during the biorientation process (McEwen *et al.*, 1997; DeLuca *et al.*, 2006; Tolić, 2018).

Other two classes of MTs that grow towards the spindle centre and have free ends are often called polar MTs and those that interact laterally with antiparallel MTs emerging from the opposite pole are known as interpolar MTs. The latter also exist in bundles and are less stable but very dynamic. They are essential for the structural integrity of the spindle by exerting sliding motions between antiparallel MTs which is powered by motor proteins, mainly kinesin members and dynein. This maintains the spindle structure during metaphase and allows spindle elongation during anaphase (Petry, 2016; Tolić, 2018).

The last class of MTs, called astral MTs, elongate outwards and towards the cell cortex. These MTs are highly dynamic and are essential to anchor and position the spindle within the cytoplasm. MT nucleation from the centrosomes and stability of astral MTs controls the number and length of MTs reaching the cell cortex. For this, once MT plus-ends contact the cell cortex, they undergo catastrophe and shrink. This is essential to establish the correct size of the spindle within the cell during assembly. Simultaneously, astral MT are regulated from the cell cortex where the dynein/dynactin motor complex binds to the MTs and pulls them towards the cortex. This fine interplay between MTs catastrophe and pulling forces allows correct organization and dynamics of the mitotic spindle (Siller and Doe, 2009; Morin and Bellaiche, 2011; di Pietro, Echard and Morin, 2016).

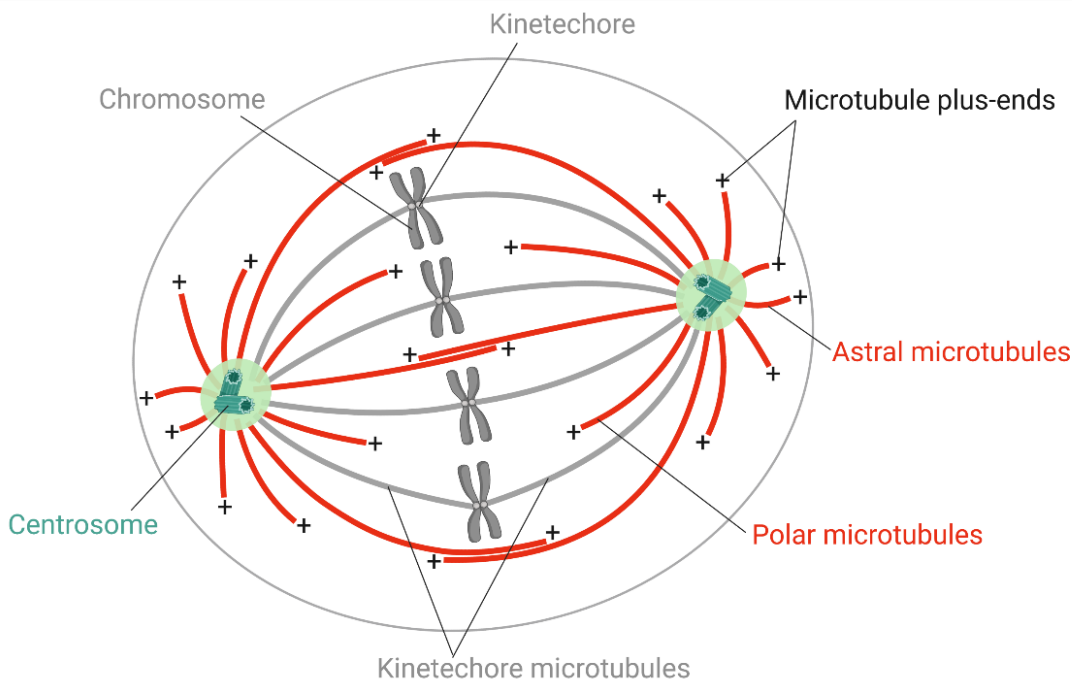


**Figure 1.4 Key components of the mitotic spindle**

*The mitotic spindle is a bipolar self-organizing structure. Three classes of microtubules are focussed with their minus-ends into spindle poles which are composed of centrosomes surrounded by pericentriolar material. Poles nucleate microtubules where microtubule plus-ends extend into the cytoplasm. Inter-polar microtubules are cross-linked with each other and kinetochore microtubules attach to kinetochores of the chromosomes. Astral microtubules extend towards the cell cortex above spindle poles.*

## 1.2 Epithelial polarity

Epithelial tissues comprise compactly packed juxtaposed cells that outline the cavities and surfaces of the body to form organ and appendage structures. They serve as a physical barrier to preserve physiological functions. These tissues can be mono- or multi-layered where each cell is tightly linked to its neighbours via several cell-cell contacts (Le Bras and Le Borgne, 2014; Rodriguez-Boulan and Macara, 2014).

One structural and functional hallmark of epithelia is that cells are highly polarised along an apical-basal axis and connected to each other by lateral junctions. This cell polarity is further polarised in a coordinated alignment across the plane of a tissue which is referred to as planar cell polarity (PCP) or tissue polarity. Cell and tissue polarity are essential for normal physiological function of many epithelia (St Johnston and Sanson, 2011; Rodriguez-Boulan and Macara, 2014).

### 1.2.1 Cell polarity

Cell polarity is defined by asymmetric distribution of cellular components within a single cell which results in apical-basolateral polarity (Macara, 2004). Three major complexes comprise the core proteins that establish this polarity by interacting and mutually excluding each other. These are the apical Crumbs and Par complexes and the basolateral Scribble complex (Figure 1.5). These complexes overlap at the apical-lateral border which comprise tight junctions (TJs) and below-situated adherens junctions (AJs). These junctions constitute the fusion point of membrane of two adjacent cells to provide cell-cell contacts (Nelson, 2003; Hartsock and Nelson, 2008; St Johnston and Sanson, 2011)

The Crumbs complex consists of Crumbs (Crb), protein associated with Lin-7 1 (Pals1) and Pals1-associated tight junction protein (PATJ). To define the apical domain, the Crumbs complex accumulates at the apical membrane near the apical-lateral border. A key function of this complex is to exclude the Par complex from the apical cell surface. For this, Pals1 binds to one member of the Par complex called partitioning-defective-6 (Par6) (Pieczynski and Margolis, 2011; St Johnston and Sanson, 2011). The other proteins in the Par complex are Par3 and atypical protein kinase C (aPKC). Par3 localisation and activity is regulated by aPKC phosphorylation and directly associates with TJs to prevent the extension of TJs into apical sites. Par6 and aPKC also maintain the integrity of the apical domain (Goldstein and Macara, 2007; Martin-Belmonte and Mostov, 2008). Another protein involved in this, is the cell division control protein 42 (Cdc42) that exists in a complex with Par3/Par6/aPKC by binding to Par6 and associating the complex with the cell cortex (Joberty *et al.*,

2000). Par6 and aPKC also bind to the lateral polarity complex to restrict it to lateral sites beneath TJs. This lateral complex consists of Scribble (Scrib), Lethal giant larvae (Lgl) and Disc large (Dlg) which antagonizes apical complex activity to define specific polarity domains (Figure 1.5) (Su *et al.*, 2012).

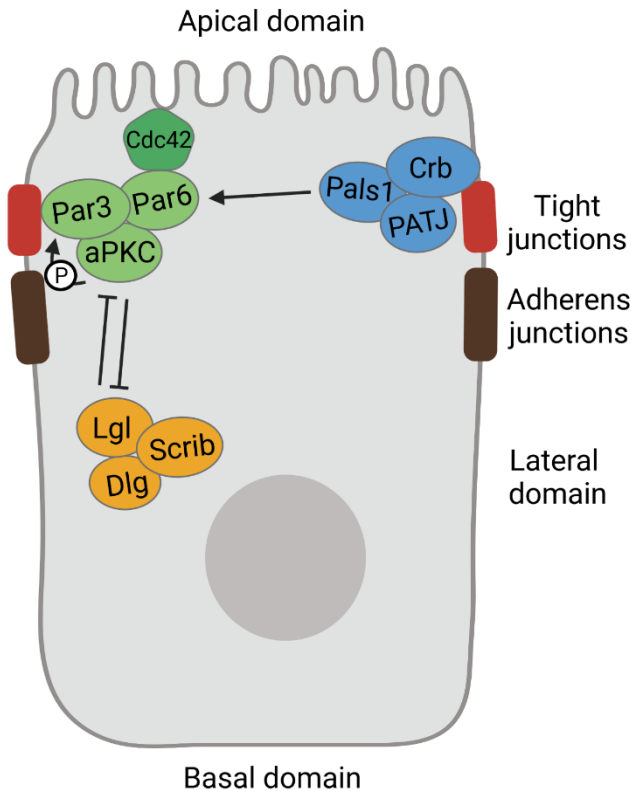


**Figure 1.5 Localisation of cell polarity complexes in epithelial cells**

*Epithelial cells establish cell polarity through interconnection of three polarity complexes that define the apico-basolateral domains. The Par and Crumbs complexes localise to the apical membrane and Par3 of the Par complex associates with tight junctions. Furthermore, the Par complex is bound to Cdc42 which stabilizes the complex at the apical membrane APKC phosphorylates Par3 to activate and localise the protein. The Par and Crumbs complex associate with each other via binding of Pals1 and aPKC The Scribble complex localises to the lateral domain. The scribble and Par complex antagonise each other to maintain their specific localisation within a cell (inhibition arrow)*

*Abbreviations: aPKC, atypical protein kinase C; Cdc42, cell division control protein 42; Crb, Crumbs 3; Dlg, Discs-large; Lgl, lethal giant larvae; Pals1, protein associated with Lin-7 1; Par, partitioning-defective; PATJ, Pals1-associated tight junction protein; Scrib, Scribble.*

### 1.2.2 Tissue polarity

PCP controls coordinated behaviour of group of cells within epithelia that is especially important during development, homeostasis and tissue repair (Goodrich and Strutt, 2011). Two signalling pathways govern this polarity by regulating the complementary and mutually exclusive distribution of several proteins that generates a distinct asymmetric distribution of these proteins within each cell (Butler and Wallingford, 2017). The transmembrane or core pathway consists of the proteins Frizzled (Fzd), Van Gogh (Vangl) and Cadherin EGF LAG seven-pass G-type receptor 1 (Celsr). This pathway is important to exchange polarity information between cells. The cytoplasmic pathway comprises the proteins Dishevelled (Dvl), Prickle (Pk) and Diversin which amplify intracellular asymmetry and translate polarity cues into cell behavioural changes (Strutt, 2008; Devenport, 2016). To generate an asymmetric localisation and polarity, Fzd, Dvl and diversin accumulate at junctions on one side of the cell whereas Vangl and Pk localise to the other. The atypical cadherin Celsr positions on both sides and bridges Fzd and Vangl between neighbouring cells. The resulting asymmetric cell pattern and more globally the tissue pattern coordinates the orientation of subcellular structures and cell behaviours by regulating cytoskeleton dynamics and cellular adhesion (Devenport, 2014; Butler and Wallingford, 2017).

## 1.3 Oriented cell division in epithelial systems

OCDs are a fundamental process that shapes proliferating and growing tissues. The underlying mechanisms have been implicated in the embryonic development of multicellular organism and in adult tissue morphogenesis (Castanon and Gonzalez-Gaitan, 2011). OCDs depend on coordinated spatiotemporal control of cell division and on direction of division, thus orientation of the mitotic spindle. The principles of spindle orientation have been part of extensive research over the past decades and initial studies in invertebrate systems have elucidated essential conserved pathways. More recent studies identified tissue-mediated regulatory mechanisms in different organs in vertebrate systems which highlighted its relevance to mammalian systems, especially its importance for epithelial tissue (Seldin and Macara, 2017; Lechler and Mapelli, 2021).

The polarised architecture of epithelia is maintained by proliferating cells that balance growth and homeostasis throughout development and homeostasis. For this, cell division occurs where the

mitotic spindle aligns along a cell axis that is either planar or perpendicular to the tissue axis. To allow expansion and elongation in two dimensions (2D), the spindle orientates planar which results in two daughter cells that remain in the same epithelial layer. This ensures simple growth of epithelial sheets. When the epithelium needs to thicken and to form multiple layers, the spindle actively aligns perpendicular which results in displacement of one daughter cell into a different tissue layer (Figure 1.6). Examples of OCDs in epithelia are development of the epidermis, hair formation and linings of the salivary ducts (Noatynska, Gotta and Meraldi, 2012; Williams and Fuchs, 2013; Panousopoulou and Green, 2014; Vorhagen and Niessen, 2014).

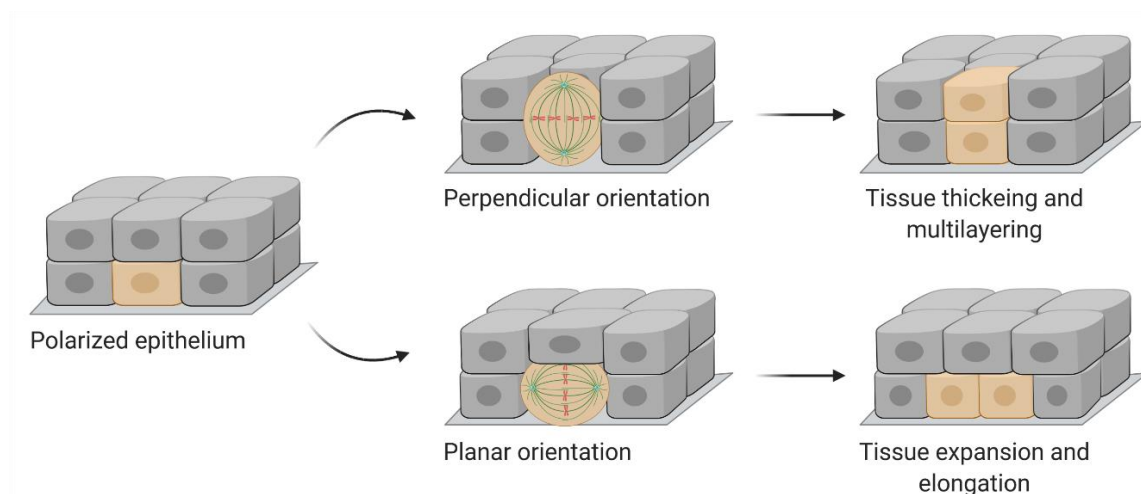


**Figure 1.6 Modes of oriented cell divisions**

*In polarised epithelia, the mitotic spindle is either oriented perpendicular (top) or planar (bottom). Perpendicular alignment results in placement of one daughter cell into a different tissue layer. This is important to generate multilayering and a certain thickness of tissues. When the mitotic spindle orientates planar, both daughter cells are born in the same plane of the tissue. This generates tissue expansion and elongation. Modified from Ragkousi & Gibson, 2014.*

The orientation of the mitotic spindle is often coupled with fate decisions of daughter cells resulting in symmetric (SCDs) or asymmetric (ACDs) stem cell divisions (Seldin and Macara, 2017). Epithelial cells typically align the spindle planar for SCDs resulting in two equivalent daughter cells that adopt the same fate. This generates expansion of cell populations. ACDs generate two daughter cells that adopt different cell fates. For this, the mitotic spindle aligns within a specific cell polarity axis and cell fate determinants unequally partition into daughter cells. One example of such cell fate determinants is Numb. This adapter protein controls fate specification by segregating to only one

daughter cell. This results in differential fate decisions which promotes cellular diversity within the tissue (Horvitz and Herskowitz, 1992; Gulino, Di Marcotullio and Screpanti, 2010; Morin and Bellaiche, 2011; van Leen, di Pietro and Bellaïche, 2020). However, this knowledge mainly arises from invertebrate systems and the role of spindle orientation during ACDs is less clear in vertebrate epithelia. For example, it was shown that the spindle aligns perpendicular to promote differential cell fate in the skin (Williams *et al.*, 2011). Whether similar mechanisms exist in other epithelia is not clear. Therefore, it is now appreciated that spindle orientation and cell fate are coupled but more studies are urgently needed to elucidate how cells balance between division modes to control tissue architecture and cell fate in advanced epithelia tissues (Ray and Lechler, 2011; Williams and Fuchs, 2013).

### 1.3.1 Mechanisms of mitotic spindle orientation

The central part in mitotic spindle orientation plays an evolutionary conserved ternary complex, referred to as spindle orientation complex. This complex consists of Gai subunits of heterotrimeric Guanine nucleotide binding proteins (G-proteins), leucine-glycine-asparagine (LGN) and nuclear mitotic apparatus (NuMA). The complex directs planar as well as perpendicular spindle orientation which is achieved by being localised either to the lateral or apical cortex, respectively (Morin and Bellaiche, 2011; Seldin and Macara, 2017). The spindle orientation complex recruits the dynein/dynactin motor complex, forming the spindle orientation machinery that executes spindle positioning (Figure 1.7) (Zheng *et al.*, 2013; Nakajima, 2018).

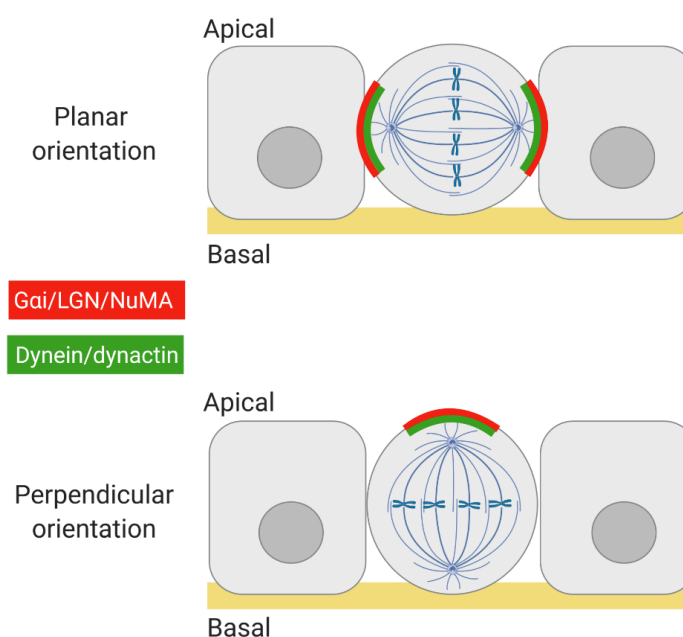


**Figure 1.7 Hierarchy of the cortical spindle orientation machinery in oriented cell divisions**

**Figure 1.7 Continued**

*In polarised epithelia, the core spindle orientation complex consisting of Gai subunits, LGN and NuMA recruits the dynein/dynactin motor complex to form the spindle orientation machinery that positions the mitotic spindle within the cell. The complex localises to the lateral cortex to promote planar orientation or accumulates at the apical site to position the spindle in a perpendicular orientation.*

**1.3.1.1 The core protein machinery of mitotic spindle orientation**

One member of the spindle orientation machinery, Gai, is a subclass of the  $\alpha$  subunit of heterotrimeric G-proteins. These proteins locate at the inner leaflet of plasma membranes and are composed of G $\alpha$ , G $\beta$  and G $\gamma$  subunits. G $\alpha$  subunits are guanosine diphosphate (GDP) -bound and associate with G $\beta\gamma$  dimers. When GDP on G $\alpha$  is exchanged with guanosine diphosphate (GTP), it leads to dissociation of the subunit from G $\beta\gamma$  and subsequently to binding of downstream effectors near the membrane (McCudden *et al.*, 2005a; Syrovatkina *et al.*, 2016). To localise correctly below the plasma membrane, the N-terminus of the G $\alpha$  subunit is modified by binding of the fatty acid myristate in a lipid modification called myristoylation (Syrovatkina *et al.*, 2016). During cell division, Gai subunits serve as an anchor to the spindle orientation machinery at the cell cortex (Du and Macara, 2004).

Vertebrate LGN, also called G-protein-signalling modulator 2 (GPSM2) is a 77 kDa protein that was identified as a binding partner of Gai subunits. The finding of LGN repeats in the N-terminal half of the sequence designated the protein's name (Mochizuki *et al.*, 1996).

LGN is expressed ubiquitously in tissues. The protein sequence comprises 8 domain structures in the N-terminal region of the molecule, a linker region and 4 repeat domains at the C-terminus (Figure 1.8) (Mochizuki *et al.*, 1996; Zhu *et al.*, 2011b). The N-terminal repeats are tetratricopeptide repeats (TPR). These repeats are antiparallel  $\alpha$ -helices consisting of 3 to 16 tandem-repeats of 34 amino acids which mediate protein-protein interactions as well as the assembly of multiprotein complexes (Sikorski *et al.*, 1990; Perez-Riba and Itzhaki, 2019). The linker region that separates the N- and C-terminal domains has no recognizable organization or binding motifs but is crucial for LGN function (di Pietro, Echard and Morin, 2016). The linker contains several phosphorylation sites from which one of the serine residues was identified as a target of aPKC (Hao *et al.*, 2010). Furthermore, the protein Dlg1 binds to the linker region of LGN in a phosphorylation-dependent manner (Zhu *et al.*, 2011a; Saadaoui *et al.*, 2014). The four C-terminal domains of LGN were described as GoLoco

motifs. These motifs are 19 amino acid-long sequences that bind  $G\alpha$  subunits when they are in the monomeric inactive (GDP-bound) state (Siderovski, Diversé-Pierluissi and De Vries, 1999; McCudden *et al.*, 2005b; Khafizov, 2009). Of note, a vertebrate homologue of LGN exists termed activator of G-protein signalling 3 (AGS3). This protein comprises the same domain and motif structures and associates with  $G\alpha$  subunits in neuronal progenitor cells in the mouse embryonic cortex. Controversially, AGS3 is not able to rescue spindle orientation defects induced by LGN depletion but also has been shown to influence OCDs (Sanada and Tsai, 2005; Saadaoui *et al.*, 2017). Thus, AGS3 mechanisms are not clear and it remains unknown if the protein shares similar functions with LGN.

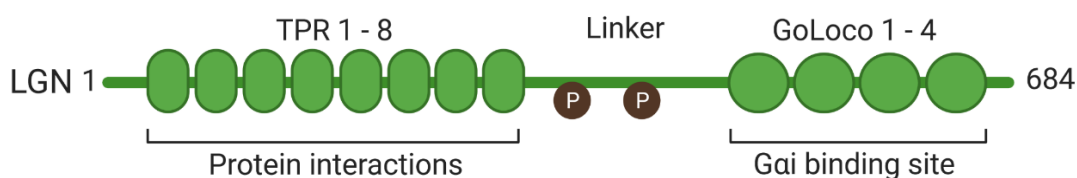


**Figure 1.8 Binding domains and motifs in the LGN sequence**

*Motifs and domain structures of the LGN sequence comprise GoLoco motifs that bind to  $G\alpha$  subunits at the cell cortex and TRP repeats that interact with other proteins such as NuMA. The central linker region harbours phosphorylation sites. Modified from Pirovano *et al.*, 2019.*

LGN simultaneously binds NuMA and  $G\alpha$ , and accumulates at the cell cortex during mitosis (Du and Macara, 2004). All four LGN GoLoco motifs can bind independently from each other to  $G\alpha$  subunits but with the same affinity (McCudden *et al.*, 2005b; Jia *et al.*, 2012). Before association with  $G\alpha$ , LGN exists in an inactivated form. The protein adapts a closed conformation via an intramolecular interaction between the TPR domains and GoLoco motifs (Du and Macara, 2004). In the closed state, GoLoco motifs 3 and 4 bind strongly with the TPR domain, whereas GoLoco motifs 1 and 2 seem to be less involved in this intramolecular interaction. Thus, GoLoco motif 1 is accessible and may bind to  $G\alpha$  to release the autoinhibited conformation. Once activated, the other  $G\alpha$  subunits are free to further bind to LGN. Additionally, LGN TPR repeats may be accessible to bind with other proteins including NuMA (Pan *et al.*, 2013; Takayanagi *et al.*, 2019).

NuMA is a ~240 kDa protein that is named after its nuclear localisation during interphase and redistribution to the cytoplasm during mitosis (Lydersen and Pettijohn, 1980). Specifically, after NEBD, NuMA localises to spindle poles and tethers MT minus-ends to the spindle poles during spindle assembly. Furthermore, the protein accumulates at the cell cortex concomitant with LGN (Merdes *et al.*, 1996; Du, Stukenberg and Macara, 2001). The protein consists of globular N- and C-terminal domains that are linked via a 1500 amino acid discontinuous coiled-coil motif (Figure 1.9) (Compton, Szilak and Cleveland, 1992). NuMA forms homodimers via its large central region. This coiled-coil region also plays a role in mitotic spindle orientation but the exact function is unspecified and has yet to be determined (Greenberg, Tan and Lee, 2018; Okumura *et al.*, 2018). The C-terminal region harbours binding sites for MTs, LGN and others, and also comprises the nuclear localisation signal (NLS) responsible for the nuclear localisation (Du *et al.*, 2002; Haren and Merdes, 2002; Gallini *et al.*, 2016). It was shown that all 8 TPR domains of LGN bind to NuMA and the proteins assemble in oligomers. These oligomers are organized as hetero-hexameric modules in which three LGN TRP domains interact with three C-terminal stretches of NuMA (Culurgioni *et al.*, 2011; Zhu *et al.*, 2011b; Pirovano *et al.*, 2019). Two MT binding sites exist where the first overlaps with LGN binding and its function is not clear, but the second region is compatible with LGN binding and is implicated in mitotic spindle orientation (Haren and Merdes, 2002; Gallini *et al.*, 2016).

Several studies showed that the N-terminal region of NuMA interacts with dynein (Kiyomitsu and Cheeseman, 2012; Kotak, Busso and Gonczy, 2012). Specifically, NuMA contains a Spindly-like motif that was recently identified as a conserved binding sequence for dynein and dynactin in the dynein/dynactin complex. This binding is essential to build the motor complex and to activate its motility (Gama *et al.*, 2017; Okumura *et al.*, 2018).

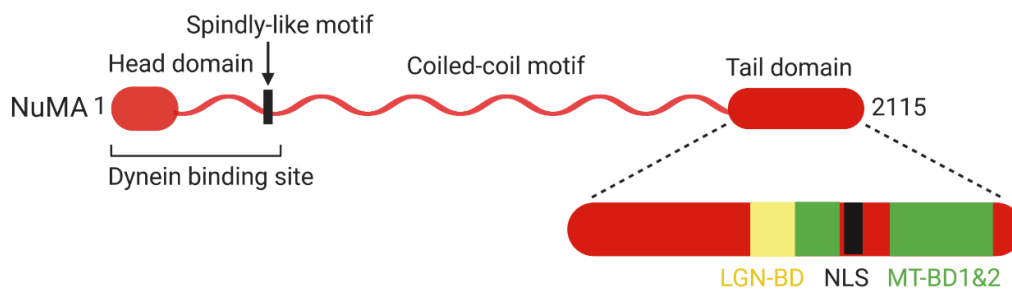


**Figure 1.9 Binding domains and motifs in the NuMA sequence**

The NuMA protein sequence comprises a head domain and a Spindly-like motif at the N-terminus that is essential for dynein binding. A central coiled-coiled motif connects the head with the tail domain in the C-terminal region. This part of the sequence harbours a LGN binding domain (LGN-BD), the nuclear localisation signal (NLS) and MT binding domains (MT-BD1/2). Modified from Kiyomitsu *et al.*, 2019.

The dynein/dynactin complex consists of the cytoplasmic motor protein dynein that transports cargos such as proteins, protein complexes, organelles or chromosomes along and towards the minus-ends of the MT cytoskeleton (Kardon and Vale, 2009). Dynein is a 1.6 MDa complex consisting of two adenosine triphosphatase (ATPase) motor domains and MT binding domains, forming dynein heavy chains (DHCs) that bind to MTs and harbour additional subunits. Each DHC binds an intermediate chain (IC) and light intermediate chain (LIC). The ICs further bind with three light chains (LCs) (Allan, 2011). It was suggested that NuMA binds to LICs to interact with dynein (Renna *et al.*, 2020). In order to function and enhance activity, dynein needs the dynactin complex as an adapter. This 1 MDa cofactor consists of more than 20 subunits, corresponding to 11 different proteins. Its structure is composed of a rod of uniform length that contains a polymer comprising the actin-related protein filament (Arp1A, Arp1B), a pointed end with Arp11 and the subunits p62, p27 and p25 as well as the heterodimeric actin-capping proteins CapZ (CAPZA and CAPZB) forming the barbed end (Moore, Li and Cooper, 2008). A flexible and extendable arm projects from the rod formed by dynactin subunits p22, p50 and p150<sup>Glued</sup> which protrudes as the flexible extension. P150<sup>Glued</sup> binds to dynein ICs and MTs (Figure 1.10) (Schroer, 2004; Urnavicius *et al.*, 2015). Together, the dynein/dynactin complex does not only transport cargoes, it can also exert tension on MTs (Roberts *et al.*, 2013).

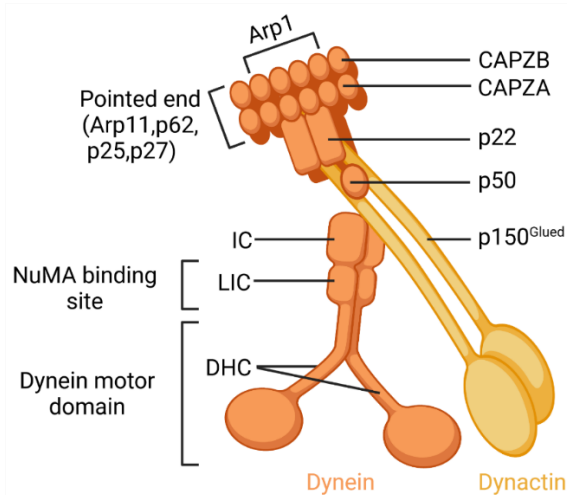


**Figure 1.10 Simplified model of the dynein/dynactin complex**

*Dynein is a motor protein consisting of several proteins. Two dynein heavy chains (DHCs) form the motor domain and bind to MTs. DHC comprise further subunits including light intermediate chain (LICs) and intermediate chains (ICs). The ICs bind to the dynactin complex which is necessary for dynein function. Dynactin consists of several subunits forming a rod on one side and an extendable arm on the other. This arm comprises the p150<sup>Glued</sup> protein that binds to MTs. Modified from di Pietro *et al.*, 2017.*

### 1.3.1.2 Current view of mitotic spindle positioning via the pulling force machinery at the cell cortex

Many studies in different organisms and tissues have identified mechanisms to position the mitotic spindle within a cell during mitosis and the general view focusses now on pulling mechanisms executed by the spindle orientation machinery that are counteracted by spindle-centering mechanism to ensure the successful rotation of the spindle (Zulkipli *et al.*, 2018; Lechler and Mapelli, 2021).

In this current perspective, specifically the pulling mechanisms have been intensively studied where the spindle orientation machinery starts to assemble at the cell cortex after NEBD to orientate the mitotic spindle in its final position during metaphase (Finegan and Bergstralh, 2019). In one hypothesis, the protein huntingtin transports members of the LGN complex and dynein/dynactin via astral MTs from the spindle poles to the cell cortex which depends on the plus-end directed motor protein kinesin 1 (Elias *et al.*, 2014). Once at the cortex, LGN is anchored to the cortex and activated by binding to Gai subunits which allows binding to NuMA. NuMA associates with the dynein/dynactin complex, possibly via association with its Spindly motif, thereby activating dynein's motility. Due to the hetero-hexameric NuMA/LGN structure, several NuMA/dynein/dynactin clusters may form at specific punctuate cortical foci which bind simultaneously to the plus-end of single astral MTs. In order to position the mitotic spindle, dynein/dynactin moves towards the spindle poles which generates a pulling force that results in movement of the spindle apparatus. In this context, dynein can inhibit astral MT growth and trigger MT catastrophes which prevents the colliding of MT plus-ends with the cell cortex and simultaneously allows the movement of the spindle towards the cortex. At the same time, pushing forces mediated by the polymerising MTs pushing forces maintain the mitotic spindle at the cell centre (Howard & Garzon-Coral, 2017).

Concurrent with this, NuMA binds to the plus-tips of astral MTs. It is possible that NuMA interacts with depolymerizing MTs and uses the energy to support spindle rotation, hence collaborates with dynein moving activity. Spindle pulling occurs until astral MTs reach cortical regions below the localisation of the spindle orientation complex which results in the position and maintenance of the mitotic spindle along a specific axis in the cell (Figure 1.11) (Laan *et al.*, 2012; Seldin, Muroyama and Lechler, 2016; Tuncay and Ebnet, 2016; Okumura *et al.*, 2018; Pirovano *et al.*, 2019).

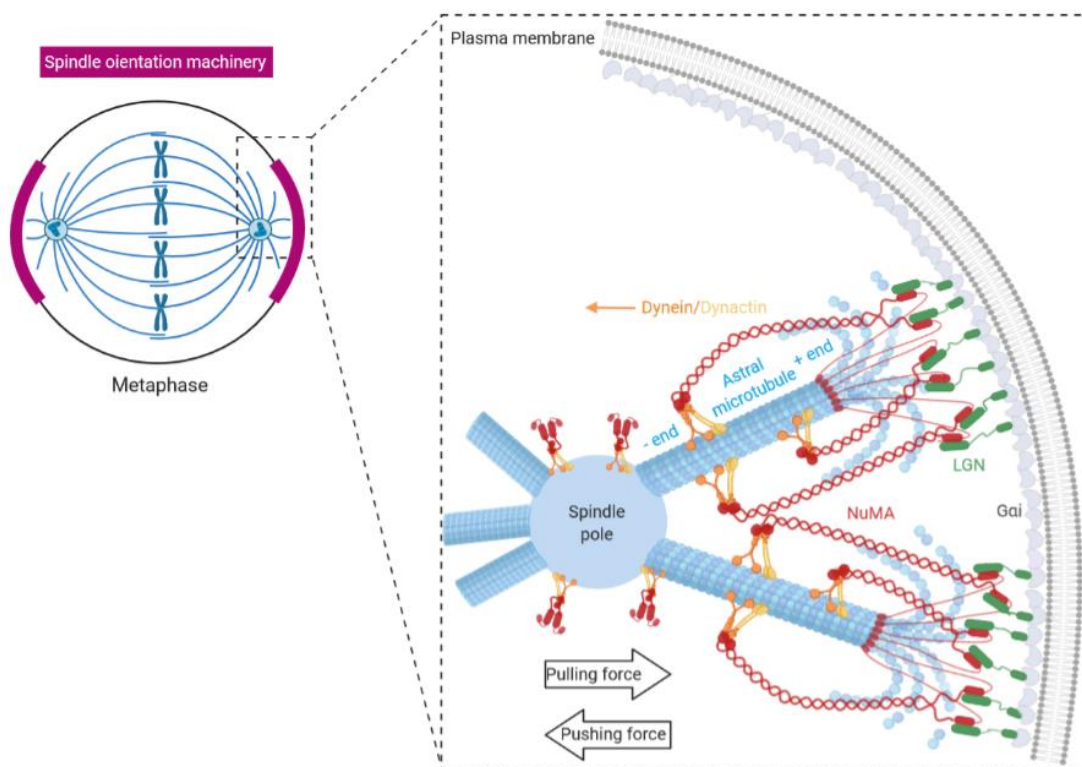


**Figure 1.11 Principle of cortical force generation to orientate the mitotic spindle**

*The schematic illustrates the current view of mitotic spindle orientation during metaphase. The LGN complex might be recruited to the cell cortex via transport along astral microtubules from the spindle pole. Gai subunits activate and anchor LGN to the cell cortex. NuMA binds to LGN and recruits the dynein/ dynactin complex. The motor complex binds to astral microtubules and moves towards the spindle pole generating a pulling force on the mitotic spindle towards the cell cortex whereas pushing forces maintain the spindle in the cell centre. Concomitantly, NuMA binds to astral MTs to support spindle positioning. Astral microtubules undergo catastrophes when reaching the cell cortex to ensure correct length of microtubules and to allow further pulling of the spindle until the final position is determined.*

Taken together, studies of the last 30 years revealed that Gai subunits and LGN function as receptors and a passive tether to specify the position of NuMA and the dynein/dynactin complex which constitute the cortical force generating machinery that captures and pulls on astral MTs to position the mitotic spindle within the cell. However, it is not well understood which signals restrict the spindle orientation complex to specific cortical sites when the complex starts to accumulate at the cortex to promote different division orientations. In addition, whether the LGN complex is always involved in spindle orientation is not clear and will be discussed below.

### 1.3.2 Regulation of mitotic spindle orientation

The mitotic spindle not only ensures faithful segregation of DNA but also defines the division plane as well as relative sizes and spatial organization of daughter cells. For this, the precise positioning of the mitotic spindle within the three-dimensional (3D) cellular environment is essential to allow error-free mitotic progression (Kotak, 2019; Rizzelli *et al.*, 2020). The control of mitotic spindle orientation is complex and requires several levels of regulatory mechanisms. These include cell geometry, external and tissue architectural cues as well as internal cues. Most but not all of them specifically regulate the localisation of the spindle orientation machinery to allow correct positioning of the spindle (di Pietro, Echard and Morin, 2016; Lechler and Mapelli, 2021).

#### 1.3.2.1 Cell geometry

Over a century ago, cellular geometry was proposed to control the plane of orientation where the elongated shape of the interphase cell determines the orientation of the mitotic spindle along the longest axis of the cell (Hertwig, 1884). This phenomenon is referred to as Hertwig's rule or long-axis rule and applies to many cell types showing that cell anisotropy acts as a major determinant of spindle orientation within the cell (van Leen, di Pietro and Bellaïche, 2020). Interestingly, due to cell rounding a certain level of memory exists in cells to remember the interphase shape in order to orient the mitotic spindle according to the long-axis rule (Cadart *et al.*, 2014). Different regulatory mechanisms were suggested in epithelia and it is not clear whether the default planar orientation along the longest axis of the cell accounts for a cell shape sensing mechanism alone or if the cortical force generating machinery is involved (Williams *et al.*, 2011; Bosveld *et al.*, 2016). Nevertheless, cell geometry plays an important role in mitotic spindle orientation.

#### 1.3.2.2 External and tissue architectural cues

Extrinsic cues can be provided by neighbouring cells and the extracellular matrix that sense signals to the dividing cell and thereby determine the division direction (Williams and Fuchs, 2013). Mechanistic understanding of such external cues greatly lags behind the knowledge about cell geometry and internal cues mainly because investigating these mechanisms is difficult and requires more advanced methodologies to analyse a tissue setting *in vivo* (Williams and Fuchs, 2013). Nevertheless, a contrary role for PCP has been proposed. During skin development, PCP regulates OCDs by favouring planar divisions possibly via *Celsr1* regulation (Oozer *et al.*, 2017; Bhattarai *et al.*, 2019). However, in this context PCP may not directly regulate spindle orientation and rather

PCP-induced cell geometry and packing of cells dictates mitotic spindle orientation (Box, Joyce and Devenport, 2019). Thus, the involvement of PCP in spindle orientation is not clear.

Because the fundamental property of epithelia is cell polarity, it can be seen as a prerequisite for the control of spindle orientation. In fact, the involvement of cell polarity in spindle orientation is established but the understanding of mechanisms is incomplete (Lechler and Mapelli, 2021). E-cadherin, a transmembrane cell-cell adhesion protein, was identified to sense and translate extrinsic signals to localise LGN to the lateral cortex during planar divisions in epithelia (Elzen *et al.*, 2009; Gloerich *et al.*, 2017). The cytosolic tail of E-cadherin can bind LGN which directs spindle orientation towards cell-cell adhesions (Gloerich *et al.*, 2017). Furthermore, E-cadherin bridges cell polarity and spindle orientation by forming a ternary complex with LGN and Scrib which possibly directs planar alignment of the mitotic spindle (Wang *et al.*, 2018). In addition, Dlg1 binding stabilizes LGN at the lateral domain (Saadaoui *et al.*, 2014). In this context, it was shown that phosphorylation of LGN by aPKC excludes LGN from the apical cell cortex and facilitates binding to Dlg1 which will ensure that cells undergo planar cell division (Hao *et al.*, 2010). The Par complex was also suggested in the regulation of spindle orientation. Par3 at the apical domain recruits the protein mammalian Insc (mInsc). In turn, mInsc links the polarity cue and the spindle orientation complex by forming a complex with Par3 and LGN (Lechler and Fuchs, 2005; Zigman *et al.*, 2005). In the developing epidermis, LGN forms a complex with Par3 and mINSC to promote accumulation of the spindle orientation machinery at the apical cortex to subsequently orientate the mitotic spindle perpendicular to the basement membrane (Lechler and Fuchs, 2005).

### 1.3.2.3 Internal cues

The third group of spindle orientation regulators are internal cues that control spindle orientation and the specific polarised localisation of the LGN complex (They *et al.*, 2007; di Pietro, Echard and Morin, 2016). It is now evident that a balanced spindle-to-cortex crosstalk initiated by dynein/dynactin and astral MT dynamics is essential to promote proper force generation and spindle orientation. Therefore, regulatory mechanisms exist that establish a connection between the cortex (dynein/dynactin) and the plus-ends of astral MTs which allows correct spindle orientation (Dogterom and Koenderink, 2019; Rizzelli *et al.*, 2020). One such regulator is mitotic interactor and substrate of Plk1 (MISP). MISP accumulates at the cell cortex and binds to plus-ends of astral MTs and dynactin which establishes a spindle-to-cortex crosstalk (Maier *et al.*, 2013; Zhu *et al.*, 2013; Kschonsak and Hoffmann, 2018). A second regulator that controls spindle-to-cortex crosstalk is the protein Lissencephaly-1 homolog (Lis1). Lis1 enhances astral MT plus-end dynamics

to establish a contact with the cell cortex which is important for cortical recruitment of dynein/dynactin (Coquelle *et al.*, 2002; Moon *et al.*, 2013).

Another aspect of the precise regulation of astral MT dynamics involves directly the dynamic plus-ends that are impacted by proteins to control astral MT instability (di Pietro, Echard and Morin, 2016). The protein G2 and S phase-expressed protein 1 (GTSE1) stabilizes MTs until it is phosphorylated by CDK1 which results in release of the protein and astral MT destabilization. This is important to allow formation of long astral MTs to favour alignment of the spindle along the long axis of the cell (Singh *et al.*, 2021). CLIP-associated protein 1 (Clasp1) also binds to the plus-tips of astral MTs. This MAP initiates and stabilizes the capture of astral MTs at the cell cortex, thereby promoting spindle positioning (Pereira *et al.*, 2006; Samora *et al.*, 2011). A third regulator at the plus-ends of astral MTs is importin- $\alpha$ 1. During mitosis, CDK1 phosphorylates importin- $\alpha$ 1 which induces activation of Targeting protein for Xklp2 (TPX2). In turn, TPX2 promotes astral MT growth and connection to the cortex (Guo *et al.*, 2021).

Recent studies identified involvement of cortical actin and actin-related proteins in spindle orientation. As such, actin subcortical clouds and myosin 10 synergize with the LGN complex to regulate spindle orientation (Kwon *et al.*, 2015). Furthermore, actin possibly stabilizes the LGN complex at the cell cortex via other proteins (Zheng *et al.*, 2013). These could be the membrane-actin crosslinkers Ezrin-radixin-moesin (ERM) proteins which control actin rigidity and stability, but also promote polarised recruitment or cortical stability of LGN and NuMA (Machicoane *et al.*, 2014).

Other internal cues that specifically control the localisation of the spindle orientation complex comprise signals from the chromosomes or spindle, from the cell cortex and from within the cytoplasm. Such chromosome-derived signal includes the Ras-related nuclear protein (Ran)-GTP gradient which comprises low levels of RanGTP at the cell periphery and high levels around chromosomes. Thereby, high levels exclude LGN and NuMA from cortical areas in the vicinity of chromosomes (spindle mid zone) after the establishment of the metaphase plate (Kiyomitsu and Cheeseman, 2012). Polo Like Kinase 1 (PLK1) acts as a spindle pole-derived regulator that negatively controls the dynein localisation by promoting NuMA-dynein/dynactin interactions distant from the spindle pole in close cortical proximity. This promotes a dynamic localisation of the force generators to sustain spindle centring (Kiyomitsu and Cheeseman, 2012; Sana *et al.*, 2018). PLK1 was also reported to exert a similar mechanism from a kinetochore localisation by excluding LGN enrichment near chromosomes and restrict the spindle orientation complex to defined cortical crescents (Tame *et al.*, 2016). Another protein that regulate the exclusion of the LGN complex from specific cortical areas include the Suppressor APC domain containing 2 (SAPCD2). SAPCD2 localises to the apical

membrane to prevent LGN accumulation at this site which favours planar orientation of the mitotic spindle (Chiu *et al.*, 2016). The tyrosine-protein kinase ABL1 regulates LGN localisation at the cell cortex. Furthermore, ABL1 phosphorylates NuMA which is essential to maintain NuMA at the cell cortex during metaphase (Matsumura *et al.*, 2012). Lastly, the protein Afadin was identified as a regulator of LGN at the lateral membrane. The protein recruits LGN and NuMA to E-cadherin adhesion to promote planar orientation of the mitotic spindle (Carminati *et al.*, 2016).

Taken together, spindle orientation is regulated via two aspects. First, the active force-generating machinery is recruited to distinct cortical regions which mainly requires cell polarity and specific signals within the cell. Secondly, in a more simple way, cell shape determines division orientation. It is becoming evident that both of these pathways cooperate to define spindle orientation depending on the developmental stage and the response to external challenges (di Pietro, Echard and Morin, 2016; Rizzelli *et al.*, 2020).

#### **1.4 Oriented cell divisions in development and disease**

The balance between proliferation and differentiation is essential for embryogenesis, organogenesis and remains crucial for tissue homeostasis and regeneration during adulthood (Vorhagen and Niessen, 2014). Neuronal and epidermal progenitors undergo primarily SCDs to expand stem cell numbers during early foetal development and change to primarily ACDs to expand differentiated cells during mid to late gestation. Therefore, one daughter cell leaves the plain where stem cells are located and migrate into overlying layers (neuronal progenitors) or suprabasal layers (epidermal progenitors) to induce multilayering of the tissue. Thus, mammalian stem cells seem to switch division modes in a developmentally manner (Noctor *et al.*, 2004; Lechler and Fuchs, 2005; Raghousi and Gibson, 2014). How somatic stem cells regulate division modes in adult tissues is poorly understood, mostly because of the lack of identified stem cell niches and the lack of techniques to track cells *in vivo* (Morrison and Kimble, 2006). Nevertheless, it was proposed that tissue homeostasis is maintained by an interplay of ACDs and SCDs that sustains the cell number and replenishes the cell pool diminished by injury or disease (Morrison and Kimble, 2006; Santoro *et al.*, 2016). Studies in fast regenerating tissues like hair follicles and blood identified populations of cycling stem cells that divide asymmetrically to replenish cell numbers. Moreover, those tissues contain quiescent stem cell populations that function as a backup or reserved pool usable after extensive tissue damage (Blanpain *et al.*, 2004; Wilson, Laurenti and Trumpp, 2009; Li and Clevers, 2010).

The capability of cells to switch between ACD and SCD during development, tissue repair and homeostasis potentially implicates the risk of defective regulations. In particular, disturbed regulation of division modes has been linked to neurological diseases and cancer. For example, patients suffering from microcephaly have small brains and are mentally disabled because of reduced numbers of cortical neurons. The cause of this are mutation in genes that encode proteins important for centrosome maturation and spindle organization. Interestingly, depletion of some of these genes results in spindle misorientation and consequently in a shift towards ACDs at the expense of SCDs. This would explain reduced neuron numbers and may provide a link of spindle orientation and development of the disease (Gruber *et al.*, 2011; Lancaster and Knoblich, 2012; Noatynska, Gotta and Meraldi, 2012).

Spindle orientation may also play a role in Huntington's disease, a neurodevelopmental disorder that is characterised by motor control loss and cognitive defects (Martin *et al.*, 2015). Huntingtin, the protein that is mutated in the disease, has been shown to regulate spindle assembly and orientation (Godin *et al.*, 2010; Elias *et al.*, 2014; Molina-Calavita *et al.*, 2014). Depletion of the protein leads to spindle orientation defects and possibly to a decrease of proliferating neuronal progenitors. In turn, this may result in an increase of differentiation generating an imbalance between division modes which may be linked to the development of the disease (Godin *et al.*, 2010).

The link between division modes and cancer is less well understood. Disruption of ACDs would generate an imbalance in cell numbers, likely increasing SCDs and excessive differentiation or the excessive expansion of stem cell numbers. This would cause hyperproliferation and possibly disruption of polarised tissue architecture which may induce malignant transformation (Pease and Tirnauer, 2011; Lechler and Mapelli, 2021). This link has been identified in some types of skin cancers where ACDs were decreased and more self-renewing and amplifying divisions occurred. This was also connected to changes in mitotic spindle orientation (Beck *et al.*, 2011; Boumahdi *et al.*, 2014). A similar phenomenon was also observed in colon cancer (Quyn *et al.*, 2010). Although, there is little evidence from these studies and others that dysregulated spindle orientation is sufficient to cause initiation of cancer, it highlights that there may be a link and it is necessary to understand whether defective spindle orientation alone suffices tumorigenesis or if it may accelerate other tumour-initiating events (Nakajima, 2018).

Taken together, intensive work in the last few years has given immense insight into division modes in different mammalian tissues and it highlighted the need of understanding the mechanisms of mitotic spindle orientation, not only in developmental biology, but also in human disease (Lu and Johnston, 2013).

## 1.5 Oriented cell division in the mammary gland

The mammary gland in humans and other mammals forms an epidermal appendage and produces milk to nourish offspring (Inman *et al.*, 2015). The gland's epithelium is organized in a network of ducts that form tree-like structures terminating in the alveolar buds (terminal end bud) and is built from two main cellular lineages. An inner layer of apical-oriented luminal epithelial cells faces the lumen and is surrounded by an outer layer of contractile myoepithelial cells that are located in the basal position adjacent to the basement membrane (Woodward *et al.*, 2005; Visvader and Stingl, 2014). Unlike other tissues, the organ undergoes major morphological changes during distinct developmental windows including embryonic, pubertal and adult stages. Before birth, the network of ducts branches and invades the fat pad but remains quiescent until puberty. In the second stage of development and under the control of hormones and other factors, the ducts rapidly outgrow which results in side branching. During every oestrus cycle, the epithelium proliferates and undergoes apoptosis until the final developmental stage occurs. Pregnancy and lactation induce rapid proliferation of the alveolar buds and development of milk-secreting alveoli. The period of weaning, when the stimuli for milk production are lost, is accompanied by apoptosis of the extended epithelium compartment and tissue remodelling back to the structure resembling the state before pregnancy. This process is also called involution. (Figure 1.12) (Dontu *et al.*, 2003; Dontu, Liu and Wicha, 2005; Inman *et al.*, 2015).

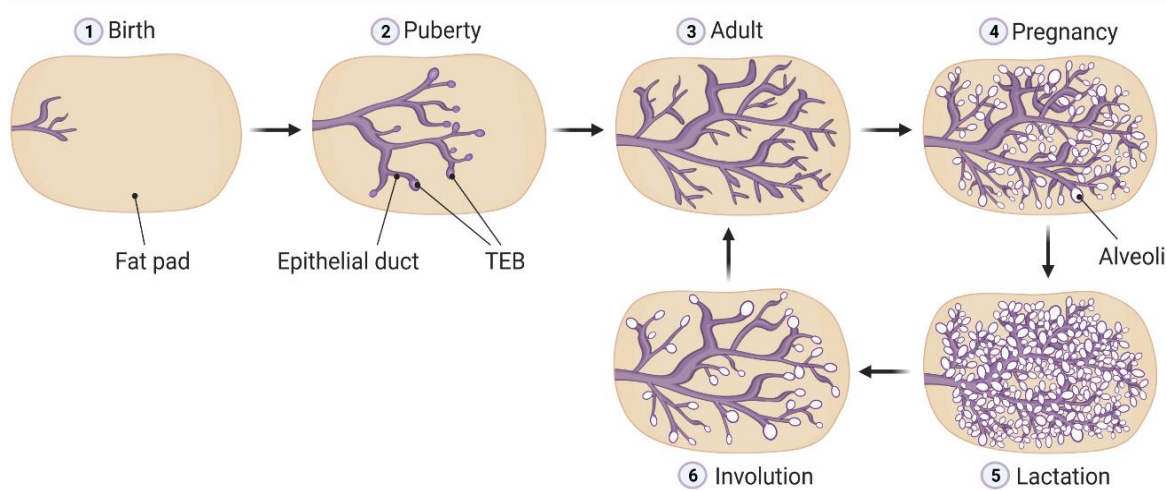


**Figure 1.12 Developmental stages of the postnatal mammary gland**

**Figure 1.12 Continued**

(1) At birth, a rudimentary ductal structure is visible in the fat pad. (2) Stimulated by hormones the ducts outgrow, elongate and branch during puberty and club-shaped structures (terminal end buds, TEB) form at the ductal tips. (3) In mature adults (virgin) the ducts have reached the boundaries and completely filled the fat pad. (4) From this stage onwards, the mammary gland undergoes cycles of growth and regeneration processes. During pregnancy, alveolar buds are formed which grow and differentiate into milk-secreting alveoli. (5) The mammary gland expands further during lactation to nourish offspring. (6) Lastly, the epithelium involutes and returns to a state that resembles that of a mature adult (virgin).

To sustain numerous pregnancies and every oestrus cycle, a compartment of MaSC resides in the gland. Although, the niche of MaSC within the epithelium and their differentiation potential have yet to be identified, it has been suggested that these cells serve developmental and homeostatic functions. MaSC give rise to the epithelium during development, enable extensive tissue expansion and remodelling during several rounds of pregnancies and provide a reservoir of cells for repair in the event of tissue damage (Woodward *et al.*, 2005; Lloyd-Lewis *et al.*, 2017). Therefore, MaSC may undergo SCDs to facilitate the growth of the tissue. Rounds of ACDs would generate diverse progeny that coordinate the development of the branching ductal tree (Joshi *et al.*, 2010). There may be slow-cycling or quiescent stem cells that remain quiescent under homeostasis and may be recruited under regenerative conditions (Bai and Rohrschneider, 2010; dos Santos *et al.*, 2013). All these hypotheses are under debate and little knowledge exists to support these. However, there is evidence that OCDs play a role in the mammary gland and deregulation may induce malignant transformation. For example, cancer stem cells from a mammary tumour model divide more frequently symmetrically than asymmetrically, thereby increasing cell numbers (Cicalese *et al.*, 2009). Although, the link between spindle orientation and changes in division modes has been proposed in other cancer models (discussed in the last chapter, 1.4), this has not been shown for the mammary gland. In a broader sense, studies of division modes and mitotic spindle orientation in the tissue has only started recently (Santoro *et al.*, 2016). Novel findings determined that the Par and Scribble polarity complexes are essential for correct mammary gland morphogenesis and loss of Par3 or Scribble lead to the formation of disorganized ducts at the basal layer or initiates transformation of the mammary epithelium. This may be an indication of increased numbers of SCDs (McCaffrey and Macara, 2009; Huang and Muthuswamy, 2010). Recent studies also identified regulators that influence the orientation of the mitotic spindle (Santoro *et al.*, 2016). These include

mInsc (Ballard *et al.*, 2015), huntingtin (Elias *et al.*, 2014), Stathmin/Stat3 (Segatto *et al.*, 2019; Morris *et al.*, 2020), Plk2 (Villegas *et al.*, 2014), Connexin 43 (Bazzoun *et al.*, 2019) and Aurora-A kinase (Regan *et al.*, 2013). Interestingly, all these proteins are indispensable for correct spindle orientation and subsequently mammary gland morphogenesis however, only huntingtin was specifically identified to regulate the localisation of the LGN complex to control spindle orientation. Thus, the protein constitutes the only identified regulator of the LGN complex in conjunction with spindle orientation and mammary gland morphogenesis. Given the growing list of regulators of the spindle orientation machinery in other epithelia and the complexity of OCDs, it can be speculated that more unknown factors contribute to the correct positioning of the mitotic spindle in mammary epithelial cells. Furthermore, as suggested in other epithelia and based on the findings described above, the orientation of the mitotic spindle coupled with cell polarization may be indispensable for regulating division types in the mammary gland. This highlights that knowledge of OCDs in the mammary gland is urgently needed to understand how these highly controlled mechanisms are accurately executed to allow proper tissue development and homeostasis.

## 1.6 The Annexin superfamily

The beginning of the discovery of an annexin superfamily lies in the late 1970s when the first member called synexin was identified (Creutz, Pazoles and Pollard, 1978). Following the description of other proteins that were initially named after their biochemical properties, including chromaffins (Creutz *et al.*, 1987), lipocortins (Flower and Blackwell, 1979) and calpactins (Glenney, Tack and Powell, 1987), it emerged that these proteins share common structural and functional characteristics. Therefore, they were grouped and renamed as “annexins” (Geisow *et al.*, 1987; Crumpton and Dedman, 1990). By definition, annexin proteins have two main features. First, they bind negatively charged phospholipids of the cytosolic phase of cellular membranes in a  $\text{Ca}^{2+}$ -dependent and reversible manner. Second, they share a common structure with two distinct regions. One harbours conserved structural core elements called annexin repeats at the C-terminus that bind to membranes and another element contains a unique head region at the N-terminus that mediates interactions with other proteins (Gerke and Moss, 2002).

Today, more than 160 members of the superfamily have been identified which are found across plants, fungi, protists, invertebrates as well as lower and higher vertebrates. The current nomenclature was proposed in the late 1990s which classifies five different groups (A-E). Group A describes human and vertebrate family members. Annexins outside vertebrates are categorized as

B for invertebrates, C for fungi and some groups of unicellular eukaryotes, D for plants and E for protists (Morgan *et al.*, 1998; Gerke and Moss, 2002; Moss and Morgan, 2004).

Twelve annexins have been identified in mammals which are referred to as annexin A1-A13 (ANXA1-13) with ANXA12 being unassigned. Based on the conserved structure, mammalian ANXAs have a core regions that consists of four (eight in ANXA6) ANXA repeats (I-IV) that are 70 to 75 amino acid residues long. Each repeat contains five  $\alpha$  helices and they are arranged in a distinct manner within the core domain so that repeat I/IV and II/III pack together. Furthermore, the core domain harbours type II  $\text{Ca}^{2+}$  binding sites that induce membrane association upon  $\text{Ca}^{2+}$  elevation. In contrast, the head regions have variable length and amino acid sequences which have phosphorylation sites and mediate interactions with different intracellular proteins (Figure 1.13) (BARTON *et al.*, 1991; Gerke, Creutz and Moss, 2005; Rintala-Dempsey, Rezvanpour and Shaw, 2008; Mirsaedi *et al.*, 2016).

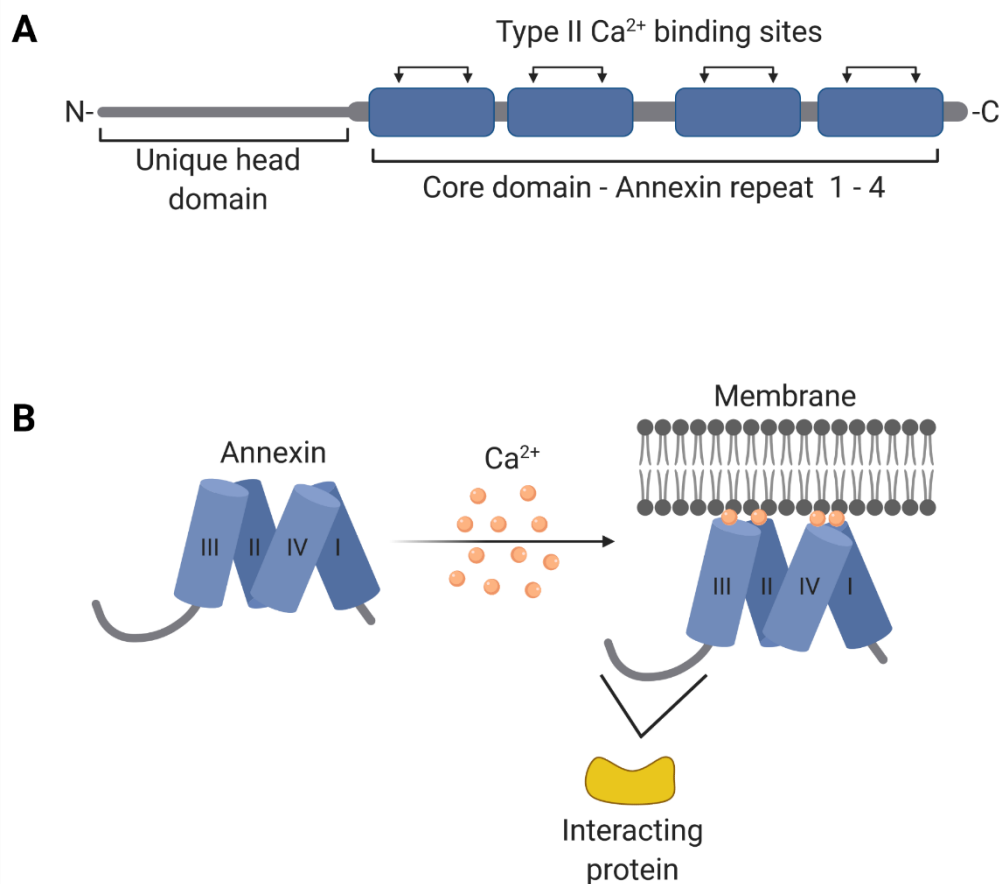


**Figure 1.13 Structure and interaction dynamics of mammalian annexins**

**Figure 1.13 Continued**

(A) The conserved structure of the ANXA family comprises a core region of four ANXA repeats (with the exception of ANXA6 that has 6 repeats) at the C-terminus. The repeats contain five  $\alpha$  helices and harbour type II  $\text{Ca}^{2+}$  binding sites. The head region at the N-terminus is variable in length and amino acid sequence making it unique for every ANXA of the family. (B) ANXAs bind to membranes in a calcium-dependent and reversible manner. In the presence of calcium, the core domain binds to phospholipids of membranes. Once associated with the bilayer, the ANXA head region mediates regulatory interactions with cellular proteins. Schematic was modified from Boudhraa *et al.*, 2016.

One well-known group of proteins that interacts with the N-terminal region of ANXAs are S100 proteins. These cytoplasmic proteins are small (10-14 kDa) dimeric EF-hand  $\text{Ca}^{2+}$ -binding proteins that only exist in vertebrates. These proteins have diverse functions including regulation of actin and MT networks, promotion of cell survival and proliferation, calcium homeostasis and mediation of muscle contraction (Mirsaeidi *et al.*, 2016). S100 dimers bind two ANXAs molecules to form heterotetrameric complexes. Several interactions have been described including ANXA11/S100A6, ANXA2/S100A10 and ANXA1/S100A11. It was proposed that S100 proteins can link two membrane-bound ANXAs to promote membrane fusion and vesicle trafficking (Gerke and Moss, 2002). Furthermore, they can bind cytoskeleton components. However, exact mechanisms are not known (Gerke, Creutz and Moss, 2005; Miwa, Uebi and Kawamura, 2008; Mirsaeidi *et al.*, 2016).

Mammalian ANXAs vary in their level of expression and tissue distribution but account for 2-4 % of total cellular protein. Some proteins are abundant and ubiquitous (ANXA1, -2, -4, -5, -6, -7, -11) whereas others are restricted to certain cell types and tissues (ANXA3 in neutrophils, ANXA8 in the skin, ANXA9 in the tongue, ANXA10 in the stomach and ANXA13 in the small intestine) (Moss and Morgan, 2004; Fu *et al.*, 2020). Within a cell, ANXAs are usually cytoplasmic where they associate with membranes, cytoskeleton components or proteins that mediate interactions between the cell and extracellular matrix. However, some members of the family are also located in the nucleus (ANXA1, -11 and -2) (Eberhard *et al.*, 2001; Tomas and Moss, 2003) or at the cell surface (ANXA1 and -2) (Solito, Nuti and Parente, 1994; BROWNSTEIN *et al.*, 2001). ANXAs are targets of post-translational modifications, mainly phosphorylation by protein tyrosine and serine-threonine kinases. Phosphorylation sites reside all over the protein sequences and can affect their membrane-binding making it an essential regulatory mechanism of ANXA functions (Gerke and Moss, 2002).

The presence of multiple ANXAs in different cell compartments led to the finding that these proteins play a role in a wide variety of fundamental cellular processes including proliferation, differentiation, apoptosis, migration, adhesion, membrane repair and inflammatory response. Most proposed mechanisms are linked to  $\text{Ca}^{2+}$  signalling and transient, reversible membrane binding. However, a major obstacle in ANXA research is the similarity in structure, localisation and membrane binding properties which suggests a functional redundancy within the superfamily and makes it difficult to confine a specific function for one ANXA. Nevertheless, more precise ANXA functions have started to elucidate and over recent years, it has become clear that they are also relevant to several human diseases and provide targets for novel therapeutic approaches (Grewal *et al.*, 2016; Grewal, 2017).

### 1.6.1 Annexin A1- Structure and function

ANXA1, originally named lipocortin-1, macrocortin or renocortin, was identified as a glucocorticoid-induced inhibitor of phospholipase A2 (Flower and Blackwell, 1979). Subsequent work showed that the 37 kDa protein can be detected in many tissues and most cell types including the nervous and endocrine system, leukocytes, lymphocytes, macrophages as well as epithelial and endothelial cells (Gerke, Creutz and Moss, 2005). ANXA1 localises at multiple cell locations such as the inner leaflet of the plasma membrane, vesicular structures, the cytoskeleton and in the nucleus. However, the protein can also traffic to the cell surface and secret in an autocrine and paracrine manner (Grewal *et al.*, 2019; Purvis, Solito and Thiemermann, 2019). Due to its widespread expression and subcellular localisation, ANXA1 is involved in a variety of cellular processes (Figure 1.14). After its first discovery, ANXA1 was described as an endogenous modulator of anti-inflammatory actions. As such, the protein was shown to up-regulate the production of anti-inflammatory cytokines and to control pro-inflammatory mediator release (Minghetti *et al.*, 1999; Ferlazzo *et al.*, 2003). Furthermore, it inhibits leukocyte transmigration through an inflamed endothelium by its secretion to the cell surface of leukocytes which promotes detachment of these cells from endothelial cells. Thus, ANXA1 serves as a negative regulator of transmigration (Getting, Flower and Perretti, 1997; Chatterjee *et al.*, 2005; de Jong *et al.*, 2017; Sheikh and Solito, 2018). Another major involvement of ANXA1 in anti-inflammatory processes is through initiation of apoptosis and regulation of apoptotic cell removal. The former involves the activation of caspase-3 activity by ANXA1 (Solito *et al.*, 2001). Furthermore, it stimulates an increase of cytosolic calcium flux which leads to dephosphorylation of the Bcl-2 associated death promotor (Bad) and thereby activating the apoptotic machinery (SOLITO *et al.*, 2003). In order to regulate cell removal upon apoptosis, ANXA1

traffics to the cell surface of apoptotic cells in a caspase- and calcium-dependent manner and co-localises with ligands that act as signalling molecules to phagocytes. Consequently, ANXA1 ensures a safe and distinctly-targeted removal of dead cells without damaging surrounding healthy tissue (Arur *et al.*, 2003; Pupjalis *et al.*, 2011; McArthur *et al.*, 2015).

Besides promoting inflammation resolution, ANXA1 is also involved in cell proliferation and differentiation. The protein is differentially expressed in fibroblasts depending on the cell cycle stage. The protein levels increase in proliferating cells compared to quiescent cells (Schlaepfer and Haigler, 1990). The mechanisms of the increase and decline are not well understood. It was shown that higher levels of ANXA1 during the cell cycle can reduce proliferation by sustaining the activation of MAPK/ERK signalling, thus blocking expression of cyclin D1 and preventing cells from entering S phase. If ANXA1 is involved in other cell cycle stages such as mitosis remains unknown (Alldridge and Bryant, 2003; Poeter *et al.*, 2013).

ANXA1 protein levels are positively correlated with the degree of differentiation of certain cell types. Studies have shown that it is associated with the regulation of differentiation in bone and muscle tissues as well as T-cells (D'Acquisto *et al.*, 2006; Bizzarro *et al.*, 2010; Han *et al.*, 2020). Furthermore, ANXA1 is highly expressed during differentiation of cells of the macrophage lineage as well as of epithelial origin (William *et al.*, 1988; Isacke, Lindberg and Hunter, 1989; Solito *et al.*, 1998). The expression also changes during embryonic development. For example, ANXA1 levels increase during murine palate development with a specific accumulation in the apical region of the epithelium at early stages and throughout the entire tissue at later stages (Chepenik *et al.*, 1995). In human embryonic skin, the protein is highly expressed in specific cell types throughout development of the embryo and in neonatal stages (Fava *et al.*, 1993). In this context, it was proposed that ANXA1 has a role in cytoskeleton function. In effect, the protein binds and bundles F- actin in a Ca<sup>2+</sup> dependent manner and co-localises with it in different cell types (Schlaepfer and Haigler, 1987; Hayes *et al.*, 2004). Based on this, ANXA1 is also enriched at lamellipodial extrusions of migrating cells where it co-localises with actin fibres (Bizzarro *et al.*, 2010; Bizzarro *et al.*, 2012). Furthermore, ANXA1 can interact with profilin, an actin-binding and actin-polymerizing protein that links the actin cytoskeleton and the plasma membrane. Therefore, ANXA1 might be involved in cell migration and in mediating and stabilizing membrane-cytoskeleton restructuring via actin dynamics (Alvarez-Martinez *et al.*, 1996; Alvarez-Martinez *et al.*, 1997; Krishnan and Moens, 2009).

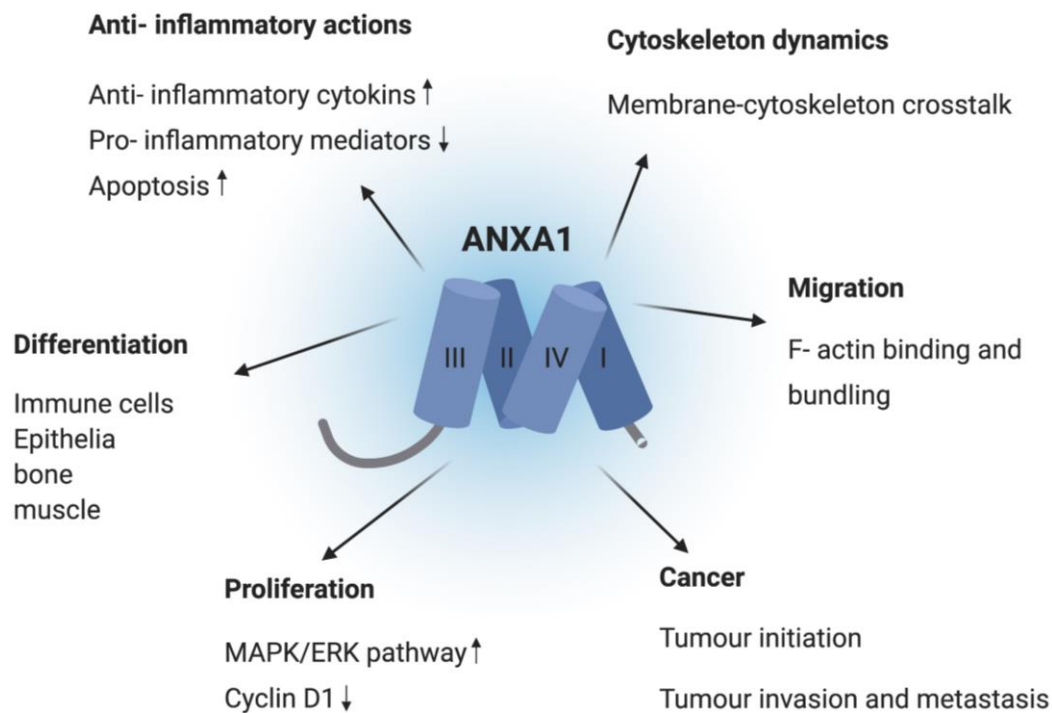


**Figure 1.14 ANXA1 implication in cellular processes**

*This diagram summarizes the functions of ANXA1 within cells.*

ANXA1 functions are partially regulated by phosphorylation. In this context, several kinases have been identified to phosphorylate ANXA1 which might be important for ANXA1-mediated signal transduction and its subcellular localisation (D'Acunto *et al.*, 2014). For example, ANXA1 is phosphorylated to localise to mitochondria or the nucleus (Yoshii *et al.*, 2000; Kim *et al.*, 2003). Similarly, phosphorylation of the protein is crucial for its membrane binding and interaction with S100A11 (Dorovkov and Ryazanov, 2004; Yazid *et al.*, 2009; Dorovkov, Kostyukova and Ryazanov, 2011; D'Acunto *et al.*, 2014).

All of these described features of ANXA1 show that the protein is involved in many cellular processes and these roles combined are essential for normal development and homeostasis. In return, the variety of ANXA1 functions leads to detrimental and widespread effects when the protein is deregulated. It is now clear that ANXA1 is implicated in various diseases including lung fibrosis, diabetes, cardiovascular diseases and several types of cancer (Grewal *et al.*, 2016; Foo *et al.*, 2019; Purvis, Solito and Thiemermann, 2019; Fu *et al.*, 2020).

Especially, ANXA1 involvement in cancer has been the focus of research over a few decades because it is differentially expressed during tumour development and progression. Therefore, it was thought to be a potential diagnostic or prognostic biomarker that can be targeted for therapy (Foo *et al.*, 2019). However, ANXA1 involvement is conflicting because levels can be up- or downregulated in different types of cancer. It was shown to be highly expressed in lung cancer, colorectal cancer, pancreatic cancer, liver cancer and melanoma which correlates with disease severity and poor prognosis caused by promoted tumour invasion and metastasis. ANXA1 levels are downregulated or deleted in thyroid cancer, cervical cancer, prostate cancer, oral squamous cell carcinoma and B-cell non-Hodgkin's lymphomas which correlates with the differentiation grade. Controversially, ANXA1 levels can be highly increased but also decreased in gastric cancer, esophageal cancer or breast cancer. Thus, the differential expression of the protein in tumour cells might be diverse or tissue specific and ANXA1 could function as an oncogene in some cancers and as a tumour suppressor in others (Bhardwaj *et al.*, 2015; Sheikh and Solito, 2018; Foo *et al.*, 2019; Shao *et al.*, 2019; Fu *et al.*, 2020).

Together, based on the described functions of ANXA1 in different cell types and tissues, its involvement in cytoskeleton dynamics and cancer, combined with the knowledge that deregulated cell division leads to tumour growth, it can be speculated that ANXA1 does play an unknown role in different cell cycle stages, especially in mitosis. Therefore, much more translational and non-translational research is required to understand the exact mechanisms of ANXA1 in normal cells and its implications in disease development.

## **1.7 Aims and objectives of this study**

Our present challenge is to understand how cells balance and control OCDs in epithelial systems to maintain a polarised architecture but to coordinate growth and homeostasis. Unlike their invertebrate counterparts which undergo a stereotyped division and always orientate the spindle in the same direction, vertebrate epithelial cells have the ability to divide in two directions. Thus, during each cell cycle, cells must inspect the conditions and make a decision. Since this decision relies on the positioning of the mitotic spindle, it is essential that we understand the mechanisms and machinery that drives spindle orientation as well as their spatiotemporal regulation (Ray and Lechler, 2011; van Leen, di Pietro and Bellaïche, 2020; Lechler and Mapelli, 2021).

It is now established that despite evolutionary conservation of protein complexes, including the spindle orientation complex, there are clear differences in the mechanisms and regulation of

spindle orientation across species and even tissue types including distinctive epithelia (Nakajima, 2018). Studies in different epithelial tissues, mainly embryonic tissue of the skin, gut and *in vitro* epithelial cell lines identified various cues that regulate spindle orientation (di Pietro, Echard and Morin, 2016; Bergstralh, Dawney and St Johnston, 2017). How these factors control division modes in conjunction, space and time and if they play roles in epithelia in general is not known. In addition, little is known about mitotic spindle orientation in adult epithelia such as the mammary gland where tissue turnover is rapid and dynamic, and must be constantly regulated. Therefore, it remains elusive which cues control spindle orientation in the mammary epithelium. Furthermore, evidence started to elucidate that dysregulation of OCDs is linked to promotion of tumorigenesis and has also been implicated in breast cancer (Santoro *et al.*, 2016). Therefore, dissecting the mechanisms of spindle orientation in the mammary epithelium is essential for enhancing our understanding of normal mammary gland biology, but also for elucidating how imbalance of OCDs contributes to abnormal cell fate and behaviour that may lead to malignant transformation.

The aim of this thesis was to identify and characterise novel factors that control mitotic spindle orientation in the mammary epithelium and determine how these mechanisms influence OCDs. Identifying novel regulators is critical in understanding how mammary cells balance division modes to accompany the constant tissue morphogenesis in a healthy mammary epithelium. This may provide further insight into normal epithelial biology but could also improve the understanding of how deregulated OCDs contribute to diseases. To address this, the main objectives were:

1. To engineer a mammary epithelial cell line expressing GFP-tagged LGN for the characterisation of the LGN cortical interactome during mitosis.
2. To characterise the LGN interactome in mitotic mammary epithelial cells for the identification of novel partners and regulators.
3. To validate a target protein-of-interest as a novel partner of LGN and investigate the dynamics of the novel protein during the cell cycle, particularly analyse the co-localisation with LGN.
4. To dissect a role of the target protein-of-interest in the regulation of the localisation of the LGN complex at the cell cortex.
5. To determine a role of the target protein-of-interest in mitotic spindle dynamics, mitotic progression and mitotic spindle orientation.

## **Chapter 2    Materials and Methods**



Methods described in this chapter detail protocols used in the reported research of this thesis. Unless otherwise stated, solutions and buffers were prepared using ultrapure water from an Alto water system (Avidity Science). For tissue culture and DNA methods, buffers and reagents were prepared with molecular biology grade water (Invitrogen) unless otherwise stated. Throughout this thesis, experiments were performed at room temperature (RT) unless otherwise stated. All schematics were generated with Biorender.com.

## **2.1 Microbial methods**

All microbiology experiments were carried out with the *Escherichia coli* (*E. coli*) strain Subcloning Efficiency™ DH5α Competent Cells (Invitrogen) that are suitable for routine cloning procedures.

### **2.1.1 Growth of bacteria**

Individual *E. coli* colonies were grown as overnight bacteria cultures in Luria-Bertani (LB) broth medium in a shaking incubator at 200 rpm and 37 °C. Transformed bacteria was plated on LB-agar plates prepared in 10 cm diameter sterile petri dishes. Ampicillin was added to give a final concentration of 100 µg/ml to select for plasmid DNA in *E. coli* cells.

### **2.1.2 Transformation of *E. coli* with plasmid DNA**

Frozen *E. coli* cells were thawed on ice (5 min). 50 ng of plasmid DNA was added to 50 µl of bacteria. The mixture was incubated on ice for 30 min before heat-shock for 45 seconds at 42 °C. Following a two-minute incubation time on ice, cells were resuspended in 1 ml S.O.C medium (Invitrogen). For recovery, bacteria was incubated shaking at 37 °C and 200 rpm for 1 hour. Cells were pelleted by centrifugation for 3 minutes at 2500 x g and resuspended in 100 µl S.O.C medium. The complete mixture was spread on LB-agar plates containing 100 µg/ml ampicillin. Plates were incubated overnight at 37 °C to achieve discrete colonies. Individual grown colonies were isolated and inoculated in LB growth medium with 100 µg/ml ampicillin to expand overnight.

## 2.2 Cell culture methods

Experiments were carried out with the human cell lines MCF-10A and HEK293. MCF-10A are human mammary epithelial cell line that was derived from benign epithelial breast tissue and spontaneously immortalized without transformation. These cells are commonly used as a normal breast cell model (Soule *et al.*, 1990). MCF-10A cells were purchased from ATCC (USA).

HEK293 cells are a cell line derived from human embryonic kidney cells by transformation with sheared Adenovirus 5 DNA. These cells are highly transfectable and widely used to produce large amounts of recombinant protein (Graham *et al.*, 1977). HEK293 cells were kindly provided by M. R. Andrews lab (University of Southampton).

### 2.2.1 Cell culture of human cell lines

Cells were maintained at 37 °C with 5 % CO<sub>2</sub> in a humid incubator. Details of media and supplements are listed in Table 2.1 and Table 2.2. Media was exchanged every two days. Cells were cultured in standard tissue culture flasks or dishes (Thermo Scientific). When reaching 100 % confluency, cells were passaged as follows. After aspirating cell culture media, cells were washed once with Dulbecco's phosphate-buffered saline (DPBS, Gibco). Detachment of cells was achieved by incubation with Trypsin-ethylenediaminetetraacetic acid (EDTA, 0.25%) (Gibco) for 10 min (MCF-10A cells) or 1 min (HEK293) at 37 °C. Fresh cell culture media was added to inhibit trypsin activity. Cells were then split at a ratio of 1:3–1:6 as required. Frozen stocks were prepared by centrifuging cell suspensions at 1220 rpm for 3 minutes and resuspending the pellet in freezing media (10 % Dimethyl sulfoxide (DMSO, Sigma) in donor horse serum for MCF-10A or 10 % DMSO in fetal bovine serum (FBS, Gibco) for HEK293). Cells were frozen at 1 °C/min in a freezing container (Mr. Frosty, Nalgene) with isopropanol and stored at -80 °C overnight. On the next day, cells were transferred to liquid nitrogen for long-term storage. Cell health was checked by assessing morphology using an EVOS™ XL Core Imaging System with a 10x objective. All cell lines were routinely tested for *Mycoplasma* contamination. Test were performed by the technicians team using the MycoAlert kit (Lonza).

**Table 2.1 Cell culture media and supplements for MCF-10A cells**

Component	Final concentration	Source and cat. number
Dulbecco's Modified Eagle Medium/F-12, GlutaMAX™ (DMEM)	-	Gibco, 10565018
Horse serum, New Zealand origin, heat- inactivated	5 %	Gibco, 16050122
Epidermal growth factor (EGF), human	20 ng/ml	Sigma, E9644
Cholera Toxin from <i>Vibrio cholerae</i>	1 ng/ml	Sigma, C8052
Hydrocortisone	100 µg/ml	Sigma, H0888
Insulin from bovine pancreas	10 µg/ml	Sigma, I1882
Penicillin/ Streptomycin	50 U/ml/ 50 µg/ml	Gibco, 15140122
Amphotericin B	500ng/ml	Gibco, 15290018

**Table 2.2 Cell culture media and supplements for HEK293 cells**

Component	Final concentration	Source and cat. number
Dulbecco's Modified Eagle Medium (DMEM, high glucose, sodium pyruvate, L-glutamine)	-	Gibco, 11965092
Fetal bovine serum, South American origin, heat- inactivated	10 %	Gibco, 10500064
Penicillin/ Streptomycin	50 U/ml / 50 µg/ml	Gibco, 15140122

### 2.2.2 Cell counting

To plate precise cell numbers, cells were trypsinized as described (see 2.2.1) to obtain cells in suspension. Cells were prepared for cell counting by mixing equal amounts of cell suspension and trypan blue (Sigma) to give a volume of 20  $\mu$ l. 10  $\mu$ l of the mixture were added to a Neubauer hemocytometer (Hirschmann Instruments). Using an inverted microscope (EVOS™ XL Core Imaging System) with a 10x objective, the number of cells in four 1 mm<sup>2</sup> squares of the chamber were counted. The following formula was used to calculate the number of cells per millilitre.

$$\frac{\text{Cells}}{\text{ml}} = \frac{\text{Counted cells}}{\text{Counted area (mm}^2\text{)} \times \text{Chamber depth (mm)} \times \text{Dilution}} \times 10^4$$

The chamber depth was 0.1 mm. To obtain the total number of cells in suspension, the number of cells per millilitre was multiplied with the total volume of cell suspension.

### 2.2.3 Cell cycle arrest at metaphase

Arrest (also called synchronisation) of large numbers of mammalian cells is a widely used technique to study distinct phases of the cell cycle. Here, MCF-10A cells were blocked in metaphase in a two-step process. First, cells were arrested in late G<sub>2</sub> phase (G<sub>2</sub>/M) by treatment with the CDK1 inhibitor RO-3306 (Vassilev *et al.*, 2006). RO-3306 (Sigma) was dissolved in DMSO to reach a concentration of 10 mM, aliquoted and stored at -20 °C. When cells were 90 % confluent, the drug was added to the media at a final concentration of 9  $\mu$ M and incubated at 37 °C for 18 h. In a second step, G<sub>2</sub>/M blocked cells were specifically arrested in metaphase. For this, RO-3306 was removed by washing the cells three times with drug-free media and immediately after, the drug MG-132 (N-(benzyloxycarbonyl) leucinylleucinylleucinal; Calbiochem) was added. MG-132 is a potent, reversible, and cell-permeable proteasome inhibitor that blocks the degradation of cyclin B during mitosis or meiosis, thus prevents transition to anaphase (Josefsberg *et al.*, 2000). MG-132 was prepared as a stock solution of 100 mg/ml in DMSO, aliquoted and stored at -20 °C. The final working concentration was 10  $\mu$ M in cell culture media. Cells were incubated at 37 °C for 6 h to block them in metaphase before further processing. Successful mitotic arrest was assessed by visualizing the cells under an EVOS™ XL Core Imaging System with a 10x objective.

### 2.2.4 Transfection using calcium phosphate

HEK293 cells were plated so that they reach 40% confluency on the day of transfection. Before transfection, cells were replenished with fresh cell culture media. For each transfection, two mixtures were prepared. The first contained DNA, 50  $\mu$ l 2.5 M calcium phosphate (Sigma) and water made up to 500  $\mu$ l. The second contained 500  $\mu$ l 2x HEPES buffered saline (HBS; Sigma). The two mixtures were combined by slowly adding the DNA to HBS. After incubation for 50 seconds, the solution was added dropwise to the cells. HEK293 were placed back in the incubator until further processing.

### 2.2.5 Gene knockdown using small interfering RNA

Small interfering RNAs (siRNAs) were used to transiently silence human *ANXA1* or *GPSM2 (LGN)*<sup>2</sup>. SiRNAs were purchased from Sigma and are listed in Table 2.3. The company predesigned all siRNAs as 21mer duplexes with dTdT overhangs that target the *ANXA1* or *LGN* mRNA sequence published in the NCBI database under NCBI Reference Sequence NM\_000700.3 or NM\_013296 respectively.

**Table 2.3 SiRNA sequences targeting human *ANXA1* and *LGN***

siRNA name	Oligo name (siRNA ID)	Batch number	Sequence (5'-3')
siANXA1#1	SASI_Hs01_00157996	HA13045083	GUGUCAAUACCAUCCUUA[dT][dT]
	SASI_Hs01_00157996_AS	HA13045084	UAAGGAUGGUUUGAACAC[dT][dT]
siANXA1#2	SASI_Hs01_00157997	HA13045081	CUAUGAUCAGAAGACUUUA[dT][dT]
	SASI_Hs01_00157997_AS	HA13045082	UAAAGUCUUCUGAUCAUAG[dT][dT]
siLGN#1	SASI_HS01_00121831	HA14330366	GGUAAUCUGGGAAACACCU[dT][dT]
	SASI_HS01_00121831_AS	HA14330367	AGGUGUUUCCCAGAUUACC[dT][dT]
siLGN#2	SASI_HS01_00121832	HA14330368	CAAGAUGCCAGUAAUUCUA[dT][dT]
	SASI_HS01_00121832_AS	HA14330369	UAGAAUUACUGGCAUCUUG[dT][dT]

AS = antisense sense strand

<sup>2</sup> For simplification, siRNA targeting *GPSM2* mRNA is referred to as siLGN hereafter.

Predesigned lipophilized siRNAs were reconstituted in nuclease free water (Eurogentec) to a final concentration of 100  $\mu\text{M}$  and kept at  $-80\text{ }^{\circ}\text{C}$  for long-term storage. For transfection, siRNAs were further diluted to 20  $\mu\text{M}$  and stored at  $-20\text{ }^{\circ}\text{C}$ . The siRNA SiGENOME RISC-Free Control (Dharmacon, #D-001220-01-05) was used as a negative control. This siRNA does not have a known target in the cells and provides a baseline for the cellular response to the transfection reagent. The control was processed similarly to siRNAs. MCF-10A cells were transfected with individual siRNAs and the control using the Lipofectamine<sup>TM</sup> RNAiMAX Transfection Reagent (Invitrogen). The final concentration of siRNAs and control added per reaction was 50 nM. Two days before transfection,  $1.5 \times 10^5$  cells were plated in six-well plates or 27 mm Nunc<sup>TM</sup> glass bottom dishes (Thermo Scientific). On the day of transfection, one hour prior to transfection cell culture media was replaced with 1.5 ml Opti-MEM I Reduced Serum Medium (Opti-MEM, Gibco) per well or dish. Two mixtures were prepared per transfection. The first contained 4.5  $\mu\text{l}$  siRNA (20  $\mu\text{M}$ ) dilutions and Opti-MEM to obtain a final volume of 150  $\mu\text{l}$ . In the second mixture 9  $\mu\text{l}$  of Lipofectamine<sup>®</sup> RNAiMAX Reagent and Opti-MEM were added to reach 150  $\mu\text{l}$ . After 5 min, the RNA mixture was slowly pipetted into the Lipofectamine mixture and left for 20 min. Then, combined reagents were added dropwise to the cells and incubated overnight (16 h). On the next day, media was replaced with fresh cell culture media. Cells were analysed 65-72 h after transfection.

### **2.2.6 Retroviral production and transduction**

Viruses have become a powerful tool for the delivery of genetic material into mammalian cells. A common type is retrovirus which transcribes its RNA into DNA to permanently incorporate genetic material into the genome of an infected cell. This strategy is widely used to generate cell lines stably expressing a protein of interest (Anson, 2004).

This section describes the general protocol of retrovirus production and transduction carried out in this thesis to generate novel cell lines. A 3<sup>rd</sup> generation viral system was used, thus the components to generate virus particles were split across three plasmids. Specific plasmids used are described in detail in chapter 2.4.2. In general, HEK293 cells were utilized as packaging cells for virus production and MCF-10A cells were infected with viruses to express the gene of interest.

The day before transfection, HEK293 were plated at  $2 \times 10^6$  cells per 10 cm dish. On the day of transfection, cells were transfected with 10  $\mu\text{g}$  transfer plasmid, 6.5  $\mu\text{g}$  packaging plasmid and 5  $\mu\text{g}$  envelope plasmid using calcium phosphate transfection as described in section 2.2.4. 48 hours after transfection, media containing the virus was collected and filtered through a sterile 0.45  $\mu\text{m}$  pore filter. At this stage, the viral supernatant was either frozen at  $-80\text{ }^{\circ}\text{C}$  or directly used for

transduction. MCF-10A cells were plated at  $5 \times 10^4$  cells per 6 well plate two days before infection. On the day of infection, 0.5 ml viral supernatant was mixed with 0.5 ml fresh cell culture media. Polybrene (Sigma), a chemical that enhances the fusion of virus particles to the cell membrane, thus increasing the infection efficiency, was added at a final concentration of 8  $\mu\text{g/ml}$ . MCF-10A cells were incubated with the virus mixture (1 ml per well) for 18 hours before the cells were refed with fresh cell culture media. Antibiotic selection started 48 hours after infection. Selection was stopped when control cells (untransduced cells) had died. After selection, cells were subjected to flow cytometry (see 2.2.7) to enrich for fluorescent cells. Cells were maintained as a polyclonal cell line as described in section 2.2.1.

### **2.2.7 Cell sorting using flow-cytometry**

Flow cytometry and cell sorting is used to purify a single cell type from a heterogeneous cell suspension based on the presence or absence of fluorescence or light signals that correlate to cell morphology, intracellular protein expression, gene expression and cellular physiology (Bonner *et al.*, 1972; Herzenberg *et al.*, 2002). In this work, fluorescence activated cell sorting (FACS) was used to enrich cells expressing enhanced green fluorescent protein (eGFP) or mCherry.

For sorting preparation, MCF-10A cells were trypsinized as described in 2.2.1, pelleted by centrifugation at 1220 rpm for 3 minutes and resuspended in DPBS (Gibco) at a concentration of  $5 \times 10^6$  cells. Cell sorting was carried out with the BD FACS Aria II system (BD Bioscience). The instrument was calibrated using non-fluorescent wild type (WT) MCF-10A cells. This negative control defined non-specific background fluorescence which was set by measuring forward (FSC) versus side scatter (SSC). By gating the cells, the background was eliminated. When available, a positive control was further used. The region of interest was then selected for the cell sort gating threshold (Figure 2.1). To sort cells expressing eGFP, the 488-nm blue laser was used with the Octagon detector array and 530/30 filter. To sort cells expressing mCherry, the same laser and detector was used with the 616/23 filter. Sorted cells were collected in fresh cell culture media. A small fraction of sorted cells was used for a post-sort test to check sorting efficiency. Finally, cells were pelleted by centrifugation at 1220 rpm for 3 min, resuspended in cell culture media and plated in tissue culture flasks or plates depending on the number of recovered cells. Media was replenished approximately 4 h after the sort to remove cell debris once the cells had adhered to the cell culture plastic.

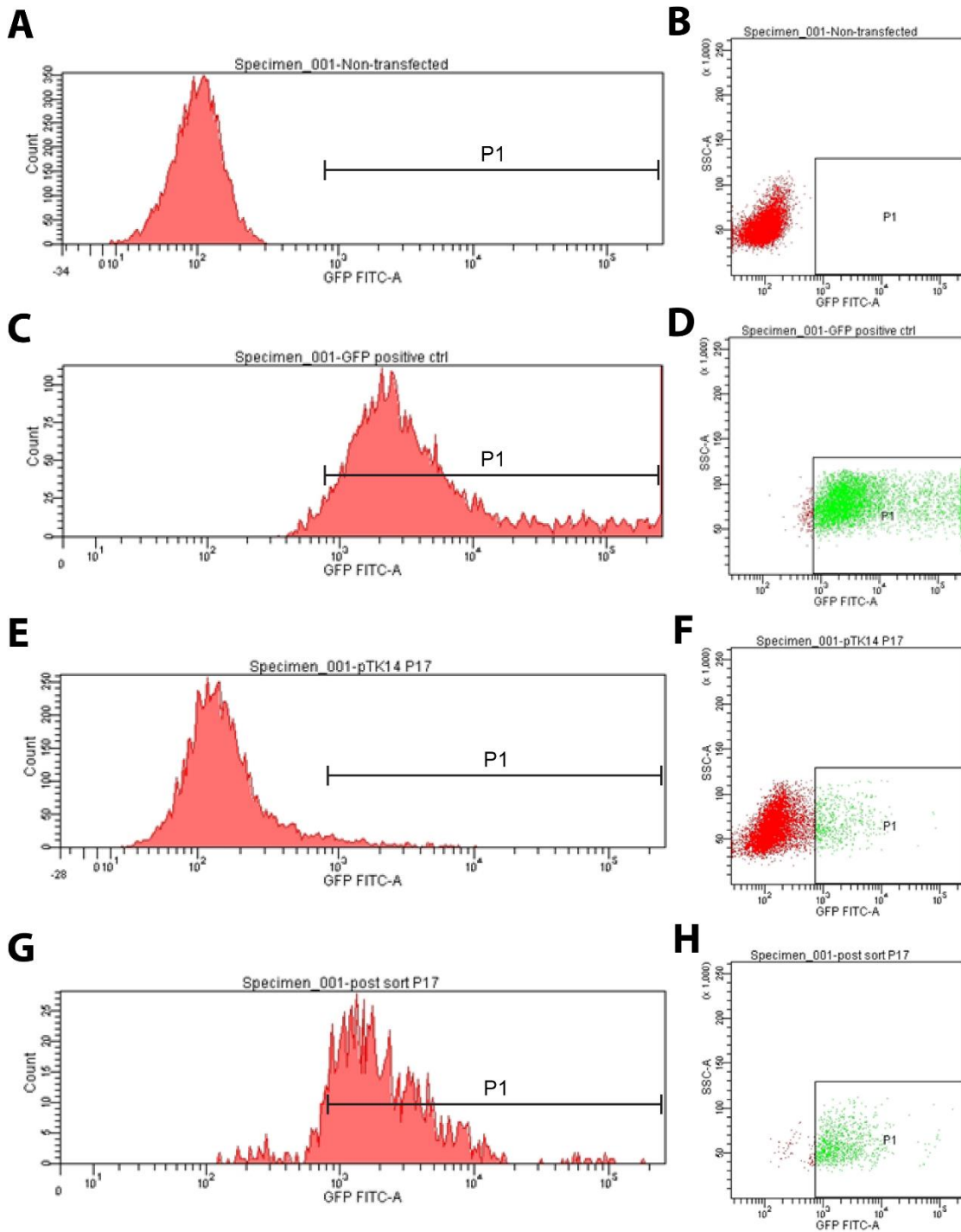


**Figure 2.1 Representative samples and controls for FACS**

(A-H) Representative histograms (left) and dot plots (right) of negative controls and single fluorescent protein expressing cells. (A-B). WT MCF-10A cells were used as a negative control to gate the sample (P1). (C-D) A positive control was used when available to further gate the region of interest (P1) (E-F) All cells (green) within the gate were sorted in the samples. (G-H) Sorting efficiency was tested with a small number of sorted cells.

## 2.3 DNA methods

Methods described in this chapter contain general protocols to modify several retroviral plasmids used to generate novel cell lines. Detailed procedures are found in the relevant chapter (see 2.4).

### 2.3.1 Purification of plasmid DNA from *E. coli*

Plasmid DNA was isolated from overnight *E. coli* cultures prepared as described in 2.1.1. When small-scale preparations were performed DNA was extracted from 3 ml bacteria culture using the QIAprep Spin Miniprep Kit (Qiagen). After following the manufacturers' instructions, DNA was eluted in 30  $\mu$ l water. For large-scale preparations, DNA was isolated from 300 ml bacteria culture using the PureLink™ HiPure Plasmid Filter Maxiprep Kit (Invitrogen) according to the manufacturer's instructions. DNA was eluted in 200  $\mu$ l water.

### 2.3.2 Amplification of DNA by polymerase chain reaction

Polymerase chain reaction (PCR) is a method to exponentially amplify specific DNA sequences by the use of a DNA polymerase, primers and deoxyribonucleoside triphosphates (dNTPs or nucleotides). The basic PCR reaction is temperature cycled and repeats three steps 30-40 times. For this, template DNA is denatured, primers are annealed to the target sequence and primers are extended with nucleotides by the DNA polymerase. The yields of amplified product can then be detected by downstream methods, such as visualization of DNA sequences on an agarose gel (Mullis and Faloona, 1987). In this thesis, specific primers were designed using the software ApE-A plasmid Editor (Version 2.0.49, <https://jorgensen.biology.utah.edu/wayned/ape/>). Primers were constructed to have a GC content around 50 %. Primers were purchased from Eurofins. DNA was amplified in a reaction mixture in a final volume of 50  $\mu$ l containing 100 ng of template DNA, 0.2  $\mu$ M forward primer, 0.2  $\mu$ M reverse primer, water and 1x OneTaq® Quick-Load® 2X Master Mix (New England BioLabs, NEB) using a T100 Thermal Cycler (Bio-Rad Laboratories). The Master Mix contained dNTPs, MgCl<sub>2</sub>, the DNA polymerase, buffers and stabilizers. Thermocycling conditions are detailed in Table 2.4. PCR reactions were carried out as duplicates. PCR products were visualised and evaluated on agarose gels.

**Table 2.4 General thermal cycling conditions for amplification of plasmid DNA**

Primer annealing temperatures and extension times (asterisks) specifically used in each experiment are detailed in the relevant chapters (see 2.4.1.1 – 2.4.1.4).

Step		Temperature	Time
Initial Denaturation		94 °C	30 sec
25 Cycles	Denaturation	94 °C	30 sec
	Annealing	60- 61 °C*	30 sec
	Extension	68°C	1 min/kb*
Final Extension		68°C	5 min
Hold		4 °C	∞

### 2.3.3 Purification of PCR products

PCR products were purified for subsequent applications using the QIAquick PCR Purification Kit (Qiagen) in accordance with the manufacturer's instructions. DNA was eluted in 40 µl water.

### 2.3.4 Agarose gel electrophoresis

Agarose gels were prepared as 1 % gels by melting agarose (Sigma) in 1x Tris-acetate EDTA buffer (TAE buffer). 1x TAE buffer was prepared from 50x TAE buffer (Sigma). SYBR™ Safe DNA Gel Stain (Invitrogen), concentrated at 1:10,000 was added to the mixture as a 1x concentration. Samples contained either a ready-to-load PCR buffer or appropriate amounts of 6x gel loading dye (NEB) were added to the DNA before loading into the wells of the gel. As a size reference, 10 µl of the Quick-Load® 100 bp DNA Ladder (NEB) or 10 µl of the Quick-Load® 1 kb DNA Ladder (NEB) were added to one well. DNA samples and markers were separated in 1x TAE buffer at 100 V for 30-60 min depending on the fragment separation required. DNA visualization and digital photography was performed with a UV transilluminator (GBox, Syngene). Images were viewed with GeneSnap software (Syngene).

### 2.3.5 Purification of DNA from agarose gels

DNA bands of interest visualised using a UV transilluminator (Syngene) were excised from agarose gels using a clean scalpel and transferred into 1.5 ml microcentrifuge tubes. Purification was performed with the QIAquick Gel Extraction Kit (Qiagen) according to the manufacturer's instructions. DNA was eluted in 30 µl water.

### 2.3.6 Restriction enzyme digestion

All restriction enzymes used in this thesis were purchased from NEB. Specific enzymes used are detailed in the relevant chapters (see 2.4.1.1 – 2.4.1.4). A typical reaction contained 1 µg of plasmid DNA or 20 µl of purified PCR product, 10 units of enzymes, 1x CutSmart® Buffer (NEB) made up to 30 µl with water. The reaction mixture was incubated in a water bath at 37 °C for 2 h to allow complete digestion. Following this, the entire mixture was loaded into wells of agarose gels and electrophoresed as described in section 2.3.4. Correctly sized DNA fragments were purified as detailed in section 2.3.5 and eluted DNA was quantified (see 2.3.9).

### 2.3.7 Ligation of vector and insert

DNA ligations were performed using a 1:3 molar ratio for digested vector and digested insert DNA (PCR product). For all reactions, 50 ng of vector were used. Based on the digested vector size and digested insert size, the following formula was used to calculate the amount of insert to be added to the reaction.

$$\text{insert mass (ng)} = \frac{3 \times \text{insert size (bp)} \times \text{vector mass (ng)}}{\text{vector size (bp)}}$$

A typical ligation reaction contained 50 ng vector, the calculated amount of insert, 1 unit T4 DNA ligase and 1x T4 DNA Ligase buffer (Invitrogen) made up to a total volume of 10 µl with water. The mixture was incubated at 16 °C overnight. On the next day, 5 µl of the ligation reaction were transformed into chemically competent *E. coli* cells as described in section 2.1.2.

### 2.3.8 Screening for positive clones

In order to screen bacterial clones that contained the vector plus insert, individual bacterial colonies grown on LB agar plates after transformation were picked and prepared as small-scale overnight cultures (Minipreps). Plasmid DNA was purified as described in section 2.3.1. Restriction enzyme digestion was performed with a mixture of 15  $\mu$ l purified plasmid DNA, 10 units of enzymes, 1x CutSmart<sup>®</sup> Buffer (NEB) and water filled up to 30  $\mu$ l. Reactions were incubated in a water bath at 37 °C for 2 h. Alongside miniprep samples, the original empty vector was digested as a control. Digested samples were electrophoresed as detailed in section 2.3.4 to identify clones that contain the DNA inserts.

### 2.3.9 Spectrophotometric quantification of DNA

Spectrophotometry can be used to calculate the concentration of DNA in a solution by using the advantage that nucleic acids absorb UV light with a peak absorbance at 260 nm. In this thesis, the concentration of DNA samples was measured using a NanoDrop ND1000 (Thermo Scientific). To generate a blank value, the absorbance at 260 nm was measured with 1.5  $\mu$ l of water. For DNA sample measurements, 1.5  $\mu$ l of each sample were loaded and measured. The purity of the sample was assessed by comparing the absorbance of the sample at 230 nm and 280 nm. The 260/280 absorbance ratio, with pure samples having a value of 1.8, indicates a possible contamination with proteins, phenol or other contaminants absorbing near that wavelength. A 230/260 ratio >1.5 indicates a sample free of contaminants.

### 2.3.10 DNA sequencing

Each DNA sequencing reaction contained a mixture of plasmid DNA and a relevant primer. 15  $\mu$ l of DNA sample (100 ng/ $\mu$ l) and 2  $\mu$ l of primer (10  $\mu$ M) were prepared. Sequencing was performed externally by the Eurofins Genomics' TubeSeq Service using the cycle sequencing technique on ABI 373XL machines. Sequencing results were viewed and analysed using the ApE-A Plasmid Editor (v2.0.49).

## 2.4 Generation of mammary cell lines

Generation of a stable cell line expressing a gene of interest from an integrated retroviral vector starts with the transfection of viral plasmids into packaging cells to produce virus particles. Then, the produced virus is used to infect host cells which results in the integration of the virus' genetic material into the host cell genome. Lastly, transduced cells are enriched by antibiotic selection to obtain more homogenous cell populations expressing the gene of interest (Cepko and Pear, 1996). In this work, retroviral transduction was used to generate various stable MCF-10A cell lines expressing fluorescence proteins or fluorescent fusion proteins. Before establishment of the cell lines, some retroviral vectors had to be modified by inserting sequences of the gene of interest.

### 2.4.1 Plasmid construction

Original plasmids used for retroviral production and cloning were purchased from Addgene. All transfer plasmids were Moloney murine leukemia virus (Mo-MLV) derived retrovirus vectors that are commonly used for gene delivery systems due to their simple and highly efficient integration into the host genome of mitotic cells (Sena-Esteves *et al.*, 2002). These plasmids had a pBABE backbone and were the pBABEpuro vector (Morgenstern and Land, 1990) or the pBABEblas version with a blasticidin marker.

The Bluescript KS(+) plasmid used for mutagenesis was kindly gifted by Dr David Bryant (Institute of Cancer Sciences/CRUK Beatson Institute, University of Glasgow). Dr Mohammed A. Mansour (Salah Elias lab, University of Southampton) assisted cloning of GFP-LGN mutants.

#### 2.4.1.1 Cloning strategy GFP control

In order to generate a control cell line expressing eGFP, the plasmid pTK14 (Addgene, #37360) expressing eGFP-LGN (referred to as pTK14-GFP-LGN) was modified (for vector map see Appendix A, Figure A.1). By using PCR (see sections 2.3.2 for the protocol), the eGFP sequence was amplified to insert a stop codon and the restriction site for PspOMI at the C-terminus of eGFP. Primer sequences, annealing temperatures and elongation times are listed in Table 2.6. The purified PCR product and the pTK14-GFP-LGN vector were restriction enzyme digested as detailed in 2.3.6 using the enzymes Bsu36I and PspOMI. The digested and purified vector and PCR product were ligated as described (section 2.3.7). After transformation (section 2.1.2), individual bacterial colonies grown on LB agar plates with ampicillin were screened for positive clones (section 2.3.8) using the restriction enzymes Bsu36I and PspOMI. Lastly, 4 positive-identified clones were sequenced to

verify the insertion of the correct sequence without point mutations. The primer used for sequencing is listed in Table 2.8. One sequenced clone without mutations was retransformed into *E. coli* cells and the plasmid was purified again as a large-scale preparation. The final vector is referred to as pTK14-GFP and the map can be found in Appendix A, Figure A.2.

**Table 2.5 Primer sequences and thermal cycling condition to generate the pTk14-GFP plasmid**

*The forward primer contains a Bsu36I restriction site (underlined). The reverse primer contains a PspOMI restriction site (underlined) and a stop codon (bold) as an overhang.*

Primer sequences 5' > 3'	Annealing temperature	Elongation time
FW: CCCGAC <u>CTGAGGA</u> AAGGGAG RV: ACAGCGGGG <u>CCCTT</u> ACTTGTACAGCTCGTCCATGCC	60 °C	1.5 min

#### 2.4.1.2 Cloning strategy ANXA1-mCherry

A gene block of the sequence for ANXA1-mCherry was synthesised by the gene synthesis service from Eurofins and cloned into the multiple cloning site of the A258 vector (provided by the company) for further cloning steps. The ANXA1 coding sequence was based on the sequence published in the NCBI database (NCBI Reference Sequence NM\_000700.3). The mCherry sequence was copied from the pTK93\_Lifeact-mCherry vector (Addgene, #46357).

The ANXA1-mCherry sequence was transferred into the pTK93-Lifeact-mCherry vector. For this, both plasmids were digested as described in section 2.3.6 with the restriction enzymes NaeI and Sall to cut out the ANXA1-mCherry and Lifeact-mCherry sequences. The vector backbone of pTK93\_Lifeact-mCherry and the cut ANXA1-mCherry sequence were ligated (see 2.3.7) and transformed into *E. coli* cells (2.1.2). Individual bacterial clones grown on LB agar plates supplemented with ampicillin were analysed as detailed in section 2.3.8 using the restriction enzyme NaeI and Sall for digestion. 4 positive clones were sent for sequencing to verify the correct gene sequence. Two primers were used annealing at the N- and C-terminus of the ANXA-mCherry insert to verify the complete sequence. Primers are listed in Table 2.8. One sequenced clone without mutations was retransformed into *E. coli* cells and the plasmid was purified again as a large-scale preparation. The final vector is referred to as pTK93-Anxa1-mCherry and the map can be found in Appendix A, Figure A.3.

### 2.4.1.3 Cloning strategy mCherry control

In order to generate a control cell line expressing the fluorescent protein mCherry, the plasmid pTK93-Lifeact-mCherry was modified. For this, the mCherry sequence was amplified using PCR (see 2.3.2) to insert the BamHI restriction site and Kozak sequence at the N-terminus of mCherry. Primer sequences, annealing temperatures and elongation times are listed in Table 2.7. The purified PCR product and the pTK93-Lifeact-mCherry vector were digested as detailed in section 2.3.6 using the restriction enzymes BamHI and Sall. Digestion of the original plasmid resulted in the cut out of the Lifeact-mCherry sequence. The digested and purified PCR product and vector were ligated (see 2.3.7) and transformed into *E. coli* cells (see 2.1.2). Individual bacterial colonies grown on LB agar plates with ampicillin were screened for positive clones as described using the restriction enzymes BamHI and Sall for digestion (see 2.3.8). 4 clones were sent for sequencing to validate the correct DNA sequence. The primer used is listed in Table 2.8. One sequenced clone without mutations was retransformed into *E. coli* cells and the plasmid was purified as a large-scale preparation. The final vector is called pTK93-mCherry. The map can be found in Appendix A, Figure A.4.

**Table 2.6 Primer sequences and thermal cycling condition to generate the pTK93-mCherry plasmid**

*The forward primer contains a BamHI restriction site (underlined) and the Kozak sequence (bold) as an overhang.*

Primer sequences 5' > 3'	Annealing temperature	Elongation time
FW: AATT <u>GGATCC</u> <b>GCCACC</b> ATGGTGAGCAAGGGCGAG RV: CTGACACACATTCCACAGGGTTCG	61 °C	1 min

**Table 2.7 Primers used to sequence cloned retroviral plasmids**

Plasmid	Primer sequences 5' > 3'
pTK14-GFP	GGCATCGACTTCAAGGAGGA
pTK93-Anxa-mCherry	1. GCCTCAATCCTCCCTTTATCC 2. CTGACACACATTCCACAGGGTTCG
pTK93-mCherry	CTGACACACATTCCACAGGGTTCG

## 2.4.2

### 2.4.2 Establishment of cell lines using retroviral transduction

All cell lines were generated with the same protocol described in section 2.2.8. All viruses were produced with the envelope plasmid pUMVC (Addgene #8449) and packaging plasmid pCMV-VSV-G (Addgene, #8454). The only varying components were the transfer plasmids and antibiotic selections used. In total, 4 different cell lines were generated that are listed in Table 2.10 which also details transfer plasmids and relevant selection strategies. The antibiotics blasticidin and puromycin were purchased from Sigma and Gibco respectively. Please note: No cell lines were generated with the LGN-mutant plasmids due to technical difficulties which are explained in the results chapter 5.2.1.

**Table 2.8 List of generated stable cell lines using retroviral transduction**

Cell line	Transfer plasmid	Antibiotic and concentration
MCF-10A_GFP-LGN	pTK14	Blasticidin, 2 µg/ml
MCF-10A_GFP	pTK14-GFP	Blasticidin, 2 µg/ml
MCF-10A_Annexin A1-mCherry	pTK93 Anxa1-mCherry	Puromycin, 1 µg/ml
MCF-10A_mCherry	pTk93-mCherry	Puromycin, 1 µg/ml

## 2.5 Protein methods

Reagents used for protein analysis were purchased from Sigma unless otherwise stated.

### 2.5.1 Protein expression analysis

#### 2.5.1.1 Protein extraction from mammalian cells

Nonidet™ P40 (NP40) buffer was used to lyse cells for protein extraction. The table on the next page lists all reagents (Table 2.11). The buffer was prepared fresh on the day of lysis. Constituents were assembled on ice with adding phenylmethylsulfonyl fluoride (PMSF) last shortly before usage.

**Table 2.9 NP40 lysis buffer ingredients**

Component	Final concentration
Tris-HCl, pH 7.4	50 mM
NaCl	250 mM
EDTA, pH 8.0	5 mM
NaF	50 mM
Na <sub>3</sub> VO <sub>4</sub>	1 mM
PMSF	1 mM
10x Protease Inhibitor Cocktail (#P2714)	1x
NP40	1 % (v/v)

For protein extraction, cell culture media was removed and cells were washed twice with cold DPBS. After complete removal of DPBS, culture dishes or plates were placed on ice and cells were scraped in NP40 buffer. Samples were transferred into precooled microcentrifuge tubes and placed on ice for 30 min with mixing every ten min. Lysates were centrifuged at 13,000 rpm for 30 min at 4 °C and clear supernatants were transferred into clean precooled microcentrifuge tubes. At this point, samples were either immediately used for protein quantification or stored at -20 °C until further processing.

### 2.5.1.2 Quantification of total protein concentration

The total protein concentration was determined with the Pierce™ BCA Protein Assay Kit (Thermo Fisher) following the manufacturer's instructions. This colorimetric assay is based on the reduction of Cu<sup>+2</sup> to Cu<sup>+1</sup> by proteins in an alkaline solution and results in a purple colour formation by bicinchoninic acid (BCA) (Smith *et al.*, 1985). The BCA/copper complex exhibits absorbance at 562 nm. The increase of absorption is directly proportional to the amount of copper reduction, hence proteins present in the sample. By referencing against standards of known concentrations of bovine

serum albumin (BSA) the total protein concentration was calculated. A BSA series dilution with different concentrations ranging from 0.1 to 1 mg/ml was prepared by diluting BSA in NP40 lysis buffer. One blank sample consisting of lysis buffer only was made. In addition, 1:10 dilutions of the protein samples were prepared with lysis buffer. 25 µl of diluted samples, BSA standards and the blank solution were added to wells of a clean 96-well microtiter plate. Standards and the blank solution were loaded as duplicates and the protein samples as triplicates. A BCA working solution was prepared by mixing 50 parts of Reagent A with 1 part of Reagent B from the kit. 200 µl of the mixture were added to each well containing standards, blanks or the samples. The plate was incubated for 30 min at 37 °C in the dark. After cooling the plate to RT, the absorbance was measured at 562 nm using a plate reader (POLARstar Omega, BMG LABTECH). Concentrations were calculated from the obtained BSA standard curve.

### **2.5.1.3 Sodium dodecyl sulphate polyacrylamide gel electrophoresis**

Proteins were separated on one dimensional gels based on their molecular weight using sodium dodecyl sulphate polyacrylamide gel electrophoresis (SDS-PAGE) according to the standard Laemmli protocol (Laemmli, 1970). This method relies on discontinuous gel electrophoresis under denaturing conditions in the presence of SDS. For this, two polyacrylamide gels were casted in two steps using the Mini-PROTEAN Tetra Cell Casting Module (Bio-Rad Laboratories). Components and concentrations for gel preparations are listed in table 2.12. First, separating gels ranging from 8-15 % were casted. Ammonium persulphate (APS) and tetramethylethylenediamine (TEMED) were added last to catalyse polymerisation. Mixtures were poured into gel chambers stopping approximately 1 cm below the bottom of the comb. Isopropanol was layered on top to remove bubbles and evenly align the separating gel. After polymerization, isopropanol was removed and remaining alcohol was washed out with water. Next, a 4 % stacking gel was prepared, poured on top of the separating gel and a comb was added to form wells. After polymerization, gels were used immediately or stored in moist tissue at 4 °C for a maximum of one week.

**Table 2.10 Components for SDS-PAGE gel preparation**

*Details of volumes for chemicals used to prepare different percentages of polyacrylamide gels for SDS-PAGE.*

Component	Separating gel (ml)				Stacking gel (ml)
	8 %	10 %	12 %	15 %	
					4 %
H <sub>2</sub> O	3.95	3.56	3.2	2.63	2.3ml
40 % 37:5:1 BIS-acrylamide	1.5	1,89	2.25	2.82	0.3
1.5 M Tris- HCl, pH 8,8	1.9	1.9	1.9	1.9	-
1 M Tris, pH 6,8	-	-	-	-	0.380
10 % SDS	0.075	0.075	0.075	0.075	0.03
10 % APS	0.075	0.075	0.075	0.075	0.03
TEMED	0.003	0.003	0.003	0.003	0.003

Protein samples were prepared by adding one part of 4x Laemmli Sample Buffer (Bio-Rad Laboratories) freshly supplemented with 5 % 2-mercaptoethanol to three parts of sample. The mixture was heated at 95 °C for 5 min, cooled down on ice and briefly centrifuged to collect condensation droplets. Polyacrylamide gels were placed in the Mini-PROTEAN Tetra cell system (Bio-Rad Laboratories) and denatured protein samples were loaded into the wells. When the total protein concentration was determined, 30 µg of protein was loaded. If protein concentrations was not known (IP experiments) 35 µl were loaded. As a reference, 2 µl of a protein molecular weight marker (Prestained Protein Ladder – Broad molecular weight, 10-245 kDa (Abcam)) were loaded in one well on the same gel. The electrophoresis chamber was filled with 1x SDS-PAGE running buffer that was prepared from a 10x concentrated buffer consisting of 250 mM Tris pH 8.3, 1.92 M glycine and 1 % (w/v) SDS. Gels were run by compressing the samples at 80 V for 20 min and separating them at 120 V for 90 min.

#### 2.5.1.4 Western blot

To visualise proteins separated in SDS-PAGE, proteins were transferred to a 0.45 µm pore nitrocellulose membrane (GE Healthcare) in a wet transfer procedure using the Mini Trans-Blot® (Bio-Rad Laboratories). For this, transfer cassettes were prepared by placing the nitrocellulose membrane on top of the polyacrylamide gel and in between two sheets of filter blot papers. These were sandwiched between two foam papers. All components were pre-soaked in 1x transfer buffer. The buffer was prepared by diluting a 10x transfer buffer consisting of 25 mM Tris and 1.92 M glycine and adding methanol to a final concentration of 20 % (v/v). The transfer cassette was assembled and placed in the transfer unit filled with 1x transfer buffer so that the negatively charged proteins in the gel are pulled towards the membrane that is facing the anode. Proteins were transferred under constant cooling for 3 h at 80 V and 0.3 A. Nitrocellulose membranes were reversely stained with Ponceau S (0.1 % (w/v) in 5% acetic acid to confirm a successful transfer. The ready-to-use staining solution was added on top of the membrane and after 1 min, membranes were rinsed several times with Tris- buffered saline (TBS) until red staining of proteins appeared as seen in Figure 2.2. The membranes were washed three times for 3 min with TBS to remove remaining dye before immunodetection of proteins. Membranes were blocked using 5 % dried skimmed milk (Marvel) dissolved in 1x TBS with Tween 20 (TBS/T). TBS/T was prepared by diluting a 10x concentrated TBS buffer consisting of 1.5 M NaCl and 200 mM Tris and adding Tween 20 to a final concentration of 0.1 % (v/v). Membranes were incubated for 1 h on a rocking table to block unspecific antibody binding sites. Primary antibodies were diluted in 5 % dried skimmed milk in 1x TBS/T at individually optimized concentrations (see Table 2.13 for relevant antibodies and dilutions used) and added to the membranes to incubate overnight at 4 °C under constant agitation. Thereafter, membranes were rinsed three times 5 min with 1x TBS/T to eliminate unbound antibody. Species-specific secondary antibodies conjugated to horseradish peroxidase (HRP) were diluted in 5 % dried skimmed milk in 1x TBS/T and applied to the membranes for 1 h on a rocking table (see Table 2.13 for relevant antibodies and dilutions). After the incubation, membranes were washed two times 5 min with 1x TBS/T to remove unbound antibody. Following one last wash with PBS, membranes were prepared for enhanced chemiluminescent (ECL) detection. For this, the SuperSignal™ West Femto Maximum Sensitivity Substrate Kit (Thermo Scientific) was used according to the manufacturer's instructions. Approximately 400 µl of the mixed solution consisting of equal amounts of the Stable Peroxide Solution and the Luminol/Enhancer Solution from the kit were added to one membrane. After incubation for 5 min in the dark, the ECL working solution was

removed and excess reagent was drained. Protein bands were visualised immediately with the Syngene PXi detection system (Syngene).

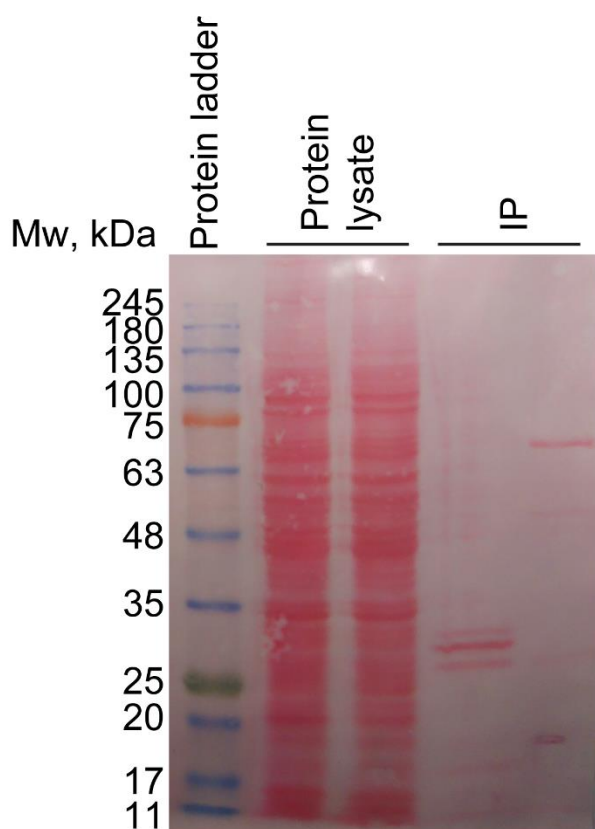


**Figure 2.2 Representative Ponceau S staining of after protein transfer**

*Staining with Ponceau S allowed confirmation of effective protein transfer from the gel to the nitrocellulose membrane. This image shows representative for all experiments staining patterns of protein lysates loaded onto the gel. Furthermore, enriched proteins after immunoprecipitation (IP) are shown.*

**Table 2.11 List of primary and secondary antibodies used for immunodetection via Western blot**  
*Details of dilutions, host species and companies from which the antibodies were purchased are provided. pH3 - phospho-Histone H3.*

Primary Antibody	Dilution	Host species	Source
Anti- $\alpha$ -tubulin DM1A	1 in 5000	Mouse	Sigma, #T6199
Anti-LGN	1 in 500	Rabbit	Sigma, #ABT174
Anti-GFP	1 in 500	Rabbit	Invitrogen, #A-11122
Anti-pH3 (Ser10)	1 in 1000	Rabbit	Sigma, #06-570
Anti-ANXA1	1 in 1000	Rabbit	Proteintech, #55018-1-AP
Anti-mCherry	1:1000	Rabbit	Abcam #ab167453
Secondary Antibody	Dilution	Host species	Source
Anti-Rabbit IgG (H+L), HRP	1 in 10,000	Goat	Invitrogen, #32460
Anti-Mouse IgG (H+L), HRP	1 in 10,000	Goat	Invitrogen, #32430

### 2.5.1.5 Quantitative Western blot analysis

The relative protein amount was quantified to reflect the ratio of protein band sizes relative to the loading control band size. This allowed comparison between protein levels in control and knockdown conditions after siRNA knockdown. Quantifications were performed using the Gel Analysis method in Fiji following the Fiji (Schindelin *et al.*, 2012) following the documentation: (<https://imagej.nih.gov/ij/docs/menus/analyse.html#gels>). Unedited images of Western blot images were opened in Fiji as grey-scale images. Using the “Rectangular selection”, a rectangle was drawn around one protein lane and selected as the first lane (Analyse>Gels>Select First Lane in Fiji). Using this first selection, the remaining protein bands were also highlighted in succession (Analyse>Gels>Select Next Lane in Fiji) which generated highlighted rectangles of the same size and alignment around each protein lane (see Figure 2.3, A). Then, profile plots were generated that represent the relative density of the rectangle contents for each protein band (Analyse>Gels>Plot Lanes in Fiji). The areas of the profiles were measured using the “Wand tool” and profile sizes were expressed as percentages of the total size of all highlighted profiles by labelling the profiles

(Analyse>Gels>Label Peaks in Fiji) (Figure 2.3, B-C). Once these measurements were obtained for the protein-of-interest and loading control, the data was pasted into Microsoft Excel to calculate the relative intensity of protein band sizes relative to the loading control (Figure 2.3, D).

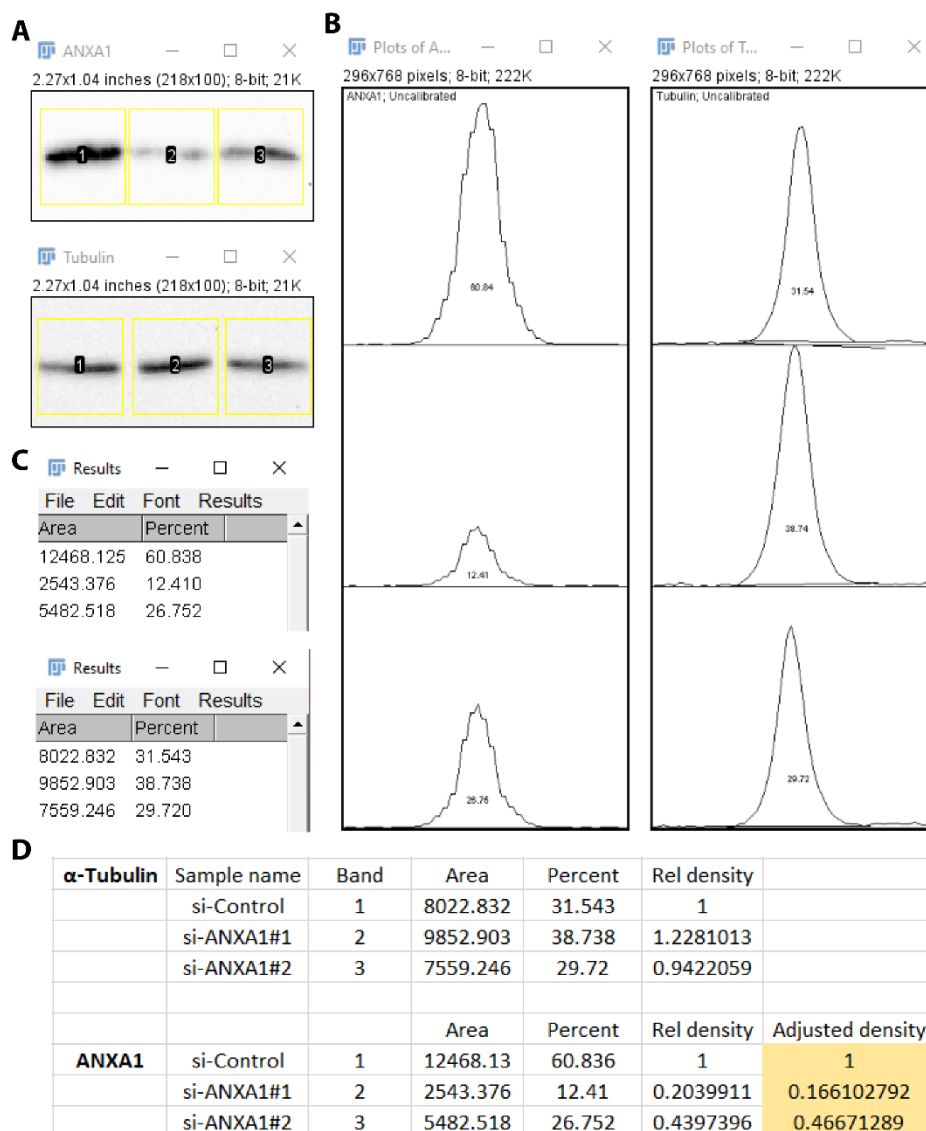


**Figure 2.3 Example of a quantification of relative protein bands sizes**

(A) Unedited Western blot images were opened in Fiji and analysed using the Gel Analysis method. Proteins bands were successively selected. (B) Profile plots of the highlighted rectangular areas were generated. The areas of the profile plots were measured. (C) Areas were expressed as percentages and exported to Microsoft Excel. (D) Adjusted relative intensity (yellow highlight) were calculated relative to the loading control ( $\alpha$ -Tubulin).

## 2.5.2 Proteomic analysis

Proteomic experiments were carried out in cooperation with the Centre for Proteomic Research at the University of Southampton. Protein samples were prepared as detailed in sections 2.5.2.1 and 2.5.2.2 and further processed by Dr Paul Skipp from the facility who also performed the mass spectrometry (MS) run (2.5.2.3).

### 2.5.2.1 Immunoprecipitation using Nano-Traps

The Nano-Traps from Chromotek, precisely the GFP-Trap and RFP-Trap systems, were used to co-immunoprecipitate (Co-IP) GFP or mCherry fusion proteins or the fluorescent proteins alone. Both systems utilized magnetic agarose beads as an affinity matrix. The protocol was identical for both Nano-Traps.

MCF-10A cells expressing the protein of interest were plated at  $6 \times 10^6$  cells per 15 cm cell culture dish. Six plates per conditions were prepared for subsequent proteomics analysis and one plate was used for Western blotting. When reaching 80 % confluency, cells were synchronized at metaphase as described in section 2.2.3 and proteins were extracted from the arrested cells as detailed in section 2.5.1.1 using a mild NP40 lysis buffer (Table 2.14). 650  $\mu$ l lysis buffer were used per plate to scrape cells.

**Table 2.12 Lysis buffer ingredients to extract proteins for immunoprecipitation**

Component	Final concentration
Tris-HCl, pH 7.4	50 mM
NaCl	150 mM
EDTA, pH 8.0	0.5 mM
NaF	30 mM
Na <sub>3</sub> VO <sub>4</sub>	1 mM
PMSF	1 mM
10x Protease Inhibitor Cocktail (#P2714)	1x
NP40	0.5 % (v/v)

All the following steps were carried out at 4 °C. 25 µl of magnetic agarose beads were used for 650 µl of protein lysate. Before incubation with the samples, beads were equilibrated by washing the bead slurry three times with ice-cold wash buffer (lysis buffer without NP40). Separation of beads from solutions was carried out with the 16-Tube SureBeads™ Magnetic Rack (Bio-Rad Laboratories). Samples were then incubated for 2 h with end-over-end rotation. Magnetic agarose beads were separated from the supernatant and resuspended in 650 µl wash buffer. Beads were washed 3 min and separated again from the supernatant which was discarded. This process was repeated two more times. When samples were subjected to Western blotting, proteins were eluted from beads by boiling in 1× Laemmli sample buffer (Bio-Rad Laboratories) containing 5 % 2-mercaptoethanol. For mass spectrometry analysis, washed beads were eluted as detailed in the next section.

### **2.5.2.2 Sample preparation for mass spectrometry**

Immunoprecipitated proteins on the beads were subjected to on-bead trypsin digestion as described (Smits *et al.*, 2013). Details of buffer compositions can be found in Table 2.15. 50 µl of Elution buffer I were added to the beads and incubated at 30 °C for 30 min in a thermoshaker. Partially denatured proteins in the supernatant were collected in a new tube before 75 µl of elution buffer II were added to the beads. Beads were further incubated at RT for 30 min in the dark before Sequencing Grade Modified Trypsin (Promega, #V511) was added to the beads at a final concentration of 5 µg/ml. This mixture was incubated for 1 h at 37 °C in a thermoshaker to allow partial digestion of the proteins from the beads. The supernatant was collected and combined with the first supernatant. This mixture was incubated overnight at 37 °C to fully digest proteins. Digested peptides were further processed by Dr Paul Skipp. Liquid was removed from the samples by vacuum concentration using the Concentrator 5310 (Eppendorf AG). Next, C18 reverse phase clean-up was performed on the digested peptides using a Waters Oasis C18 plate (Waters, UK). In a series of washing steps, samples were desalted and enriched for MS.

**Table 2.13** Ingredients of elution buffers for on-bead tryptic digestion

*DTT-Dithiothreitol, IAA-iodoacetamide.*

Elution buffer I	Final concentration
Urea	2 M
Tris, pH 7.5	50 mM
DTT	1 mM
Elution buffer II	Final concentration
Urea	2 M
Tris, pH 7.5	50 mM
IAA	5 mM

### 2.5.2.3 Mass Spectrometry

Samples were analysed with liquid chromatography coupled to tandem mass spectrometry (LC-MS/MS). For this, peptide extracts were separated on an Ultimate 3000 RSLC nano system (Thermo Scientific) using a PepMap C18 EASY-Spray LC column, 2  $\mu\text{m}$  particle size, 75  $\mu\text{m}$  x 75 cm column (Thermo Scientific) over a 140 min (single run) linear gradient of 3–25% buffer B (0.1% formic acid in acetonitrile (v/v)) in buffer A (0.1% formic acid in water (v/v)) at a flow rate of 300 nL/min. Peptides were introduced using an EASY-Spray source at 2000 V to a Fusion Tribrid Orbitrap mass spectrometer (Thermo Scientific). Data hits were searched with the Proteome Discoverer software (Thermo Scientific) against the human Uniprot KB database and filtered for a false discovery rate (FDR) of 1 %. Identified proteins and corresponding data values were exported to Microsoft Excel for further data analysis described in section 2.7. The mass spectrometry proteomics data have been deposited to the ProteomeXchange Consortium via PRIDE partner repository (Perez-Riverol *et al.*, 2019) with the dataset identifier PXD027452.

## 2.6 Microscopy methods

This section contains general protocols to stain specific proteins via immunocytochemistry and specific imaging methods and settings. Individual staining procedures used for relevant experiments were further detailed in the results chapters. PBS used to prepare buffers was made by dissolving PBS tablets (Sigma) in water to yield a final concentration of 0.01 M and autoclaved before usage. Image analysis was performed in Fiji unless otherwise stated.

### 2.6.1 Immunocytochemistry

Cells were plated on coverslips (22mm diameter, 0.13 to 0.17mm thick; Fisherbrand) in six-well plates in densities appropriate to the experiment. On the day of staining, cells were washed once with DPBS before fixation. Details about antibodies used are listed in Tables 2.16 and 2.17.

Depending on the target protein, four different fixation and staining protocols were performed:

i) Cells were fixed with 4 % paraformaldehyde (PFA, Fisher Scientific) for 20 min and permeabilized with 0.5 % (v/v) Triton-X-100 (Sigma) in PBS for ten min. To block unspecific binding sites, 0.1 % (v/v) Triton-X-100 in PBS with 3 % (v/v) BSA (Sigma) was applied for 1 h. Primary antibodies were diluted accordingly in blocking solution and incubated in a humidified chamber at 4 °C overnight. 100 µl of antibody solution was used per coverslip. On the next day, cells were washed three times for 5 min with 0.1 % (v/v) Triton-X-100 in PBS. The secondary antibody was diluted accordingly in blocking solution and 100 µl were applied per coverslip for 1 h at RT. Cells were washed two times for 5 min with 0.1 % (v/v) Triton-X-100 in PBS. DNA was stained with the cell-permeable stain Hoechst 33342 (Sigma). The dye was prepared as a stock solution by diluting it with water to a final concentration of 10 mg/ml, aliquoted and stored at -20 °C. As a working solution, the stain was further diluted in PBS to reach a concentration of 25 µg/ml and added to the cells for 3 min. Cells were washed two times for 5 min with PBS before mounting with VECTASHIELD® Antifade Mounting Medium (Vector Laboratories). Coverslips were sealed with clear nail polish. Samples were stored at 4 °C.

ii) Cells were fixed by adding ice-cold methanol (Sigma) to the cells and incubated at -20 °C for 10 min. After washing the cells twice for 5 min with PBS, 0.5 % (v/v) Triton-X-100 in PBS was applied to the cells for 2 min for permeabilization. All further staining steps were performed as described under i), PFA fixation.

iii) Cells were fixed with 3 % paraformaldehyde + 0.25 % glutaraldehyde + 0.2 % NP40 in Brinkley buffer 1980 ((BRB80) 80 mM Piperazine-N,N'-bis(2-ethanesulfonic acid) (PIPES), 1 mM MgCl<sub>2</sub> hexahydrate, 1 mM Ethylene glycol-bis( $\beta$ -aminoethyl ether)-N,N,N',N'-tetraacetic acid (EGTA)) for 1 min, followed by incubation with 3 % paraformaldehyde + 0.25 % glutaraldehyde in BRB80 for 10 min and with 0.1 M ammonium chloride in BRB80 for 10 min. Cells were washed two times for 5 min with BRB80, permeabilized with PBS and 0.5 % Triton X-100 for 10 min, washed again twice in BRB80 and finally blocked in 3 % BSA and 0.2 % NP-40 in BRB80 for 1 h. Primary antibodies were diluted accordingly in blocking solution and incubated in a humidified chamber at 4 °C overnight. 100  $\mu$ l of antibody solution was used per coverslip. On the next day, cells were washed three times for 5 min with 0.2 % NP-40 in BRB80. The secondary antibody was diluted accordingly in blocking solution and 100  $\mu$ l were applied per coverslip for 1 h at RT. Cells were washed two times for 5 min with 0.2 % NP40 in BRB80. DNA was stained with 25  $\mu$ g/ml Hoechst 33342 for 3 min and washed for 5 min with 0.2 % NP40 in BRB80. After a final wash PBS for 5 min cells were mounted with VECTASHIELD® Antifade Mounting Medium (Vector Laboratories). Coverslips were sealed with clear nail polish. Samples were stored at 4 °C.

iv) Cells were fixed with 10 % trichloroacetic acid (TCA) in water for 7 min on ice followed by incubation with ice-cold methanol at -20 °C for 10 min. After washing the cells twice for 5 min with PBS, 0.5 % (v/v) Triton-X-100 in PBS was applied to the cells for 2 min for permeabilization. All further staining steps were performed as described under i), PFA fixation.

**Table 2.14 List of primary antibodies used for immunocytochemistry**

*Anti-GFP IgG1 $\kappa$  (clones 7.1 and 13.1) was kindly provided by Marcin Przewloka lab (University of Southampton).*

Primary Antibody	Dilution	Host species	Source
Anti- $\alpha$ -tubulin DM1A	1 in 1000	Mouse	Sigma, #T6199
Anti-LGN	1 in 200	Rabbit	Sigma, #ABT174
Anti-NuMA	1 in 100	Rabbit	Novus Biologicals, #NB500-174
Anti-GFP	1 in 500	Chicken	Abcam, #ab13970

**Table 2.16 Continued**

Anti-GFP IgG1 $\kappa$ (clones 7.1 and 13.1)	1 in 500	Mouse	Sigma, #11814460001
Anti-Gai1	1 in 20	Mouse	SantaCruz, #sc-56536
Anti-ANXA1	1 in 200	Rabbit	Proteintech, #55018-1-AP
Anti-ANXA1	1 in 100	Mouse	Proteintech, #66344-1-Ig
Anti- $\gamma$ -tubulin AK-15	1 in 300	Rabbit	Sigma, #T3320,
Anti- $\gamma$ -tubulin (Clone Gtu-88)	1 in 300	Mouse	Sigma, #T5326
Anti-p150 <sup>Glued</sup>	1 in 100	Mouse	BD Biosciences, #610473
Anti-mCherry	1 in 300	Rabbit	Abcam, #ab167453

**Table 2.15 List of secondary antibodies used for immunocytochemistry**

Secondary Antibody	Dilution	Host species	Source
Anti-rabbit Alexa Fluor 488 IgG (H+L)	1 in 400	Goat	Invitrogen, #11008
Anti-rabbit Alexa Fluor 594 IgG (H+L)	1 in 400	Goat	Invitrogen, #11037
Anti-mouse Alexa Fluor Plus 488 IgG (H+L)	1 in 400	Goat	Invitrogen, #A32723
Anti-mouse Alexa Fluor 594 IgG (H+L)	1 in 400	Goat	Invitrogen, #A21125

**Table 2.17 Continued**

Anti-mouse Alexa Fluor Plus 647 IgG (H+L)	1 in 400	Goat	Invitrogen, #A32728
anti-chicken Cross-Adsorbed, Alexa Fluor® 633 IgY (H+L)	1 in 400	Goat	Invitrogen, #A21103

For all antibodies used, control conditions were tested where the primary antibody was abolished. This helped to estimate the background emanating from treatment with the secondary antibody or determine any unspecific signal arising from the staining procedure. Furthermore, controls were performed where secondary antibodies were excluded to estimate autofluorescence in the cells. An example of the control conditions is shown in Figure 2.4. This figure represents results for all other antibodies used in this study where no unspecific signal or background noise was protected.

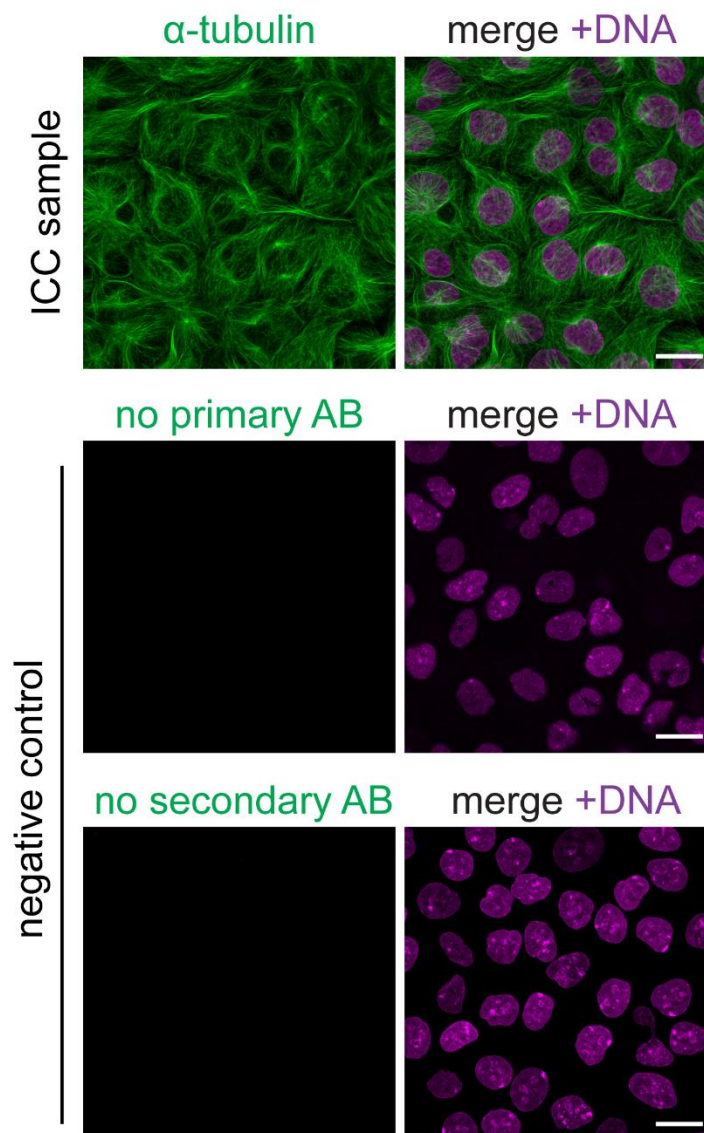


**Figure 2.4 Representative immunocytochemistry staining controls**

*Representative confocal images of immunocytochemistry staining and controls used to test the antibody performance in MCF-10A cells.  $\alpha$ - tubulin staining (ICC sample) serves as an example for all other antibodies used in this study. Cells were fixed with 4 % PFA and stained for  $\alpha$ - tubulin (green). DNA (magenta) was visualised with Hoechst 33342. For negative controls, primary or secondary antibodies were abolished as indicated. Scale bar, 25  $\mu$ m.*

### 2.6.2 Proximity ligation assay

The proximity ligation assay (PLA), also referred to as Duolink™ PLA technology, is an antibody-based methodology to detect protein-protein interactions *in situ* at endogenous protein level in cells and tissues (Fredriksson *et al.*, 2002; Alam, 2018). The assay detects two proteins of interest that are in close proximity (distance < 40 nm) by exploiting the binding of two specific antibodies from different species to the proteins. The experimental procedure is illustrated in Figure 2.5. In this work, PLA technology was used to detect proximal association of ANXA1 and LGN. The Duolink™ PLA from Sigma was used (#DUO92102) according to the manufacturer's protocol. MCF-10A cells expressing GFP-LGN were plated on small coverslips (16 mm diameter, 0.13 to 0.17 mm thick; Fisherbrand). When confluent, cells were fixed with methanol and stained with primary antibodies as described in the standard immunofluorescence protocol above (Section 2.6.1, II). Samples were incubated with rabbit anti-ANXA1 and mouse anti-GFP antibodies. As a negative control, cells were incubated with anti-ANXA1 or anti-GFP antibody alone. As a positive control, cells were labelled with rabbit anti-LGN and mouse anti-GFP antibodies. For all conditions, cells were incubated with relevant antibodies at 4 °C overnight. Once antibodies were bound, two oligonucleotide-labelled secondary antibodies, called PLA probes, were prepared. For this, Anti-Rabbit PLUS and Anti-Mouse MINUS (#DUO92002 and DUO92004) probes were diluted 1:5 in blocking solution and incubated for 20 min. In the meantime, cells were washed three times for 5 min with 0.1 % (v/v) Triton-X-100 in PBS to remove unbound antibodies. 40 µl of diluted PLA probes were added to the cells and incubated for 2 h at 37 °C in a humidified chamber. Then, cells were washed two times for 5 min with PLA wash buffer A (Sigma, #DUO82046) to remove unbound probes. For the next ligation step, ligation buffer containing connector oligonucleotides was diluted 1:5 in water and ligase was added at 1:40 (1 U/µl) just before incubation with cells. 40 µl of the ligation mixtures were added per coverslip and incubated for 30 min at 37 °C in a humidified chamber. During this time, connector oligonucleotides hybridize with the oligonucleotides of the probes and the ligase forms a closed circle of the connector oligonucleotides if the probes are in close proximity. This circle DNA forms a template DNA for the following rolling circle amplification. This final step was performed in dimmed light due to light sensitivity of the amplification buffer. After ligation, cells were washed twice for 2 min with PLA wash buffer A. The amplification reaction was prepared by diluting amplification buffer 1:5 in water and adding the Phi29 pol polymerase at 1:80 (10 U/µL) immediately prior to incubation. 40 µl of the mixture were added per coverslip and incubated for 2.5 h at 37 °C in a light protected humidified chamber. Finally, cells were washed once for 5 min with PLA wash buffer B (#DUO82048) and two more times for 5 min with PBS before mounting with

mounting medium containing DAPI (#DUO82040). Coverslips were sealed with nail polish and stored at 4 °C.

During the rolling circle amplification, fluorescence-labelled oligonucleotides hybridize to the amplicon to produce discrete fluorescent spots (PLA signals). Due to the short stability of the PLA signal, samples were imaged the next day using confocal microscopy as described below (section 2.6.3).

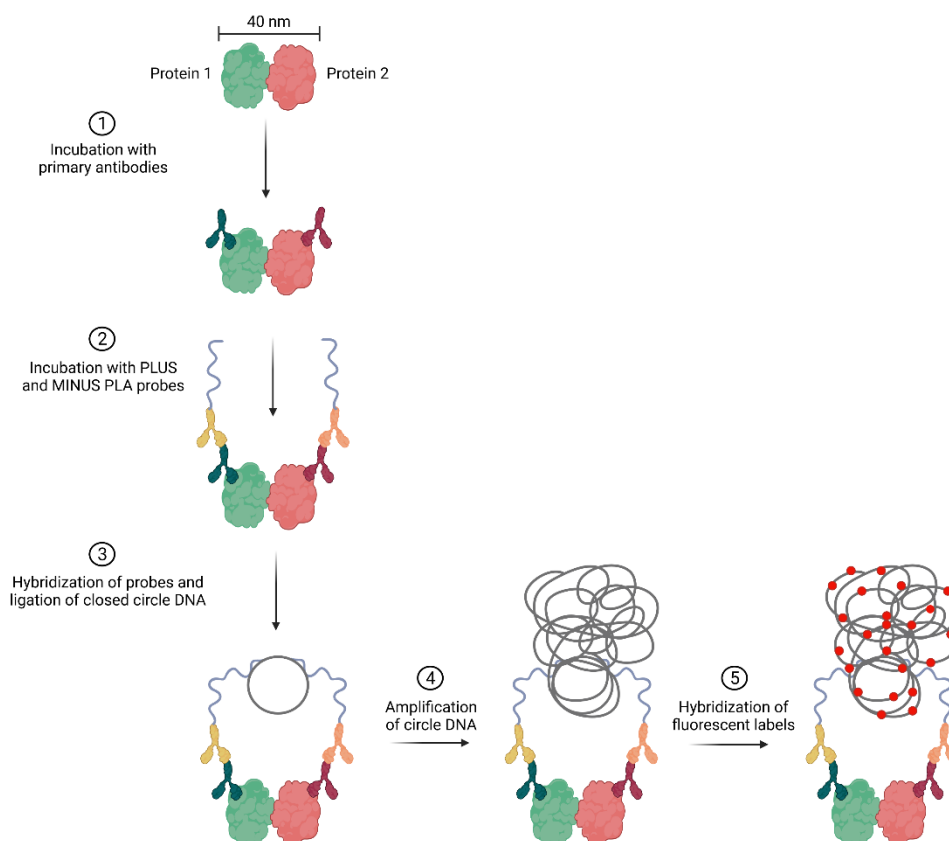


**Figure 2.5 Schematic of the principle of PLA technology**

*Protein- protein interactions are detected between proteins that are less than 40 nm in proximity. 1. Specific primary antibodies are added that bind to proteins of interest. 2. Oligonucleotide- labelled PLUS and MINUS PLA probes bind to protein- bound antibodies. 3. When proteins of interest are in close proximity, connector oligonucleotides link with PLA probes and are ligated to a closed circle. 4. The circle DNA is amplified to generate many copies attached to the PLA probes. 5. Fluorescence- labelled oligonucleotides hybridize with the amplified circle DNA and produce discrete fluorescent spots that can be detected with standard microscopy. Generated with Biorender.com.*

### 2.6.3 Confocal imaging of fixed cell preparations

Imaging of fixed cells was performed with a Leica TCS SP8 AOBS Inverted Confocal Laser Scanning Microscope (Leica Microsystems) with a Tuneable Spectral detector (SP detector) 350-800 nm (2 x PMT (Photomultiplier tube)). Samples were imaged using either 20x HC PI Apo CS2 1.30 N.A. objective or 63x HC PI Apo CS2 1.30 N.A. objective with glycerol immersion. The Z-plane was analysed with Z-stacks containing 0.2 to 0.3  $\mu\text{m}$  increments. Images were processed and analysed using Fiji.

### 2.6.4 Live cell microscopy

In this study, WT MCF-10A cells or cells expressing GFP-LGN were imaged during cell division. For every live cell imaging experiment, Hoechst 33342 was used to label DNA. When mitotic spindle dynamics were imaged, the fluorogenic and cell-permeable probe SiR-Tubulin (Cytoskeleton Inc) which labels MTs, was used (Lukinavičius *et al.*, 2014). The probe was dissolved in DMSO to reach a final concentration of 1 mM and stored at -20 °C. For imaging, cells were plated in 27 mm Nunc™ Glass Bottom Dishes (Thermo Scientific) in appropriate numbers. On the day of imaging, DNA was stained by incubating cells in cell culture media supplemented with 100 ng/ml Hoechst 33342 for 30 min before observation. When cells were also labelled with SiR- Tubulin, cell culture media containing Hoechst 33342 was replaced with fresh culture media containing the probe at a final concentration of 100 nM. Cells were further incubated for 2 h. After rinsing the cells three times with DPBS to remove excess DNA stain and microtubule probe, Phenol Red-free DMEM/F12 media (Gibco) supplemented with the regular additives except antibiotics (see Table 2.1 in section 2.2.1) and 25 mM HEPES buffer was added to the cells. Images were acquired at 37 °C with a DeltaVision Elite microscope (GE Healthcare) coupled to a sCMOS max chip area 2,048 x 2,048 camera (G.E. Healthcare). For each recording, image stacks of 30 to 40 planes at 0.6  $\mu\text{m}$  increments were acquired using a PlanApo 60x/1.42 Oil objective (Olympus) with 2x2 binning. Images were taken every 2.5 to 5 min for 3 to 5 h. Exposure times were 250 msec and 5 % laser power for GFP (excited at 475 nm and 575 nm respectively), 50 msec and 2 % laser power for labelled DNA (excited at 390 nm) and 80 msec and 2 % laser power for labelled MTs using the DAPI-FITC-mCh-Cy5 filter set. Images were deconvolved using the DeltaVision software SoftWoRx (Version 6.5.2) and further processed in Fiji.

### 2.6.5 Spindle orientation analysis

Spindle orientation was measured in metaphase MCF-10A cells that were fixed and stained with anti- $\gamma$ -tubulin antibody and Hoechst 33342. The spindle axis was defined by drawing a 30-pixel wide line across both spindle poles and repositioned along the Z-axis using the “Reslice” function. For this, the whole stack of Z-sections was used that had 0.2  $\mu\text{m}$  increments. The spindle angle ( $\alpha_z$ ) was measured with the “Angle Tool” at the intersection between the spindle axis and a line drawn parallel to the substratum (Figure 2.6).

### 2.6.6 Spindle oscillation measurements

Spindle oscillations in the z- and xy-view were measured from cells imaged during time-lapse microscopy. The cells labelled with SiR-Tubulin were measured at every time point starting from metaphase onset until the end of metaphase, until cells died or until the end of the video if the cells did not progress through mitosis.

#### 2.6.6.1 Spindle oscillation in the z-view

To measure spindle oscillations in the z-axis, substacks of every frame to be analysed were generated with the “Subhyperstack Maker” function. Spindle angles were determined similarly to fixed cells described in section 2.6.5 (Figure 2.6). Spindle angles were displayed as positive values unless spindle poles changed direction. In this case, angles were calculated as negative angle values.

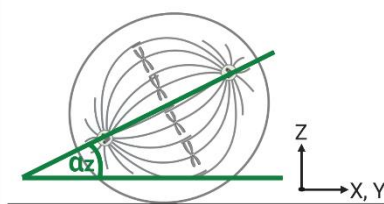


**Figure 2.6 Schematic of spindle oscillation measurements in z-view**

*Illustration of spindle angle measurements of fixed and live cells in the z view.  $\alpha_z$  represents the spindle angle calculated between the spindle axis and substratum (green line). Spindle angles of fixed cells were measured at metaphase stage. Spindle angles obtained from live cell imaging were measured at every time point starting from the first frame of metaphase onset until the last frame of metaphase, until cells died or until the end of the video if the cells did not progress through metaphase.*

### 2.6.6.2 Spindle oscillation in the xy-view

Spindle oscillations in the xy-plane from cells imaged during time-lapse microscopy were measured by drawing a 1 pixel-wide line crossing both spindle poles to define the spindle axis at metaphase entry. Using the “Draw tool”, this line was permanently embedded in every z-section and every frame. The first time point was considered as the initial spindle oscillation angle with a value of  $0^\circ$ . In the next frame, a new line was drawn (1 pixel wide) crossing both spindle poles and added to the specific frame using the “Overlay tool” to define the new spindle axis. The oscillation angle was measured with the “Angle Tool” by drawing an angle intersecting the initial spindle axis and current spindle axis as shown in Figure 2.7. In the following frames, the spindle oscillation was measured likewise as the angle between the newly drawn line across the spindle axis and the original spindle axis. Clockwise spindle oscillations were considered as positive angle values and spindle movements in the other direction as negative values.

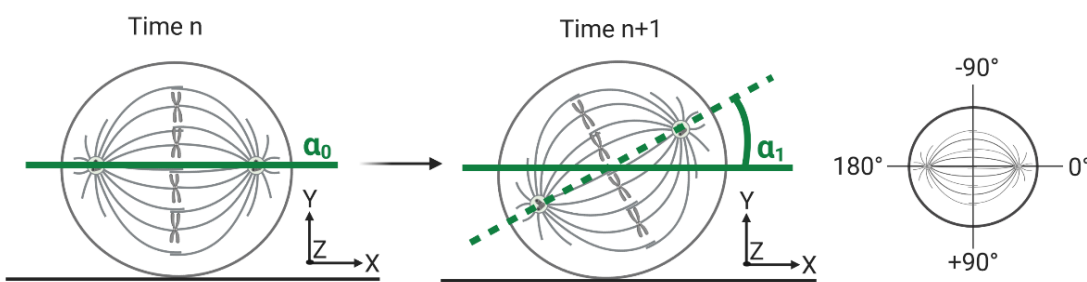


**Figure 2.7 Schematic of spindle oscillation measurements in xy-view**

*Illustration of spindle oscillation measurements in the xy- view of live cells. Left,  $\alpha_0$  represents the initial orientation of the mitotic spindle (green line) at the first frame of metaphase (Time n) with an angle value of  $0^\circ$ . Middle, in the next frame (Time n+1),  $\alpha_1$  represents the angle measured between the original spindle axis and the new axis (dashed green line). Right, spindle oscillation movements clockwise were measured as positive angle values. Movements in the other direction were calculated as negative angle values. Created with BioRender.com*

### 2.6.6.3 Quantification of spindle oscillations

In order to quantify measured spindle oscillations, changes over time in the angle of the metaphase spindles were analysed. For this, the relative and absolute rotations in the z- and xy-view were calculated as described (Saadaoui *et al.*, 2014). The following formulas represent the applied calculations for rotations in the z view but were also used for xy-rotations:

$$(I) \quad \text{Absolute z rotation per minute, } \Delta z(ij) = \frac{\sum_{t=i}^{j-1} |\alpha_{z(t+1)} - \alpha_{z(t)}|}{\Delta t_{ij}}$$

$$(II) \quad \text{Relative z rotation per minute, } \delta z(ij) = \frac{\sum_{t=i}^{j-1} (\alpha_{z(t+1)} - \alpha_{z(t)})}{\Delta t_{ij}}$$

Relative and absolute spindle oscillation deviations between frames called frame transitions were calculated manually by subtracting measured values of one frame from the previous frame. For both equations, the starting time point ( $t=i$ ) was the first frame of metaphase onset and the last time point ( $t=j$ ) was the last frame before anaphase onset. Thus,  $\Delta t_{ij}$  represents the duration of metaphase.

### 2.6.6.4 Quantification of the oscillation index

The oscillation index represents a measure of the degree of spindle movements during metaphase. Spindle angle deviations  $> 10^\circ$  between two frames were counted as oscillation events which was quantified for measured spindle angles in the z- and xy-view. The oscillation index was calculated as the percentage of oscillation events with respect to the total number of frames.

### 2.6.7 Metaphase plate tracking

Metaphase plates of cells imaged with time-lapse microscopy were tracked in the xy-view using Imaris software (Bitplane). First, a maximum intensity z projection was created and videos were cropped to the time frames corresponding to metaphase starting from the first frame of metaphase until the last frame of metaphase, until cells died or until the end of the video if the cells did not progress through metaphase. DNA metaphase plates were segmented using the Surface module

and the centre of the DNA was marked with a point. The movement of this centre point was then tracked automatically over time (Figure 2.8). Movement tracks were reported as x/y coordinates of the individual positions starting from position 0/0.

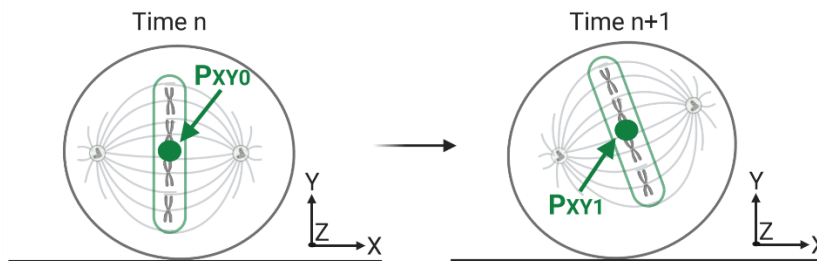


**Figure 2.8 Schematic of metaphase plate tracking**

The metaphase plates of MCF-10A cells imaged during time-lapse microscopy were tracked using Imaris software. Using the surface module, the DNA plates were segmented and the centre point was labelled at the initial position ( $P_{xy0}$ ) at metaphase entry. The position of the centre point was reported for every time frame until the end of metaphase, until cells died or the video ended.

Movement of the metaphase plate was quantified as the displacement length. For this, cells entering anaphase and completing mitosis were analysed only. Displacement length was the length of DNA displacement from the starting point to the last frame of metaphase. For this, the direct distance between the two positions were measured as illustrated in Figure 2.9. The velocity was determined as the mean speed of metaphase plate movement. This was calculated by the total track length divided by tracking time (metaphase plate congression time).

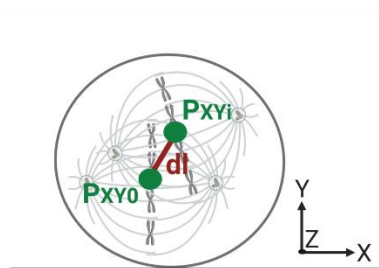


**Figure 2.9 Schematic of determining the displacement length of the DNA plate during metaphase**

Displacement lengths were identified as the distance between the initial position of the centre point (green) at metaphase entry ( $P_{xy0}$ ) and the last position before anaphase ( $P_{xyi}$ ).

### 2.6.8 Quantification of cortical fluorescence intensity

Fluorescence intensities profiles were measured for fixed MCF-10A cells in prometaphase or metaphase. Custom macros were used in Fiji. To compare signals from different proteins analysed in the same cells, intensity values were corrected by subtracting background fluorescence intensities. Average profiles were calculated from individual profiles. The script to measure cortical fluorescence intensity in prometaphase cells was kindly written by Dr Xavier Morin and can be found in Appendix C (Ecole Normale Supérieure, CNRS, Inserm, Institut de Biologie de l'Ecole Normale Supérieure (IBENS), PSL Research University, Paris, France).

#### 2.6.8.1 Cortical fluorescence intensities of metaphase cells

Fluorescence intensity profiles at the cell cortex of metaphase cells stained with anti-LGN, anti-ANXA1 or anti-Gai1 antibodies were measured as described previously (di Pietro *et al.*, 2017). First, one z-section was defined that showed the optimal fluorescence intensity of the proteins of interest. Then the macro was run and a circle was mapped around the cell cortex in the specific z-stack using the "Oval Tool". The macro defined the circle's radius and centre. Next the position of the metaphase plate was mapped by drawing a line along the DNA plate using the "Line Tool". The macro extended this line towards the cell cortex to define the starting position for the measurement. After defining these parameters, the fluorescence intensity was measured at the circle's radius distance along a 5-pixel long line overlapping the cell cortex. The length of the line compensated for irregularities in the circularity of the measured cell. This was repeated by scanning the whole cortex for 280 successive positions (2° intervals) starting (and finishing) from the point facing the metaphase plate. Thus, position 0 and 180 face the chromosome plate (central cortex) and position 90 and 270 face spindle poles (lateral cortex) as illustrated in Figure 2.10. The maximum intensity pixel values were retained for every position and exported to Microsoft Excel for further analysis.

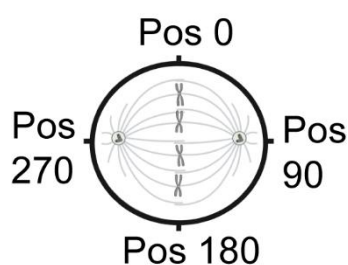


**Figure 2.10** Schematic of positions along the cortex

**Figure 2.11 Continued**

*Cortical fluorescence intensities of proteins at the cell cortex were measured clockwise in 1° intervals for 360 successive positions starting from position 0. The starting position was defined by a line along the metaphase plate in the centre of the cell.*

**2.6.8.2 Cortical fluorescence intensities of prometaphase cells**

Profiles of ANXA1 and LGN at the cell cortex of prometaphase cells were measured similarly to metaphase cells. One z-section was defined that showed the optimal fluorescence intensity of the proteins of interest. To account for more elongated cell shapes, a line was drawn along the cell contour using the “Freehand Tool”. The macro fit an ellipse to this contour and determined the ellipse’s radius. By adapting the line position to the radius of the ellipse, the macro measured the fluorescent intensities values along a 30 pixel-long radial line overlapping the cortex. The whole cell contour was scanned at 280 successive positions (every 2°) starting (and finishing) at the ellipse’s short axis assuming the metaphase plate will align with the long axis of the ellipse. Thus, positions measured along the cortex are equivalent to positions in metaphase cells. The maximum intensity pixel values were retained for every position and exported to Microsoft Excel for further analysis.

**2.6.9 Astral microtubule measurements**

For analysis of astral MTs, cells were fixed with glutaraldehyde as described in section 2.6.1, III and stained  $\alpha$ -tubulin antibody.

**2.6.9.1 Quantification of astral microtubule intensity**

Z-stacks were summed up and images were duplicated. For one image, cells surrounding the cell-of-interest were cropped out so that only the cell contour with the mitotic spindle of the cell-of-interest remained. Using the “Subtract background” function, the background of this cell was corrected for uneven illuminated background with the rolling ball algorithm (Sternberg, 1983) set to 50 pixels. For the same image, objects of interest (MTs) were separated from background by adjusting the threshold using the default setting and manual fine-tuning to define correct objects. These objects were segmented by creating a selection which generated a region of interest (ROI) mapping the structure of the mitotic spindle. Next, the image was cropped further to remove all structures not corresponding to the mitotic spindle between spindle poles and another ROI was

generated. Then, the ROIs were placed over the unmodified copy of the image and the intensities of the total spindle ( $I_{total}$ ) and the spindle between poles ( $I_{spindle}$ ) were measured (Figure 2.11, A). Background fluorescence was taken into account by measuring the intensity of a small area within the cytoplasm of the cell not overlapping  $\alpha$ -tubulin signals. Pixel intensity values were exported to Microsoft Excel. The relative fluorescence intensity of astral MTs was calculated with the formula shown in Figure 2.11, B) from background- corrected intensities.

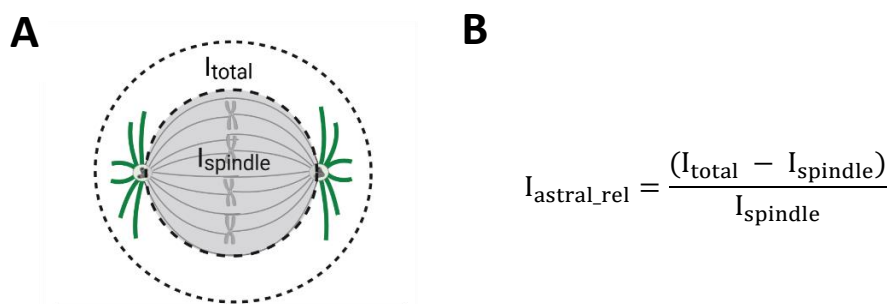


**Figure 2.11 Schematic of the quantification of astral microtubule intensity**

*A. Fluorescence intensity of the entire mitotic spindle ( $I_{total}$ ) as well as the fluorescence intensity of the inner mitotic spindle ( $I_{spindle}$ ) were measured. B. The relative astral microtubule intensity was calculated by subtracting the total spindle intensity by the spindle intensity divided by spindle intensity.*

#### 2.6.9.2 Quantification of astral microtubule length and pole to cortex distance

Astral MT length was quantified by drawing a line along the longest MT extending towards the cell cortex on each side of the spindle poles (Figure 2.12, A). The lengths of these lines were retained and exported to Microsoft Excel. The ratio of the astral MT length was calculated by dividing the longer length by the shorter length.

The pole-to-cortex distance was measured by drawing a line on each side of the spindle pole towards the closest cell cortex in line with the spindle axis (Figure 2.12, B). Length of those lines were measured and exported to Microsoft Excel. The ratio of the pole-to-cortex distance was calculated by dividing the longer distance by the shorter distance.

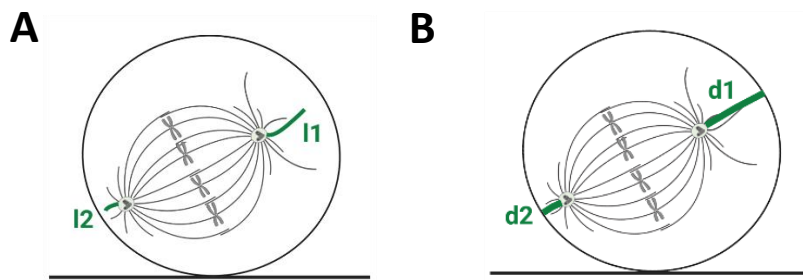


**Figure 2.12 Schematic of quantification astral microtubule length and pole-to-cortex distance**

*A. The length of astral microtubules of metaphase cells was measured by drawing a line along the longest microtubules extending towards the cell cortex on each side of the spindle poles (green lines). B. The pole-to-cortex distance was determined by drawing a line from the spindle poles towards the cell cortex in line with the spindle axis (green lines).*

#### 2.6.10 Co-localisation analyses using line-scans

TO measure the relative fluorescent intensity at the cell cortex a 30 pixel-wide line was drawn across the middle of the cell covering both cell borders using the “Line Tool”. The “Plot Profile” function revealed the fluorescent intensity profile along the drawn line in a two-dimensional graph. X and y values representing the distance along the drawn line and pixel intensities, were exported to Microsoft Excel for further analysis.

#### 2.6.11 Quantification of mitotic index

The mitotic index represents a measure of the proportion of mitotic cells within a cell population. In this work, the mitotic index was calculated for the number of metaphase cells in a population of cells synchronized at G<sub>2</sub>/M or metaphase. For every condition, cells were plated on coverslips and arrested in the specific cell cycle stage as described in section 2.2.3 and fixed with 4 % PFA (see section 2.6.1, i). Nuclei were stained with Hoechst 33342. For 3 independent experiments 10 images at different positions in the coverslips were taken using confocal microscopy with 20x magnification. The number of metaphase plates and interphase nuclei were counted manually using the “Multi-Point Tool”. The mitotic index was calculated as the percentage of the number of metaphase cells in respect to the total number of cells per image.

## 2.7 Bioinformatics analyses of mass spectrometry data

This chapter describes the analyses of MS data obtained as detailed in section 2.5.2. The raw data was first filtered manually to subtract proteins from the control condition that were considered as background noise. All further methods described in this chapter were performed by Dr Farahnaz Sadat Golestan Hashemi (Salah Elias lab, University of Southampton).

### 2.7.1 Construction of protein- protein interaction networks

Proteins were filtered against the Contaminant Repository of Affinity Purification (CRAPomeCRAPome) database. This online resource functions as a quality control to remove protein contaminants supplying noise signals to MS studies (Mellacheruvu *et al.*, 2013). Proteins with a score of 180 were considered as noise and were removed. The remaining proteins with an identified UniProtKB ID were mapped to Ensembl IDs. From these Ensembl IDs, the human protein-protein-interaction (PPI) network was constructed using the Search Tool for the Retrieval of Interacting Genes/Proteins (STRING) PPI database (v. 11) (Szklarczyk *et al.*, 2018). Based on high-throughput experiments, databases and co-expression sources, protein interactions were derived with an interaction confidence score of  $\geq 0.6$ . The resulting PPI network was downloaded from the STRING database and imported into the Cytoscape software platform (Version 3.7.2) for further visualization and analyses (Shannon *et al.*, 2003). Singleton nodes which represent proteins with no interactions were omitted from the initial network. In the next step, sub-networking was performed. For this, a new network was created by selecting the bait protein LGN and its immediate associated neighbour proteins.

### 2.7.2 Gene Ontology and pathway enrichment analyses

Functional characterisation of the constructed PPI networks was performed by gene overrepresentation- or enrichment analyses to identify Gene Ontology (GO) biological processes as well as curated pathways associated with the PPI network. For this, the ClueGO plugin in Cytoscape was used. This plugin extracts representative functional biological information for large lists of genes or proteins based on the latest publicly available data from multiple annotation and ontology resources that are automatically accessed from ClueGO (Bindea *et al.*, 2009; Mlecnik, Galon and Bindea, 2018). Curated pathways were referenced from the databases GO Biological Process, Kyoto Encyclopedia of Genes and Genomes (KEGG) pathways, and Reactome Pathways. For GO data,

testing was restricted to pathways with experimental evidence (EXP, IDA, IPI, IMP, IGI, IEP) and Traceable Author Statement (TAS).

## 2.8 Statistical analysis

Statistical significance of the overrepresentation of enriched genes in pathways and biological processes were analysed with the GlueGo plugin using the hypergeometric test (Fisher's Exact Test). For multiple testing, functional groups with the Bonferroni step-down correction method was used. The related terms which share similar associated genes were fused to reduce redundancy. All other statistical analyses and generation of graphs was performed using GraphPad Prism software (Version 8.4.3). Graphs were compiled with Adobe Illustrator CS6. Comparison of conditions (e.g. control vs. treatment) was performed with unpaired Student's t-tests. For all analysis, a P value  $\leq 0.05$  was considered statistically significant. P value significance was reported as follows:  $p \leq 0.0001$ , \*\*\*\*;  $p \leq 0.001$ , \*\*\*;  $p \leq 0.01$ , \*\*;  $p \leq 0.05$ , \*;  $p > 0.05$ , n.s., not significant. Individual tests used, as well as the number and type of replicates for each experiment were specified in the relevant figure legends. In all figures, error bars correspond to SEM unless otherwise stated.

**Chapter 3    Generation of a stable cell line expressing  
GFP-LGN to uncover mechanisms of oriented cell  
divisions in mammary epithelial cells**



### 3.1 Introduction

Force generation during mitotic spindle orientation is assigned to dynein and NuMA, while the recruitment to the cell cortex is attributed to LGN which in turn is localised by Gai subunits (described in chapter 1.3.1.2). Therefore, LGN constitutes the crucial adapter between the cell cortex and pulling forces and has been part of extensive research to evaluate its dynamics (Du *et al.*, 2002; Morin and Bellaiche, 2011; di Pietro, Echard and Morin, 2016; Kiyomitsu, 2019).

It is now determined that LGN has a cell cycle-dependent subcellular localisation with a diffuse distribution in the cytoplasm and in some cell types non-specifically in the nucleus during interphase but at the cell cortex during mitosis. Concomitant with the change of distribution within the cell, LGN protein levels vary throughout the cell cycle with a peak during mitosis (Blumer, Chandler and Lanier, 2002; Kaushik *et al.*, 2003; Du and Macara, 2004; Fukukawa *et al.*, 2010). The protein starts to accumulate all around the cortex during prometaphase and its localisation is soon after restricted to two crescents at the cell cortex above the spindle poles where it remains until telophase (Kiyomitsu and Cheeseman, 2012). This localisation is specifically polarised in epithelia where LGN accumulates symmetrically above both spindle poles on lateral sides which results in positioning of the spindle parallel to the basement membrane and favours planar cell divisions (Morin, Jaouen and Durbec, 2007; Zheng *et al.*, 2010; Peyre *et al.*, 2011). Additionally, LGN positions in a crescent above one spindle pole on the apical domain leading to position of the spindle orthogonal to the basement membrane and perpendicular divisions (Lechler and Fuchs, 2005; Williams *et al.*, 2011). Metaphase localisation of LGN has also been determined in the mammary epithelium (Elias *et al.*, 2014; Ballard *et al.*, 2015). Thus, the cortical accumulation of LGN has been established and due to LGN constituting the crucial adapter in the spindle orientation machinery, it displays an ideal candidate to study novel spindle orientation mechanisms in the mammary epithelium. Therefore, the aim of this chapter was to generate a mammary epithelial cell line expressing a GFP-LGN fusion protein. The ambition was to trace the dynamics of the protein during the cell cycle and to utilize the GFP-tag for affinity purification allowing to investigate LGN interactors (Chapter 4). Another aim was to generate a second cell line, expressing GFP alone to serve as a control condition in experiments. In order to use these cell lines for further investigations, the expression pattern of GFP-LGN and GFP as well as mitotic behaviour and spindle dynamics of MCF-10A cells expressing the proteins were analysed. Co-localisation with known interaction partners were examined to exclude any interference of GFP with normal LGN function. Overall, this chapter describes the characterisation of novel mammary epithelial cell lines to study the LGN environment and behaviour during mitosis.

## 3.2 Results

Genetic material was permanently integrated into the genome of MCF-10A cells by retroviral transduction to stably express GFP-LGN or GFP. Genetically modified cells were characterised to study protein expression, subcellular localisation and mitotic behaviour.

### 3.2.1 Expression and dynamics of GFP-LGN does not alter cell dynamics

To evaluate the localisation and expression pattern of GFP-LGN and GFP, immunofluorescence and confocal imaging as well as Western blotting was performed. The subcellular localisation of GFP-LGN, GFP and endogenous LGN was compared during interphase and metaphase. Endogenous LGN had a diffuse localisation in the cytoplasm during interphase. Mitotic cells in metaphase showed an accumulation of LGN at the lateral cell cortex in a crescent shape. Noteworthy, GFP-LGN extended beyond the lateral crescent in some cells showing a more dynamic localisation at the cell cortex. Immunofluorescence staining for GFP revealed a similar subcellular localisation of GFP-LGN. During interphase the protein was diffuse throughout the cytoplasm but accumulated at the lateral cortex during metaphase. In contrast, GFP remained in the cytoplasm throughout the analysed cell cycle stages (Figure 3.1, A). To evaluate protein levels of LGN, GFP-LGN and GFP, cells were synchronized at G<sub>2</sub>/M and metaphase. The expression of phospho-Histone 3 validated that cells were in mitosis. GFP-LGN and GFP showed a stable expression. Endogenous LGN levels increased slightly during metaphase compared to late interphase (G<sub>2</sub>/M) (Figure 3.1, B).

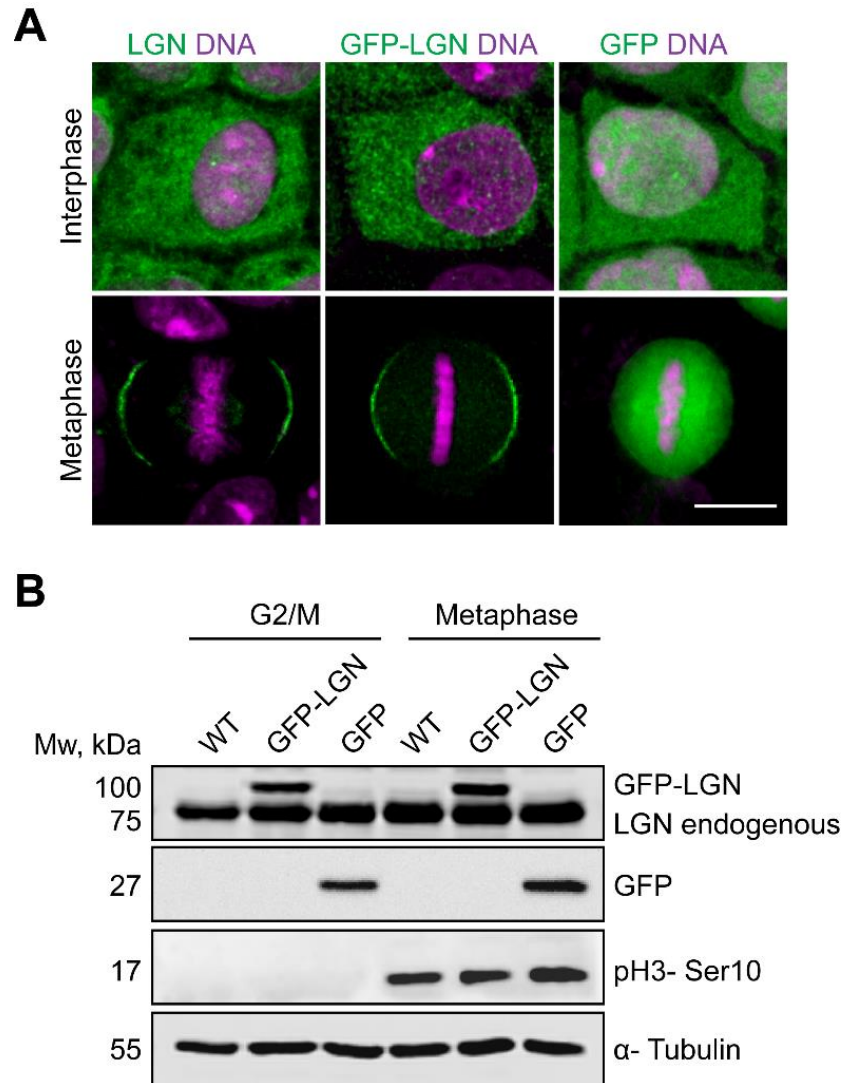


**Figure 3.1 Localisation and expression levels of LGN, GFP-LGN and GFP in interphase and metaphase**

(A) Representative confocal images of the subcellular localisation of LGN, GFP-LGN or GFP in MCF-10A cells during interphase and metaphase. Cells were fixed with methanol and stained for LGN or GFP (green). DNA (blue) was visualised with Hoechst 33342. Scale bar, 10  $\mu$ m. (B) Immunoblot of LGN, GFP-LGN, GFP and phospho-Histone H3 (pH3- Ser10) levels in WT MCF-10A and MCF-10A expressing GFP-LGN or GFP arrested at G<sub>2</sub>/M or metaphase. GFP was detected with anti-GFP antibody. Endogenous LGN and GFP-LGN was detected with anti-LGN antibody.  $\alpha$ -Tubulin was used as a loading control.

The specific behaviour of GFP-LGN or GFP and the dynamics of MCF-10A cells were analysed during mitosis using time-lapse microscopy. When cells expressing GFP-LGN entered mitosis, GFP-LGN started to accumulate at the cell cortex during prometaphase after NEBD and when condensed chromosomes started to align at the metaphase plate. GFP-LGN remained localised at the cortex until late telophase when it started to relocate to a diffuse distribution in the cytoplasm upon the start of a new cell cycle (Figure 3.2, A). Cells expressing GFP showed a uniform distribution of the protein in the cytoplasm. The localisation did not change during mitotic progression (Figure 3.2, B). The expression of GFP-LGN or GFP had no effect on the dynamics of mitosis when compared to WT cells (Figure 3.2, C). Cells entered the different phases of cell division in a timely similar manner. WT cells spend 55 min in mitosis, therefrom 13 min to form a metaphase plate and 35 min to enter anaphase. In comparison, GFP-LGN cells spend on average 54 min in mitosis, therefrom 13 min to align chromosomes and 36 min from NEBD to chromosome segregation at anaphase (Figure 3.2, D-F). GFP expressing cells spend 52 min in mitosis. Cells progressed to anaphase 35 min after NEBD and chromosomes aligned within 12 min.

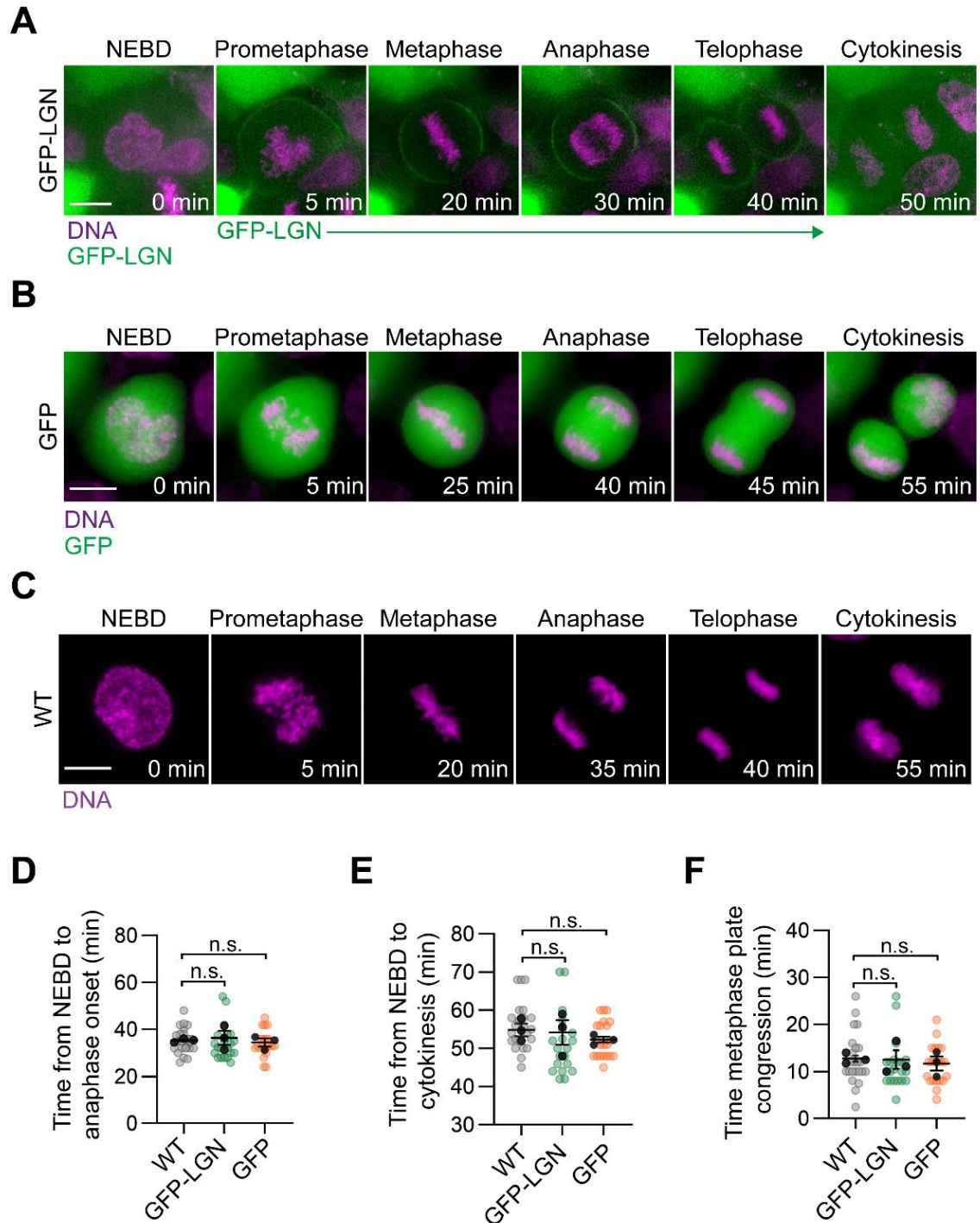


**Figure 3.2 Expression of GFP-LGN or GFP does not influence mitotic dynamics of MCF-10A cells**  
 (A-C) Representative images from time-lapse microscopy of cells expressing GFP-LGN (green, A), GFP (green, B) or WT MCF-10A (C). DNA (magenta) was stained with Hoechst 33342 30 min before recording. Images were acquired every 2.5 min. Scale bar, 10  $\mu$ m. (D) Time from nuclear envelope breakdown (NEBD) to anaphase. (E) Time from NEBD to cytokinesis. (F) Duration of metaphase plate congression. Data represent individual cells with means (black dots)  $\pm$  SEM from three independent experiments. WT  $n = 23$ ; GFP-LGN  $n = 21$ ; GFP  $n = 23$ . Student's  $t$ -test; n.s. no significant difference.

To exclude any changes on mitotic spindle dynamics the length of the spindle as well as the spindle angle were determined. Compared to WT cells, the expression of GFP-LGN or GFP alone had no effect on the size of the mitotic spindle which was measured as the distance between spindle poles (Figure 3.3 A middle, B). Spindles of WT cells were on average 11.7  $\mu\text{m}$  long. Cells expressing GFP-LGN or GFP exhibited spindles lengths of 12.2  $\mu\text{m}$  and 11.8  $\mu\text{m}$  respectively. Furthermore, all cell lines, independent of the expression of a recombinant protein, displayed on average small spindle angles of 4.0° (WT), 3.5° (GFP-LGN) or 4.1° (GFP) (Figure 3.3 A right, C).

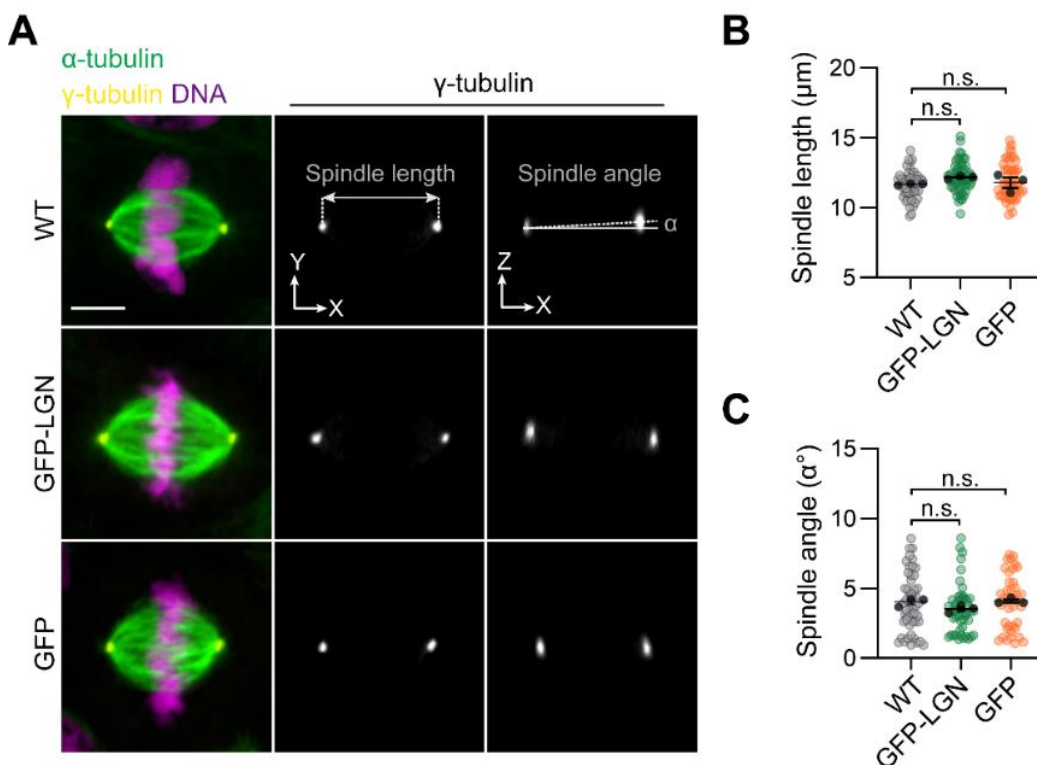


**Figure 3.3 Mitotic spindle characteristics are not affected by the expression of GFP-LGN or GFP in MCF-10A cells**

(A) Representative confocal images of metaphase mitotic spindles in WT MCF-10A cells and MCF-10A expressing GFP-LGN or GFP. Cells were fixed with methanol and stained for  $\alpha$ -tubulin (green) and  $\gamma$ -tubulin (yellow). DNA (blue) was visualised with Hoechst 33342. Xy-views of the shown cells ( $\gamma$ -tubulin signal) were used to determine spindle length as illustrated. Orthogonal views (xz) of the depicted cells ( $\gamma$ -tubulin signal) were used to measure spindle angle  $\alpha$  as illustrated. Scale bar, 10  $\mu\text{m}$ . (B) Spindle length of metaphase spindles in WT MCF-10A cells, MCF-10A expressing GFP-LGN or GFP. (C) Spindle angles of metaphase spindles in WT MCF-10A cells, MCF-10A expressing GFP-LGN or GFP. Data represent individual cells with means (black dots)  $\pm$  SEM from three independent experiments. WT  $n = 51$  cells; GFP-LGN  $n = 56$  cells; GFP  $n = 53$  cell. Student's  $t$ -test; n.s. no significant difference.

### 3.2.2 GFP-LGN co-localises with the spindle orientation machinery

Immunofluorescence staining and confocal imaging as well as line-scan analysis was performed to study the metaphase subcellular localisation of GFP-LGN or GFP with members of the spindle orientation machinery compared to the localisation of the investigated proteins in WT cells. As shown previously, LGN accumulated at the lateral cortex in WT cells. A corresponding line-scan analysis of relative fluorescence intensity showed intensity peaks at the cortex and almost no signal in the cytoplasm. Co-staining of GFP-LGN and LGN showed a co-localisation in a crescent shape at the lateral cortex. Line-scans illustrated a similar intensity profile as compared to WT cells and a spatial overlap of GFP and LGN with peaks at the cell cortex. Co-staining of GFP with LGN identified a cytoplasmic localisation of GFP and a lateral localisation of endogenous LGN. Corresponding line-scans showed high signals throughout the cytoplasm for GFP and a similar intensity profile for LGN as seen in WT cells with peaks at the cell cortex. There was no overlap of signals between GFP and LGN (Figure 3.4).

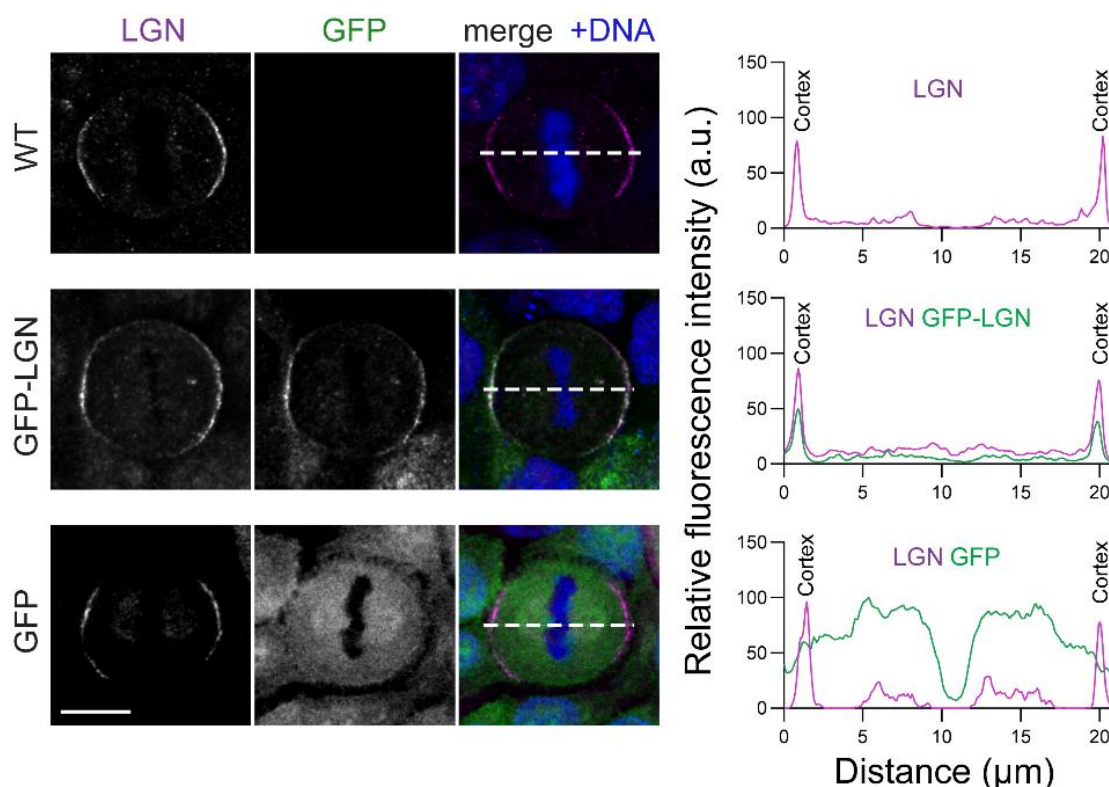


**Figure 3.4 Co-localisation of GFP-LGN or GFP with LGN during metaphase**

*Left: Representative confocal images of LGN cortical localisation in WT MCF-10A cells and localisation of LGN with GFP-LGN or GFP during metaphase. Cells were fixed with methanol and stained for LGN (magenta) and GFP (green, not WT cells). DNA (blue) was visualised with Hoechst 33342. White dotted lines indicate measured fluorescence intensity profiles. Scale bar, 10  $\mu\text{m}$ .*

**Figure 3.4 Continued**

Right: Line-scan profiles of fluorescence intensity corresponding to images on the left showing distribution of indicated proteins.

In WT cells, NuMA accumulated in a crescent shape at the lateral cortex and strongly at the spindle poles which was represented in the line-scans with peaks at the cell cortex and poles. Co-staining of GFP-LGN and NuMA identified a lateral co-localisation and the corresponding line-scans confirmed a spatial overlap at the cell cortex. Co-staining of GFP and NuMA showed a cytoplasmic localisation of GFP and accumulation of NuMA at the lateral cortex and spindle poles. Line-scans illustrated no overlap of fluorescence intensities but the typical intensity profile observed for NuMA in WT cells and an even distribution of GFP in the cytoplasm (Figure 3.5).

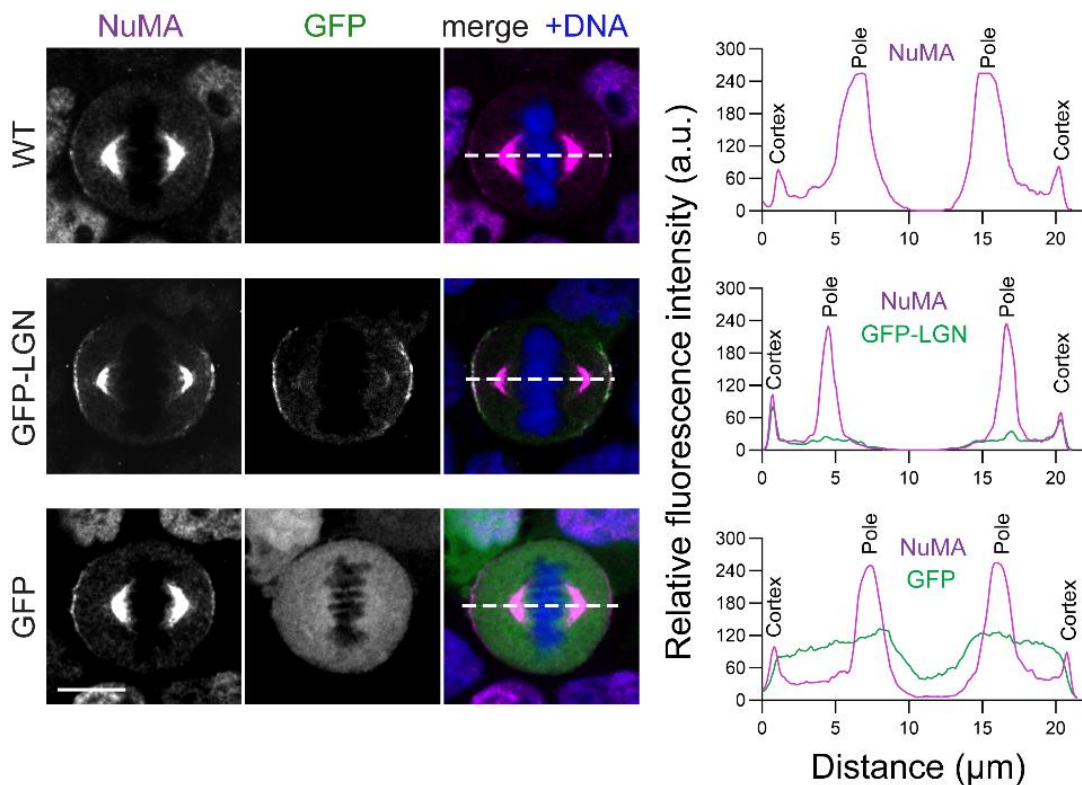


**Figure 3.5** Co-localisation of GFP-LGN or GFP with NuMA during metaphase

**Figure 3.5 Continued**

*Left: Representative confocal images of NuMA cortical localisation in WT MCF-10A cells and localisation of NuMA with GFP-LGN or GFP during metaphase. Cells were fixed with methanol and stained for NuMA (magenta) and GFP (green, not WT cells). DNA (blue) was visualised with Hoechst 33342. White dotted lines indicate measured fluorescence intensity profiles. Scale bar, 10  $\mu$ m. Right: Line-scan profiles of fluorescence intensity corresponding to images on the left showing distribution of indicated proteins.*

In WT cells, P150<sup>Glued</sup> had a typical accumulation at the lateral cortex and a strong signal at the spindle. Line-scans confirmed this localisation by showing peaks at the cortex and high intensity values and peaks around the poles. Staining of GFP-LGN and P150<sup>Glued</sup> illustrated a co-localisation at the cortex which was also seen in the corresponding line-scans with a signal overlap at the cortex. Compared to WT cells, the antibody combination generated relatively high signals in the cytoplasm and a strong spindle pole signal in the GFP channel. Similarly, a strong cytoplasmic fluorescence signal was observed when analyzing GFP and P150<sup>Glued</sup>. Here, the signal was even stronger and overlapped with cytoplasmic GFP. Nevertheless, line-scans showed no spatial overlap at the cell cortex but peaks of P150<sup>Glued</sup> at the cortex and around spindle poles and an even distribution of GFP in the cytoplasm (Figure 3.6).

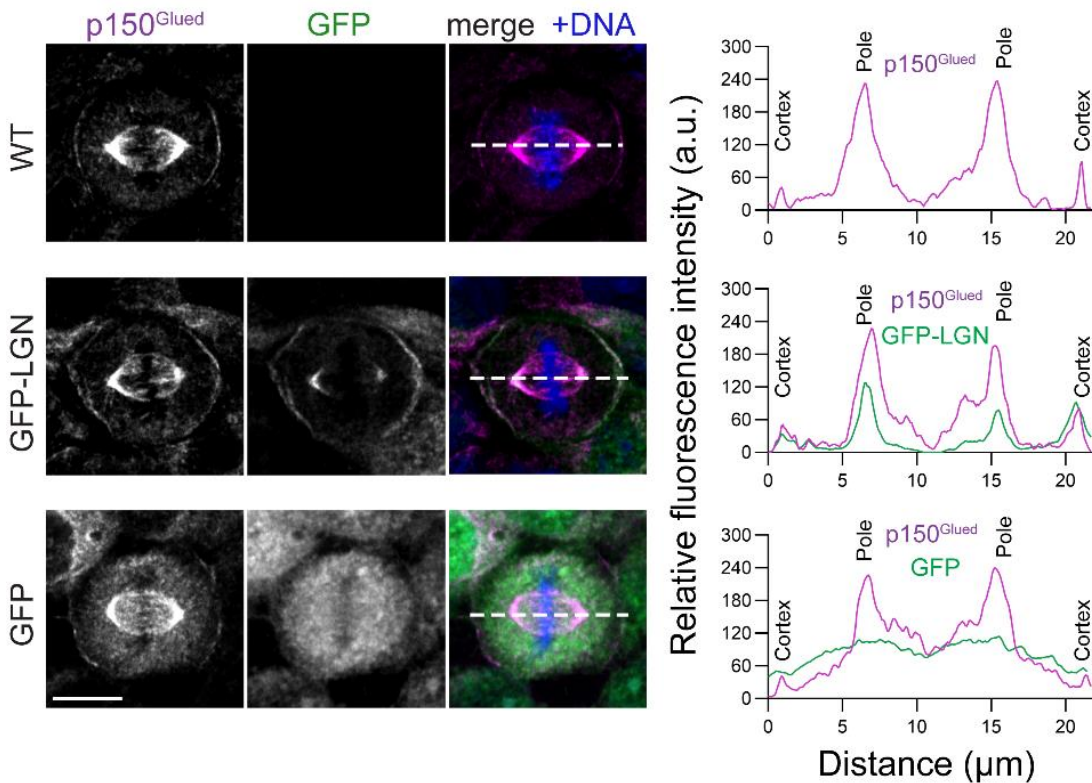


**Figure 3.6 Co-localisation of GFP-LGN or GFP with p150<sup>Glued</sup> during metaphase**

*Left: Representative confocal images of p150<sup>Glued</sup> cortical localisation in WT MCF-10A cells and localisation of p150<sup>Glued</sup> with GFP-LGN or GFP during metaphase. Cells were fixed with methanol and stained for p150<sup>Glued</sup> (magenta) and GFP (green, not WT cells). DNA (blue) was visualised with Hoechst 33342. White dotted lines indicate measured fluorescence intensity profiles. Scale bar, 10  $\mu\text{m}$ . Right: Line-scan profiles of fluorescence intensity corresponding to images on the left showing distribution of indicated proteins.*

Lastly, analysis of the subcellular localisation of G $\alpha$ i1 showed a distribution of the protein around the cell cortex with a stronger accumulation at lateral sides in WT cells. Line-scans represented a strong signal at the cortex and low levels in the cytoplasm. Co staining with GFP-LGN revealed a co-localisation at the lateral cortex as seen from similar intensity profiles with peaks at the cortex. GFP and G $\alpha$ i1 did not show a spatial overlap. GFP was distributed in the cytoplasm and G $\alpha$ i1 accumulated at the lateral cortex as seen in the other cell lines. Line-scans confirmed this localisation with no signals overlapping (Figure 3.7).

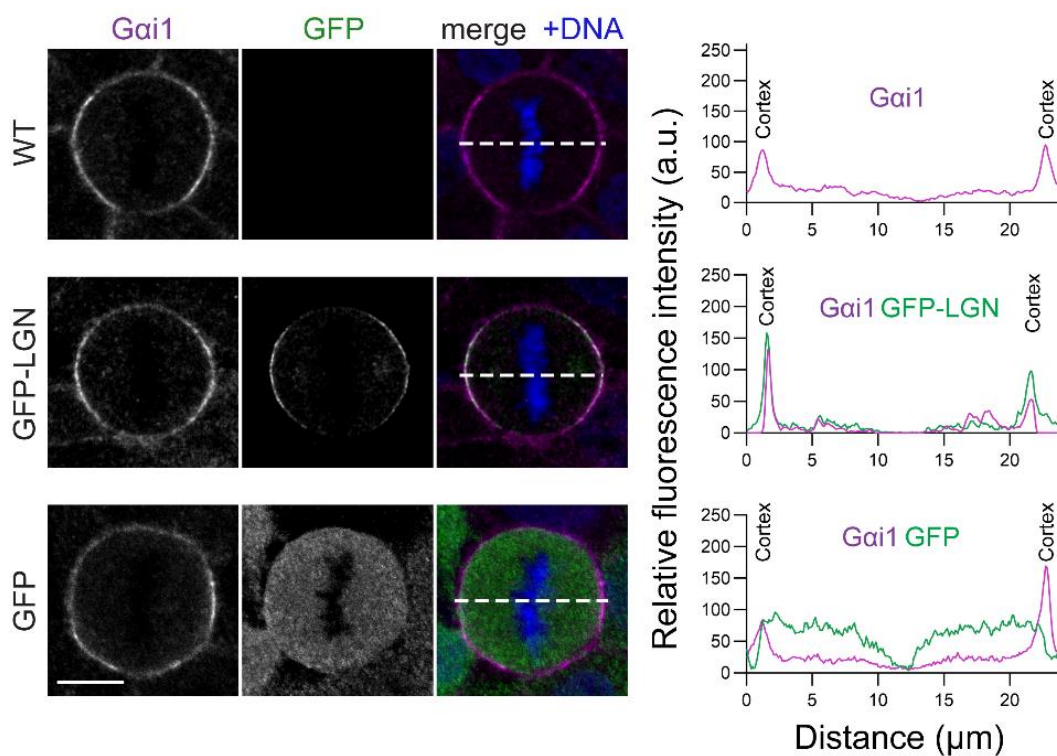


**Figure 3.7 Co-localisation of GFP-LGN or GFP with Gai1 during metaphase**

*Left: Representative confocal images of Gai1 cortical localisation in WT MCF-10A cells and localisation of Gai1 with GFP-LGN or GFP during metaphase. Cells were fixed with methanol and stained for Gai1 (magenta) and GFP (green, not WT cells). DNA (blue) was visualised with Hoechst 33342. White dotted lines indicate measured fluorescence intensity profiles. Scale bar, 10  $\mu\text{m}$ . Right: Line-scan profiles of fluorescence intensity corresponding to images on the left showing distribution of indicated proteins.*

Taken together, these results showed that expression of GFP-LGN or GFP did not influence the mitotic behaviour of MCF-10A cells and cells progressed through mitosis in a timely similar manner. GFP-LGN showed a cortical accumulation similar to endogenous LGN whereas GFP alone remained in the cytoplasm throughout the cell cycle. Furthermore, the dynamics of GFP-LGN mirrored the localisation of endogenous LGN by co-localizing with other members of the spindle orientation machinery. In contrast, GFP distributed equally in the cytoplasm during metaphase and showed no spatial overlap with any members of the spindle orientation machinery.

### 3.3 Discussion

To date the only mitotic function of LGN was described as an adapter protein between cortical Gai subunits and NuMA which results in anchoring the spindle orientation complex to the cortex. Gai subunits cover the inner cell surface completely and do not contribute to the polarised localisation of the LGN complex during mitosis (di Pietro, Echard and Morin, 2016). NuMA has diverse functions during mitosis including spindle pole assembly, MT binding and recruitment of dynein/dynactin to the cell cortex (Sun and Schatten, 2006). Because of the specific function of LGN it provided an ideal target to study the dynamics of the spindle orientation machinery and was therefore chosen in this work to generate a mammary cell line expressing GFP-LGN. When generating novel cell lines, it is important to characterise the behaviour of cells to exclude any cellular changes that might influence the outcome of downstream applications. To serve as a valuable tool, the behaviour of cells expressing GFP-LGN and the control GFP were evaluated.

#### 3.3.1 Expression of GFP-LGN does not alter mitotic dynamics in mammary epithelial cells

GFP is a stable fluorescent protein that originated in jellyfish. Although GFP is foreign to other systems, it can be expressed in virtually all systems and it is not toxic to cells (Zimmer, 2002). Here, the expression of GFP alone in MCF-10A cells showed a strong fluorescent signal in the cytoplasm which did not change during the cell cycle. This is because GFP's only function is to emit green fluorescence. Therefore, the protein remains localised in the cytoplasm without any changes or effect on cells. Another advantage of GFP is that it does not alter the function or localisation when part of a fusion protein (Zimmer, 2002). This was proven here by comparing the localisation of endogenous LGN with GFP-LGN. Both proteins showed a relocalisation during the cell cycle from cytoplasmic during interphase to cortical in metaphase which reflects normal dynamics of LGN and has been described in various tissues and cell types (Blumer, Chandler and Lanier, 2002; Kaushik *et al.*, 2003; Du and Macara, 2004; Morin, Jaouen and Durbec, 2007). Therefore, the expressed GFP-LGN fusion protein showed a normal cellular distribution identical to endogenous LGN. Live cell imaging supported these results and more importantly confirmed the timing of the cortical localisation that has been described in HeLa cells (Kiyomitsu and Cheeseman, 2012). This is the first time that time-lapse imaging showed the behaviour of LGN during mitosis in mammary cells and supported the findings that LGN has the same conserved dynamics in different cell types and tissues. Not only did time-lapse imaging reveal the cortical accumulation of LGN, it also excluded any changes in the timing of cell division. The overall cell cycle length of MCF-10A cells is 21 h, from

which cells spend less than 1 h in mitosis (Araujo *et al.*, 2016). This is in accordance with the timing recorded in this study. Thus, expression of GFP-LGN or GFP did not slow down or accelerate cell division of MCF-10A cells.

Based on immunoblot analysis, it was shown that endogenous LGN is detected as two bands whereas GFP-LGN is only detected as a single protein band. Two possible explanations arise from this. First, this could be the phosphorylated and non-phosphorylated forms of LGN which were detected in previous work (Du, Stukenberg and Macara, 2001; Fukukawa *et al.*, 2010). However, this would not explain why GFP-LGN does not show two bands. A second possibility is that the LGN antibody detects the LGN homologue AGS3. These proteins share 57 % sequence identity with AGS3 having a slightly smaller molecular weight (Blumer, Chandler and Lanier, 2002). It may be possible that the shared sequence part between the proteins is detected by the LGN antibody. Nevertheless, specific protein signals were detected for GFP-LGN and endogenous LGN at expected protein sizes with endogenous LGN levels being higher in mitotic cells compared to interphase conditions. These cell cycle-dependent changes with a peak during mitosis have been reported for the protein and gene level in HeLa cells (Whitfield *et al.*, 2002; Du and Macara, 2004) and in the breast cancer cell line T47D (Fukukawa *et al.*, 2010). However, the increase was less prominent in this study. One explanation for the differences may be the drug treatment to arrest cells and the timing of analysis. In previous studies, cells were arrested in G<sub>1</sub> or S phase and LGN levels were traced over several time points after the release while cells progressed through the cell cycle. Protein levels only started to rise towards G<sub>2</sub>/M indicated by elevating levels of cyclin B. From this point, LGN levels only increased minimal until the end of M phase where levels decreased significantly (Du and Macara, 2004; Fukukawa *et al.*, 2010). Due to inhibition of CDK1 and arrest at G<sub>2</sub>/M in this work, it can be speculated that LGN levels were already increased and did not change much more. Thus, the small changes of protein levels reflect the patterns observed in previous studies however, it remains to be determined if LGN levels also significantly decrease outside M phase in MCF-10A cells.

GFP-LGN or GFP levels were stable indicating that the unknown mechanisms regulating the increase of endogenous LGN had no effect on GFP-LGN or GFP. Ectopic expression of the proteins was driven by the constitutive simian virus 40 (SV40) promoter which was shown to be relatively weak compared to other common promoters such as the cytomegalovirus (CMV) promoter (Zheng and Baum, 2005; Qin *et al.*, 2010). Thus, GFP-LGN and GFP were not strongly overexpressed. Nevertheless, expression of these proteins resulted in a change of protein content within the cells and it was important to evaluate specific cellular processes relevant to the biological question. In this case, spindle length and spindle angles were measured to exclude changes in mitotic spindle assembly and spindle orientation. Unaffected spindle angles suggested that spindle orientation was

executed normally. This was also reported in other studies where even the strong overexpression of GFP-LGN under a CMV promotor had no influence on spindle orientation (Saadaoui *et al.*, 2017; Pirovano *et al.*, 2019). Thus, elevated LGN levels did not disturb normal execution of spindle orientation. This could be expected because NuMA, dynein/dynactin (p150<sup>Glued</sup>) and Gai accumulated normally at the lateral cortex suggesting that binding of LGN to Gai1 and NuMA was not affected by the GFP-tag. Thus, normal formation of the LGN-complex was possible. Similarly, spindle sizes did not change confirming that spindle assembly was normal.

In conclusion, expression of GFP-LGN or GFP in mammary epithelial cells did not alter the dynamics of the cell cycle, mitosis or spindle dynamics. Furthermore, expression of GFP alone constituted a reliable control and the fusion protein resembled normal behaviour of endogenous LGN. With the characterisation of the generated cell lines and confirmation of non-altered cell dynamics, the GFP-LGN cell line represented a reliable tool for the proteomic study in the next chapter that utilized the cell line to characterise the LGN interactome.

**Chapter 4 Characterisation of the LGN interactome in  
dividing mammary epithelial cells reveals ANXA1 as a  
novel partner**



## 4.1 Introduction

Traditionally, key proteins involved in specific biological processes have been identified by genetic studies or loss-of-function experiments. Now, with the development of high-throughput technologies it is possible to define all protein components of biological processes using large-scale proteomic approaches (Walczak and Heald, 2008; Petry, 2016). Proteomics is the study of the proteome which describes the set of proteins encoded by the genome (Wilkins *et al.*, 1996). It allows identifying of all proteins in any given cell including all isoforms and modifications, interactions as well as structural description and higher-ordering complexes (Tyers and Mann, 2003). Proteomics can be divided into three main categories. One comprises the micro-characterisation of proteins to identify proteins and their modifications. Another category studies protein-protein interactions (PPIs) and the last constitutes differential expression analyses to compare protein levels which could be used in a disease-specific manner for diagnostic markers or therapeutic targets (Pandey and Mann, 2000). For all areas, MS is a widely used technique to identify the proteome. MS measures the mass-to-charge ratio ( $m/z$ ) of gas phase ionized analytes. For this, mass spectrometers consist of an ion source that converts the molecule samples into gas-phase ions, a mass analyser that separates the ions based on the  $m/z$  ratio and a detector that records the number of hits at each ratio. One strategy to detect proteins is the enzymatically production of peptides from intact proteins that are then subjected to the mass spectrometer (Bottom-up proteomics). Therefore, a protein mixture is usually digested with the protease trypsin and produced peptides are fragmented and subjected to LC-MS/MS. Then, peptides are identified by comparing measured protein masses to theoretical masses generated from genome databases (Han, Aslanian and Yates, 2008; Gundry *et al.*, 2010; Zhang *et al.*, 2013).

In the past, proteomic approaches were applied in different studies that analysed components of spindle elements. These included the centrosome (Andersen *et al.*, 2003), metaphase chromosomes (Uchiyama *et al.*, 2004), spindle microtubules (Mack and Compton, 2001), as well as the entire mitotic spindle (Sauer *et al.*, 2005; Bonner *et al.*, 2011) and its phosphorylation sites (Nousiainen *et al.*, 2006; Malik *et al.*, 2009; Rao *et al.*, 2016). Together, these studies characterised more than 1000 different proteins that are associated with the spindle apparatus, including hundreds of uncharacterised ones. Interestingly, LGN and other well-known cell division proteins were not identified. One explanation could be low abundance under the conditions of the experiments which made components difficult to detect. It is also possible that the methodical approach led to loss of proteins during purification caused by harsh biochemical treatments used

to isolate spindle structures. Therefore, proteins that might only transiently associate with the structures or constitute minor components can only be detected with additional procedures with less harsh biochemical treatment (Walczak and Heald, 2008).

More recent studies did not isolate entire structures of the spindle, but used Co-IP to purify individual protein complexes. Thereby, a protein of interest is used as a bait and pulled down with its associated factors using an antibody that targets the bait. This antibody is bound to an immobilizing matrix such as agarose or magnetic agarose beads which enriches the precipitated protein and its binding partners but prevents association of unspecific components. Therefore, Co-IP allows the identification of the complete array of interacting proteins involved in a specific regulation or signalling pathway (Free, Hazelwood and Sibley, 2009; Moresco, Carvalho and Yates, 2010).

A popular tool for Co-IP are Nano-Traps. This strategy is based on Camelid antibodies which are devoid of light chains and bind their antigen via a single variable domain, known as Nanobody. This Nanobody can be coupled to agarose or magnetic agarose beads which is known as a Nano-Trap allowing for efficient and rapid protein purification. Nano-Traps have proven to be a reliable method for biochemical studies such as enzyme activity assays, chromatin IPs in cells expressing fluorescent DNA binding proteins or MS and they can be engineered in many different ways. One version, called GFP-Trap, uses a 13 kDa-GFP binding fragment that recognizes GFP or GFP-fusion proteins and has been utilized in hundreds of studies in different species (Hamers-Casterman *et al.*, 1993; Rothbauer *et al.*, 2008; Fellingner and Rothbauer, 2009).

Given the minimal knowledge of regulation of spindle orientation in the mammary gland, it is critical to understand the protein interactions of the LGN complex during mitosis. To date, there is no study investigating the overall proteome of the spindle orientation complex during mitosis. Therefore, the aim of this chapter was to identify LGN protein interactions in mammary epithelial cells during metaphase, the time point of active spindle orientation. For this, the GFP-Trap system and MS was combined to characterise the complete set of the LGN interactome. The identified PPIs were bioinformatically analysed using gene enrichment tools. Together, these analyses identified a set of known and previously unknown partners of LGN.

## 4.2 Results

The proteomic workflow including synchronization of cells and Co-IP was validated and MS was performed. Results were analysed in collaboration with Dr Farahnaz Sadat Golestan Hashemi (Elias lab, University of Southampton). Contributions were specified in the relevant sections.

### 4.2.1 Co-immunoprecipitation of GFP-LGN from interphase and mitotic cells

The Co-IP protocol provided by the company was tested for GFP-LGN expressing cells and the fusion protein was successfully pulled down. As seen in figure 4.1, GFP-LGN enriched in the IP compared to the input. Furthermore, only a small amount of unbound protein remained (Supernatant after binding) and no protein was detectable in the supernatants during washing.

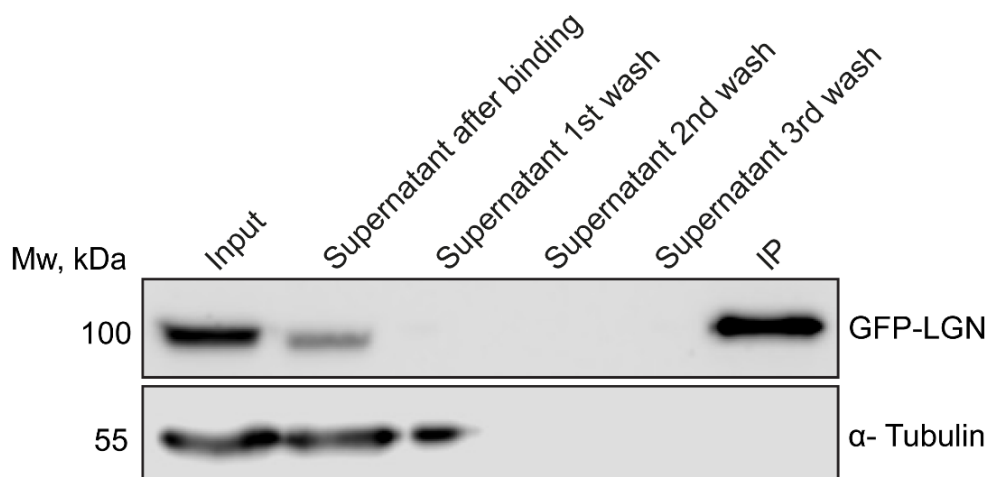


**Figure 4.1 Immunoprecipitation of GFP-LGN from MCF-10A cells using GFP-Trap**

*Immunoblot of GFP-LGN levels during GFP-Trap immunoprecipitation. The protein was isolated from whole cell lysates (input) of MCF-10A cells expressing GFP-LGN and analysed in the supernatant after binding, during three washing steps and in the immunoprecipitate (IP). GFP-LGN was detected with anti-GFP antibody.  $\alpha$ -Tubulin levels were used as a measure of washing efficiency.*

The protocol was further tested with WT MCF-10A and cells expressing GFP. The isolation of GFP-LGN was confirmed and furthermore, GFP alone was pulled down but no signal was detected in WT cells. No endogenous LGN was isolated in any of the conditions (Figure 4.2).

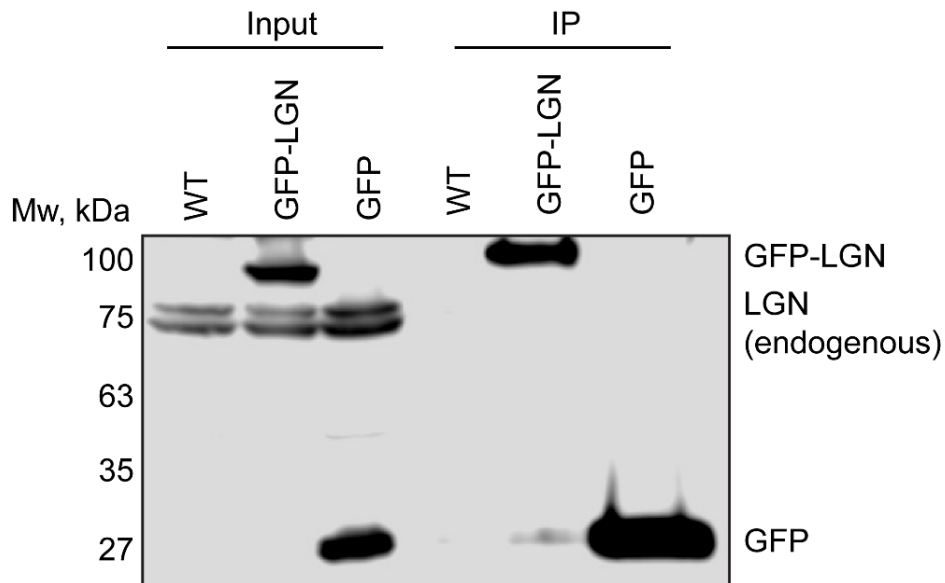


**Figure 4.2 GFP-Trap specifically immunoprecipitates GFP and GFP-LGN**

*Immunoblot of affinity purifications using GFP-Trap in WT MCF-10A cells and MCF-10A cells expressing GFP-LGN or GFP. Endogenous LGN, GFP-LGN and GFP levels were analysed in whole cell lysates (input) and in the immunoprecipitate (IP). GFP and GFP-LGN were detected with anti-GFP antibody. Endogenous LGN was detected with anti-LGN antibody.*

To characterise the proteome of GFP-LGN in mitosis, cells had to be arrested in their cell cycle. For this, several tests were performed to confirm the successful and efficient accumulation in metaphase. Brightfield microscopy showed that 6 h after treatment with MG-132, cells expressing GFP-LGN or GFP were enriched in mitosis compared to the control where GFP-LGN cells were arrested at G<sub>2</sub>/M (Figure 4.3).

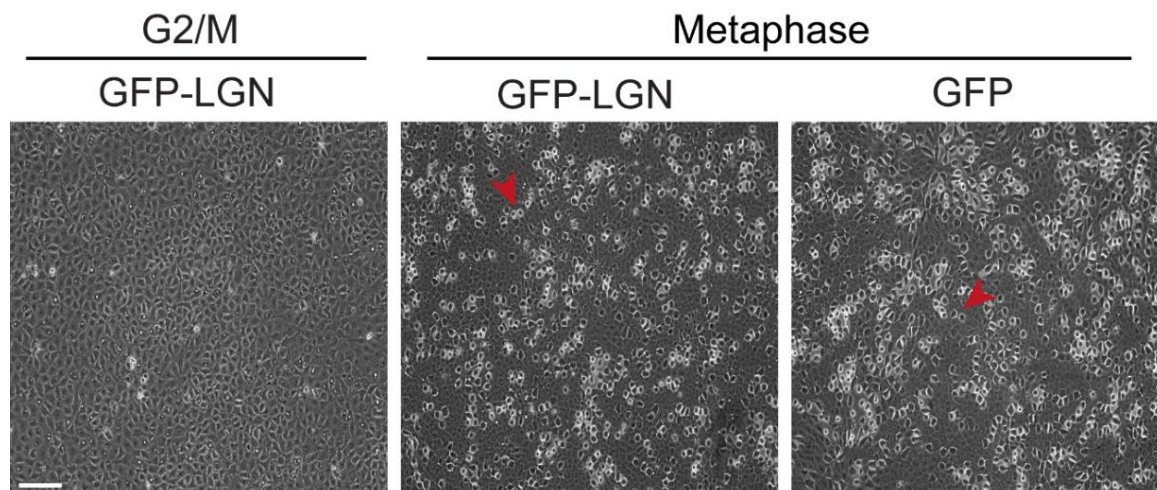


**Figure 4.3 Cell cycle arrest of MCF-10A cells expressing GFP-LGN or GFP**

*Representative light microscopy images of MCF-10A cells arrested at  $G_2/M$  phase or metaphase. To accumulate cells at  $G_2/M$ , cells were incubated with CDK1 inhibitor RO-3306. Metaphase arrested cells were generated by treatment with RO-3306 for 18h which was washed out and cells were further treated with proteasome inhibitor MG-132 for 6h. Cells were imaged 18h after RO-3306 treatment for  $G_2/M$  arrest or after MG-132 treatment (6h after treatment start). Enrichment of mitotic cells is seen by accentuated brighter cells. Examples of mitotic cells are indicated (red arrowheads). Scale bar, 200 $\mu$ m.*

To determine the accumulation of cells in metaphase, immunofluorescence staining and confocal microscopy was performed at the 6 h time point. DNA staining showed that chromosomes fully aligned in the chromosome plate in MCF-10A cells expressing GFP-LGN or GFP when accumulated in metaphase. Interphase nuclei were visible when arrested at  $G_2/M$ . Staining with anti- $\alpha$ -tubulin antibody revealed that mitotic spindles were fully assembled. Furthermore, GFP-LGN localised specifically at the cell cortex during metaphase but was diffuse in the cytoplasm in interphase. Cells expressing GFP alone showed a uniform localisation of the protein in the cytoplasm independent of the cell cycle stage (Figure 4.4).

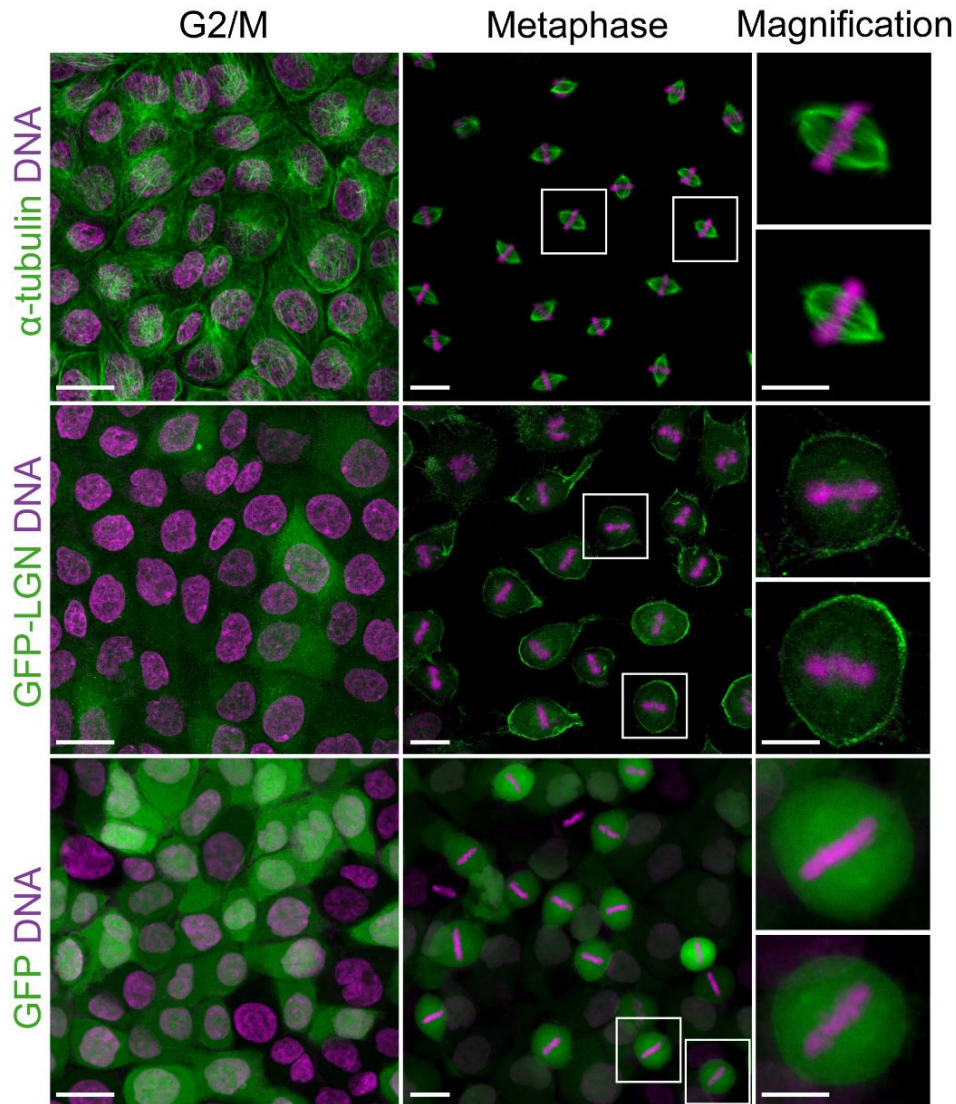


**Figure 4.4 Localisation of GFP-LGN or GFP in cell cycle arrested MCF-10A cells**

*Representative confocal images of interphase microtubules, metaphase mitotic spindles and the subcellular localisation of GFP-LGN or GFP in cells arrested at G<sub>2</sub>/M using CDK1 inhibitor RO-3306 or arrested at metaphase using RO-3306 and proteasome inhibitor MG-132. Cells were fixed with methanol and stained for GFP or  $\alpha$ -tubulin (green). DNA (blue) was visualised with Hoechst 33342. Insets show higher magnification of framed regions. Scale bars, 10  $\mu$ m.*

The mitotic index was calculated to evaluate the percentage of mitotic cells when arrested in metaphase compared to interphase. For this, the number of interphase nuclei and metaphase plates were counted and the number of chromosome plates was divided by the total number of cells counted (Figure 4.5, A). Less than 0.5 % percent of cells were mitotic in interphase condition

whereas in the metaphase arrested state, 52 % of GFP-LGN cells and 45 % of GFP cells were mitotic (Figure 4.5, B).

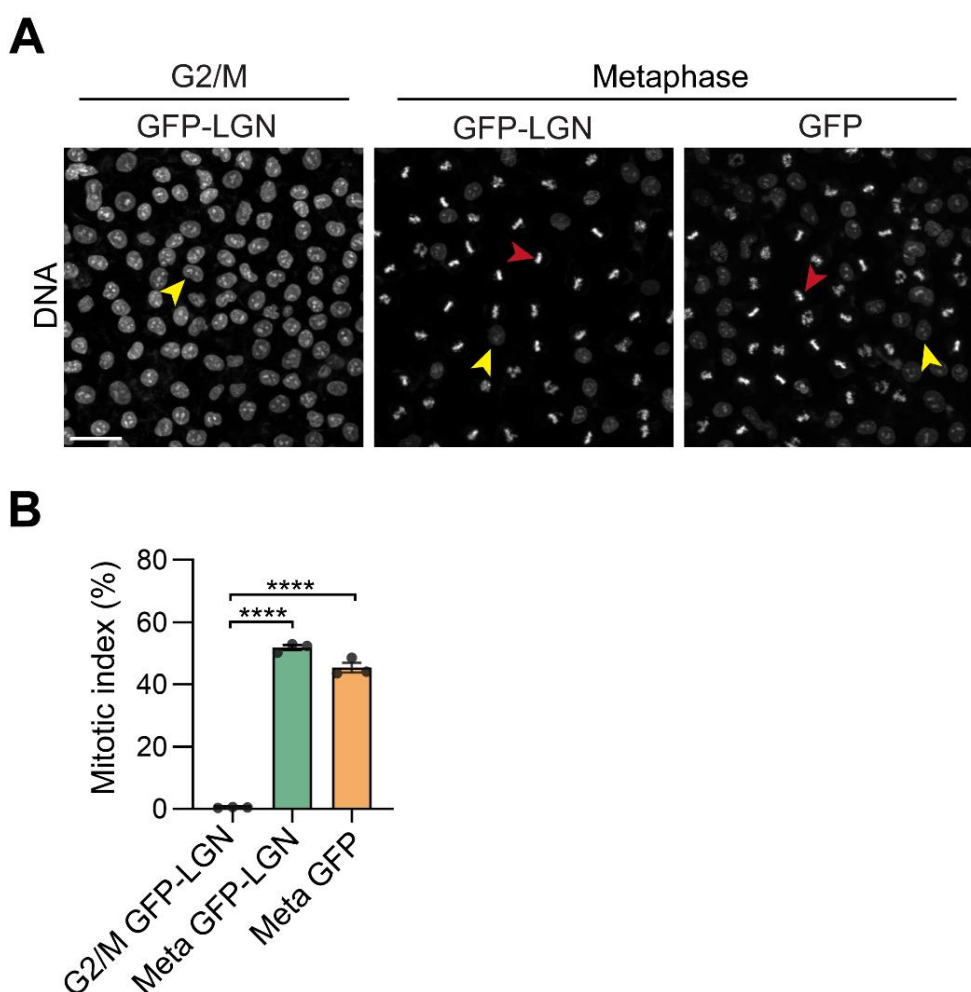


**Figure 4.5 Mitotic index in cells arrested at G<sub>2</sub>/M or metaphase**

(A) Representative confocal images of interphase nuclei and metaphase plates in MCF-10A cells arrested at G<sub>2</sub>/M phase or metaphase. Cells were arrested at G<sub>2</sub>/M using CDK1 inhibitor RO-3306. Accumulation of metaphase cells was achieved by treatment with RO-3306 and proteasome inhibitor MG-132. Cells were fixed with 4 % PFA and DNA was stained with Hoechst 33342. Yellow arrowheads indicate interphase nuclei. Red arrowheads point to metaphase plates. Scale bar, 50 μm. (B) Percentage of mitotic cells in GFP-LGN cells arrested at G<sub>2</sub>/M or metaphase and GFP cells arrested at metaphase. Meta, metaphase. Data represent means (black dots) ± SEM from three independent experiments. For each experiment, 10 images were analysed (n total= 30 per condition). Student's t-test; \*\*\*\*p ≤ 0.0001.

#### 4.2.2 Protein-protein interaction network of LGN during mitosis

MS data was obtained from mitotic MCF-10A cells expressing GFP-LGN or GFP. The experiment was performed twice. All samples revealed large numbers of proteins associated with LGN. In the first and second experiment 1165 and 2061 protein hits were identified respectively. In the GFP control, 730 and 1764 proteins were identified for experiment 1 and 2 respectively. Members of the spindle orientation machinery were identified (Table 4.1). LGN, NuMA and proteins of the dynein/dynactin complex were detected in both experiments. However, a G $\alpha$ i subunit were only found in the second experiment. Furthermore, tubulin-  $\alpha$  and  $\beta$  and other members of the tubulin family (see Appendix B1 for details) were identified.

**Table 4.1 Members of the spindle orientation machinery identified by MS**

*Summary of proteins identified in mitotic MCF-10A cells that co- purified with GFP-LGN in two independent experiments (Exp1, Exp2). Presence in the data is indicated with ticks. Absence is highlighted with a line. Proteins were identified by manual search of the MS data.*

Gene	Description	Exp 1	Exp 2
GPSM2	G-protein-signaling modulator 2, LGN	✓	✓
NUMA1	Nuclear mitotic apparatus protein 1	✓	✓
GNAI3	Guanine nucleotide-binding protein G(i) subunit alpha-3, G $\alpha$ i3	-	✓
DYNC1H1	Cytoplasmic dynein 1 heavy chain 1	✓	✓
DYNC1/2*	Cytoplasmic dynein 1 intermediate chain 2	✓	✓
DYNLRB1*	Dynein light chain roadblock-type 1	✓	✓
DCTN1	Dynactin subunit 1 (p150)	✓	✓
DCTN2	Dynactin subunit 2 (p50)	✓	✓
ACTR1A	Alpha-centractin, Arp1	-	✓
CAPZA2	F-actin-capping protein subunit alpha-2	-	✓

\*not present in the final protein- protein interaction network after filtering and subtraction of background

The results described so far were obtained by manual search of the datasets. Before analysis of the samples using bioinformatics tools, background proteins were manually subtracted. For this, the GFP-LGN data set was compared to the GFP data and protein hits also found in the control were removed. To further improve the signal to noise ratio, the remaining proteins were considered against the CRAPOME database which acted as a quality control to remove protein contaminants known to generate noise signals in mass spectrometry studies. After this step, 491 (Experiment 1) and 664 (Experiment 2) proteins were below the CRAPOME threshold and were used to retrieve a STRING interaction network. After elimination of single nodes (proteins that did not show any interaction), a STRING network with 338 nodes (human proteins) and 1146 edges (protein-protein interactions) was generated for the first experiment. A PPI network with 444 nodes and 1737 edges was retrieved for the second experiment. Further filtering the network by selecting LGN (GPSM2) and its closest associated proteins (subnetworking) identified 18 nodes with 39 edges (experiment 1) and 24 nodes with 53 edges (Experiment 2) (Table 4.2).

**Table 4.2 Number of protein hits before and after interaction network generation**

*Summary of total numbers of proteins identified in two independent MS experiments (Exp1, Exp2) in mitotic MCF-10A cells expressing GFP-LGN. Furthermore, the number of remaining proteins after filtering and STRING network retrieval are shown as well as the number of protein hits that were filtered with CRAPOME database (score  $\leq 180$ ). Final protein numbers in the STRING output and LGN subnetwork had an interaction confidence score of  $\geq 0.6$ . CRAPome analysis and STRING output was generated by Dr Farahnaz Sadat Golestan Hashemi.*

	Raw data	Filtered proteins after CRAPome	String output Nodes/edges	LGN subnetwork Nodes/ edges
Exp 1	1165	491	338/1146	18/39
Exp 2	2061	664	444/1737	24/53

Comparison of the STRING interaction networks between the two experiments revealed that more proteins were enriched in the second experiment. Furthermore, when comparing protein hits most proteins were unique to the experiments and only 77 proteins were common (Figure 4.6).



**Figure 4.6 Number of enriched proteins and overlap between two independent MS experiments**

*Total number of proteins enriched in the GFP-LGN pulldown fraction from mitotic MCF-10A cells expressing GFP-LGN. Two independent experiments were performed showing unique protein hits and overlap between the experiments.*

The final subnetwork of experiment 1 is shown in Figure 4.7 (see Appendix B2 for confidence/interaction scores). The majority of the identified proteins in the network constituted known regulators of spindle orientation, spindle assembly or ACDs in other tissues and cell types. NUMB, Par3 (PARD3) and mINSC (INSC) that connected with LGN (GPSM2) were previously described as regulators of ACDs (Lechler and Fuchs, 2005; Zigman *et al.*, 2005; El-Hashash and Warburton, 2012). LGN (GPSM2) further showed an association with NuMA (NUMA1) which in turn associated with proteins of the dynein/dynactin complex (DYNC1H1 and DCTN2) as well as  $\gamma$ -tubulin (TUBG1). Other known regulators of spindle assembly and orientation were Clasp1 (Pereira *et al.*, 2006; Samora *et al.*, 2011). PLK1 (Kiyomitsu and Cheeseman, 2012; Sana *et al.*, 2018), importin-  $\alpha$ 1 (KPNA2) (Guo *et al.*, 2021), Ran (Kiyomitsu and Cheeseman, 2012) and Eukaryotic translation initiation factor 3 subunit E (EIF3E) (Morris and Jalinot, 2005). Haus6 (Lawo *et al.*, 2009) and Cyclin-B1-interacting protein 1 (CCNB1) (Yu and Yao, 2008) are involved in spindle assembly and were identified as connections. Three proteins were previously undescribed to be involved in mitotic functions. These included ANXA1, Serum amyloid A-1 protein (SAA1) and S100A11 from which the first two proteins showed a link with LGN.

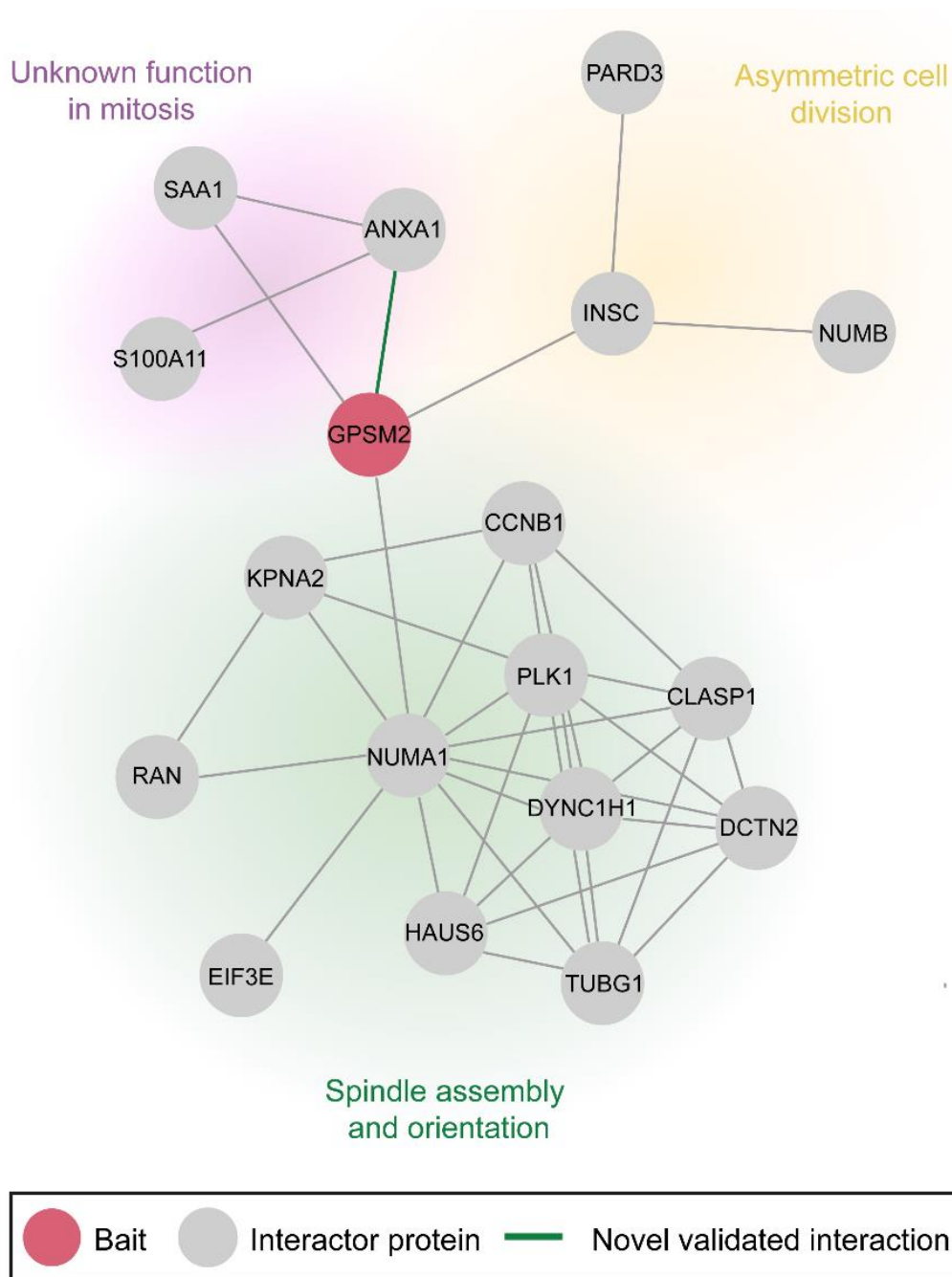


**Figure 4.7** Known and novel interaction partners of LGN identified in a STRING protein interaction network

*STRING* network of LGN (GPSM2, red) and its first neighbours (grey) of known and unknown mitotic functions as specified. The green line indicates the validated interaction in this study. To generate the network, subnetworking was performed by selecting LGN and its closest interactors in the entire retrieved *STRING* network using Cytoscape software. The network was generated by Dr Farahnaz Sadat Golestan Hashemi and further annotated by the author of this thesis.

Many of the proteins identified in the LGN subnetwork in the first experiment were also present in the subnetwork in the second experiment (see appendix B3 for the network). As seen in table 4.3 NuMA, members of the dynein/dynactin complex, Insc, Numb, PLK1, Ran, CLASP1 and KPNA2 were identified in both experiments. Interestingly, also the three proteins with no known function in mitosis were also found in the repeated experiment. However, the proteins PARD3, TUBG1, CCNB1, EIF3E and HAUS6 were not present in the LGN subnetwork of the second experiment. However, other proteins known as regulators of spindle orientation or assembly were identified. These included Arp1 (Clark and Meyer, 1999), CAPZA2 (Jo *et al.*, 2015), Gai3 (Du and Macara, 2004), AGS3 (Sanada and Tsai, 2005) and MAPK3 (Tang *et al.*, 2011). Other proteins had no specific function in mitosis.

**Table 4.3 Comparison of members of the LGN subnetwork in two independent MS experiments**

*List of proteins found in the LGN subnetwork in two independent MS experiments (Exp1, Exp2).*

*Presence in the individual experiment is indicated with ticks. Absence is highlighted with a line.*

*Proteins were identified by manual search of the MS data.*

Gene	Description	Exp 1	Exp 2
<b>GPSM2*</b>	<b>G-protein-signalling modulator 2</b>	✓	✓
NUMA1*	Nuclear mitotic apparatus protein 1	✓	✓
DCTN2*	Dynactin subunit 2	✓	✓
DYNC1H1*	Cytoplasmic dynein 1 heavy chain 1	✓	✓
INSC*	Protein inscuteable homolog	✓	✓
NUMB*	Protein numb homolog	✓	✓
PLK1*	Serine/threonine-protein kinase PLK1	✓	✓
RAN*	GTP-binding nuclear protein Ran (Fragment)	✓	✓
CLASP1*	CLIP-associating protein 1	✓	✓
KPNA2*	Importin subunit alpha-1	✓	✓
ANXA1	Annexin A1	✓	✓

Table 4.3 Continued

S100A11	Protein S100-A11	✓	✓
SAA1	Serum amyloid A protein	✓	✓
PARD3*	Partitioning defective 3 homolog	✓	-
TUBG1*	Tubulin gamma-1 chain	✓	-
CCNB1*	G2/mitotic-specific cyclin-B1	✓	-
EIF3E*	Eukaryotic translation initiation factor 3 subunit E	✓	-
HAUS6*	HAUS augmin-like complex subunit 6	✓	-
ACTR1A*	Alpha-centractin, Arp1	-	✓
BRD4	Bromodomain-containing protein 4	-	✓
CACNA1B	Voltage-dependent N-type calcium channel subunit alpha-1B	-	✓
CAPZA2*	F-actin-capping protein subunit alpha-2	-	✓
CASP3	Caspase-3	-	✓
CASP6	Caspase-6	-	✓
CEP78	Centrosomal protein of 78 kDa	-	✓
GNAI3*	Guanine nucleotide-binding protein G(i) subunit alpha-3	-	✓
GPSM1*	G-protein-signalling modulator 1, AGS3	-	✓
MAPK3*	Mitogen-activated protein kinase 3, ERK1	-	✓
PTPN11	Tyrosine-protein phosphatase non-receptor type 11	-	✓

\*proteins with known function in mitotic spindle assembly and orientation

### 4.2.3 Functional enrichment analysis of the LGN interaction network

To evaluate in which processes the identified proteins were involved in, gene enrichment analysis was performed. Grouping based on GO Biological Process revealed that from the entire interaction network (experiment 1) 55.6 % of the proteins were enriched for organelle organization which is referred to as processes at the cellular levels that result in assembly, organization or disassembly of an organelle including the cytoskeleton. In the context of mitotic spindle dynamics, organelle organisation includes spindle organisation and localization (Ashburner *et al.*, 2000; 2021). The rest contributed to nuclear chromosome segregation (18.5 %), establishment of localisation in the cell (2.5 %) and membrane organization (1.2 %). Biological processes that were not linked to mitosis were combined in the group “Other biological processes” (22.2 %) (Figure 4.8). Similar GO processes involved in chromosome organization, organelle organization, protein localisation and other biological processes were also enriched in the second experiment (Appendix B4).

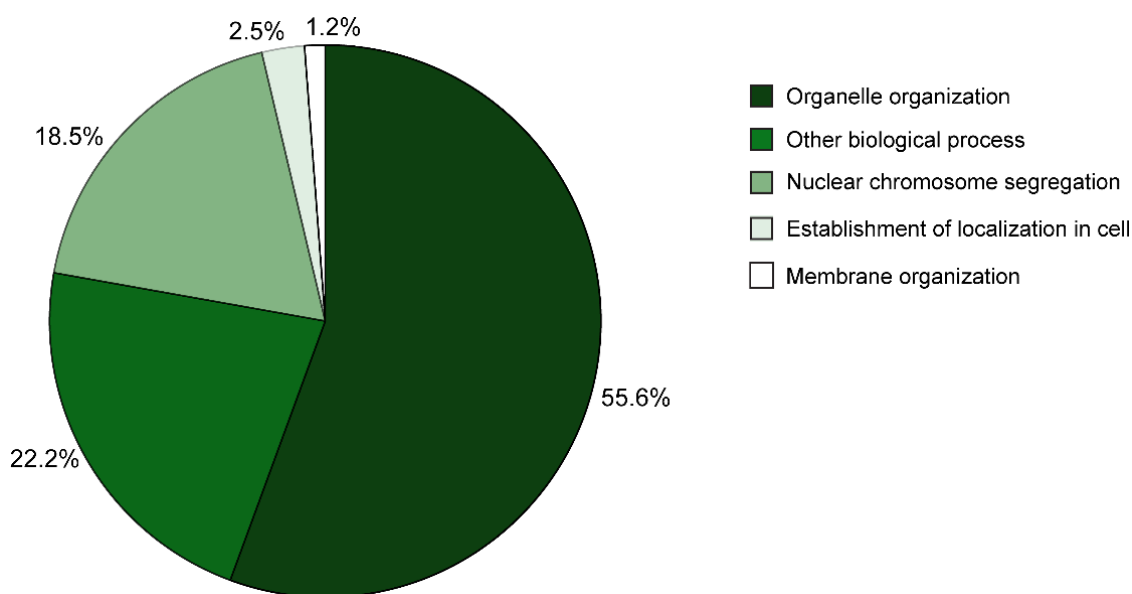
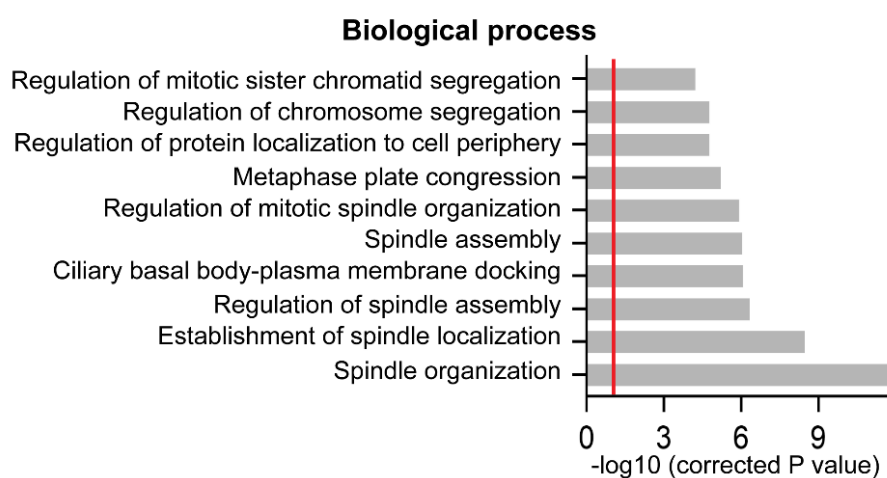


**Figure 4.8 Classification of identified proteins based on their biological function**

Percentage of proteins involved in enriched Gene Ontology biological processes. Gene enrichment analysis was performed with the entire STRING network of the first MS experiment. Hypergeometric test (Fisher's Exact Test) was used to calculate the statistical significance of the overrepresentation of enriched functional processes with the Bonferroni step-down correction from multiple tests.  $P \leq 0.05$  was considered significant. 100% = 338 proteins. Analysis was performed by Dr Farahnaz Sadat Golestan Hashemi.

Gene enrichment analysis of the LGN subnetwork (experiment 1) showed that members of this interaction network were significantly enriched for GO biological processes such as spindle organization, spindle localisation, spindle assembly, metaphase plate congression and others (Figure 4.9, A). Furthermore, these analyses revealed that proteins were enriched for specific pathways including regulation of PLK1 activity, recruitment of NuMA, centrosome maturation and others (Figure 4.9, B). Similar GO biological processes and pathways were significantly enriched in the second experiment (Appendix B5).

**A**



**B**

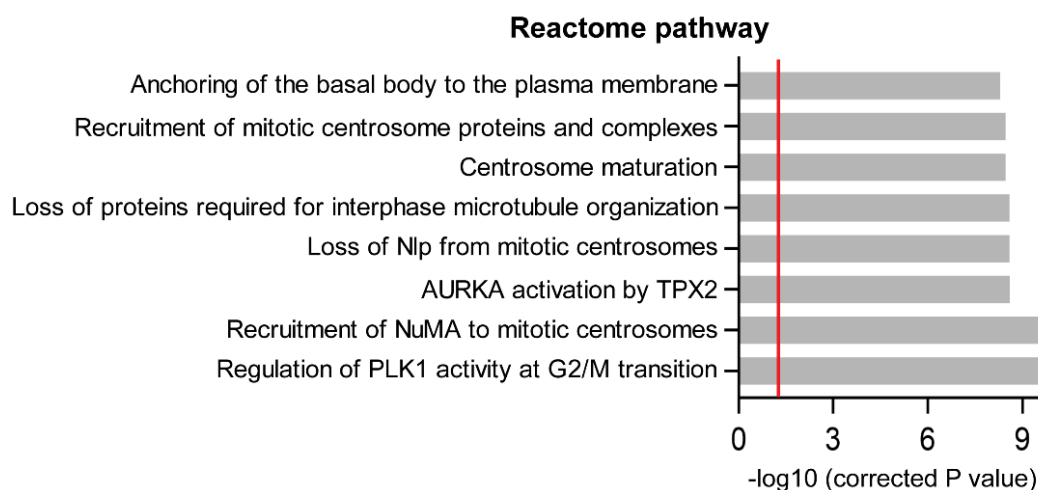


**Figure 4.9 Gene enrichment analysis of significantly enriched biological processes and pathways from proteins in the LGN subnetwork**

**Figure 4.9 Continued**

(A) Significantly enriched Gene ontology biological processes associated with the proteins in the LGN subnetwork. (B) Significantly enriched Reactome pathways associated with the proteins in the LGN subnetwork.  $P \leq 0.05$  ( $-\log_{10} = 1.3$ , red line) was considered significant for all enrichment analyses. Hypergeometric test (Fisher's Exact Test) was used to calculate the statistical significance of the overrepresentation of enriched genes in functional processes and pathways with the Bonferroni step-down correction method from multiple tests using ClueGO App. Analysis was performed by Dr Farahnaz Sadat Golestan Hashemi.

Taken together, the results showed that using the GFP-Trap system, GFP-LGN and GFP alone were successfully isolated from stable MCF-10A cell lines expressing the fusion protein or the fluorescent protein alone. Furthermore, enrichment in metaphase was achieved by cell cycle arrest with a distinct localisation of GFP-LGN at the cortex and GFP in the cytoplasm. The LGN interactome of mitotic MCF-10A identified by MS analysis comprised members of the spindle orientation complex and many known regulators of spindle assembly and spindle orientation. Bioinformatics analysis confirmed that proteins had specific functions in biological processes related to mitosis. Specifically, proteins in the LGN subnetwork had enriched biological functions and pathways important for e.g. spindle organization, spindle assembly and localisation of proteins in the cells. Lastly, a set of proteins was identified that had no previously known function in mitosis.

**4.3 Discussion**

A collective mechanism of the cooperation of signals and regulators that drive oriented cell divisions remains elusive, especially in polarised epithelial tissues such as the mammary gland. Therefore, it is essential to understand the protein interactome of the spindle orientation machinery during spindle positioning at metaphase. Due to the complex nature of dynamic mitotic processes, the optimization and validation of sample preparation is essential for a proteomics study to identify low abundant and dynamic proteins (Aldarmahi and Al-Rabia, 2015). Thus, to allow the best conditions to study the LGN interactome in a spatial and temporal fashion, several protocols were optimized to accumulate cells in metaphase and immunoprecipitate GFP-LGN from MCF-10A cells. This was essential to isolate proteins in a manner that allows efficient peptide preparation for

subsequent MS analysis with the final goal to identify and characterise the LGN protein interactome.

#### **4.3.1 Characterising the complete LGN interactome requires optimal conditions**

In a global effort to identify LGN interactors at the cell cortex during mitosis, several methodologies were used. To isolate GFP-LGN from mitotic cells in high homogeneity, sufficient numbers and at best conditions, previously described protocols were tested and methodologies from past studies were expanded (Josefsberg *et al.*, 2000; Vassilev *et al.*, 2006; Fellingner and Rothbauer, 2009; Kiyomitsu and Cheeseman, 2012). The final procedure involved cell cycle block at metaphase. The technique of cell cycle arrest is an ideal tool to study certain events during the cell cycle and many methods have been established to accumulate cells at specific phases. Thereby, it is essential that the methods used are reversible and non-toxic (Davis, Ho and Dowdy, 2001; Amin and Varma, 2017). Common agents to arrest cells at G<sub>2</sub>/M phase are nocodazole and colchicine and have been used in studies investigating mitotic spindle dynamics (Kaushik *et al.*, 2003; Kiyomitsu and Cheeseman, 2012; Kotak, Busso and Gonczy, 2012; Fulcher *et al.*, 2019; Pirovano *et al.*, 2019). These agents disrupt MT dynamics by inducing MT depolymerization (Blajeski *et al.*, 2002). Although this is a reversible process and cells progress through mitosis upon release from these blocks, these chemicals have relatively high toxicity and it can lead to metabolic perturbations. Moreover, cells treated with nocodazole, can return to interphase precociously by mitotic slippage (Amin and Varma, 2017). Therefore, using these chemicals to identify the LGN interactome was not beneficial because MTs are essential in the mitotic spindle and its dynamics (Wittmann, Hyman and Desai, 2001). Disruption of MTs may influence the protein composition in cells and therefore bias the outcome of the proteomics study. Thus, milder drugs were used in this work that reversely inhibited catalytic activity of enzymes instead of disrupting cellular structures. By inhibiting CDK1 activity to block cells at G<sub>2</sub>/M and further inhibiting the proteasome to arrest cells at metaphase, a great proportion of cells could be enriched in metaphase where GFP-LGN accumulated at the lateral cell cortex. This proves that this protocol constitutes an ideal system to arrest cells in mitosis without disturbing cellular dynamics, specifically spindle orientation dynamics.

Another methodology that had to be tested was the use of the GFP-Trap system. This method led to the successful isolation of GFP-LGN from mitotic MCF-10A cells. Nano-Traps are extraordinarily efficient tools for Co-IPs and have several advantages over common antibody-based IPs. In contrast to other affinity resins, the affinity ligand (i.e. the Nanobody) is covalently linked to the matrix, and virtually no protein comes off the Nano-Traps. Protein contaminants from the beads are frequently

seen in Immunglobulin G (IgG)-based or streptavidin-based pull-downs and can mask potential interaction partners of the precipitated protein during SDS-PAGE or other methods of analysis. The small size and surface of the Nanobody reduces unspecific binding or background. Lastly, proteins can directly be digested from the beads (on-bead digestion) for MS analysis. This provides a powerful set of tools for proteomic studies directly at the protein level in a given cell state (Ong and Mann, 2005). Therefore, the GFP-Trap system was highly applicable for the purpose of the proteomics approach in this thesis and furthermore it has been used previously in several studies to identify protein interactions between members of the spindle orientation machinery. Work by Kotak et al. showed that NuMA fused with GFP precipitates with the dynein/dynactin complex (Kotak, Busso and Gonczy, 2012). Another study used GFP-NuMA for Co-IP and pulled down LGN besides other factors (Sana *et al.*, 2018). These examples show that GFP-Trap is a reliable tool to isolate known regulators of the spindle orientation complex during mitosis. However, the aim of this work was to use a member of the spindle orientation machinery to characterise the interactome and identify novel binding partners. This was similar to a previous approach. The study by Chiu et al. used G $\alpha$ i as a bait to identify interaction partners. Besides the known binding partners, such as LGN, the poorly characterised SAPCD2 protein was identified and subsequent functional analyses revealed its role in spindle orientation (Chiu *et al.*, 2016). Kiyomitsu & Cheeseman used LGN to define the complete set of interacting proteins that dictate the regulation of asymmetric dynein localisation during mitosis (Kiyomitsu and Cheeseman, 2012). Using Co-IP, they identified NuMA, various G $\alpha$ i subunits, and the dynein/dynactin complex. Although in both studies interactions with known and novel partners were identified, it is possible that many candidates were missed. This assumption is based on the fact that the studies were carried out with HEK293 and HeLa cells and treatment with nocodazole to arrest cells in metaphase. As discussed above, nocodazole treatment can be toxic and disturb cellular dynamics needed for spindle positioning. Furthermore, HEK293 and HeLa cells are unable to polarize. However, as discussed in the introduction (Chapter 1.3.2.2) polarity cues play a major role in spindle orientation processes (Knoblich, 2008; di Pietro, Echard and Morin, 2016; Nakajima, 2018a). Therefore, combining the usage of MCF-10A cells that are able to polarize, mild drug treatments to arrest cells at metaphase and the GFP-Trap system constituted the ideal conditions for the purpose of this proteomics study.

### 4.3.2 Reproducibility of the proteomics approach

MS analysis is the method of choice for proteome characterisation and the subsequent computational analysis places the raw data into a biological context (Cardoza *et al.*, 2012). This workflow was used here to identify the proteome of the spindle orientation machinery and its binding partners. Two independent experiments were performed and the core protein machinery was identified in both experiments. However, only a small fraction of proteins overlapped in both samples and the majority of hits were unique to the different experiments. Although this highlights that the experimental approach was reliable, it raises the question how repeatable and reproducible the proteomics data is.

Minor changes in the cellular environment can immensely influence the protein composition and subsequently the MS results. Thus, careful sample preparation is essential to maintain the distribution and abundance of proteins that ensures sufficient and high-quality signals (Dong *et al.*, 2016). This starts with maintaining healthy viable cells and continues with accurate protein lysis, co-IP procedures and MS sample preparation. In this work, it was important to accumulate MCF-10A cells in metaphase. Although the protocol for arresting cells during mitosis was successful, certain variations in the percentage of mitotic cells between experiments were seen. It is possible that the conditions for a metaphase arrest were different such as reaching the correct cell cycle stage during drug treatment. Depending on which cell cycle stage cells started with, not all cells completed a cell cycle and reached the correct phase needed to be arrested specifically in metaphase. This could be due to delayed cell cycle progression and activated cell cycle checkpoints (Elledge, 1996). Furthermore, it is highly debated if cells can be synchronized in a whole culture because this would mean that cells have identical DNA content, protein content and cell size to progress through the whole cell cycle simultaneously (Cooper, 2003; Cooper, 2019). Therefore, the presence of non-mitotic cells, different mitotic indices and asynchronous cells (different cellular content in metaphase cells) in the different experiments could have influenced the MS results. To achieve a true synchronized cell culture with a mitotic index of 100 %, a different approach called selective synchronization should be used. One example would be mitotic shake off, where cells arrested in metaphase can be removed from the cell population to produce 100 % mitotic cells (Fox, 2004).

Another critical factor in repeatability of proteomic experiments is retaining proteins, especially protein complexes, throughout sample preparation. Thereby, protein degradation constitutes the limiting factor because it can destroy the integrity and spatial localisation of molecules in the sample (Cañas *et al.*, 2007). During the Co-IP procedure, it was important to maintain a cool

environment to prevent protein degradation. Any changes and differences in the sample handling could explain the results of the two MS experiments.

A third aspect in repeatability is that proteomic analysis is very complex when using LC-MS/MS starting from tryptic digestion of proteins, phase separation of peptides, acquirement of peptide spectra and finally matching of those spectra to database sequences to identify protein hits (Tabb *et al.*, 2010). Fluctuations can occur due to technical setup. For example, minor differences in LC can alter the order of elution or change which peptides are selected for MS/MS fragmentation. Subsequently this leads to misidentification by database search algorithms (Liu, Sadygov and Yates, 2004).

In conclusion, the experimental approach created variations in the cellular protein composition because of the fluctuating synchronization results. Furthermore, preparations of peptides for MS was a complex process executed in collaboration with the Proteomics facility. Therefore, the human factor and variations in sample handling may have also influence the results. A study by Liu *et al.* showed that at least 10 experiments are needed to reach protein identification similarity of 95 % (Liu, Sadygov and Yates, 2004). Thus, more experiments should be carried out to generate more repeatable results. Nevertheless, the identification of the core spindle orientation machinery and various known regulators of spindle positioning and spindle assembly in both experiments cannot deny the robustness of the methodology in this study.

### **4.3.3 The mitotic LGN interactome in mammary epithelial cells comprises known and novel regulators of mitotic spindle dynamics**

Characterising PPIs via co-IP and MS constitutes an ideal method to study protein functions of specific cellular mechanisms. By choosing a specific bait, a selective set of proteins within a complex can be analysed (Phizicky and Fields, 1995). One disadvantage of this method is the coupling to an affinity matrix which can create a binding environment for contaminant proteins. Such proteins that create background signals in the sample are present in large numbers in cells and include ribosomal proteins, metabolic enzymes and chaperones (Berggård, Linse and James, 2007). Many of these contaminants were present in the data in this study. Although, a control condition was used to detect sticky proteins that bind to the matrix and GFP alone, such controls can fail to capture all contaminants due to variations in the sample or sample preparation. Thus, the CRAPOME database was used to further remove background signals which helped to further discriminate between specific and non-specific protein hits (Mellacheruvu *et al.*, 2013). This resulted in the generation of PPI networks that closest associated with LGN and showed for the first time a set of proteins

involved in spindle orientation in mammary epithelial cells. The presence of members of the core spindle orientation machinery including Gai1, LGN and NuMA and the force generators dynein/dynactin proved that the LGN complex was active during purification. This suggests, that cells were in the phase of spindle positioning during metaphase. This is in accordance with previous studies showing that this complex orientates the mitotic spindle in the mammary gland (reviewed in Santoro *et al.*, 2016). Gene enrichment analysis further supported the observation because several GO categories comprised organelle organization, spindle organization, spindle assembly and metaphase plate congression. Such gene enrichment analysis are an important measure to assess the biological significance of the proteomics result and extract functional and biological information from the list of protein hits. This helps to provide biological insight into the underlying mechanisms and can be used as a proof of concept (Wu, Hasan and Chen, 2014). The biological processes and pathways identified in this study are essential during mitosis and proof that the detected proteins were not random hits which strengthens the accuracy of the proteomics approach. However, when interpreting the protein network results, the individual connections between nodes need to be carefully considered. While generating protein connections, the STRING database assigns scores to proposed protein links based on the estimated likelihood that the association is biologically relevant, specific and reproducible, given the supporting evidence (Roth *et al.*, 2016). This means that these scores do not indicate the strength or specificity of a connection and only represents the likelihood of being true. Furthermore, this connection is presented as functional but not necessarily physical. Thus, a STRING interaction between two proteins is based on database search and predictions and does not necessarily represent a true connection or true binding between the proteins in the given condition. Additionally, an association is also presented when two proteins act antagonistically (Szklarczyk *et al.*, 2020). All of this needs to be considered when analyzing the identified proteins in the LGN subnetwork. For example, many proteins found in the LGN subnetworks that are described below are known regulators of spindle orientation and assembly but not all of the connections shown between these proteins have been proven. Thus, their biological relevance, especially in the mammary gland, is not clear and can only be validated with experiments (Snider *et al.*, 2015). Nevertheless, the generated LGN network is essential to assign putative roles to uncharacterised proteins in this context and to identify relationships between proteins that form known complexes or functional connections in other systems (e.g. cell types, spatiotemporal organization).

One surprising find in the LGN network was AGS3 (GPSM1). This protein was originally described to be expressed in testes and brain (Blumer, Chandler and Lanier, 2002). With the identification of

AGS3 in mammary cells, it can be speculated that the protein is expressed in more tissues than known so far. In fact, the protein is also expressed in the lung and kidney which supports this argument and shows that AGS3 might be more ubiquitously expressed than established so far (Nadella *et al.*, 2010; Choi *et al.*, 2016). As described in the introduction chapter (see 1.3.1.1), AGS3 shares the same structure with LGN but its function remains controversial. In one study, depletion of the protein leads to spindle orientation defects (Sanada and Tsai, 2005). However, this is in contrast to a more recent study where the protein did not localise cortically in radial glial cells of the mouse embryonic cortex, in chick embryonic spinal cord neural progenitors, and in Madin-Darby canine kidney (MDCK) cells and was not required for planar spindle orientation (Saadaoui *et al.*, 2017). It is not clear why this is in contrast to the earlier work and highlights that the mechanisms of this protein are unknown and may also be tissue-specific. With the identification of AGS3 in this study, it can be speculated that the protein was part of the wider LGN network. Thus, AGS3 may play a role in spindle orientation in the mammary epithelium. Further studies are needed to elucidate this and identify if the protein plays a role in mammary cells that has not been identified yet.

As mentioned above, many proteins identified in the LGN network are known regulators of spindle orientation and assembly. Most of the constructed connections were linked to NuMA in the network, which is not surprising because NuMA involvement in spindle assembly and orientation is established (Cleveland, 1995; Kiyomitsu and Boerner, 2021). These proteins included  $\gamma$ -tubulin and PLK1 which strongly associate with centrosomes and thus were directly connected to NuMA (Shu and Joshi, 1995; Sumara *et al.*, 2004; Lénárt *et al.*, 2007). The identification of these proteins shows that not only cortical proteins or proteins in close contact with the cortex were pulled down which would be more favoured due to the main localisation of LGN. However, LGN accumulation at spindle poles has been observed during mitosis and the protein may undergo dynamic movements between the cortex and spindle which would explain the composition of the protein network (Zheng *et al.*, 2013; Elias *et al.*, 2014). Additionally, other proteins were identified that bind to MTs and localised around the metaphase plate. For example Haus6, one of the eight subunits comprising the Augmin complex, binds and bundles MTs to control MT density within the spindle (Zhu *et al.*, 2008; Lawo *et al.*, 2009; Uehara *et al.*, 2009; David *et al.*, 2019). Another example is Ran. Besides its function to regulate the localisation of the LGN complex by forming the RanGTP gradient around chromosomes, it is also involved in MT stability and nucleation for correct spindle assembly (Goodman and Zheng, 2006; Kiyomitsu and Cheeseman, 2012; Bird, Heald and Weis, 2013). These examples indicate that the LGN network also expands inwards and towards the spindle midzone.

However, proteins associating with astral MTs plus-ends were also identified. One such protein is Clasp1. It was suggested that the protein can promote LGN cortical stabilization via astral MTs-cell cortex contact which would explain the connection between Clasp1 and NuMA in the interaction network (Bird, Heald and Weis, 2013). This further shows that the LGN network comprises proteins at the cell cortex, at chromosomes and the spindle structure itself and highlights that mitotic spindle processes are regulated at many cellular levels (di Pietro, Echard and Morin, 2016).

Based on the discussion earlier, the connections between the individual nodes in the network need to be considered carefully. For example the integration site protein 6 (Int-6) constitutes the EIF3E subunit of the eukaryotic translation initiation factor EIF3 and has been directly linked to NuMA in the network. EIF3E associate with the metaphase spindle and loss of the protein leads to spindle alterations and chromosome segregation defects which indicates that the protein may play a role in spindle assembly (Morris and Jalinot, 2005). Because STRING establishes a link when two proteins contribute together to a specific biological function, the connection to spindle assembly may explain the connection to NuMA (Szklarczyk *et al.*, 2019). Interestingly, depletion of EIF3E affects CyclinB/CDK1 kinase activity and CDK1 was recently shown to destabilize astral MTs which would also predict a link to spindle dynamics between these proteins (Morris and Jalinot, 2005; Singh *et al.*, 2021). Intriguingly, cyclin B1 (CCNB1) was identified in the LGN subnetwork. Although this theoretical link between EIF3E-CDK1-CCNB1 can be speculated from the recent findings (Morris and Jalinot, 2005; Singh *et al.*, 2021), it was not translated into the protein network and the link between the proteins was established via NuMA the PPI network. In fact, NuMA acts as a downstream target of cyclin B during mitosis (Gehmlich, Haren and Merdes, 2004). Thus, STRING may have calculated a higher interaction score between cyclin B and NuMA (0.900) and between EIF3E and NuMA (0.701) based on the available evidence and possibly established no confidence that the other two connections are biological meaningful (Szklarczyk *et al.*, 2020). Only further studies can provide insight if the connection between EIF3E and cyclin B/CDK1 is truly relevant.

All of the proteins described above play essential roles during mitosis and their depletion leads to detrimental defects in spindle assembly and -orientation (di Pietro, Echard and Morin, 2016). However, these regulators were mostly identified in non-polarised epithelia and it remains elusive if the same mechanisms occur in polarised tissues. With the identification of these proteins in this proteomics study, a first insight was provided that these proteins were present around the LGN complex in mammary epithelial cells. Thus, these regulators may also play roles in spindle regulation in the mammary epithelia. Further functional studies will be essential to discover which of these regulators truly function across epithelial cell types.

Within the group of identified proteins were polarity proteins. These included Par3 that is essential for correct spindle orientation in epithelial systems including the mammary gland (McCaffrey and Macara, 2009; Hao *et al.*, 2010). Interestingly, also mINSC that forms a complex with Par3 and LGN in the epidermis and retina was in the LGN subnetwork (Lechler and Fuchs, 2005; Zigman *et al.*, 2005). The finding of these proteins in this thesis suggests that a similar Par3/mINSC/LGN mechanisms may occur in mammary cells. In fact, a previous study showed that mINSC and LGN form a complex at the apical cortex in MaSCs and it was suggested that Par3 may be involved in this localisation (Culurgioni *et al.*, 2011). How this complex contributes to OCDs is not known. However, this new finding supports the existence of such complex in mammary cells and adds another evidence of the involvement of apical polarity factors in spindle orientation (Santoro *et al.*, 2016). Another interesting discovery is Numb within the LGN-mINSC-Par3 cluster which was found to retain in one daughter cell in asymmetrically dividing MaSCs (Tosoni *et al.*, 2015). Although a link to the polarity complex has not been shown in the mammary gland, an interaction with the Par complex was identified in MDCK cells (Wang *et al.*, 2009). Thus, a combination of Par3, mINSC and Numb may be possible. Furthermore, this identified protein trio suggests that cells displayed perpendicular oriented spindles with LGN accumulated at the apical domain. However, as discussed earlier, the generated STRING network is based on available information on protein associations and these information are mostly incomplete which leads to varying annotation details and reliability (Szklarczyk *et al.*, 2018). Therefore, the protein network does not necessarily represent the true biological state of the analysed system and it cannot be ruled out that the cells mainly oriented their mitotic spindle planar which is not supported by the STRING database. This hypothesis is based on the fact that the raw data of the MS experiments also included members of the Scribble complex and AJs (see Appendix B1). Due to the filtering process and STRNG network retrieval, these proteins were not present in the final LGN subnetworks. However, the identified E-cadherin and Scribble proteins have been shown to interact with LGN to accumulate the spindle orientation machinery at the lateral cortex to favour planar orientation of the mitotic spindle (Saadaoui *et al.*, 2014; Gloerich *et al.*, 2017; Wang *et al.*, 2018; Porter *et al.*, 2019). Therefore, two conclusions can be drawn. First, the identification of members of different polarity complexes suggests that cells were polarised at the time of GFP-LGN isolation. Second, the pool of cells used for the pulldown contained cells with mitotic spindles oriented planar and perpendicular. Thus, it is possible that the interaction with other polarity proteins was missed by STRING. In fact, more peptides were identified for Scribble than for Par3 which supports the favouring of planar spindle orientation. Furthermore, in an *in vitro* 2D culture system where cells show a flat morphology, it is more likely that the LGN complex accumulated at the lateral cortex to promote planar divisions due

to the long-axis rule and the lack of association with other cells and a 3D microenvironment (Théry *et al.*, 2007; Toyoshima and Nishida, 2007; Kapałczyńska *et al.*, 2018). Therefore, further experiments should be carried out to be confident that the observations seen in this proteomic study represent the real interactions and are reproducible.

Together, these findings show that the LGN interactome of mammary epithelial cells comprised a large number of known regulators of spindle dynamics in non-polarised cell types and although not described yet it can be speculated that these proteins play a role in regulation of spindle dynamics in the mammary gland. Furthermore, it highlights that in polarised mammary epithelial cells, polarity cues are involved, possibly in conjunction with these known regulators.

The findings so far comprised proteins with previously described functions in mitosis. However, the aim of this study was to identify novel regulators of mitotic spindle orientation. Thus, a striking finding was the identification of ANXA1, S100A11 and SAA1 which have no known function in cell division. The connection between these proteins was surprising because no literature evidence exists that LGN associates with ANXA1 or SAA1. However, SAA1 and ANXA1 are known to be involved in anti-inflammatory processes by activating G protein-coupled receptors (Sheikh and Solito, 2018; Abouelasrar Salama *et al.*, 2020). During the analysis, a connection in a G $\alpha$ i signalling pathway in the Reactome database was identified that could link LGN and ANXA1/SAA1. However, it was not possible to identify the source of this evidence. Nevertheless, since LGN associates with G $\alpha$ i subunits, it can be speculated that this created the link to these new proteins.

It is well established that ANXA1 interacts with the S100 protein family such as S100A11 which explains the connection in the protein network (Boudhraa *et al.*, 2016; Mirsaeidi *et al.*, 2016). ANXA1 is expressed in several tissues and involved in cellular processes such as proliferation, apoptosis, differentiation and migration. Consequently, dysregulation of the protein levels have been implicated in the development and progression of a large number of tumours including breast cancer (Lim and Pervaiz, 2007). Because ANXA1 has not been described to play a role in mitosis but its known involvement in important cellular processes, makes it an exciting candidate for further functional studies. Thus, the next chapter investigated the potential association of LGN and ANXA1.



**Chapter 5 ANXA1 is a novel partner of LGN:  
Characterisation of the ANXA1 and LGN binding**



## 5.1 Introduction

About 40 years ago, while searching for novel scaffolding and bridging proteins that could connect membranes and proteins, the first ANXAs were discovered. Subsequent, gene knockdown approaches and knockout mouse models have shown that these proteins function in a variety of critical cellular processes (Mirsaeidi *et al.*, 2016; Grewal, 2017). ANXA1 has become a prominent member of its family due to its widespread effects ranging from early development to maintaining the homeostatic environment, immune regulation and disease development (Sheikh and Solito, 2018). Deregulation of the protein often correlates with cancer and its role in tumour initiation and metastasis has become evident. It is also involved in other diseases which made the protein object of many different research fields including cardiology, neurology, endocrinology and oncology (Moss and Morgan, 2004; Sheikh and Solito, 2018). However, in the past most ANXA1 studies focussed on different expression levels of the protein in certain processes and diseases. More specific pathways and modes of action have only started to elucidate but only in conjunction of a diseased state. Thus, there is a lack of basic knowledge about functions and mechanisms of the protein in normal tissue homeostasis. Especially, knowledge about ANXA1 actions in epithelial systems, including in the mammary gland, is greatly missing. A few studies highlighted that the protein is expressed in myoepithelial cells of the basal compartment in the mammary epithelium and in epithelial cells of lobular acini (Schwartz-Albiez *et al.*, 1993; Ahn *et al.*, 1997; Shen *et al.*, 2006). Furthermore, one work showed that ANXA1 expression levels change during mammary gland cycles with high levels in the non-pregnant state, decreased levels during pregnancy and undetectable levels during lactation. Only after weaning when the mammary glands undergoes extensive tissue turnover to return to the original state, ANXA1 is highly expressed again (HORLICK *et al.*, 1991). This suggests that the protein may play an essential role in mammary gland morphogenesis.

To date, ANXA involvement in regulatory functions in mitosis has only been described for ANXA11. Specifically, the protein is required for midbody formation to enable completion of cytokinesis (Tomas, Futter and Moss, 2004). However, no other ANXA has been described to be involved in mitosis. In the last chapter, the LGN interaction network identified ANXA1 as a direct connector to LGN which implicates that the protein has a novel, previously unknown role in cell division and specifically in spindle orientation. In order to investigate this new link further, the aim of this chapter was to validate and characterise the binding of the two proteins. Furthermore, ANXA1 subcellular localisation during the cell cycle was investigated and co-localisation studies with LGN

and NuMA were performed. Together, these analyses gave an insight into the ANXA1 spatiotemporal behaviour during the cell cycle.

## 5.2 Results

The novel connection between LGN and ANXA1 was verified with biochemical methods. Furthermore, ANXA1 dynamics in mammary epithelial cells were characterised.

### 5.2.1 Validation of an association between ANXA1 and LGN

In the last chapter it was shown that IP of GFP-LGN precipitates ANXA1 that could be identified by MS. In order to validate this, co-IP and Western blotting was performed. As shown in figure 5.1, pulldown of GFP-LGN co-precipitated ANXA1 but isolation of GFP alone showed no detection of ANXA1.

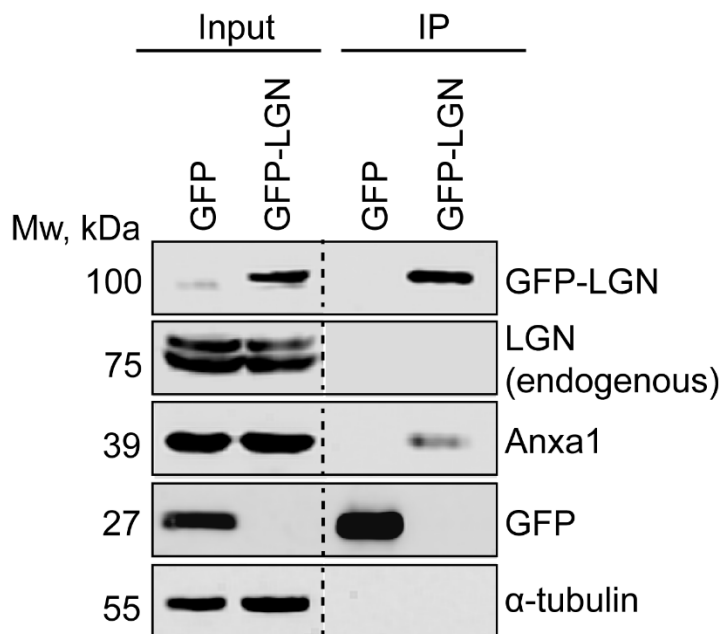


**Figure 5.1 Immunoprecipitation of ANXA1 via GFP-LGN pulldown**

*Immunoblot of affinity purification using GFP-Trap in mitotic MCF-10A cells expressing GFP-LGN or GFP. Cells were synchronized in metaphase using CDK1 inhibitor RO-3306 and proteasome inhibitor MG-132 before lysis. Endogenous LGN, GFP-LGN, GFP and ANXA1 levels were analysed in whole cell lysates (input) and in the immunoprecipitate (IP). GFP and GFP-LGN were detected using anti-GFP antibody. Endogenous LGN was detected using anti-LGN antibody.  $\alpha$ -Tubulin levels were used as a loading control.*

To further validate an association, reverse IP was performed. Due to the easy and efficient use of Nano-Traps, another system called RFP-Trap, was utilized which recognises amongst others the fluorescence protein mCherry. For this, a cell line expressing ANXA1-mCherry was generated. Furthermore, a control cell line expressing mCherry alone was established. Before performing an IP, the novel cell lines were characterised. The localisation and expression levels of the recombinant proteins were evaluated by immunofluorescence and confocal microscopy as well as Western blotting (Figure 5.2). The subcellular localisation of endogenous ANXA1, ANXA1-mCherry and mCherry was analysed in interphase and metaphase cells. ANXA1 showed a localisation at the membrane in both cell cycle stages. Furthermore, it was distributed in the cytoplasm in both phases. Similarly, Anxa1-mCherry was found at the cell membrane in interphase and metaphase as well as distributed in the cytoplasm. MCherry alone showed a localisation in the cytoplasm but not at the cell membrane. Immunoblotting revealed ANXA1-mCherry expression levels similar to endogenous ANXA1. Likewise, mCherry showed comparable levels.

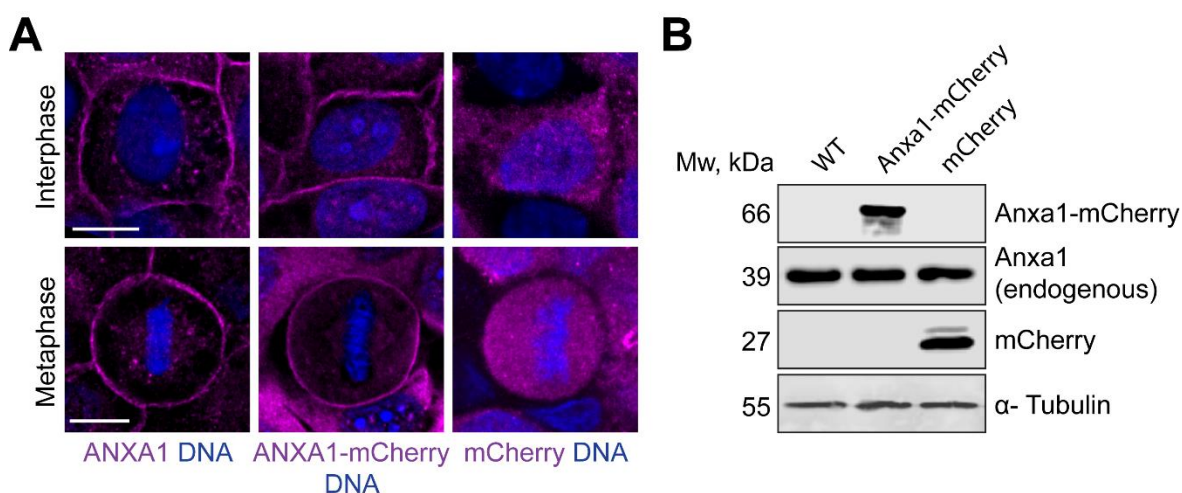


**Figure 5.2 Localisation and expression levels of ANXA1, ANXA1-mCherry and mCherry in interphase and metaphase**

(A) Representative confocal images of the subcellular localisation of ANXA1, ANXA1-mCherry and mCherry in MCF-10A cells during interphase and metaphase. Cells were fixed with methanol and stained for ANXA1 or mCherry (magenta). DNA (blue) was visualised with Hoechst 33342. Scale bar, 10  $\mu$ m. (B) Immunoblot of endogenous ANXA1, ANXA1-mCherry and mCherry levels in WT MCF-10A, MCF-10A expressing ANXA1-mCherry or mCherry. ANXA1-mCherry and mCherry were detected with anti-mCherry antibody. Endogenous ANXA1 was detected with anti-ANXA1 antibody.  $\alpha$ -Tubulin levels were used as a loading control.

After confirming that ANXA1-mCherry accumulates at the cell cortex during metaphase, a reverse IP was performed where the fusion protein was isolated. MCherry alone was pulled down as a control condition. As seen in Figure 5.3, Anxa1-mCherry and mCherry can be isolated with the RFP-Trap method. Furthermore, when Anxa1-mCherry was immunoprecipitated, one LGN band was detected in the IP but not in the mCherry control.

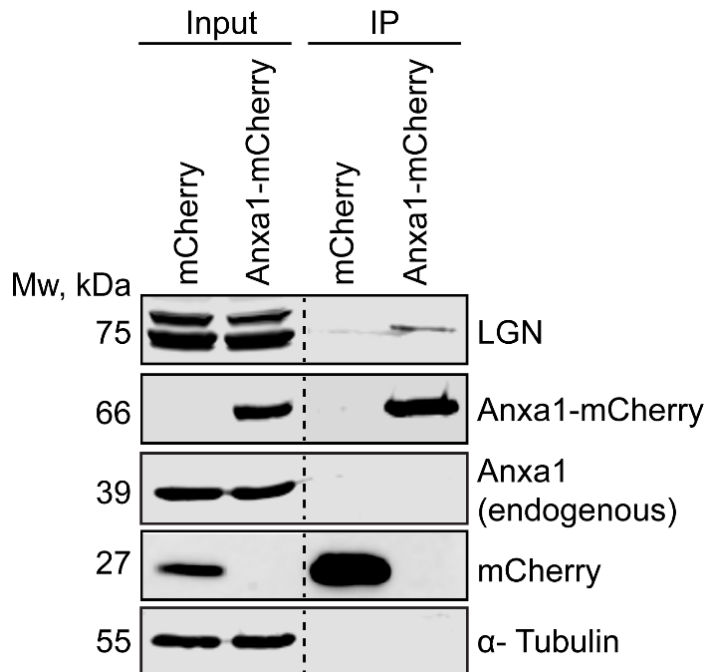


**Figure 5.3 Immunoprecipitation of LGN via ANXA1-mCherry pulldown**

*Immunoblot of affinity purification using RFP-Trap in mitotic MCF-10A cells expressing ANXA1-mCherry or mCherry alone. Cells were synchronized in metaphase using CDK1 inhibitor RO-3306 and proteasome inhibitor MG-132 before lysis. Endogenous ANXA1, ANXA1-mCherry, mCherry and LGN levels were analysed in whole cell lysates (input) and in the immunoprecipitate (IP). ANXA1-mCherry and mCherry were detected with anti-mCherry antibody. Endogenous ANXA1 was detected with anti-ANXA1 (rabbit) antibody  $\alpha$ -Tubulin levels were used as a loading control.*

Finally, PLA technology was used to visualise an association between LGN and ANXA1 in GFP-LGN cells. When antibodies against GFP and ANXA1 were applied, PLA signals were identified in interphase and metaphase but with more signal in mitotic cells indicating that ANXA1 and LGN showed close proximity. The fluorescent spots in metaphase overlapped with cortical GFP-LGN (Figure 5.4, A). Furthermore, a positive control detecting association between GFP-LGN and LGN showed signals in the cytoplasm in interphase and fluorescent spots specifically at the lateral cortex in metaphase (Figure 5.4, B). No signals were detected in the negative control (Figure 5.4, C).

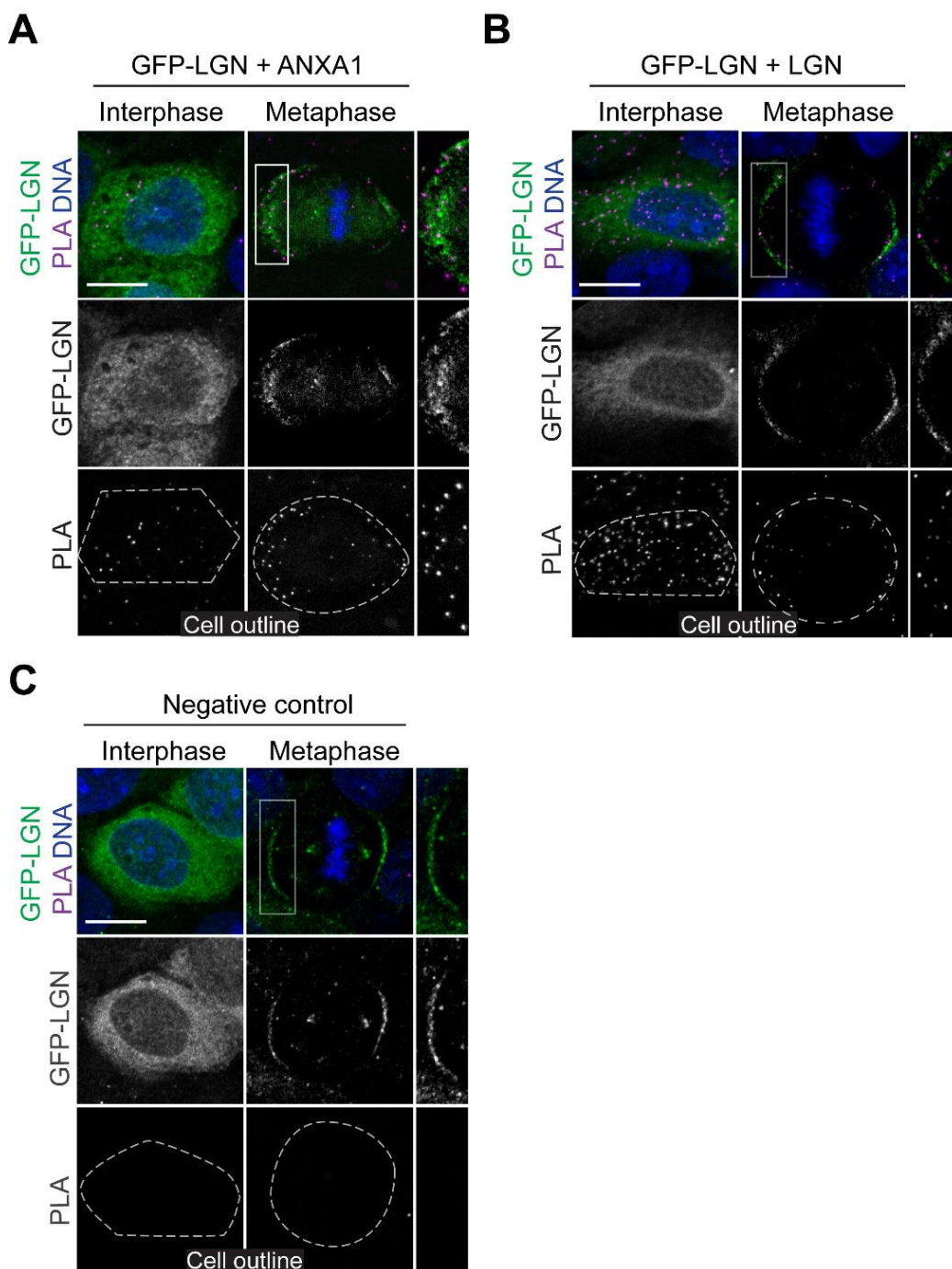


**Figure 5.4** In situ detection of an LGN and ANXA1 interaction in metaphase and interphase cells  
*Figure Representative confocal images of sample and control conditions of the proximity ligation assay (PLA) in interphase and metaphase MCF-10A cells expressing GFP-LGN (green). Cells were fixed with methanol. DNA (blue) was visualised with DAPI. PLA signals are shown in magenta. Insets on the right show magnified images of the framed region. White dashed lines indicate cell contours. Scale bars, 10  $\mu$ m. (A) GFP-LGN and ANXA1 PLA. Anti-GFP and anti-ANXA1 antibodies were used for the assay. (B) Positive control, GFP-LGN and LGN PLA. Anti-GFP and anti-LGN antibodies were used for the assay. (C) Negative control. Only anti-ANXA1 antibody was used.*

### 5.2.2 ANXA1 shows a cell-cycle dependent localisation

ANXA1 was characterised in WT MCF-10A cells. Immunofluorescence and confocal microscopy detected ANXA1 along the cell cortex and in the cytoplasm in every stage of the cell cycle. Interestingly, the protein was not uniformly distributed at the cell cortex or inside the cells. Although, it localised at the cell cortex in all stages, the accumulation of ANXA1 varied. During interphase, ANXA1 distributed everywhere at the cortex. With entering mitosis (prophase), the protein still showed a cortical localisation but the accumulation changed and it was less evenly distributed in prophase. However, in prometaphase the localisation changed more drastically and less protein localised at the lateral cortex above the spindle poles compared to the central cortex. From metaphase to cytokinesis, ANXA1 showed a more uniform distribution at the cortex as seen in interphase. Its location in the cytoplasm changed with entering mitosis. During interphase, ANXA1 evenly distributed inside the cell but was excluded from areas close to the cell cortex. With entering mitosis, the protein strongly accumulated around separated centrosomes where the mitotic spindle began to assemble. From prometaphase to anaphase, ANXA1 remained specifically localised around the mitotic spindle and DNA and was excluded from other areas in the cytoplasm. When the spindle started to disassemble (telophase), ANXA1 was still located around microtubules and separated chromosomes which continued into cytokinesis (Figure 5.6).

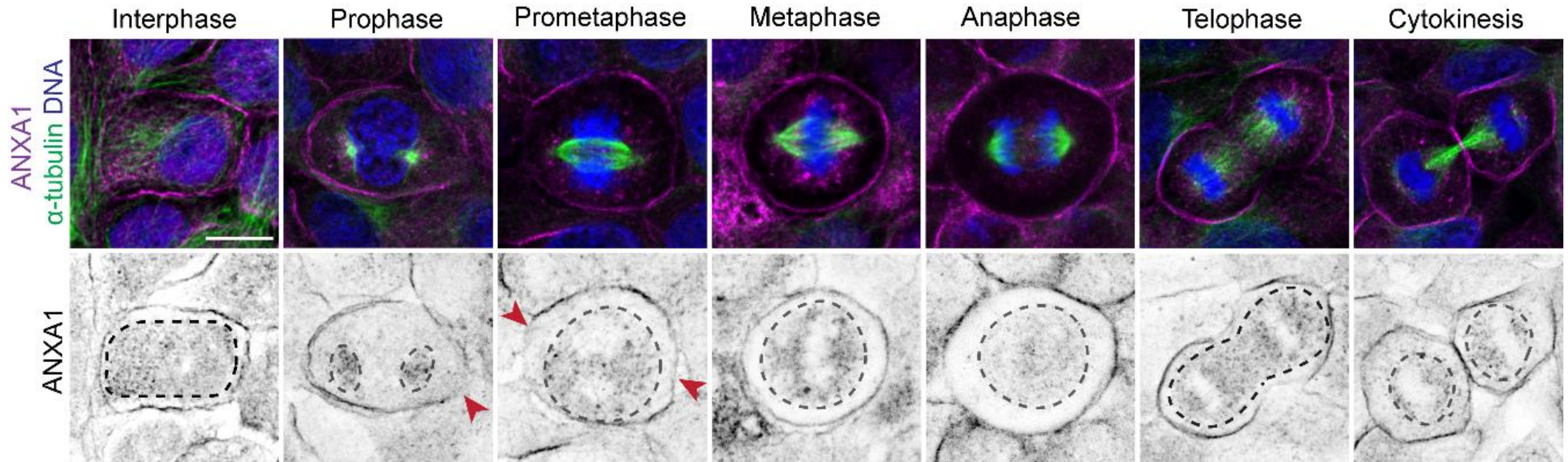


**Figure 5.5 Distinct subcellular localisation of ANXA1 during the cell cycle**

*Representative confocal images of the localisation of endogenous ANXA1 in WT MCF-10A cells during the indicated stages of the cell cycle. Cells were fixed with methanol and stained for ANXA1 (magenta) and  $\alpha$ -tubulin (green). DNA (blue) was visualised with Hoechst 33342. Dashed lines indicate cytoplasmic ANXA1 distribution. Red arrowheads point to varying ANXA1 levels at the cell cortex. Scale bar, 10  $\mu$ m.*

### 5.2.3 ANXA1 localises with LGN to the cell cortex during mitosis

The dynamics of ANXA1 and LGN were analysed in different cell lines. In MCF-10A cells expressing GFP-LGN, both proteins showed a cell-cycle dependent subcellular localisation. ANXA1 localisation resembled the observation in WT cells (see 5.2.3). Similarly, GFP-LGN cellular distribution mimicked what was observed in time-lapse imaging in chapter 3 (see 3.2.1). ANXA1 distributed evenly at the cortex and cytoplasm during interphase, whereas GFP-LGN was only diffuse in the cytoplasm. After start of mitosis (prophase), ANXA1 accumulated at specific cortical areas and around DNA and GFP-LGN was distributed mainly in the cytoplasm but also started to accumulate at the cortex. Interestingly, cortical areas where ANXA1 localised less, showed more GFP-LGN signal. This became more evident in prometaphase where GFP-LGN strongly accumulated at the lateral but not at the central cortex. In contrast, ANXA1 localised mainly centrally and only very low levels were seen at the lateral cortex. In metaphase cells when the chromosome plate was not in the middle of the cell (offcentered), ANXA1 strongly accumulated at the cortex closest to the DNA. GFP-LGN localised on the opposite cortex furthest away from the DNA and where ANXA1 levels were lower. In metaphase cells where the chromosome plate was centred, ANXA1 showed a more even distribution at the cortex and GFP-LGN was localised in the typical crescent shape at the lateral membrane. During anaphase and cytokinesis, ANXA1 remained evenly localised at the cortex and around DNA, whereas GFP-LGN was localised at the lateral cortex during anaphase but redistributed to the cytoplasm during cytokinesis (Figure 5.7, A).

The localisation changes of ANXA1 and GFP-LGN were quantified by determining the fluorescence intensity profiles along the cell cortex (Figure 5.7, B-C). Using a custom macro in Fiji, the maximum pixel intensity was measured at 280 positions at the cortex starting at position 0 at the central cortex and moving clockwise (Figure 5.7, D). In prometaphase cells, GFP-LGN showed intensity peaks at lateral sites and less signal at the central cortex. In contrast, ANXA1 intensity peaks were at the central cortex and less signal was detected at lateral areas. In centred metaphase cells, GFP-LGN showed a similar intensity plot as in prometaphase cells where strong signals were detected at the lateral cortex and low intensities at the central cortex. Intensities for ANXA1 changed compared to prometaphase cells and the peaks at the central cortex were less high and almost the same as lateral intensities.

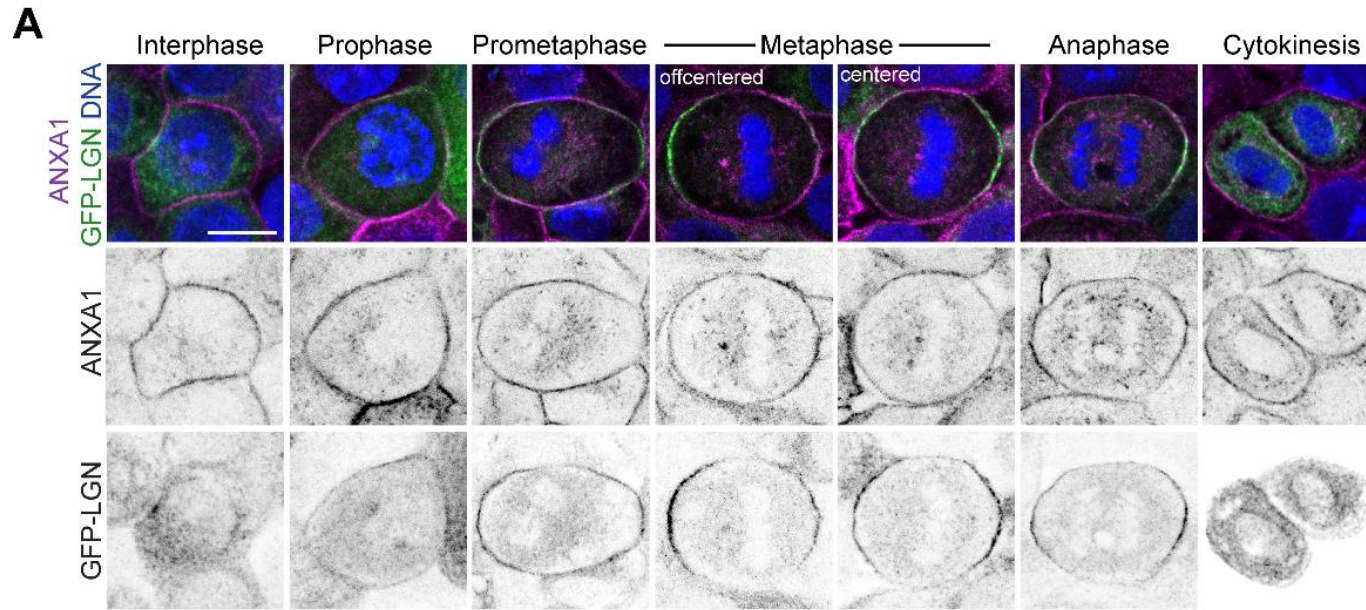
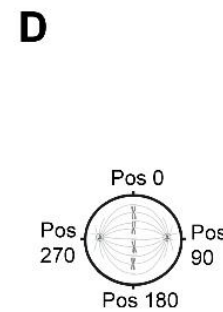
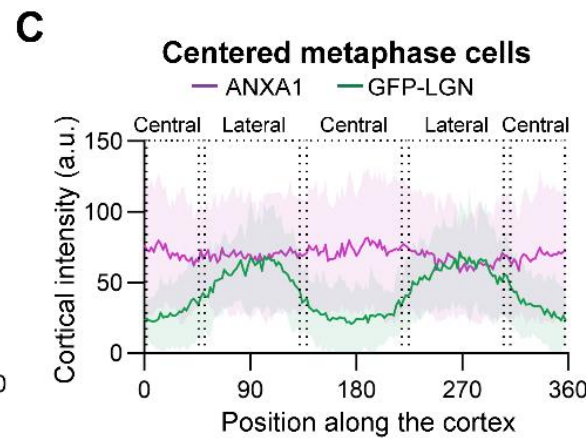
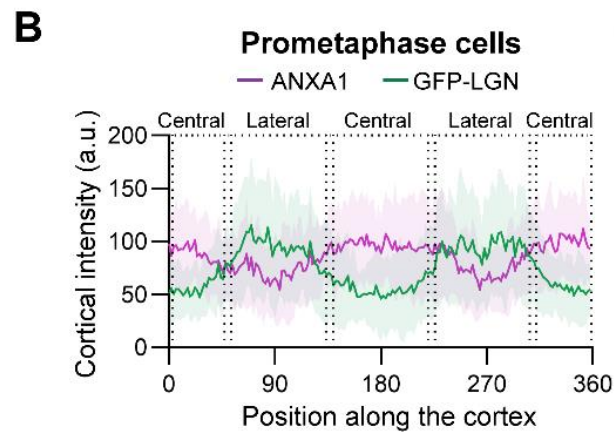


**Figure 5.6 Co-localisation dynamics of GFP-LGN and ANXA1 during the cell cycle**

(A) Representative confocal images of the co-localisation of endogenous ANXA1 with GFP-LGN in MCF-10A cells expressing GFP-LGN (green) analysed at the indicated stages of the cell cycle. Cells were fixed with methanol and stained for ANXA1 (magenta). DNA (blue) was visualised with Hoechst 33342. Scale bar, 10  $\mu$ m. (B-C) Cortical fluorescence intensity profiles of GFP-LGN and ANXA1 from prometaphase cells (C, n=23 cells) and metaphase cells (D, n=36 cells). Graphs show the average for n cells  $\pm$  SD. (D) Schematic illustrating the positions along the cell cortex corresponding to coordinates in



To evaluate co-localisation dynamics of endogenous LGN with ANXA1, the MCF-10A cell line expressing ANXA1-mCherry was utilized. Immunofluorescence and confocal imaging revealed a similar subcellular localisation as seen before. ANXA1-mCherry distributed in the cytoplasm with exclusion near the cortex in interphase and underwent a localisation change during mitosis where it accumulated around DNA. The protein localised at the cell cortex in all stages of the cell cycle but with a more distinct localisation in prometaphase where the protein strongly accumulated at the central area but less at the lateral cortex. LGN was diffuse in the cytoplasm during interphase. Upon entry of mitosis, the protein changed localisation and started to accumulate at the cortex in prometaphase. Co-localisation with ANXA1 revealed that cortical LGN was found in areas where ANXA1-mCherry was low and LGN was excluded from the central cortex where ANXA1-mCherry levels were higher. In metaphase where the chromosome plate was centred, LGN localised in a crescent shape at the lateral cortex and ANXA1-mCherry distributed equally at the cortex. LGN redistributed to the cytoplasm after anaphase whereas ANXA1-mCherry remained at the cortex.

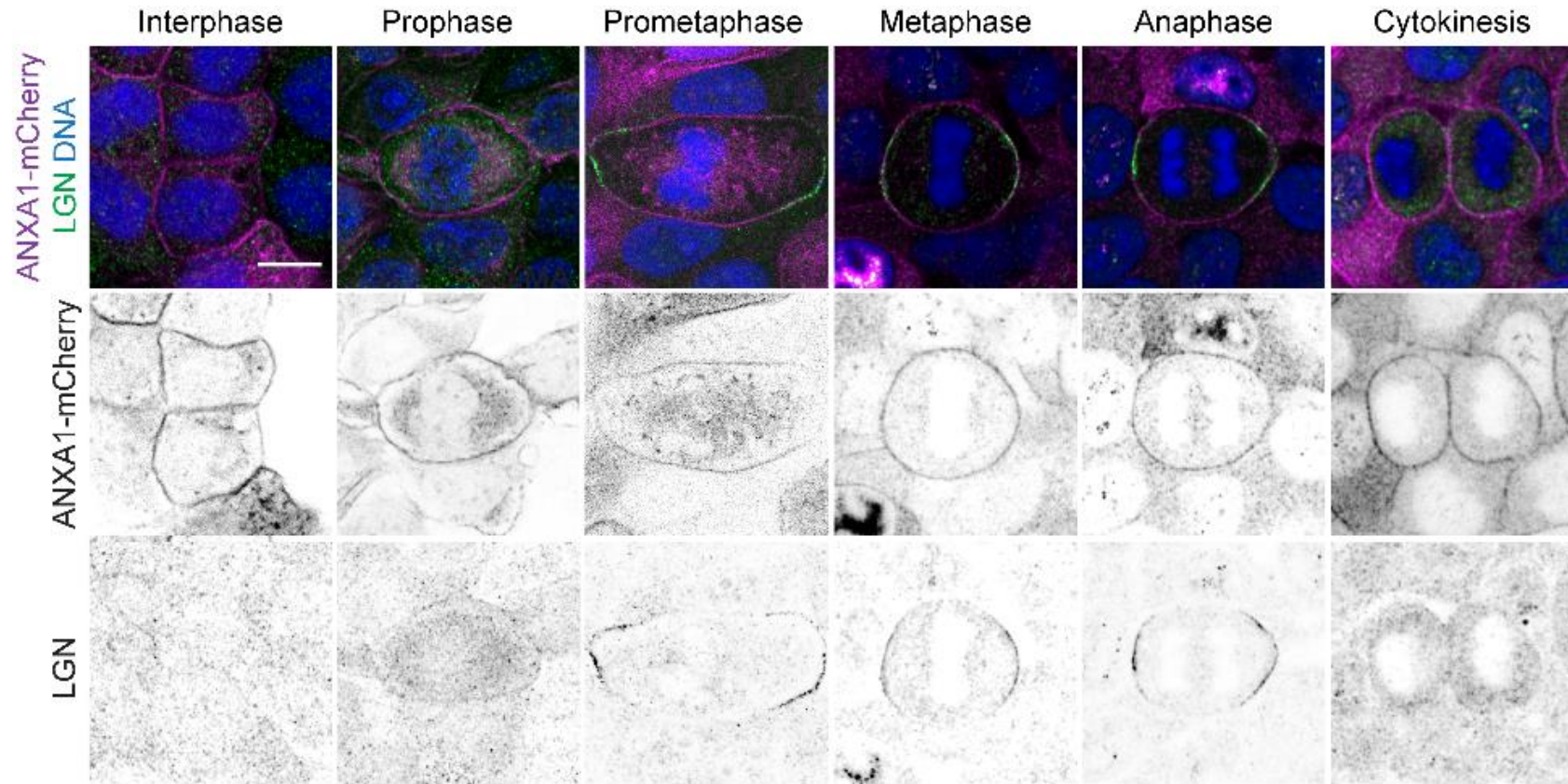


**Figure 5.7 Co-localisation dynamics of ANXA1-mCherry and LGN during the cell cycle**

*Representative confocal images of the co-localisation of endogenous LGN with ANXA1-mCherry in MCF-10A cells expressing ANXA1-mCherry (magenta) analysed at the indicated stages of the cell cycle. Cells were fixed with methanol and stained for LGN (green). DNA (blue) was visualised with Hoechst 33342. Scale bar, 10 μm.*

Lastly, co-localisation of endogenous ANXA1 with endogenous LGN or NuMA was analysed. The antibody combination for LGN and NuMA only allowed TCA fixation to detect the proteins. However, the staining method did not show specific localisations of the proteins in all cell cycle stages and therefore only metaphase cells were imaged. LGN accumulated in a crescent shape at the lateral cortex and ANXA1 showed a uniform distribution along the cortex and around the mitotic spindle/metaphase plate (Figure 5.9, A). Co-localisation with NuMA revealed a similar distribution where ANXA1 accumulated everywhere at the cortex and around the mitotic spindle/metaphase plate. NuMA localised as a lateral crescent and at spindle poles (Figure 5.9, B).

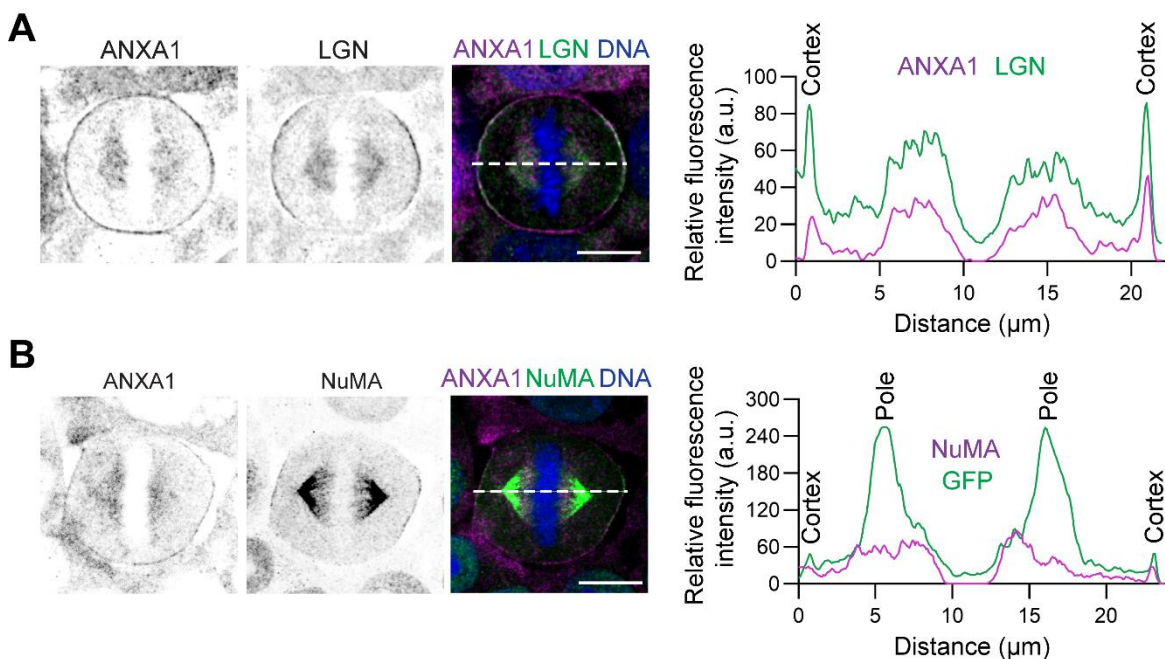


**Figure 5.8 Co-localisation of ANXA1 with endogenous LGN and NuMA**

(A-B) Left: Representative confocal image of the co-localisation of endogenous ANXA1 with endogenous LGN (A) and NuMA (B) in WT MCF-10A cells at metaphase stage. Cells were fixed with 10 % TCA and stained for ANXA1 (magenta) and LGN or NuMA (green). DNA (blue) was visualised with Hoechst 33342. White dotted lines indicate measured fluorescence intensity profiles. Scale bar, 10  $\mu\text{m}$ . Right: Line-scan profiles of fluorescence intensity corresponding to images on the left showing distribution of indicated proteins.

Together, these experiments showed that ANXA1 accumulated at the cell cortex during the cell cycle with an enriched localisation at the central cortex during prometaphase. Furthermore, the protein showed a distinct distribution around the mitotic spindle and DNA during mitosis. Co-localisation studies of ANXA1 and LGN revealed specific accumulation patterns of the proteins during prometaphase but an overlapping localisation at the lateral cortex during metaphase when the chromosome plate was aligned in the centre of the cell. Similar to LGN, NuMA and ANXA1 co-localised during metaphase at the lateral cortex.

### **5.3 Discussion**

The study of PPIs is critical to understand the biology of certain systems. One big challenge in this is the recognition of a specific association of a protein with the isolated protein-of-interest within the huge list of identified interactions. Thus, it is essential to employ different methods to assess the specificity of an interaction (Miteva, Budayeva and Cristea, 2013). This includes biochemical methods such as co-IP and Western blotting, interaction assays as well as co-localisation studies using immunofluorescence techniques (Free, Hazelwood and Sibley, 2009). Since ANXA1 was predicted to directly associate with LGN in the STRING interaction network but no experimental evidence was available, this putative association had to be validated using biochemical methods. All of the used techniques helped to validate if the newly identified protein can be considered physiologically relevant or if this novel interaction is an artefact or non-specific. Furthermore, it gave for the first time an insight into ANXA1 dynamics in mammary epithelial cells.

#### **5.3.1 ANXA1 and LGN associate at the cell cortex during metaphase**

One important method to reduce the number of unspecific protein associations is the use of negative controls in the same MS experiment. This is critical to eliminate protein hits that bind to the resin matrix or antibody used in the IP. Therefore, the identification of several peptides for one protein in the sample but none in the control condition increases the possibility that the candidate is specifically interacting and not a false-positive hit (Free, Hazelwood and Sibley, 2009). In this study, ANXA1 was not identified in the control condition which was the first indication that the protein is an abundant component within the LGN interactome and more likely an interactor within the spindle orientation machinery. However, it was suggested that interacting protein should be identified in at least two independent experiments to be considered significantly valid (Free,

Hazelwood and Sibley, 2009). Thus, co-IPs were performed and it could be validated that the isolation of GFP-LGN also immunoprecipitated ANXA1. Furthermore, reverse IP was conducted to isolate LGN as a prey by using the newly identified protein ANXA1 as a bait. Interestingly, only one LGN protein band was pulled down. Since it is not clear whether the two LGN protein bands always observed in this work represent phosphorylated and non-phosphorylated protein or the LGN homologue AGS3, it cannot be concluded why only one protein band was detected. It be interesting to investigate further whether ANXA1 associates with phosphorylated or non-phosphorylated LGN or specifically with LGN and not AGS3. Nevertheless, this approach was an excellent method to analyse the ANXA1-LGN association. This reciprocal IP approach has been used in the past to validate interactions within mitotic protein complexes performed in a large-scale proteomics study. The authors could show that from 728 interactions around 79 % of pair-wise interactions had similar localisation and were reciprocally confirmed which highlights that this approach can be used to validate interactions and identify novel protein complexes (Hutchins *et al.*, 2010). Reciprocal IP can be challenging due to the possibility of low abundance of bait or prey proteins and this approach cannot distinguish between direct and indirect interactions. However, it constitutes a valuable tool to support predicted protein associations within the analysed system and could confirm in this study that there is at least an indirect binding between ANXA1 and LGN (Miteva, Budayeva and Cristea, 2013). With the Co-IP approach, it could be shown that the proteins are associated in mitotic MCF-10A cells. However, further confirmation via visual interaction methods can help for validation and specifically provide information about the localisation of the putative interaction (Gullberg and Andersson, 2010). Thus, PLA was used to identify the *in situ* localisation of the ANXA1-LGN association. This assay detects two associated protein when their distance is less than 40 nm. This is not small enough to proof a physical interaction but shows that these proteins are in very close proximity (Alsemarz, Lasko and Fagotto, 2018). PLA signals were detected in the cytoplasm of interphase cells where both proteins are localised during this specific cell cycle stage. Furthermore, detection of close proximity of the proteins at the cell cortex in mitotic cells confirmed a specific association at the subcellular localisation of LGN during metaphase. Immunofluorescence analysis of the subcellular localisation of ANXA1 revealed that the protein is also found at the cell cortex during mitosis. Thus, both proteins shared the same spatiotemporal localisation and an association was possible. It is unlikely that these signals were non-specific because the negative condition confirmed that probes do not generate signals in the absence of specific antibody labelling. PLA technology combines dual recognition of two antibodies targeting specific proteins and uses a split reporter approach (PLA probes). Thus, the method is highly selective and sensitive and cross-reactivity as well as non-specific detection is vastly minimized (Weibrecht *et al.*, 2010). Therefore,

it can be concluded that the PLA technique combined with the co-IP experiments validated that ANXA1 is part of the LGN interactome during metaphase and showed that the two proteins at least indirectly associate with each other allowing for further characterisation of ANXA1 and its implication in mitotic spindle orientation.

### **5.3.2 ANXA1 displays a distinct subcellular localisation during the cell cycle**

Functions of proteins are determined by their subcellular localisation. Therefore, it is essential to explore the spatiotemporal dynamics of a protein as part of the characterisation of the novel candidate (Pan *et al.*, 2021). Imaging techniques including immunofluorescence constitute a widely used tool to investigate the localisation of proteins and was also used in this study to investigate the subcellular localisation of ANXA1 during the cell cycle. As part of the ANXA super family, the protein was described to bind to phospholipids and associates with cellular membranes (Gerke and Moss, 2002). Specifically, it has been shown to localise to the plasma membrane in macrophages and HeLa cells (Diakonova *et al.*, 1997; Rescher, Zobiack and Gerke, 2000; Radke *et al.*, 2004). These studies investigated ANXA1 localisation in interphase cells and found that the protein was not uniformly distributed along the cortex. This is in accordance with the observation in MCF-10A cells highlighting that the protein might exhibit similar localisation patterns in different cell types. However, no study to date has shown the subcellular localisation of ANXA1 during mitosis. Only the work by Tomas and Moss revealed the cellular distribution of a member of the ANXA family during cell division. The group showed that ANXA11 accumulates within the mitotic spindle during cell division and is recruited to the midbody during late telophase in skin epithelial cells (Tomas and Moss, 2003; Tomas, Futter and Moss, 2004). Interestingly, the accumulation around the spindle resembles the localisation of ANXA1 observed in this study which highlights that the protein may have similar functions as its family member. Although no literature exists about this localisation, several hypotheses may explain the accumulation around the spindle. The vesicular distribution of ANXA1 may be one aspect. The protein associates with the endoplasmic reticulum (ER) and endosomal membranes, specifically early endosomes where it is involved in vesicular trafficking (Seemann *et al.*, 1996; Diakonova *et al.*, 1997; Rescher, Zobiack and Gerke, 2000). It has been shown that endosomes start to concentrate around the spindle poles and central spindle with entering mitosis (Takatsu *et al.*, 2013; Miserey-Lenkei and Colombo, 2016). Thus, it is possible that the localisation of ANXA1 around the mitotic spindle is linked to the accumulation of endosomes around these structures. However, no evidence exists for this and further experiments are needed to perform co-localisation studies with ER and endosomal markers to verify that ANXA1 associates

with such structures in mammary epithelial cells. Another explanation may be its binding to F-actin. Several studies showed that the protein binds and bundles F-actin in vitro (Glenney, Tack and Powell, 1987; Schlaepfer and Haigler, 1987). Furthermore, it co-localises with cortical actin in interphase cells (Campos-Gonzalez, Kanemitsu and Boynton, 1990; Diakonova *et al.*, 1997). Several studies have suggested that F-actin localises around the spindle (Farina *et al.*, 2016; Inoue *et al.*, 2019; Kita *et al.*, 2019) and this was also observed in MCF-10A cells (unpublished data, Elias lab). Therefore, it might be possible that ANXA1 and F-actin associate around spindle structures.

In conclusion, the specific localisation of ANXA1 in mammary epithelial cells showed for the first time the dynamics of the protein during the cell cycle. It will be interesting to investigate this further to specifically address the spatiotemporal localisation in vesicular structures and at the mitotic spindle.

### 5.3.3 The distribution of ANXA1 and LGN at the cortex is spatiotemporally regulated

Cells control protein localisation to regulate biological processes. Thus, proteins must be precisely targeted to specific subcellular regions to enable their correct function (Borner, 2020). The identification of an ANXA1/LGN connection via co-IP provided the first evidence that the proteins share the same localisation during metaphase. Subsequent biochemical methods validated an association between the proteins at the lateral cortex. Another approach in the spatiotemporal analysis of two proteins is imaging techniques to directly visualise the proteins' subcellular localisation. These methods revealed specific distribution patterns for ANXA1 and LGN where the proteins showed a mutually exclusive localisation at the cell cortex. It is known that regulatory mechanisms exist to restrict LGN to specific cortical regions to establish the spindle orientation axis. For example, the protein ABL1 suppresses LGN accumulation at certain cortical regions to restrict LGN accumulation at apical sites in the mouse epidermis (Matsumura *et al.*, 2012). Similarly, high levels of a RanGTP gradient around chromosomes restrict LGN to two lateral cortical crescents (Kiyomitsu and Cheeseman, 2012). It is possible that ANXA1 exerts similar mechanisms on LGN at the cortex during prometaphase. Higher levels of the protein were observed at the central cortex and only low signals were seen at lateral sites. Thus, it can be speculated that high ANXA1 levels do not permit accumulation of LGN at the central cortex. A similar dynamic is known for SAPCD2 (Chiu *et al.*, 2016). The protein accumulates at the apical cortex to exclude LGN from this cortical localisation in epithelial cells to promote planar orientation of the spindle. Interestingly, SAPCD2 was identified in a proteomics approach where it was shown to bind to LGN. It was suggested, that SAPCD2 binding reduces the affinity of LGN to G $\alpha$ i, thereby preventing the binding of LGN at the

apical cortex (Chiu *et al.*, 2016). It might be possible that high ANXA1 levels also block the binding of LGN to Gai at the central cortex and therefore, allowing accumulation of LGN at the lateral cortex (Figure 5.10, A). However, further studies will be needed to proof this hypothesis.

Because ANXA1 was identified to associate with LGN, the remaining questions exists how the protein can simultaneously bind to LGN during metaphase but also exclude it from cortical areas during prometaphase. It is possible that once LGN accumulates at the lateral cortex ANXA1 contributes to the stabilisation of the protein. This is known from another regulator. The protein Afadin accumulates uniformly around the cell cortex and co-localises with LGN in a crescent shape above spindle poles. It was suggested that the protein binds to LGN to recruit it to the cortex where LGN then associates with Gai subunits (Carminati *et al.*, 2016). Thus, Afadin is not specifically involved in restricting LGN to certain cortical areas but it supports the anchoring and stabilization of the protein. It is possible that a more uniform ANXA1 distribution along the cell cortex during metaphase exerts similar mechanisms with LGN at lateral sites. This suggests that the protein is no longer restricting LGN to the lateral cortex but rather stabilizing it which would then allow the recruitment of NuMA (Figure 5.10, B). Experiments enabling the dissection of a temporal regulation of the accumulation of LGN via ANXA1 during prometaphase and metaphase will be essential to elucidate how ANXA1 promotes the specific accumulation of LGN during mitosis. Nevertheless, the co-localisation experiments showed that ANXA1 and LGN exhibit a spatiotemporal regulated cortical localisation during the cell cycle where ANXA1 may be a potential regulator of the polarised localisation of LGN. To address this, the next chapter investigated how loss of ANXA1 from MCF-10A cells influences the localisation of the spindle orientation machinery.

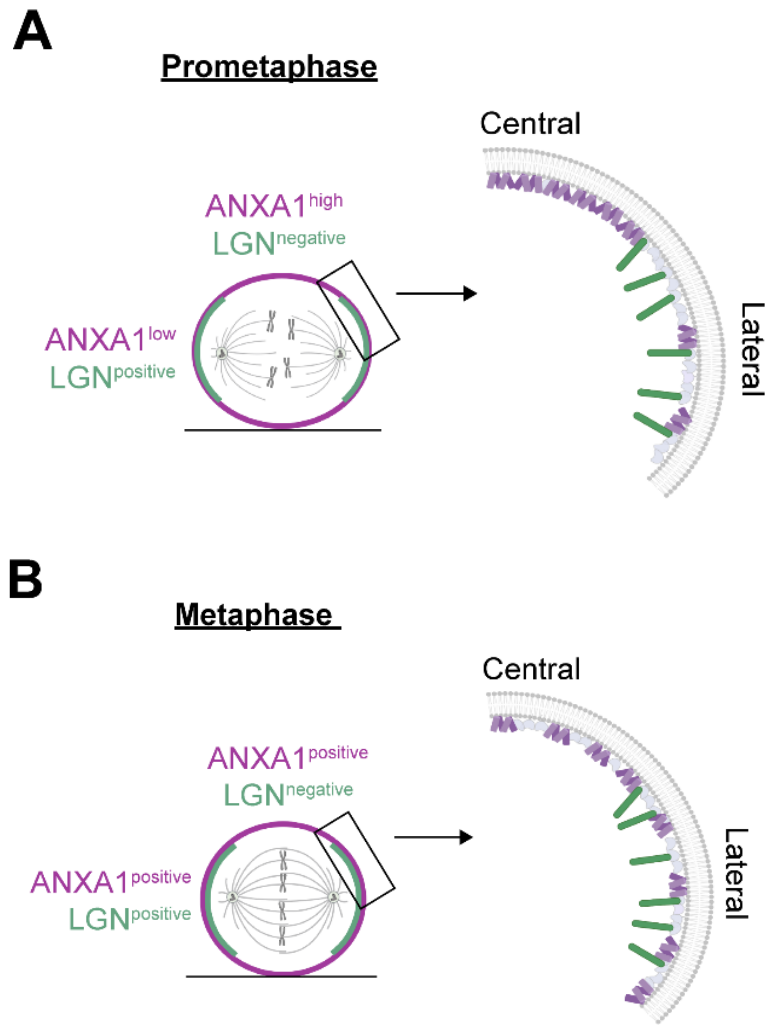


**Figure 5.9 Schematic of ANXA1 and LGN cortical dynamics during mitosis**

(A) During prometaphase, high levels of ANXA1 localise to the central cortex. In contrast, only low levels distribute at lateral sites. The strong accumulation of ANXA1 restricts LGN distribution to the lateral cortex. (B) During metaphase, ANXA1 is uniformly distributed along the cortex, whereas LGN is still localised to the lateral cortex only. It is possible that ANXA1 stabilizes LGN at the cortex by binding to the protein at lateral sites.

## **Chapter 6 ANXA1 coordinates the polarised cortical localisation of LGN during mitosis**



## 6.1 Introduction

It is widely established that the core Gai/LGN/NuMA ternary complex is essential for accurate spindle orientation (di Pietro, Echard and Morin, 2016). Studies in HeLa cells and keratinocytes showed that loss of Gai results in reduced accumulation of NuMA or the dynein/dynactin complex at the cell cortex (Woodard *et al.*, 2010; Kotak, Busso and Gönczy, 2014). Similarly, LGN depletion affects cortical NuMA and dynein/dynactin levels and NuMA loss impairs dynein/dynactin cortical localisation (Seldin *et al.*, 2013; Kotak, Busso and Gönczy, 2014). Studies in tissues showed similar effects where loss of LGN leads to aberrant localisation of NuMA and dynein/dynactin (Morin, Jaouen and Durbec, 2007; Konno *et al.*, 2008; Zheng *et al.*, 2010). This highlights that loss of one of the core proteins of the ternary complex results in aberrant recruitment of their downstream interactors which affects recruitment of force generators. Subsequently, this causes spindle orientation defects which can result in improper tissue morphogenesis.

Not only is it essential, that the entire ternary complex is recruited to the cell cortex, its distinct position also determines the orientation of division. Therefore, the spindle orientation machinery adopts a polarised cortical localisation (Nakajima, 2018). Multiple proteins have been implicated in this specific recruitment. These include members of polarity complexes, junctional adhesion proteins, scaffolds or other proteins (described in chapter 1.3.2.2 and 1.3.2.3). In the past, genetic and RNAi interference (RNAi)-based functional genomic screens have led to the identification of such regulators and mechanism of mitotic spindle orientation. RNAi is a biological process that induces silencing of post-translational gene expression in response to introduction of double-stranded RNA (dsRNA) into a cell. This RNA targets complementary mRNA for degradation which results in highly specific silencing of genes (Fire *et al.*, 1998; Mocellin and Provenzano, 2004; Dana *et al.*, 2017). DsRNAs that are 21-23 nucleotides long are termed siRNAs. These constructs are widely used in research to induce a temporary gene expression knockdown against a specific target to study the effects of loss-of-function mutation. Thus, siRNA technology provides an excellent tool to characterise the function of a specific protein (Duxbury and Whang, 2004).

In the last chapter, a spatiotemporal localisation of ANXA1 and LGN was shown at the cell cortex during mitosis. This suggests that ANXA1 may be involved in the polarised accumulation of the spindle orientation machinery. Therefore, the aim of this chapter was to elucidate the function of ANXA1 in mitosis and its involvement in the dynamics of the spindle orientation machinery. For this, siRNA technology was used to suppress endogenous ANXA1 protein levels and study the effect

on localisation and recruitment of the spindle orientation machinery. Furthermore, siRNA targeting *LGN* was utilized to investigate the cortical localisation of ANXA1. Overall, these analyses described the implication of ANXA1 in the recruitment of the spindle orientation machinery to the lateral cortex during mitosis.

## 6.2 Results

*ANXA1* or *LGN* were transiently silenced in MCF-10A cells expressing GFP-LGN or WT cells. Reduced protein levels were validated using Western blotting. Time-lapse microscopy or immunofluorescence and confocal microscopy was performed to analyse the localisation of the spindle orientation machinery or ANXA1.

### 6.2.1 siRNA targeting *ANXA1* results in knockdown of the protein

Protein levels of ANXA1 and LGN were analysed when cells were treated with si-Control or si-ANXA1#1/2. ANXA1 levels were normalised to the control and were significantly reduced by more than 50 % in cells transfected with si-ANXA1#1 or si-ANXA1#2 compared to cells transfected with si-Control (Figure 6.1, A-B). LGN levels did not change in knockdown conditions compared to the control (Figure 6.1, A-C).

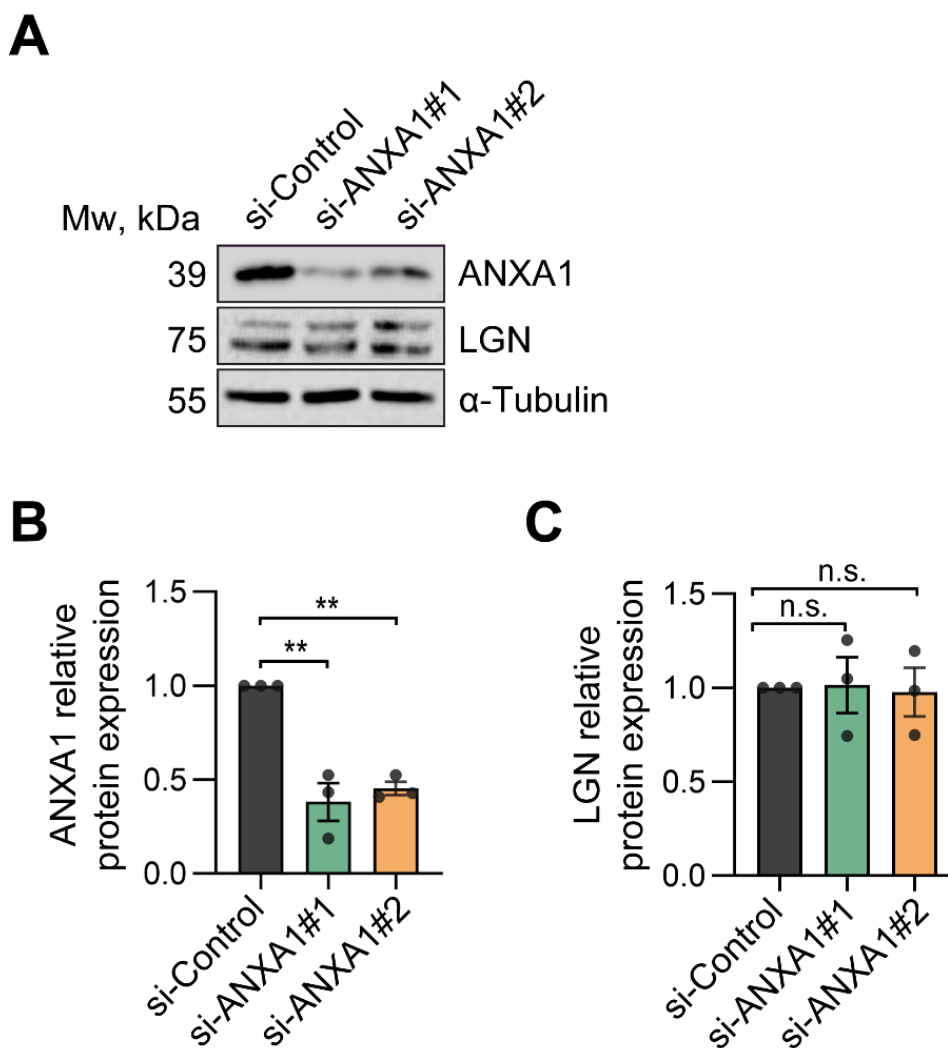


**Figure 6.1 Protein levels after ANXA1 knockdown using siRNA**

(A) Immunoblot of ANXA1 and LGN levels in cells after ANXA1 depletion. Cells were transfected with si-Control or two different siRNA constructs targeting ANXA1 (si-ANXA1#1, si-ANXA1#2) and analysed 72 h later.  $\alpha$ -Tubulin was used as a loading control. (B) Quantification of normalized ANXA1 protein levels in cells transfected with si-Control, siANXA1#1 or siANXA1#2. (C) Quantification of normalized LGN protein levels in cells transfected with si-Control, siANXA1#1 or siANXA1#2. Data represent means (black dots)  $\pm$  SEM from three independent experiments. Student's t-test; \*\* $p \leq 0.01$ , \*\*\* $p \leq 0.001$ , n.s. no significant difference.

### 6.2.2 Loss of ANXA1 leads to misplacement of GFP-LGN during mitosis

Time-lapse microscopy of MCF-10A expressing GFP-LGN was performed to determine how depletion of ANXA1 affects the cortical localisation dynamics of GFP-LGN during mitosis. For this, cells treated with si-Control and siANXA1#1 were analysed. In all conditions, the protein started to accumulate at the cortex during prometaphase. However, significant differences became obvious during metaphase. In si-Control, GFP-LGN accumulated mainly bilaterally (77.34 %) in the typical crescent shape above the spindle poles and remained localised until telophase. Around 23 % of cells showed a central or circumferential localisation (Figure 6.2, A; C). In si-ANXA1#1, the percentage of GFP-LGN bilateral localisation decreased to 21 % and different phenotypes were detected. The most prominent localisation showed for more than half of the cells a central accumulation near chromosomes instead of only at the lateral cortex. Another phenotype showed a circumferential localisation where the protein distributed everywhere at the cell cortex. Lastly, GFP-LGN was also localised unilaterally on one side of the cell from metaphase to telophase (Figure 6.2, A-C). Overall, there was a significant increase in abnormal localisation of GFP-LGN when ANXA1 was depleted with 78 % showing aberrant placement and only a small proportion exhibiting normal bilateral accumulation. Compared to the control condition where ANXA1 was present, the proportions were reversed and around 77 % of cells showed bilateral localisation and only a small percentage displayed aberrant localisation (Figure 6.2, D).

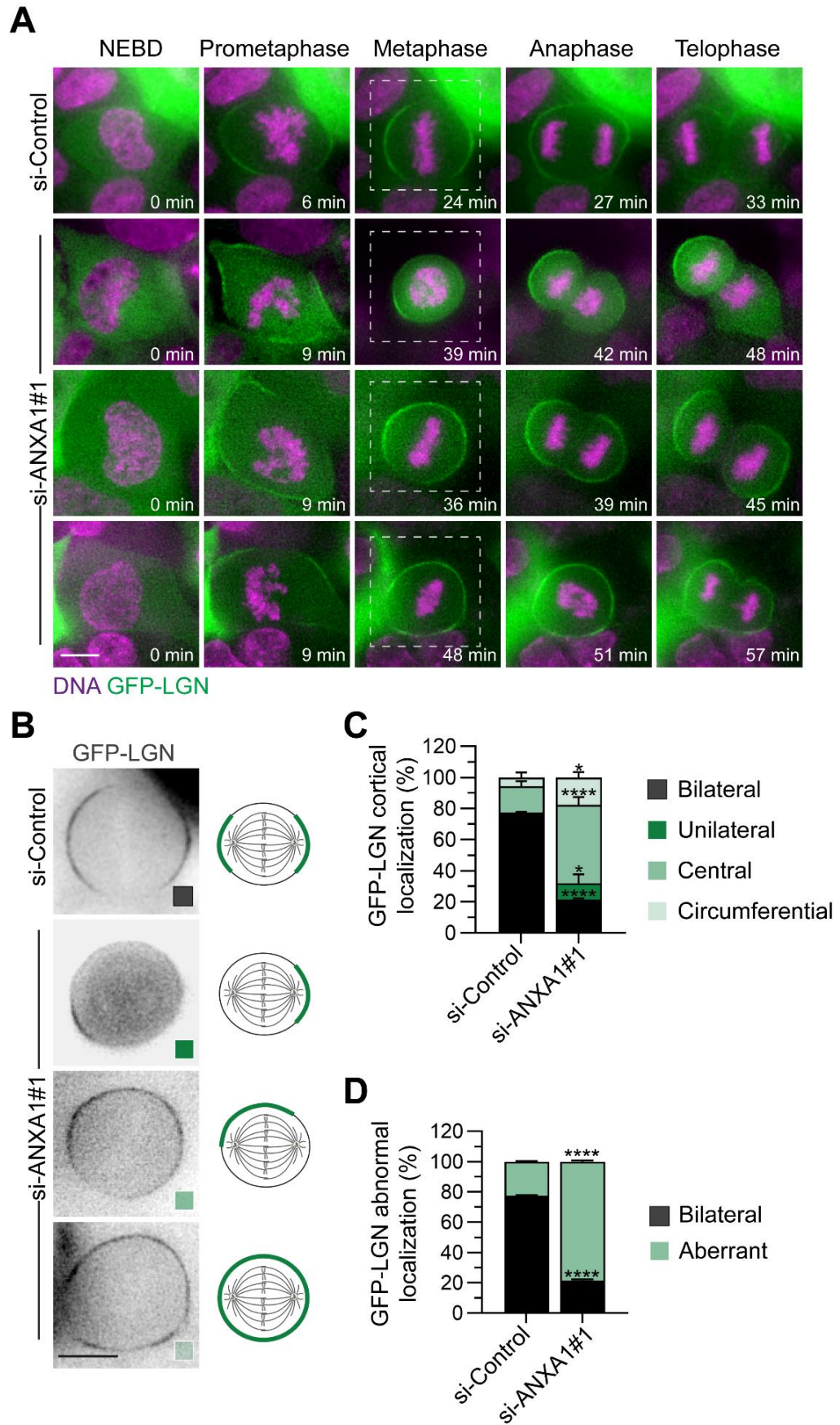


Figure 6.2 ANXA1 depletion induces defects in GFP-LGN cortical localisation during mitosis

**Figure 6.2 Continued**

(A) Representative phenotypes from time-lapse imaging of GFP-LGN (green) cortical localisation during mitosis in control cells and after ANXA1 depletion. Cells were transfected with si-Control or si-ANXA1#1 65 h prior to imaging. DNA (magenta) was stained with Hoechst 33342 30 minutes before imaging. Images were acquired every 3 min. (B) Inverted images and corresponding schematics on the right show magnified images of the framed regions in A. Coloured squares indicate phenotypes quantified in C. (C) Percentage of observed phenotypes in si-Control and si-ANXA1#1. (D) Percentage of abnormal localisation of GFP-LGN in si-Control and si-ANXA1#1. Data represent means + SEM from three independent experiments. Student's *t*-test; \* $p \leq 0.05$ , \*\*\*\* $p \leq 0.0001$ . Scale bars, 10  $\mu\text{m}$ .

**6.2.3 Loss of ANXA1 affects the localisation of the core spindle orientation machinery**

To better understand how ANXA1 knockdown affected the localisation of the spindle orientation machinery, immunofluorescence and confocal imaging was used. Immunolocalisation of LGN, NuMA or p150<sup>Glued</sup> during metaphase revealed significant changes in siRNA conditions. In si-Control, the highest proportion of cells showed for LGN, NuMA and p150<sup>Glued</sup> the typical +crescent-shaped localisation at the lateral cortex above spindle poles. Furthermore, NuMA and p150<sup>Glued</sup> accumulated at spindle poles. A small proportion of cells displayed a central and circumferential distribution of LGN. This was also overserved for NuMA and for p150<sup>Glued</sup> where the proteins localised unilaterally, centrally or were absent in cells (Figure 6.3). When using two different siRNAs against ANXA1, the localisation proportions changed. Less than 17 % of the cells showed a bilateral LGN localisation. The majority of cells displayed a central localisation. To a smaller extend LGN was found circumferentially placed or unilaterally which was not significantly different to the control (Figure 6.3, A left, B left). NuMA displayed a similar localisation where the bilateral distribution was decreased and the protein mostly showed a central localisation. It was also found more unilateral or to a small but not significant proportion absent in the cells. NuMA localised still to the spindle poles in siRNA conditions (Figure 6.3, A middle, B middle). Although, p150<sup>Glued</sup> displayed more variable cortical localisation in the control with around 20 % of cells showing a unilateral, central or absent phenotype, the protein localisation was greatly affected when ANXA1 levels were reduced in the cells. The bilateral localisation decreased from 78 % to less than 15 %. p150<sup>Glued</sup> was still found at the spindle poles, however, almost half of the cells lacked cortical p150<sup>Glued</sup> localisation. The protein also accumulated more unilaterally and centrally. A small but not significant proportion of cells showed a circumferential distribution (Figure 6.3, A right, B right).

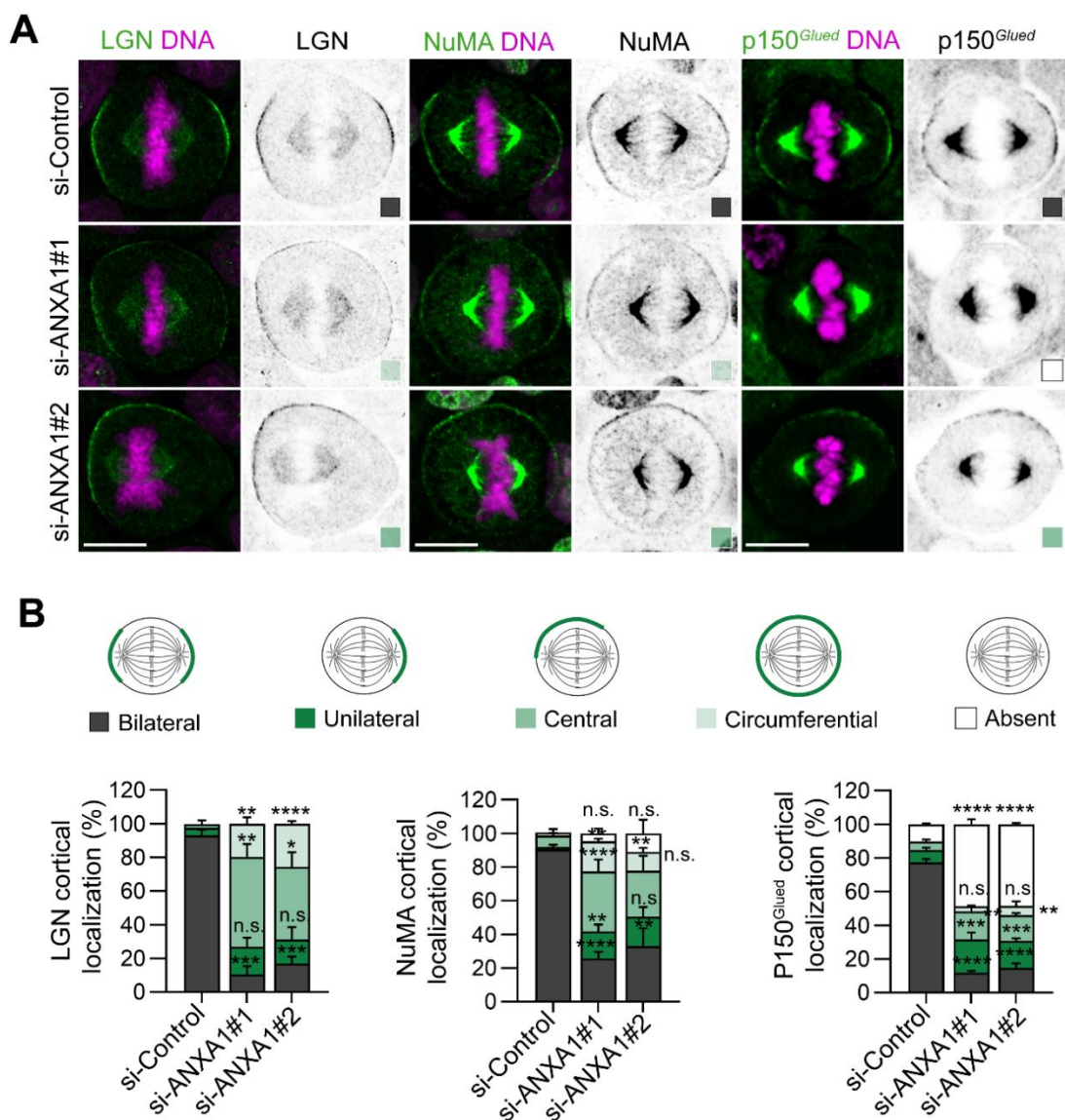


**Figure 6.3 ANXA1 depletion results in cortical misplacement of the spindle orientation machinery** (A) Representative confocal images of the cortical localisation of LGN, NuMA and p150<sup>Glued</sup> in control cells and after ANXA1 depletion. WT MCF-10A cells were transfected with si-Control, si-ANXA1#1 or si-ANXA1#2 72 h prior to fixation with methanol. Cells were stained for the indicated proteins (green). DNA (magenta) was visualised with Hoechst 33342. Coloured squares indicate phenotypes quantified in B. Scale bars, 10  $\mu$ m. (B) Percentage of cortical localisation phenotypes illustrated in the schematics (top). Left: Quantification of LGN localisation. Middle: Quantification of NuMA localisation. Right: Quantification of p150<sup>Glued</sup> localisation. Data presented as means  $\pm$  SEM from 3 independent experiments. LGN: si-Control n=70 cells; si-ANXA1#1 n=51 cells; si-ANXA1#2 n=43 cells. NuMA: si-Control n=73; si-ANXA1#1 n=62; si-ANXA1#2 n=45. p150<sup>Glued</sup>: si-Control n=79; si-ANXA1#1 n=101; si-ANXA1#2 n=99. Student's t-test; \* $p \leq 0.05$ , \*\* $p \leq 0.01$ , \*\*\* $p \leq 0.001$ , \*\*\*\* $p \leq 0.0001$ , n.s. no significant difference.

Next, the localisation of G $\alpha$ i1 was analysed. G $\alpha$ i1 accumulated everywhere at the cell cortex with increased levels at lateral sites in the control as well as knockdown conditions. To quantify the localisation of the protein, bilateral localisation was considered when G $\alpha$ i1 showed an enrichment at the lateral cortex as shown in Figure 6.4, A, si-Control. No differences were observed in the different conditions (Figure 6.4, B). Around 70 % of control cells and 60 % of ANXA1-depleted cells showed a bilateral accumulation of the protein. Furthermore, G $\alpha$ i1 accumulated centrally with a slightly higher proportion in siRNA condition. Similarly, the protein localised circumferentially in all conditions with a minimal higher percentage in ANXA1-depleted cells. To better quantify the distribution of G $\alpha$ i1 along the cell cortex, a custom macro in Fiji was used to measure the fluorescence intensity (Figure 6.4, C). The line-scans confirmed the phenotypes observed in Figure 6.4, A-B. For all conditions, signal intensity was highest at lateral sites and lower in central regions. Compared to si-Control, siRNA conditions showed slightly higher fluorescence intensity at the central cortex and therefore a flatter peak at lateral sites which was consistent with the observation that in ANXA1-depleted cells the proportions of central and circumferential accumulation of G $\alpha$ i1 were higher.

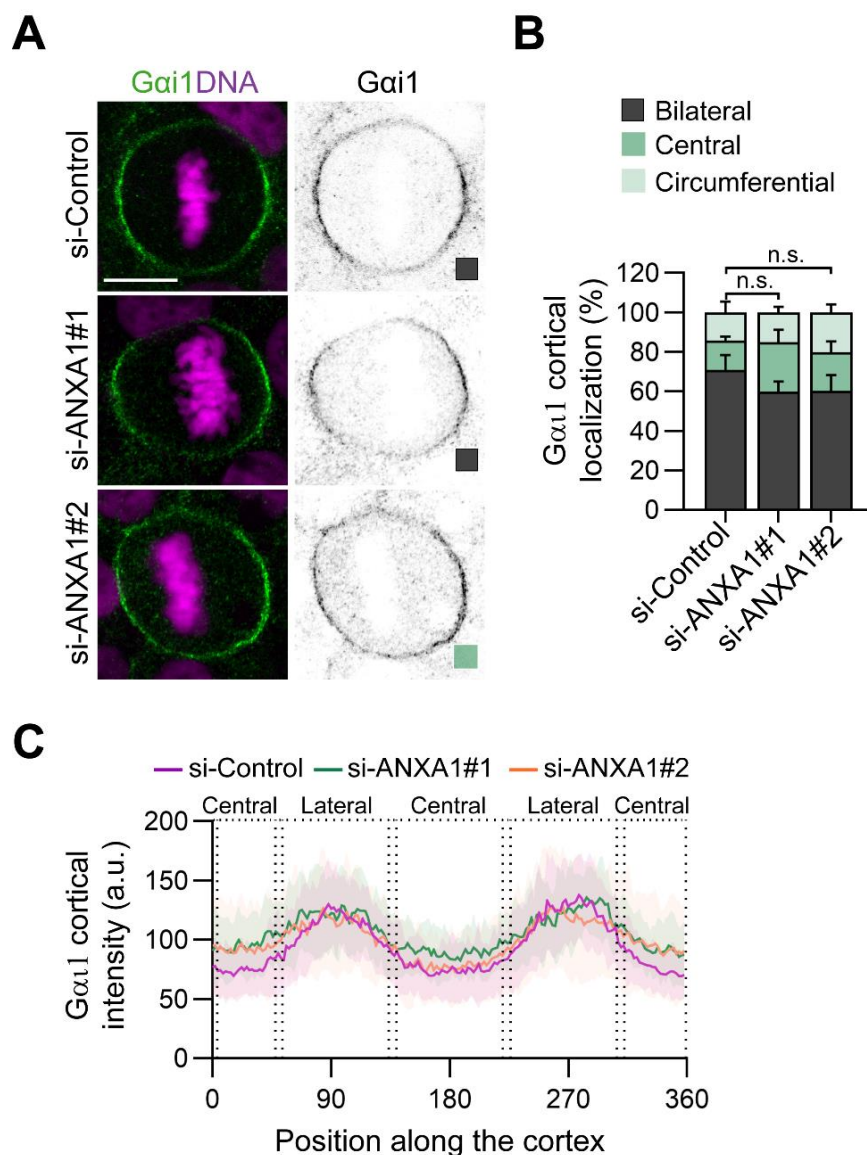


**Figure 6.4 ANXA1 depletion has no effect on cortical localisation of Gai1**

(A) Representative confocal images of the cortical localisation of Gai1 in control cells and after ANXA1 depletion. Cells were transfected with si-Control, si-ANXA1#1 or si-ANXA1#2 72 h prior to fixation with 4 % PFA. Cells were stained for Gai1 (green). DNA (magenta) was visualised with Hoechst 33342. Coloured squares indicate phenotypes quantified in B. Scale bar, 10  $\mu$ m. (B) Percentage of Gai1 cortical localisation. Data presented as means  $\pm$  SEM from 3 independent experiments. si-Control n=71; si-ANXA1#1 n=54; si-ANXA1#2 n=69. Student's t-test; n.s. no significant difference. (C) Cortical fluorescence intensity profiles of Gai1 in si-Control (n=32 cells), si-ANXA1#1 (n=26 cells) and si-ANXA1#2 (n=28 cells). Graphs show the average for n cells  $\pm$  SD.

### 6.2.4 Loss of LGN does not alter ANXA1 dynamics

Loss of ANXA1 greatly affected the cortical localisation of LGN. To determine if loss of LGN influences ANXA1 dynamics, *LGN* was depleted in WT MCF-10A cells. Two different siRNA sequences were utilized and both constructs resulted in a reduction of LGN protein levels compared to the control (Figure 6.5, A). A greater knockdown was achieved with siLGN#2 with relative protein levels decreased to 0.13 compared to the control (1.0). However, siLGN#1 also reduced LGN levels significantly to 0.24 (Figure 6.5, B). siRNAs targeting *LGN* had no effect on ANXA1 protein levels. Although, protein levels were slightly reduced in siLGN#1 compared to the control, no significant difference was observed. ANXA1 levels increased minimally in siLGN#2 but also not significantly (Figure 6.5, C).

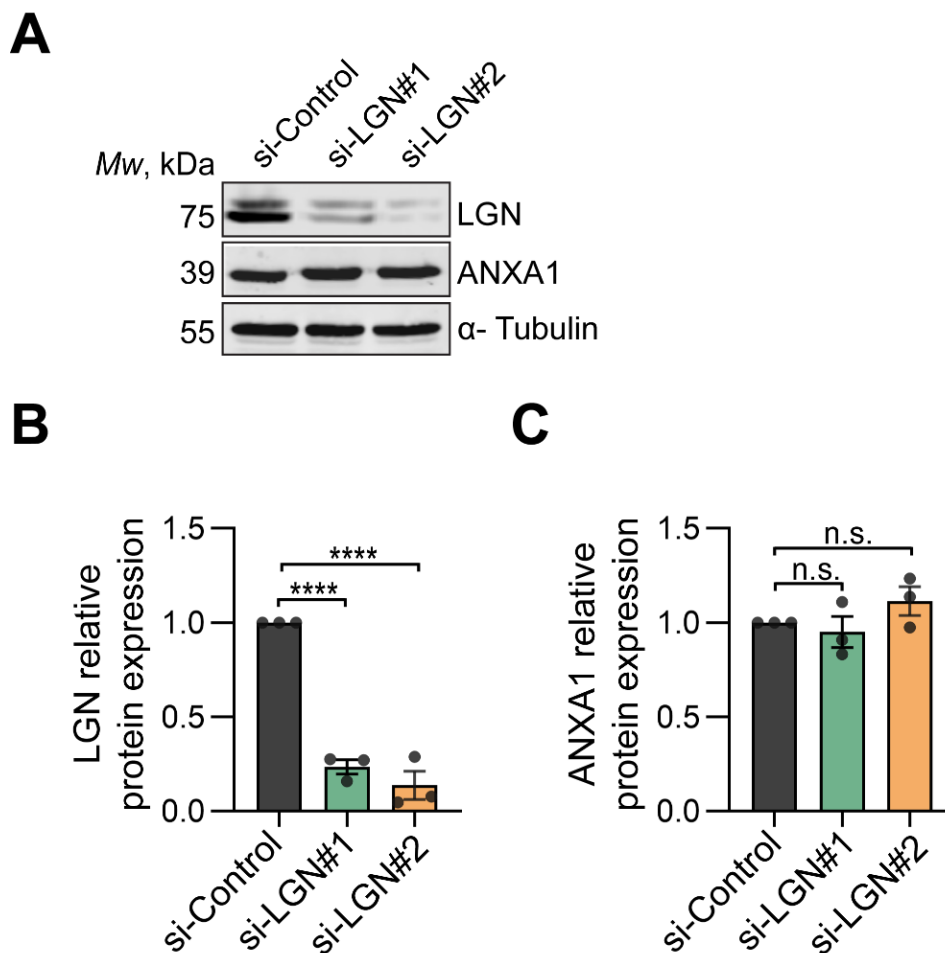
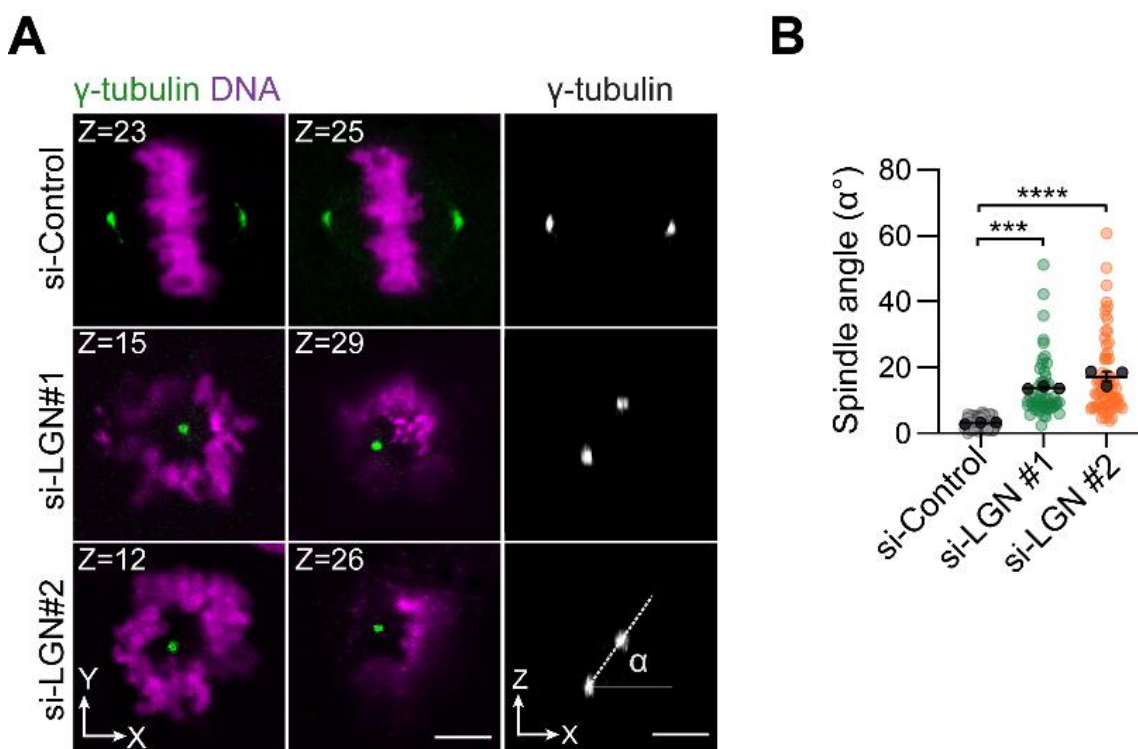


Figure 6.5 Protein levels after LGN knockdown using siRNA

**Figure 6.5 Continued**

(A) Immunoblot of *LGN* and *ANXA1* levels in cells after *LGN* depletion. Cells were transfected with *si-Control* or two different *siRNA* constructs targeting *LGN* (*si-LGN#1*, *si-LGN#2*) and analysed 72 hours later.  $\alpha$ -Tubulin was used as a loading control. (B) Quantification of normalized *LGN* protein levels in cells transfected with *si-Control*, *siLGN#1* or *siLGN#2*. (C) Quantification of normalized *ANXA1* protein levels in cells transfected with *si-Control*, *siLGN#1* or *siLGN#2*. Data represent means (black dots)  $\pm$  SEM from three independent experiments. Student's *t*-test; \*\*\*\* $p \leq 0.0001$ , *n.s.* no significant difference.

To evaluate the impact of *LGN* knockdown on spindle orientation during metaphase, the localisation of the spindle poles in the *z*-plane and spindle angles in *si-Control* and *siRNA* conditions were determined. For this, cells were stained with anti- $\gamma$ -tubulin antibody to label spindle poles. In control cells, poles were almost in the same focal plane of the *z*-axis. In contrast, in *LGN* depleted cells, spindle poles were found in different (further apart) *z*-planes (Figure 6.6, A). Consistently, quantification of spindle angles revealed that control cells exhibited spindle angles of less than 5°, whereas *siLGN#1/2* significantly increased angles to >10° (Figure 6.6, B).



**Figure 6.6** *LGN* depletion leads to spindle orientation defects

**Figure 6.6 Continued**

(A) Representative confocal images of z-sections (0.3  $\mu\text{m}$  per stack) with maximum spindle pole intensity. Cells were transfected with si-Control, si-LGN#1 or si-LGN#2 72 h prior to fixation with methanol. Cells were stained for  $\gamma$ -tubulin (green). DNA (magenta) was visualised with Hoechst 33342. Orthogonal views (xz) of the depicted cells ( $\gamma$ -tubulin signal) was used to measure spindle angle  $\alpha$  as illustrated. Scale bars, 5  $\mu\text{m}$ . (B) Quantification of spindle angles. Data represent individual cells with means (black dots)  $\pm$  SEM from three independent experiments. si-Control n=68, si-LGN#1 n=50, si-LGN#2 n=67. Student's t-test; \*\*\* $p \leq 0.001$ , \*\*\*\* $p \leq 0.0001$ .

Next, the effect of LGN knockdown on NuMA and ANXA1 localisation was analysed. As expected, loss of LGN resulted in changes in NuMA cortical localisation. Although the protein still accumulated at the spindle poles, a significant reduction of bilateral localisation was observed with less than 20 % of the cells showing NuMA bilateral accumulation compared to 80 % in the control. In more than 60 % of the cells NuMA was absent from the cortex NuMA was also found increased at the central cortex, unilateral or circumferential but no significant differences were seen (Figure 6.7, A-B). In contrast, depletion of LGN had no effect on ANXA1 localisation during metaphase. The protein showed an accumulation around the chromosome plate in the cytoplasm and a uniform distribution along the cell cortex. Cortex localisation was quantified with the custom macro in Fiji and pixel intensity measurements showed similar fluorescence profiles for all conditions (Figure 6.7, C-D).

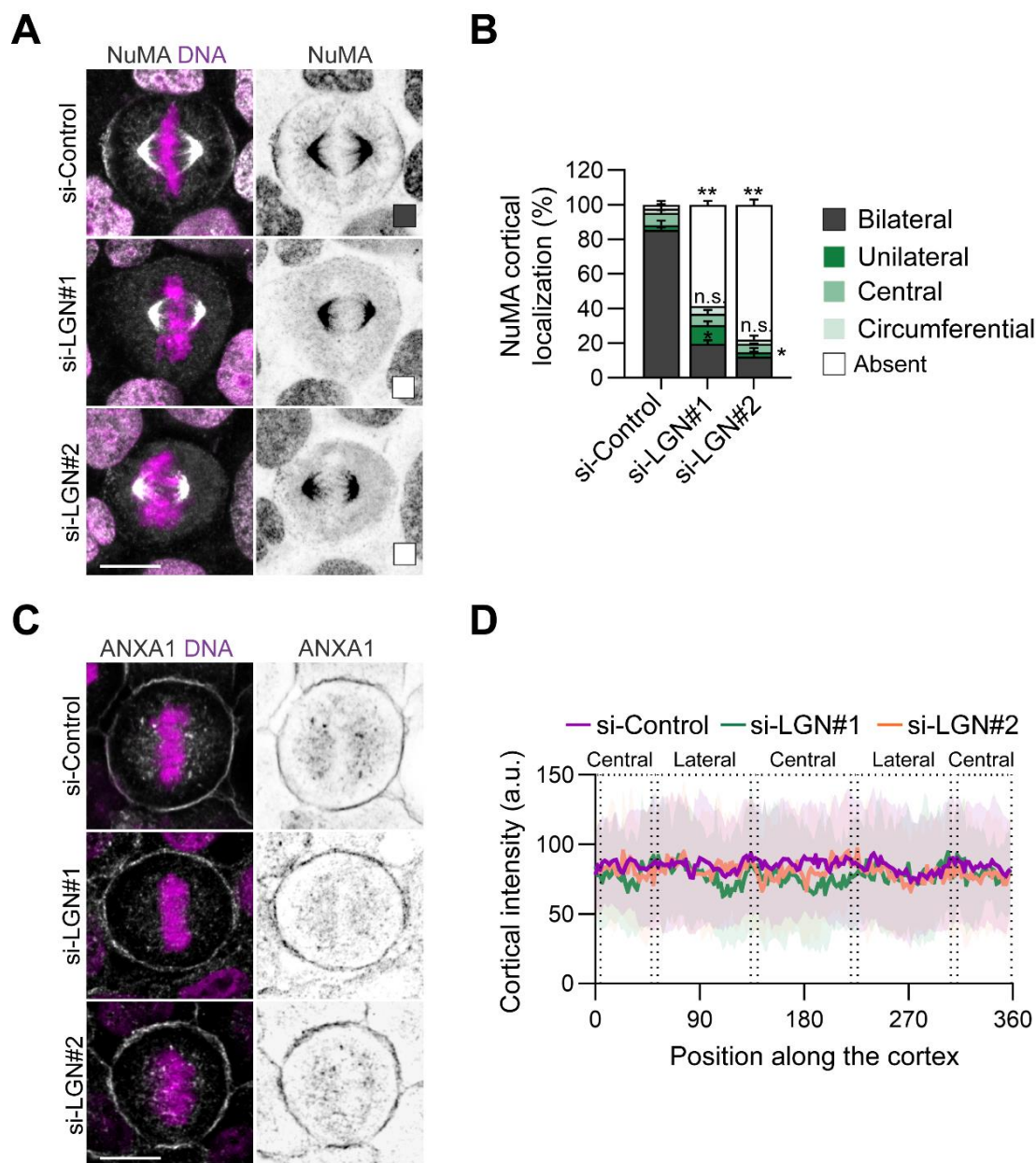


**Figure 6.7 Cortical localisation of NUMA and LGN after LGN depletion LGN depletion leads to cortical misplacement of NuMA but has no effect on ANXA1 localisation**

(A) Representative confocal images of the cortical localisation of NuMA in control cells and after LGN depletion. Cells were transfected with si-Control, si-LGN#1 or si-LGN#2 72 h prior to fixation with 4 % PFA. Cells were stained for NuMA (grey). DNA (magenta) was visualised with Hoechst 33342. Coloured squares indicate phenotypes quantified in B. Scale bar, 10  $\mu$ m. (B) Percentage of NuMA cortical localisation. Data presented as means  $\pm$  SEM from 3 independent experiments. si-Control n=42; si-LGN#1 n=46; si-LGN#2 n=41. Student's t-test; \* $p \leq 0.05$ , \*\* $p \leq 0.01$ , n.s. no significant difference. (C) Representative confocal images of the cortical localisation of ANXA1 in control cells and after LGN depletion.

**Figure 6.7 Continued**

Cells were transfected with *si-Control*, *si-LGN#1* or *si-LGN#2* 72 h prior to fixation with methanol. Cells were stained for ANXA1 (grey). DNA (magenta) was visualised with Hoechst 33342. Scale bar, 10  $\mu\text{m}$ . (D) Cortical fluorescence intensity profiles of ANXA1 in *si-Control* ( $n=41$  cells), *si-LGN#1* ( $n=26$  cells) and *si-LGN#2* ( $n=25$  cells). Graphs show the average for  $n$  cells  $\pm$  SD.

Together, these results showed that ANXA1 knockdown was achieved using a siRNA approach without affecting LGN protein levels. Additionally, loss of ANXA1 resulted in dramatic changes in the cortical localisation of GFP-LGN during mitosis as well as misplacement of LGN, NuMA and p150<sup>Glued</sup> during metaphase but it had no effect on the cortical localisation of Gai1. Furthermore, utilization of siRNA targeting LGN greatly reduced endogenous LGN levels but had no effect on ANXA1 protein levels. Loss of LGN resulted in increased spindle angles and cortical misplacement of NuMA. However, ANXA1 localisation was not disturbed upon LGN loss.

**6.3 Discussion**

Loss-of-function approaches such as RNA interference, are used widely to repress the transcription or translation of gene expression which leads to a reduction of protein levels without genomic modifications. The resulting phenotypes caused by the specific perturbation help to study the WT function of the targeted gene (Housden *et al.*, 2017; Zimmer *et al.*, 2019). This approach has been used in the past to study ANXA1 functions. It was shown that knockdown of the gene influences multiple signalling pathways that are critical for epithelial-mesenchymal-transition (EMT). Furthermore, depletion of ANXA1 decreases proliferation, invasion, motility and leads to loss of polarity in cancer cells (Maschler *et al.*, 2010; Fang *et al.*, 2016; Wei *et al.*, 2021). This shows that loss of the protein significantly affects essential pathways and cellular processes and highlights the importance of the protein. With the identification of ANXA1 as a novel part of the LGN interactome and its dynamic co-localisation with LGN, it is intriguing that the protein might play specific roles in the dynamics of the spindle orientation machinery. To test this, a knockdown approach using siRNA to target ANXA1 was applied to transiently suppress gene expression and study the effect on the localisation of the spindle orientation machinery. This helped to gain insight into the mechanistic nature of ANXA1 in mitosis.

### 6.3.1 ANXA1 is required to localise the LGN-NuMA-Dynein/Dynactin complex to the lateral cortex during mitosis

The use of siRNA constitutes an ideal method to perturb gene expression because it can be easily delivered to cells and it generates hypomorphic phenotypes (Housden *et al.*, 2017). siRNA constructs that target the same gene can have different knockdown efficiencies depending on the gene region they bind to. Although, algorithms perform quite well to design the most efficient RNA sequences, it is essential to test multiple constructs for the target gene (Han, 2018). Therefore, the first step in such loss-of-function experiments is the analysis of protein levels to evaluate the efficacy of the gene knockdown. In this study, two siRNA constructs were tested and more than 50 % of ANXA1 protein levels were reduced after siRNA treatment in both conditions. This is in accordance with previous studies who achieved similar knockdown efficiencies (Maschler *et al.*, 2010; Fang *et al.*, 2016; Wei *et al.*, 2021). The use of siRNA to inhibit mRNA rarely causes complete loss-of-function and some level of the mRNA and protein is still detectable. Furthermore, protein stability can delay the detection of phenotypes if such protein has a long half-life (Housden *et al.*, 2017). The half-life of ANXA1 is 35 hours in proliferating cells which explains why not more protein was knocked down in the experiments (Schlaepfer and Haigler, 1990). To achieve a complete knockout other techniques should be favoured. However, this could cause other disadvantages. For example, using Crispr/Cas9 to generate a knockout cell line can be a long procedure and the experimental process can cause genotoxic stress which may harm the cells and cause effects on downstream applications (Housden *et al.*, 2017). Therefore, siRNA constitutes a mild treatment and ideal method to transiently deplete ANXA1. However, phenotypes needed to be carefully analysed and compared to the control to evaluate the specific effect of loss of ANXA1 on the localisation of the spindle orientation machinery.

The experiments identified that LGN protein levels were not affected by siRNA depletion of ANXA1. This shows that the ANXA1 mRNA was specifically targeted and LGN mRNA was not influenced. Thus, ANXA1 mechanisms act on LGN protein dynamics and not on gene level. Upon loss of ANXA1, GFP-LGN and endogenous LGN accumulation at the cortex was significantly disturbed and the proteins distributed not only lateral but also more circumferential and near chromosomes (central). This highlights that in the absence of ANXA1 LGN is no longer polarised to a crescent shape above spindle poles. Similar effects were observed when previously identified regulators of LGN were depleted. For example ERM proteins promote polarised localisation of LGN and loss of these proteins lead to misplaced LGN during metaphase (Machicoane *et al.*, 2014). Similarly, depletion of Afadin or Dlg1 lead to failure in the bilateral accumulation of LGN at the cell cortex (Saadaoui *et al.*,

2014; Carminati *et al.*, 2016; Porter *et al.*, 2019). These studies also showed that depletion of the regulators not only disrupts LGN placement but also affected cortical NuMA recruitment and subsequently dynein/dynactin localisation without disturbing their spindle pole localisation. This was also observed upon ANXA1 loss which highlights that correct LGN localisation is essential for correct recruitment of the spindle orientation machinery to the cell cortex. Two elegant studies proved this downstream effect further. Di Pietro *et al.* artificially induced a polarised localisation of Gai subunits which led to the accumulation of LGN and NuMA at the same sites (di Pietro *et al.*, 2017). Okumura *et al.* showed that light-induced targeting of NuMA to central regions of the cell cortex also localised dynein/dynactin to these areas (Okumura *et al.*, 2018). Thus, it can be speculated that ANXA1 loss-induced incorrect localisation of LGN led to further recruitment of NuMA and subsequently dynein/dynactin to the same aberrant sites.

Interestingly however, the majority of cells lacked cortical accumulation of the motor complex. The control of dynein/dynactin at the cortex is not well understood but involves other regulatory mechanisms besides the LGN complex. These include spindle-to-cortex crosstalks where e.g. the proteins MISP and Lis1 are essential for the correct cortical accumulation of the motor complex (Moon *et al.*, 2013; Zhu *et al.*, 2013). Thus, depletion of ANXA1 may not only affect the LGN cortical localisation and subsequently other members of the spindle orientation machinery, it may also be involved in other regulatory mechanisms of spindle orientation (discussed in more detail in the next chapter).

Loss of ANXA1 did not affect Gai cortical dynamics. This suggests that the ANXA1-mediated polarisation of LGN might be a Gai-independent mechanism and ANXA1 only acts on LGN and downstream proteins. This supports the general assumption that Gai serves as an anchor to recruit LGN to the cortex but is not involved in the specific polarisation (di Pietro, Echard and Morin, 2016). It will be interesting to determine how ANXA1 and Gai subunits cooperate with each other spatially to accumulate LGN at the cortex.

### 6.3.2 ANXA1 acts upstream of LGN

Since ANXA1 loss leads to disruption of LGN cortical localisation and affects downstream recruitment of NuMA and dynein/dynactin, it was important to evaluate if LGN can have an effect on ANXA1 cortical accumulation. Two siRNA sequences were utilized to transiently knockdown LGN. Protein levels were reduced in both conditions by around 80 % or more. In contrast, ANXA1 protein levels did not change which shows that loss of LGN has no effect on ANXA1 gene expression dynamics. Not surprisingly, loss of LGN resulted in mostly absent NuMA from the cortex and only

accumulation of the protein at spindle poles. Subsequently, this led to mitotic spindle orientation defects with cells exhibiting more oblique divisions. It is well established that depletion of LGN exerts these downstream effects and confirmed that LGN functions to recruit the other members of the spindle orientation machinery to execute proper spindle orientation in mammary epithelial cells (Yasumi *et al.*, 2005; Morin, Jaouen and Durbec, 2007; Zheng *et al.*, 2010; Peyre *et al.*, 2011). Loss of LGN had no effect on the cortical localisation of ANXA1 indicating that ANXA1 acts upstream of LGN. This approach of deciphering if the potential novel regulator of spindle orientation acts on the spindle orientation machinery or downstream was also used in the work investigating the functions of Afadin and Dlg1 (Saadaoui *et al.*, 2014; Carminati *et al.*, 2016). Both studies showed that depletion of LGN did not alter the localisation of the novel regulators and proved that LGN lies downstream. Together with the finding that loss of ANXA1 results in detrimental defects of the LGN complex cortical localisation but not Gai, it can be concluded that ANXA1 acts upstream as a novel regulator of the polarised localisation of LGN at the cell cortex. This allows recruitment of NuMA and dynein/dynactin to establish a bilateral localisation of the spindle orientation machinery. Since the correct localisation of this complex is essential for spindle positioning (di Pietro, Echard and Morin, 2016), it was important to analyse the involvement of ANXA1 in mitotic dynamics. Therefore, the next chapter investigated how ANXA1 can influence positioning of the mitotic spindle and mitotic progression.



## **Chapter 7 ANXA1 is required for correct spindle orientation and mitotic progression**



## 7.1 Introduction

Each step of the cell cycle depends on the completion of prior steps. Specifically in mitosis, cells require sufficient time to complete every single phase because at some point, it becomes an irreversible transition from metaphase to anaphase which subsequently leads to transmission of genetic material from one cell generation to the next (Meraldi, Draviam and Sorger, 2004). Therefore, it is essential that individual phases and events during cell division are tightly regulated because deregulation has detrimental effects (Hayashi and Karlseder, 2013). Several mitotic defects can influence the outcome of mitosis. Normally, the mitotic spindle assembles from two centrosomes that form the two spindle poles. Due to failures earlier in the cell cycle, supernumerary centrosomes can be present which lead to the formation of multipolar spindles. Once a cell with multiple spindle poles progresses through mitosis, more than two daughter cells may be generated and the genetic material would be distributed unequally to daughter cells resulting in genetic imbalance. Over time, this would lead to populations of cells with elevated levels of incorrect chromosome numbers leading to unregulated growth characteristics seen in tumorigenesis (Sluder and Nordberg, 2004; Maiato and Logarinho, 2014). Other defects in spindle assembly may lead to incorrect spindle positioning. Especially, proper dynamics of astral MTs are indispensable in this process. Shorter astral MTs may influence the distance between the spindle and cell cortex leading to incorrect spindle positioning. Additionally, abnormal astral MTs may also affect pulling force transmissions between dynein/dynactin and the spindle. Therefore, astral MTs length, density as well as stability play an indispensable role for correct spindle orientation resulting in the correct placement of the daughter cells (di Pietro, Echard and Morin, 2016). Another mitotic defect facilitates inaccurate chromosome segregating such as chromosome bridges. This error is observed during the metaphase/anaphase transition where sister chromatids do not separate and a stretch of DNA is observed in the spindle midzone. Eventually these bridges break during anaphase when the spindle elongates which can lead to fusion of these broken chromatin pieces with other broken chromatin structures forming novel structural chromosome aberrations. This can result in genetic heterogeneity, a hallmark of cancer development (Pampalona *et al.*, 2016; Baudoin and Cimini, 2018; Finardi, Massari and Visintin, 2020).

All of the above examples highlight that accurate spindle assembly and orientation is essential for proper mitosis (Hayashi and Karlseder, 2013). The list of proteins implicated in these processes is continuously increasing and includes proteins involved in astral MT dynamics, centrosome organization, membrane organization and many others (Rizzelli *et al.*, 2020). However, a confined understanding of these dynamics is needed.

ANXA1 was identified as a novel regulator of the subcellular localisation of members of the spindle orientation machinery in the last chapter. Because these proteins are essential for correct positioning of the mitotic spindle, the aim of this chapter was to investigate how ANXA1-mediated polarization of the spindle orientation complex influences spindle orientation. This would help to better understand how regulators of spindle orientation play a role in mitotic dynamics and the correct outcome of cell division. For this, loss-of-function experiments were performed by using siRNA to knockdown ANXA1 protein levels. The mitotic timing as well as positioning of the mitotic spindle during metaphase were analysed. Furthermore, astral MT structure and dynamics of metaphase spindles were characterised. Overall, these analyses elucidated the impact of ANXA1 loss-induced misplacement of the spindle orientation machinery on mitotic progression and spindle orientation.

## 7.2 Results

Using the same siRNA constructs as in the last chapter, transient knockdown of ANXA1 was achieved. Time-lapse microscopy as well as immunofluorescence and confocal imaging were used to analyse the effect of ANXA1 loss on mitosis. Furthermore, dynamics of mitotic spindle orientation and movements were dissected. Lastly, astral MTs were examined.

### 7.2.1 Loss of ANXA1 leads to mitotic defects and mitotic delay

To characterise the effects ANXA1 loss had on mitotic progression, time-lapse microscopy of MCF-10A WT cells transfected with si-Control or si-ANXA1#1 was performed. MTs were labelled with a fluorogenic probe and DNA was stained with Hoechst 33342 to allow tracking of mitotic spindle dynamics and chromosomes. Cells were imaged throughout mitosis and striking differences between control and ANXA1-depleted cells were observed (Figure 7.1, A). The number of cells that completed mitosis were vastly decreased under siRNA conditions (Figure 7.1, B). 100 % of control cells progressed through mitosis but only 57 % of si-cells finished cell division whereas the remaining proportion of cells arrested in metaphase. Concomitantly, in siRNA conditions, cells spent more time in mitosis. This became evident when examining the duration from NEBD to anaphase and metaphase plate congression. Control cells spent on average 39 min from entry into mitosis to anaphase onset whereas si-cells completing mitosis entered anaphase after 54 min which is the duration MCF-10A cells normally need to complete mitosis (quantified in chapter 3, section

3.2.1). This delay was mainly caused by a dramatic increase of metaphase congression in ANXA1-depleted cells compared to si-Control with 58 min or 11 min respectively time spent (Figure 7.1, C-D).

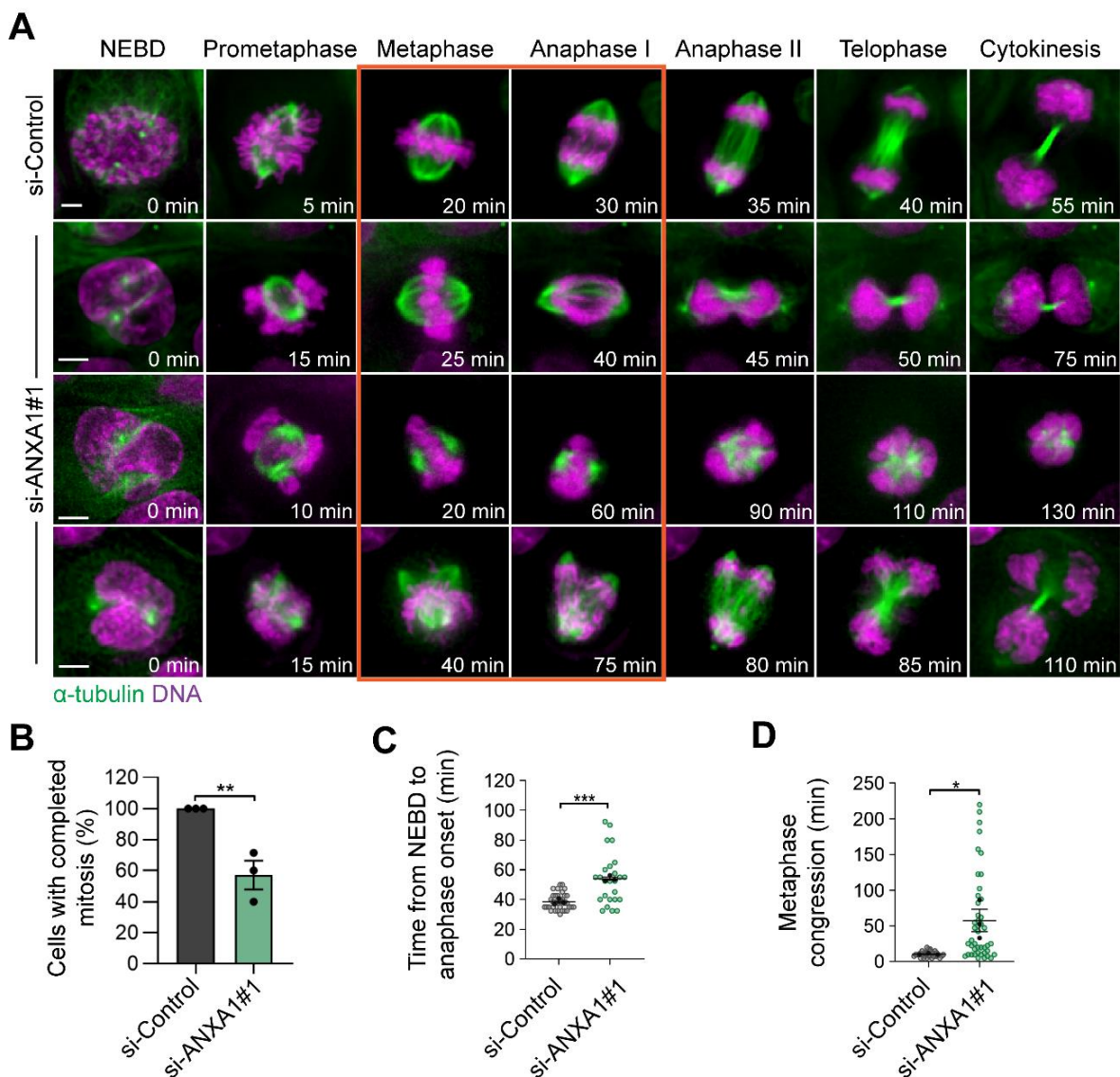


**Figure 7.1 ANXA1 depletion results in aberrant mitotic timing**

(A) Representative phenotypes from time-lapse imaging of WT MCF-10A cells during mitosis in control cells and after ANXA1 depletion. Cells were transfected with si-Control or si-ANXA1#1 65 h prior to imaging. Before imaging, microtubules were labelled with SiR-tubulin (green) for 2 h and DNA (magenta) was stained with Hoechst 33342 for 30 min. Images were acquired every 2.5 min. Scale bar, 5  $\mu$ m. Framed region (orange) is shown as inverted images in Figure 7.2, A. (B) Percentage of cells completing mitosis in si-Control and si-ANXA1#1. Data represent means (black dots)  $\pm$  SEM from three independent experiments.

**Figure 7.1 Continued**

(C) Quantification of the time from NEBD to anaphase onset in control cells and ANXA1-depleted cells. Data represent individual cells with means (black dots)  $\pm$  SEM from three independent experiments. (D) Quantification of the duration of metaphase plate congression in control cells and ANXA1-depleted cells. Data represent individual cells with means (black dots)  $\pm$  SEM from three independent experiments. For all graphs, si-Control n=33, si-ANXA1#1 n=44. Student's t-test; \* $p \leq 0.05$ , \*\* $p \leq 0.01$ , \*\*\* $p \leq 0.001$ .

The observed time delays and failures in completing mitosis were also accompanied by characteristic phenotypes illustrated in figure 7.2, A. Absence of ANXA1 resulted in chromosome segregation defects seen as chromosome bridges. These were also observed in control cells. However, around 32 % of siRNA cells showed these phenotype compared to 10 % in the control condition. Phenotypes also included spindle assembly defects such as small abnormal spindles and multipolar spindles which were not seen in the control. ANXA1 depletion showed that 32 % of the cells had a small abnormal spindle and 14 % of cells assembled multipolar spindles. Overall, ANXA1 depletion resulted in a significantly decrease in normal mitosis and a vast increase in abnormal mitosis. Around 90 % of si-cells displayed one of the three phenotypes described whereas only 10 % of control cells showed abnormalities (Figure 7.2, B-C).

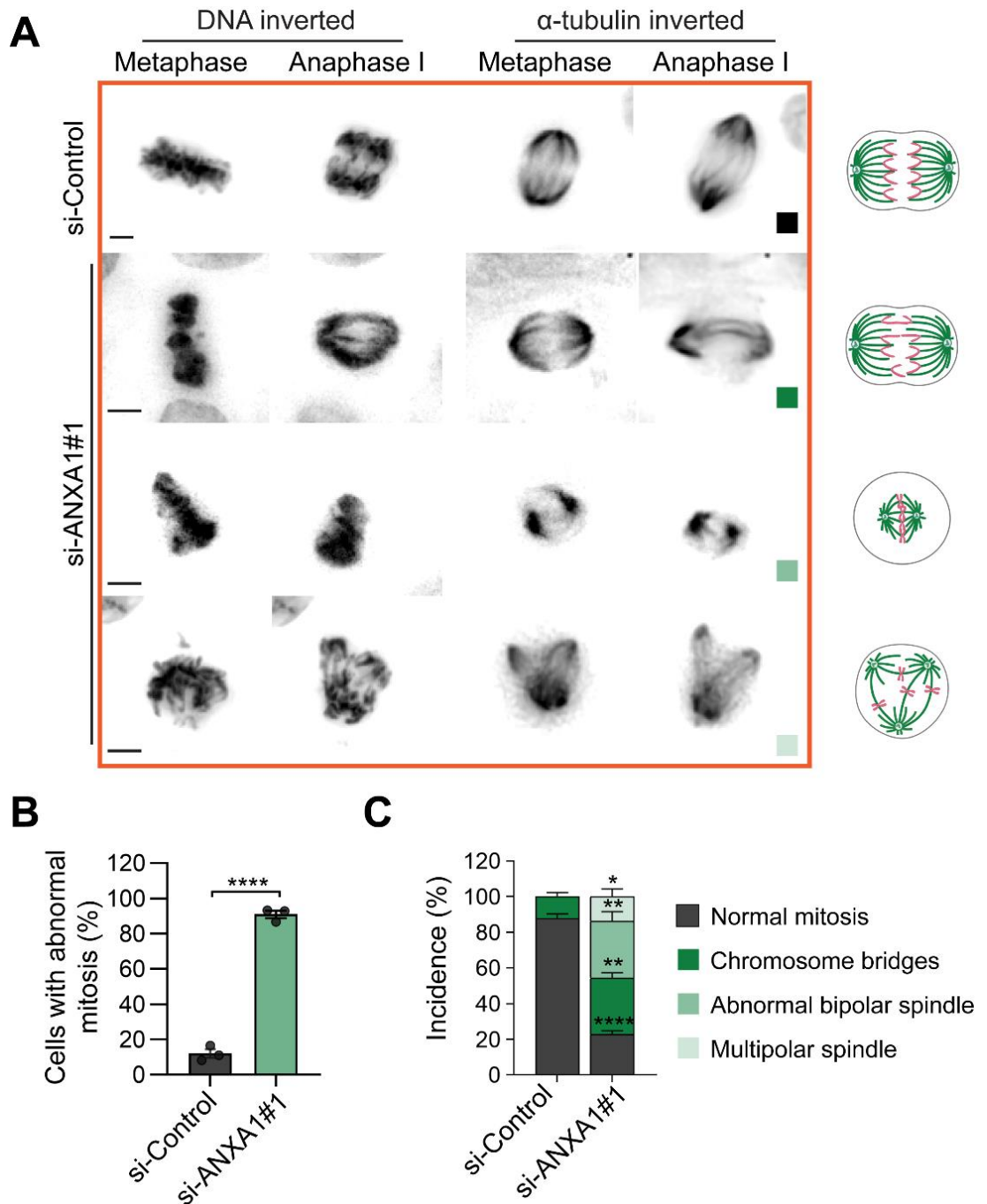


**Figure 7.2 ANXA1 depletion induces mitotic defects**

(A) Inverted images of metaphase and anaphase phenotypes and corresponding schematics on the right show images of the framed regions in Figure 7.1, A. Coloured squares indicate phenotypes quantified in C. (B) Percentage of cells with mitotic defects in control cells and ANXA1-depleted cells. Data represent means (black dots)  $\pm$  SEM from three independent experiments. (C) Percentage of observed phenotypes in si-Control and si-ANXA1#1. Data represent means + SEM from three independent experiments. For all graphs, si-Control  $n=33$ , si-ANXA1#1  $n=44$ . Student's *t*-test; \* $p \leq 0.05$ , \*\* $p \leq 0.01$ , \*\*\*\* $p \leq 0.0001$ . Scale bar, 5  $\mu$ m.

### 7.2.2 Loss of ANXA1 increases spindle oscillation and metaphase plate movement

To further dissect spindle dynamics during metaphase, movements of the mitotic spindle were measured in cells imaged using time-lapse microscopy. First, orientation and movement of the spindle in the z-axis were analysed. Spindle angles were tracked over time by measuring the spindle angle for every time point from the first frame of entering metaphase to the last before anaphase onset or if cells did not progress through mitosis until the cells died or the video ended. As shown in figure 7.3, A-B, control cells depicted small spindle angles with the spindle almost aligned parallel to the basement membrane throughout metaphase. In contrast, siRNA cells showed greater spindle angles with more tilted spindles during metaphase progression. To quantify the differences, the oscillation index was calculated which determines the frequency by which the spindle angle changed  $> 10^\circ$  between two successive frames. In si-Control no oscillation was seen, whereas in si-ANXA1#1 29 % of frame transitions were accompanied by oscillations (Figure 7.3, C). Based on this, 82 % of ANXA1-depleted cells but no control cells had at least one oscillation event (Figure 7.4, D). To quantify z-rotation changes over time, the absolute and relative z-rotation were calculated which determined angle changes per 1 min. No differences between si-Control and si-ANXA1#1 were observed (Figure 7.4, E-F).

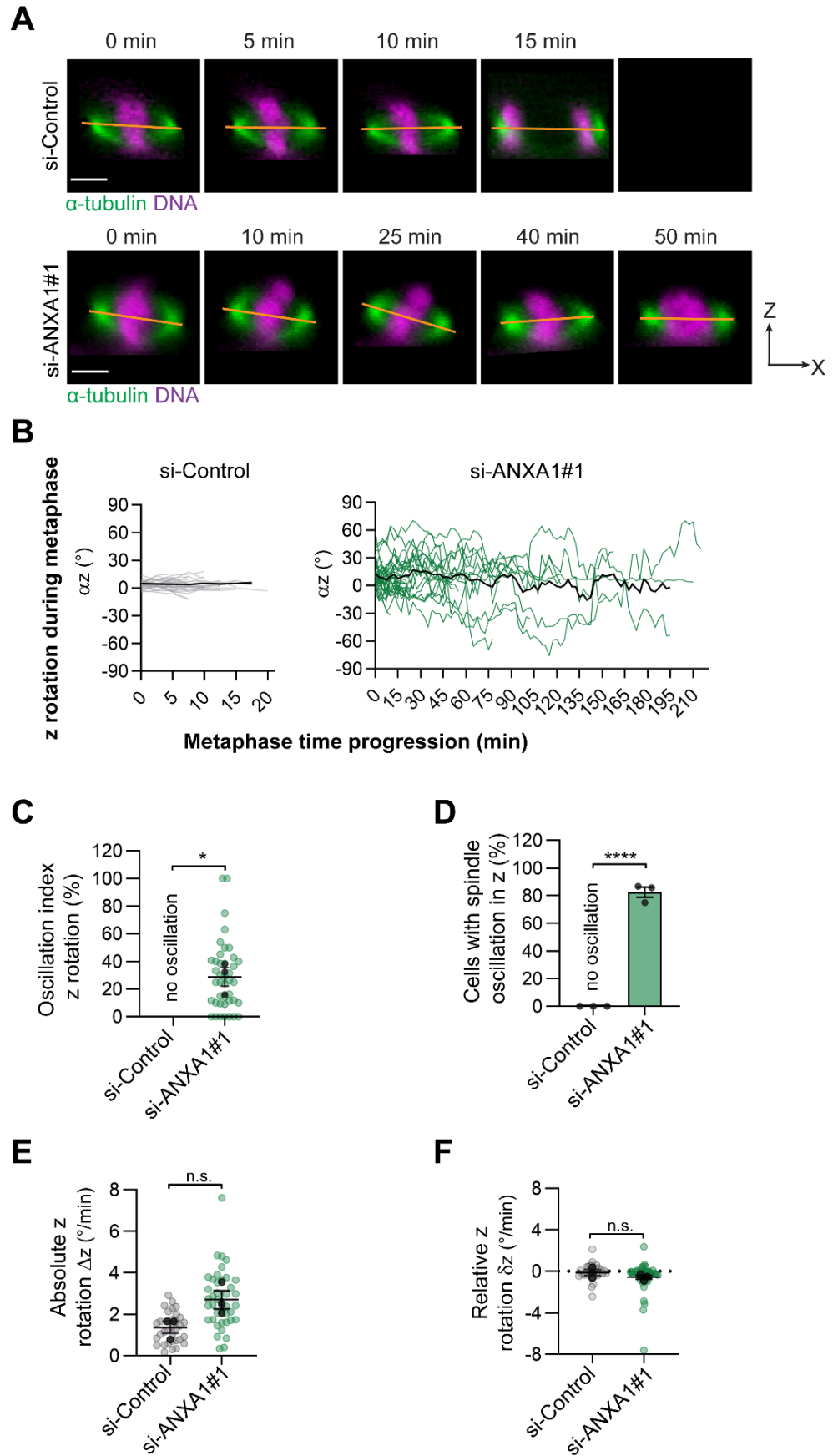
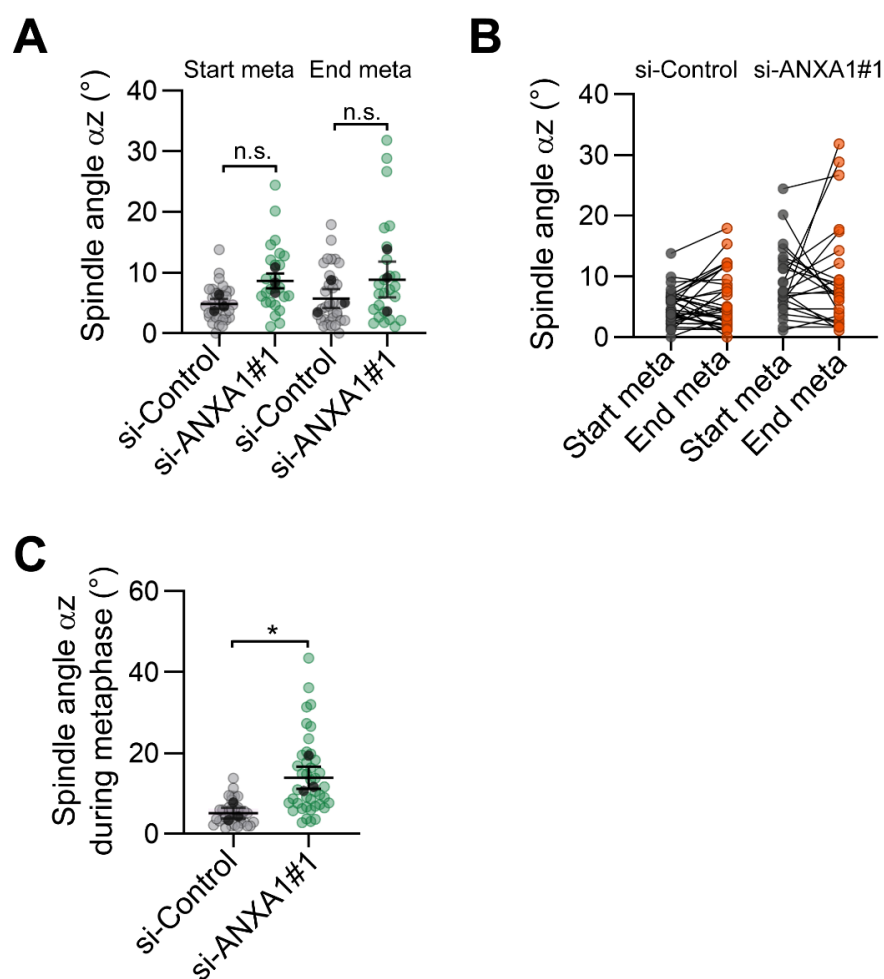


Figure 7.3 ANXA1 depletion leads to excessive z-rotations of the mitotic spindle

**Figure 7.3 Continued**

(A) Representative orthogonal views ( $xz$ ) from time-lapse imaging of WT MCF-10A cells during metaphase in controls and after ANXA1 depletion. Cells were transfected with si-Control or si-ANXA1#1 65 h prior to imaging. Before imaging, MTs were labelled with SiR-tubulin (green) for 2 h and DNA (magenta) was stained with Hoechst 33342 for 30 min. Images were acquired every 2.5 min. Orange line indicates spindle axis. Scale bar, 5  $\mu\text{m}$ . (B) Z-rotation changes during metaphase in si-Control (left) and si-ANXA1#1 (right). Spindle angle  $\alpha_z$  was measured as the angle between the spindle axis and basement membrane at every time point from the beginning of metaphase to the last frame before entering anaphase or if cells did not progress through mitosis until the cells died or the video ended. Grey and green lines correspond to individual cells. Black lines represent the average spindle angles of all analysed cells. (C) Quantification of the oscillation index for si-Control and si-ANXA1#1 representing frequency of mitotic spindles changing positions  $> 10^\circ$  between two successive frames in the z-axis. Data represent individual cells with means (black dots)  $\pm$  SEM from three independent experiments. (D) Percentage of cells with spindle oscillations in the z-axis in si-Control and si-ANXA1#1. Data represent means (black dots)  $\pm$  SEM from three independent experiments. (E) Absolute z-rotation for si-Control and si-ANXA1#1 representing absolute z rotation changes per minute. Data represent individual cells with means (black dots)  $\pm$  SEM from three independent experiments. (F) Relative z-rotations for si-Control and si-ANXA1#1 representing z-rotation changes per minute with respect to directional changes. Data represent individual cells with means (black dots)  $\pm$  SEM from three independent experiments. For all graphs, si-Control  $n=33$ , si-ANXA1#1  $n=44$  cells. Student's t-test; \* $p \leq 0.05$ , \*\*\*\* $p \leq 0.0001$ , n.s. no significant difference.

Quantification of spindle angles at the beginning and at the end of metaphase showed that there is no difference in the orientation of the spindle when cells that complete mitosis enter metaphase or exit metaphase. Control cells oriented their spindle on average in an angle of  $5^\circ$  whereas in siRNA cells the spindle angle was  $9^\circ$ . At the end of metaphase, the spindle angle slightly increased for si-Control to  $6^\circ$  and remained  $9^\circ$  for si-ANXA1#1 (Figure 7.4, A). However, when spindle angles of individual cells were plotted it became evident that siRNA cells showed bigger changes from start to end of metaphase compared to the control (Figure 7.4, B). Calculation of the mean spindle angle during metaphase for all cells (independent of completing mitosis) highlighted that on average cells depleted of ANXA1 oriented their mitotic spindle at  $14^\circ$ . Control cells exhibited spindle angles of  $5^\circ$  showing that the orientation of the mitotic spindle was consistent in control cells throughout mitosis but varied when ANXA1 is absent in cells (Figure 7.4, C).



**Figure 7.4 Spindle angle measurements during metaphase in ANXA1-depleted cells**

(A) Quantification of spindle angles in control cells and ANXA1-depleted cells at the beginning and end of metaphase. Spindle angles were measured at the first frame of entering metaphase (Start meta) and at the last frame before anaphase onset (End meta) in cells completing mitosis imaged during time-lapse microscopy. Spindle angle  $\alpha_z$  was measured as the angle between the spindle axis and basement membrane. Meta, metaphase. Data represent individual cells with means (black dots)  $\pm$  SEM from three independent experiments. si-Control  $n=33$ , si-ANXA1#1  $n=25$ . Student t-test; n.s. no significant difference. (B) Spindle angle  $\alpha_z$  at the beginning of metaphase (Start meta) and at the end of metaphase (End meta) in si-Control and si-ANXA1#1 plotted from data in A. Data represent individual cells with means. si-Control  $n=33$ , si-ANXA1#1  $n=25$ . (C) Average spindle angle  $\alpha_z$  during metaphase in si-Control and si-ANXA1. Spindle angles were measured at every time point from the beginning of metaphase to the last frame before entering anaphase or if cells did not progress through mitosis until the cells died or the video ended. Data represent individual cells with means (black dots)  $\pm$  SEM from three independent experiments. si-Control  $n=33$ , si-ANXA1#1  $n=44$  cells. Student's t-test;  $*p \leq 0.05$ .

Tilted spindles upon ANXA1 depletion were confirmed by immunofluorescence and confocal microscopy. For this, cells were stained with anti- $\alpha$ -tubulin and anti- $\gamma$ -tubulin antibodies. Spindle poles of control cells were almost in the same z-plane. However, in siRNA cells, spindle poles were in different focal planes (Figure 7.5, A). Different locations of the poles within the z-axis indicated tilted spindles which was confirmed by measuring the spindle angles. For both siRNA constructs, spindle angles were greater than 15 ° whereas in the control spindle angles were on average 4 ° (Figure 7.5, B).

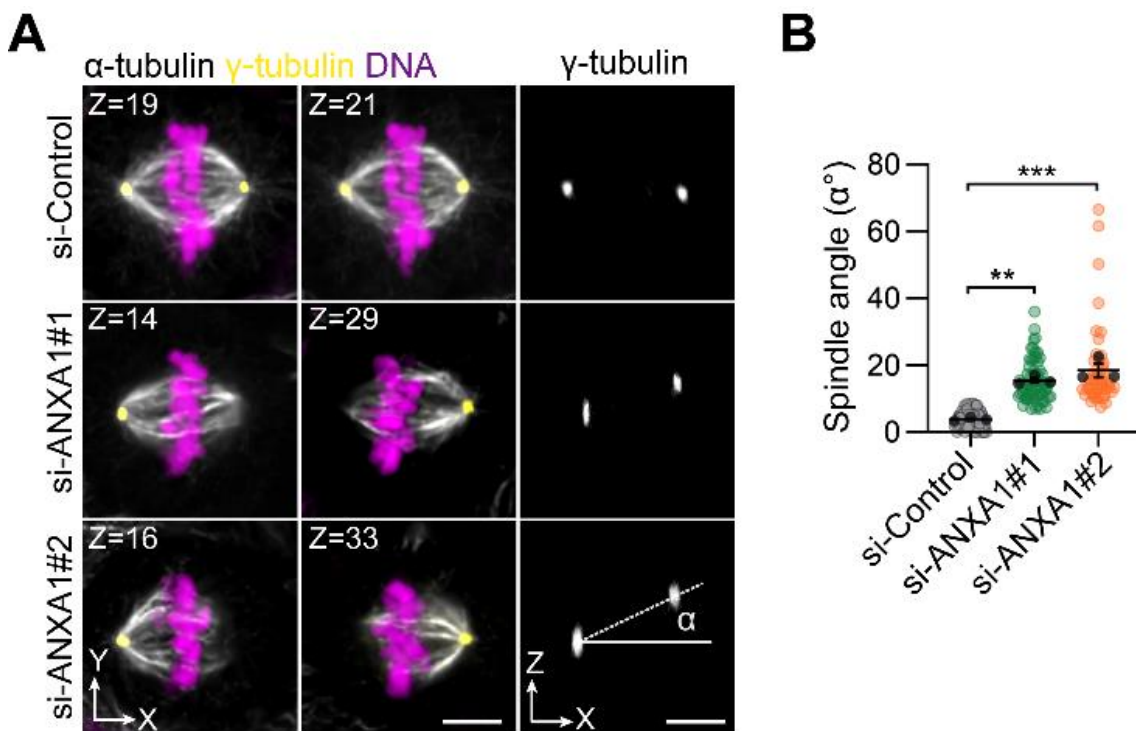


**Figure 7.5 ANXA1 depletion leads to spindle orientation defects**

(A) Representative confocal images of z-sections (0.2  $\mu\text{m}$  per stack). Cells were transfected with si-Control, si-ANXA1#1 or si-ANXA1#2 72 h prior to fixation with methanol. Cells were stained for  $\alpha$ -tubulin (grey) and  $\gamma$ -tubulin (yellow). DNA (magenta) was visualised with Hoechst 33342. Orthogonal views (xz) of the depicted cells ( $\gamma$ -tubulin signal) were used to measure spindle angle  $\alpha$  as illustrated. Scale bars, 5  $\mu\text{m}$ . (B) Quantification of spindle angles in control cells and ANXA1-depleted cells. Data represent individual cells with means (black dots)  $\pm$  SEM from three independent experiments. si-Control  $n=71$ , si-LGN#1  $n=65$ , si-LGN#2  $n=49$ . Student's t-test; \*\* $p \leq 0.01$ , \*\*\* $p \leq 0.001$ .

Similar to analysis of z-rotations, movements of the spindle in xy-plane were determined. The axis of the spindle (a line drawn across the middle of both spindle poles) was tracked from the start of metaphase until the last frame before entering anaphase or if cells did not progress through mitosis until the cells died or the video ended. ANXA1-depleted cells showed greater spindle angle movements compared to the control (Figure 7.6, A-B). This was quantified by calculating the oscillation index. Around 11 % of control cells showed a change of the spindle orientation  $> 10^\circ$  between two successive time points whereas this increased significantly in siRNA conditions where cells oscillated with a frequency of 29 % (Figure 7.6, C). Based on this, 92 % of ANXA1-depleted cells exhibited oscillations and 35 % of control cells oscillated at least once during metaphase (Figure 7.6, D). Quantification of the absolute and relative xy-rotation revealed no significant differences in the spindle orientation changes over time (Figure 7.6, E-F).

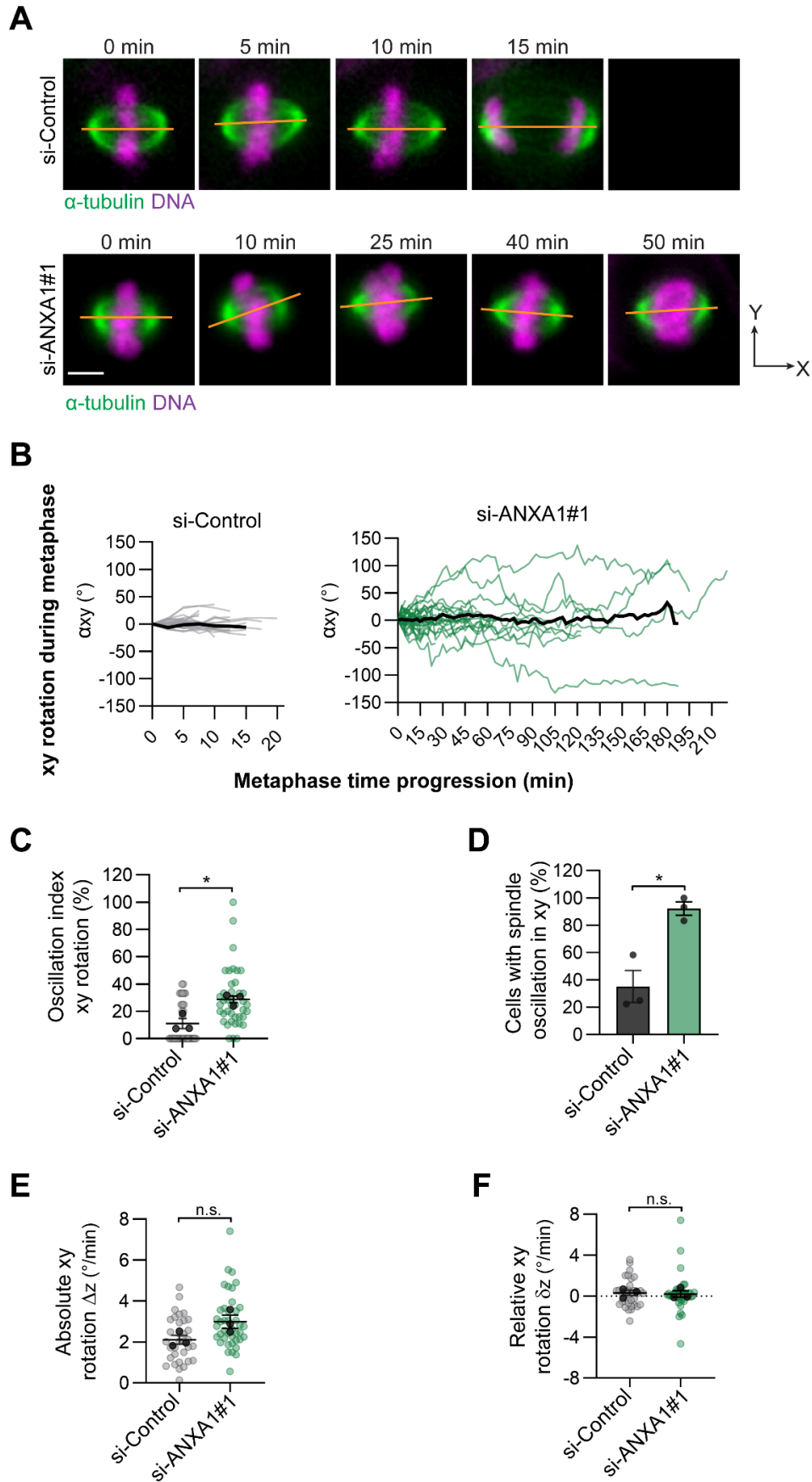


Figure 7.6 ANXA1 depletion leads to increased xy-rotations of the mitotic spindle

**Figure 7.6 Continued**

(A) Representative images in the xy-view from time-lapse microscopy of WT MCF-10A cells during metaphase in control cells and after ANXA1 depletion. Cells were transfected with si-Control or si-ANXA1#1 65 h prior to imaging. Before imaging, MTs were labelled with SiR-tubulin (green) for 2 h and DNA (magenta) was stained with Hoechst 33342 for 30 min. Images were acquired every 2.5 min. Orange line indicates spindle axis. Scale bar, 5  $\mu$ m. (B) Xy-rotation changes during metaphase in si-Control (left) and si-ANXA1#1 (right). Spindle angle  $\alpha_{xy}$  was measured as the angle between the initial spindle axis at the first frame of entering metaphase and the axis position at the current time point. Spindle angles were measured at every time point until the last frame before anaphase onset or if cells did not progress through mitosis until the cells died or the video ended. Grey and green lines correspond to individual cells. Black lines represent the average spindle angles of all analysed cells. (C) Quantification of the oscillation index for si-Control and si-ANXA1#1 representing frequency of mitotic spindles changing positions  $> 10^\circ$  between two successive frames in the xy-plane. Data represent individual cells with means (black dots)  $\pm$  SEM from three independent experiments. (D) Percentage of cells with spindle oscillations in the xy-plane in si-Control and si-ANXA1#1. Data represent means (black dots)  $\pm$  SEM from three independent experiments. (E) Absolute xy-rotation for si-Control and si-ANXA1#1 representing absolute xy-rotation changes per minute. Data represent individual cells with means (black dots)  $\pm$  SEM from three independent experiments. (F) Relative xy-rotations for si-Control and si-ANXA1#1 representing xy-rotation changes per minute with respect to directional changes. Data represent individual cells with means (black dots)  $\pm$  SEM from three independent experiments. For all graphs, si-Control n=33, si-ANXA1#1 n=44 cells. Student's t-test; \* $p \leq 0.05$ , n.s. no significant difference.

A striking observation during time-lapse microscopy was that mitotic spindles not only oscillated more frequently in the xy- plane, the spindle apparatus also changed location within the cell during metaphase. This was quantified by tracking the movement of the metaphase plate over time. Comparison of chromosome plate tracks during metaphase showed that ANXA1-depleted cells as well as control cells moved further away from the starting position (Figure 7.7, A-C). However, when measuring the distance between the starting point and the position before entering anaphase, control cells covered a significantly shorter distance compared to si-ANXA1#1 (Figure 7.7, D). Calculation of the speed of movement revealed no difference in how fast the mitotic spindle moved (Figure 7.7, E).

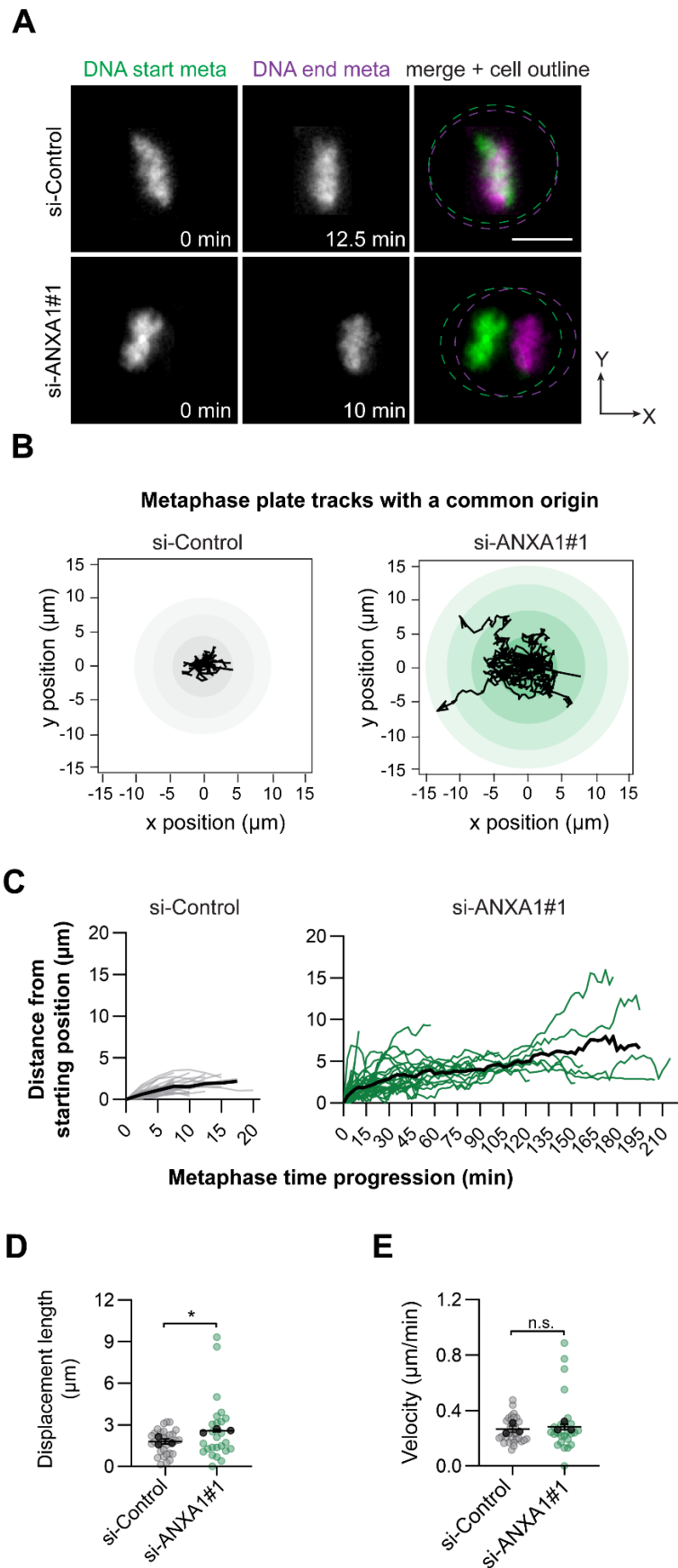


Figure 7.7 ANXA1 depletion leads to increased mitotic spindle displacement

**Figure 7.7 Continued**

(A) Representative images of the position of DNA metaphase plates at the start (green) and end of metaphase (magenta) from time-lapse microscopy of WT MCF-10A cells in control cells and after ANXA1 depletion. Cells were transfected with si-Control or si-ANXA1#1 65 h prior to imaging. DNA was stained with Hoechst 33342 for 30 min before imaging. Images were acquired every 2.5 min. Dashed lines indicate cell contours. Scale bar, 10  $\mu$ m. (B) Origin-aligned metaphase plate tracks in the xy plane of control cells (left) and ANXA1 depleted cells (right). Chromosome plates were tracked from the first frame of entering metaphase to the last frame before anaphase onset. Black lines correspond to individual cells. si-Control n=33, si-ANXA1#1 n=44 cells (C) Distance from starting position during metaphase in si-Control (left) and si-ANXA1#1 (right). Distance was measured as the length between the initial metaphase plate position at the first frame of entering metaphase and the position at the current time point. Distance was measured at every time point until the last frame before anaphase onset or if cells did not progress through mitosis until the cells died or the video ended. Grey and green lines correspond to individual cells. Black lines represent the average spindle angles of all analysed cells. (D) Displacement length from the starting point to the position at the end of metaphase in si-Control and si-ANXA1#1 that completed mitosis. (E) Velocity of metaphase plate movements for cells completing mitosis calculated by dividing the track length by the time cells spent in metaphase. For D-E, data represent individual cells with means (black dots)  $\pm$  SEM from three independent experiments. Si-Control n=33, si-ANXA1#1 n=25 cells. Student's t-test; \* $p \leq 0.05$ , n.s. no significant difference.

**7.2.3 Loss of ANXA1 alters astral microtubule dynamics**

To evaluate the observed effect of the spindle misplacement on structure of the spindle, immunofluorescence and confocal imaging was used to specifically analyse dynamics of astral MTs. In response to ANXA1 depletion, significant defects were observed. In control cells, the mitotic spindle localised in the middle of the cell with astral MTs extending evenly towards the closest cell cortex. In contrast, mitotic spindles in siRNA cells were misplaced and elongation and buckling of astral MTs were observed (Figure 7.8, A). This was confirmed by quantifying the ratio of astral MT length and the pole-to-cortex distance (Figure 7.8, B-C). The length of astral MTs in control cells were the same on both poles resulting in a ratio of around 1.0. However, the ratio increased to around 2.0 under siRNA conditions. Similarly, in control cells the distance from spindle poles to the cortex was the same resulting in a ratio of around 1.0, whereas it increased to 1.8 when ANXA1 was

depleted. Quantification of astral microtubule intensity revealed no difference indicating that the total number of astral microtubules did not change (Figure 7.8, D).

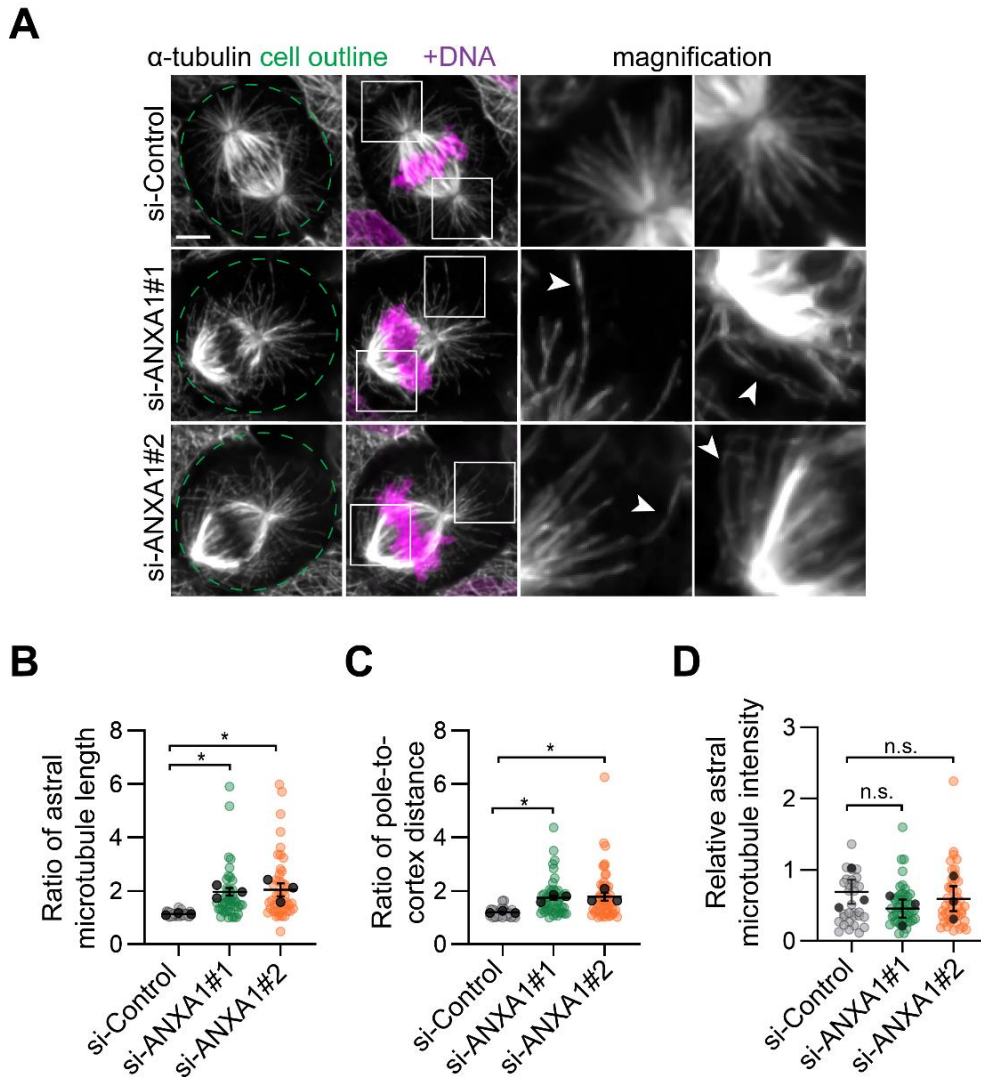


**Figure 7.8 ANXA1 depletion leads to astral microtubule defects**

(A) Representative confocal images of maximum intensity projections of astral microtubules. Cells were transfected with si-Control, si-ANXA1#1 or si-ANXA1#2 72 h prior to fixation with glutaraldehyde. Cells were stained for  $\alpha$ -tubulin (grey). DNA (magenta) was visualised with Hoechst 33342. Insets show magnified images of framed regions. White arrowheads indicate elongated and buckled astral microtubules. Green dotted lines outline the cell contour. Scale bar, 5  $\mu$ m. (B) Ratio of astral microtubule length in si-Control, si-ANXA1#1 or si-ANXA1#2 cells. (C) Ratio of pole-to-cortex distance in si-Control, si-ANXA1#1 or si-ANXA1#2 cells. (D) Relative astral microtubule intensity in si-Control, si-ANXA1#1 or si-ANXA1#2 cells. For all graphs, data represent individual cells with means (black dots)  $\pm$  SEM from three independent experiments. Si-Control  $n=31$ , si-ANXA1#1  $n=46$ , si-ANXA1#2  $n=47$ . Student's  $t$ -test; \* $p \leq 0.05$ , n.s. no significant difference.

Taken together, these results showed that ANXA1 depletion delayed mitotic progression and induced mitotic defects including spindle misassembly and chromosome segregation defects. Furthermore, knockdown of ANXA1 resulted in increased spindle rotation of the mitotic spindle in the z-axis and xy-plane leading to random spindle orientation and enhanced spindle movement. Lastly, ANXA1 depletion affected astral MT dynamics showing increased buckling and elongation.

### **7.3 Discussion**

Mitotic spindle assembly and segregation of chromosomes need to be tightly regulated and executed to allow accurate mitotic progression and cell division (Prosser and Pelletier, 2017). Failure in a mitotic phase can generate a snowball effect where one error leads to more defects and subsequently to abnormal mitotic outcome (Hayashi and Karlseder, 2013). Because ANXA1 regulates LGN localisation in early mitosis and loss of the protein creates defects in the accumulation of the spindle orientation machinery, it was intriguing to speculate that this had downstream effects on the following mitotic phases. To dissect this, mitotic spindle orientation and specific mitotic dynamics were studied.

#### **7.3.1 ANXA1 is required for accurate spindle assembly and mitotic progression**

Since mitosis involves a series of finely-tuned and regulated steps and therefore, the timing of these steps can vary for individual cells. This becomes specifically important when capturing, attaching and aligning chromosomes at the metaphase plate to allow correct chromosome segregation. Thus, individual cells may need more or less time to complete this step. Therefore, when analysing data from time-lapse imaging, mitotic events need to be investigated at the single-cell level and a sufficient numbers of cells are required to obtain statistically significant conclusions (Meijering *et al.*, 2008; Olziersky *et al.*, 2018). When applying this approach in this study, it became obvious that upon depletion of ANXA1, cells displayed a mitotic delay. Specifically, loss of the protein resulted in extraordinary long metaphase and a delay to anaphase progression. Sometimes cells died in this process which was an indication of an activated SAC (Visconti, Della Monica and Grieco, 2016). Previous studies investigating the role of MISP observed similar phenotypes. After depletion of the protein, the time for cells entering anaphase was drastically delayed and only 50 % of cells completed mitosis. The remaining cells were arrested in metaphase because the SAC was active. When investigating the presence of the SAC marker BubR1, it was not only detected in cells

with misaligned chromosomes leading to incorrect kinetochore-MT attachments and activation of the SAC, it was also observed weakly at kinetochores of correctly aligned metaphase plates (Musacchio and Salmon, 2007; Zhu *et al.*, 2013). Activation of the SAC was not investigated after ANXA1 knockdown. However, cells depleted of ANXA1 showed abnormal spindle phenotypes including aberrant bipolar spindles and multipolar spindles. Although, misaligned chromosomes were not observed, it is possible that the SAC was active. It can be speculated that defective spindle structures upon ANXA1 loss were still able to align chromosomes but had insufficient kinetochore-MT attachments or lacked tensions in the intra-kinetochore regions between sister chromatids. Therefore, it is conceivable that a functional metaphase state was not achieved and the SAC was activated to arrest cells in metaphase (Zhu *et al.*, 2013).

Another explanation for the mitotic delay may be the association of ANXA1 with endosomes. Recently, endosome-associated proteins have been implicated in mitotic dynamics and spindle assembly (Das, Hehnlly and Doxsey, 2015). For example, the proteins Rab5 and Rab11 associate with endosomes and deletion of the proteins lead to mitotic delay and SAC activation (Capalbo *et al.*, 2011; Hehnlly and Doxsey, 2014). Specifically, Rab11-endosomes organize around mitotic spindles and spindle poles to ensure proper spindle pole construction and MT tensions needed to satisfy the SAC. In this context, it was suggested that these endosomes act as carriers to recruit and organize MT nucleating- and spindle pole proteins to mitotic spindle poles through dynein which is essential for proper spindle assembly (Hehnlly and Doxsey, 2014). Since ANXA1 associates with endosomes, accumulates around the mitotic spindle and loss of the protein results in similar phenotypes as Rab11 deletion, it can be speculated that ANXA1 may affect spindle assembly and mitotic progression via endosome-linked mechanisms. Intriguingly, ANXAs have been proposed to have a regulatory role for Rab proteins, possibly through protein interactions (Rentero *et al.*, 2018). No specific mechanisms have been reported for this. Therefore, these results in this thesis unfold an exciting new field of future ANXA1 investigations for further functional exploration to dissect this possible link.

Not only did loss of the protein increase the number of cells unable to complete mitosis, for the proportion of cells that transitioned to anaphase, a vast amount displayed chromosome segregation defects. The observed chromosome bridges can arise from fused sister chromatids that are not correctly separated during metaphase-anaphase transition. Although, these defects are thought to mainly occur due to DNA replication defects, it is also possible that they can be caused by inaccurate mitotic spindle attachment (Finardi, Massari and Visintin, 2020). In this context, it was proposed that attachment of MTs to chromosomes is needed to remove proteins that hold

sister chromatid together. Furthermore, differential changes of kinetochore MT length, such as one shortens and the other opposing elongates during anaphase, may result in incorrect segregation (Pampalona *et al.*, 2016). Since loss of ANXA1 resulted in spindle assembly defects, it can be speculated that the formed spindles satisfied the SAC but led to unstable MTs and incorrect MT shortening causing bridging chromosomes. The occurrence of this segregation phenotype has been observed previously in mammalian cells that were depleted of regulators involved in spindle dynamics. For example, loss of the mitotic cortex tension regulator vimentin leads to chromosome bridges due to loss of a round cell shape during mitosis (Serres *et al.*, 2020). Similarly, depletion of Lis1 results in severe chromosome segregation defects (Faulkner *et al.*, 2000; Moon *et al.*, 2013). This highlights that correctly assembled spindles with established contacts of MTs to kinetochores and cellular space for the spindle to elongate at anaphase onset are critical for correct chromosome segregation. Based on the findings that ANXA1 loss leads to spindle assembly defects, it can be speculated that this subsequently resulted in chromosome segregation errors. However, if ANXA1 plays an active role in spindle assembly and/or alignment of chromosomes or if loss of the proteins influences spindle checkpoint regulation via other proteins involved in these dynamics remains elusive. In this context it is noteworthy that the LGN interactome identified proteins known to be involved in kinetochore- MT dynamics and silencing of the SAC which included Haus6 and Clasp1 (Lawo *et al.*, 2009; Manning *et al.*, 2010). Thus, it may be possible that there is an unknown link between ANXA1 and these proteins.

In conclusion, ANXA1 exerts a critical role in mitotic progression and faithful segregation of chromosomes. It will be interesting to investigate underlying ANXA1-dependent MT dynamics and mitotic progression with a possible connection to its endosomal regulatory dynamics.

### **7.3.2 ANXA1 enables proper mitotic spindle positioning and planar spindle orientation**

In the sequence of the different mitotic events, spindle positioning and orientation during metaphase is one of the most consequential processes because it dictates the division outcome for the daughter cells in a spatial manner (Morin and Bellaiche, 2011). The depletion of proteins that have been identified to control the localisation of the spindle orientation machinery has dramatic effects on the positioning and orientation of the mitotic spindle within cells (di Pietro, Echard and Morin, 2016). Similarly, depletion of ANXA1 resulted in displacement, excessive oscillation and misorientation of the mitotic spindle demonstrating the importance of the protein in correct mitotic spindle dynamics. Mitotic spindles showed rocking and flipping movements during metaphase which led to excessive oscillations of the spindle sometimes for hours when ANXA1 was depleted.

Interestingly, oscillation events were also observed in the control. This constitutes normal behaviour because it is common that spindle motilities including a variety of rotational as well as back and forth movements take place during metaphase to position the spindle (Larson and Bement, 2017). Usually, in cultured cells with a flat morphology and an intact spindle orientation regulation, the spindle orients parallel to the growth surface and in the centre along the longest axis of the cell. Depending on the position of the spindle at the onset of metaphase, the spindle undergoes more or less stereotyped extensive rotation in the xy-plane but ultimately the spindle orients within  $\sim 10^\circ$  of its final orientation at anaphase onset. Thus, spindles exert relatively short or long rotations depending on the initial orientation that is either close or far from the final position. Besides these rotations, spindles also undergo movements back and forth where they move away from the centre, close to the cortex and back (Adams, 1996; Peyre *et al.*, 2011; Larson and Bement, 2017; Lee *et al.*, 2018). Because these movements were observed in control conditions when ANXA1 was present, it can be concluded that these oscillations are part of the normal mitotic processes in mammary epithelial cells. However, an unanswered question is why the spindle exerts movements and rotations even if it already starts with an almost ideal position at the entry of metaphase. It is possible that oscillations and movements represent a type of testing behaviour where the spindle probes the cortex to find a signal for the correct or “ideal” location. This would be a location within the correct cell axis, such as the longest axis and parallel to the substratum in cultured cells. Furthermore, this would also correspond to the cortical accumulation of the spindle orientation machinery that ensures proper positioning in the correct axis and helps to centre the spindle. Once this is achieved, anaphase onset can be triggered which suggests that oscillation serves as a part of mechanisms ensuring anaphase onset only when spindles are correctly positioned (O’Connell and Wang, 2000; Larson and Bement, 2017).

Although it has been shown that misoriented spindles can delay anaphase, eventually cells do progress through mitosis. Thus, it may be possible that misplaced spindles can trigger metaphase arrest to some extent but further regulations may be involved that trigger mitotic progression (Samora *et al.*, 2011; Dunsch *et al.*, 2012; Zhu *et al.*, 2013). Nevertheless, this hypothesis would explain why oscillation was detected in the control and furthermore, it highlights that this could have also triggered the longer metaphase period in ANXA1 depleted cells. Upon loss of ANXA1, excessive oscillation was observed in all axes indicating that spindle orientation was vastly disturbed. The effect was observed immediately after entry into metaphase, implying that this was not caused by the prolonged metaphase and mitotic arrest. It can be speculated that the misplacement of the spindle orientation machinery described in the last chapter (Chapter 6) caused the errors in spindle positioning. Based on the hypothesis that the mitotic spindle might search the

cortex for the ideal location, it might have been unable to find that signal needed for the correct localisation within the cell because the spindle orientation machinery was not able to catch and position the spindle in the right axis. It can be excluded that movement of the spindle itself was impaired upon loss of ANXA1, because the absolute rotations in the z- and xy-plane were not different to the control. Furthermore, the relative rotations were similar which allows to conclude that the mitotic spindle did not show a specific directional biased movement away from the original orientation. Hence, the orientation defects observed in ANXA1-depleted cells were more likely to occur due to a failure of orienting the spindle in the right position and not from the inability to move the spindle (Saadaoui *et al.*, 2014). One explanation for the oscillations and excessive movements may be the impaired astral MT dynamics that were observed. Under normal conditions, astral MTs establish a contact with the cell cortex which leads to catastrophe and shrinkage needed for optimal MT length and positioning of the mitotic spindle (di Pietro, Echard and Morin, 2016). However, in a deregulated state astral MT can continue to grow along the cell cortex. For instance, uncontrolled MISP levels lead to unstable and elongated astral MTs because the link between plus-ends and dynein/dynactin is lost. Consequently, a proper attachment at the cell cortex is disturbed which result in spindle positioning defects (Zhu *et al.*, 2013; Kschonsak and Hoffmann, 2018). Similarly, depletion of Clasp1 and the MT-associated protein MAP4 induces pushing and depolymerisation-uncoupled pulling events where the spindle is destabilized and misoriented (Samora *et al.*, 2011). It is likely that impaired localisation of LGN and NuMA causes improper association of dynein/dynactin and astral MTs which leads to incorrect spindle positioning (Bird, Heald and Weis, 2013). Since loss of ANXA1 interfered with the localisation of the LGN complex, it can be speculated that this led to stabilization of MTs resulting in continuous growth and buckling of astral MTs which was observed as elongated MTs pushing against the cell cortex. Astral MT intensity was similar to the control upon loss of ANXA1 indicating that the nucleation of MTs was not affected. Thus, the defects were rather a consequence of unbalanced spindle-to-cortex connections initiated by the disturbed dynein/dynactin localisation which resulted in unbalanced forces on the mitotic spindle and subsequently displacement of the spindle away from the cell centre (Kschonsak and Hoffmann, 2018). It would be interesting to track the dynamics of astral MTs in live cell imaging experiments which would allow to determine if astral MTs are more stable and long-lived upon ANXA1 loss. Furthermore, to test whether observed effects stem from unbalanced forces generated by a defective cortex-to-spindle association, cells could be treated with low doses of nocodazole. Reestablishment of spindle positioning defects after treatment would verify that unbalanced forces generated the misplacement of the mitotic spindle. It is intriguing to speculate this scenario because it is possible that ANXA1 maintains balanced forces on astral MTs by regulating MT-actin

crosstalk at the cell cortex. ANXA1 interacts with vimentin which was recently shown to control the actin network organization during mitosis and ensures proper mitotic progression (Xiao *et al.*, 2017; Duarte *et al.*, 2019; Serres *et al.*, 2020). Furthermore, ANXA1 can directly bind and bundle F-actin (Glenney, Tack and Powell, 1987; Schlaepfer and Haigler, 1987). Thus, it may be possible that ANXA1 regulates the interplay between the actomyosin cortex and the spindle via the spindle orientation machinery. However, further studies will be needed to uncover the mechanisms of this potential ANXA1-mediated regulation of actin dynamics and the crosstalk with spindle dynamics to better understand the role of the protein in regulating spindle orientation via cortical pulling forces.

Ultimately, the defect in spindle positioning resulted in a more perpendicular orientation of the spindle in the z-axis rather than parallel to the substratum. Interestingly, for ANXA1-depleted cells that completed mitosis, the spindle angle was not significantly different to the control at the beginning of metaphase or at the end before anaphase onset (although there was a trend to increased spindle angles). However, spindle angles were on average higher during metaphase. It is possible that ANXA1-depleted cells were initially able to position the mitotic spindle in a more planar orientation at the entry of mitosis because of the stereotypical positioning along the longest cell axis in cultured cells, although the LGN complex was misplaced (Bosveld *et al.*, 2016). However, because of oscillations to find the signal for the best localisation, the cells may have continued to oscillate and the maintenance of the planar orientation may have failed. Spindle oscillation throughout metaphase and later stages is LGN- and MT-dependent and possibly regulated by MT dynamics via actin mechanisms that anchor the spindle to the cortex (Corrigan *et al.*, 2013). Therefore, oscillations with constant changes between planar to perpendicular orientations due to astral MT defects and inability to anchor the spindle to the cortex due to absent dynein/dynactin, may have resulted in higher measured spindle angles during metaphase. Based on this, it may be possible that the SAC was inactivated sometimes when the spindle was positioned in a planar orientation leading to progression of some ANXA1-depleted cells, whereas it remained active for other cells. In fact, previous studies reported that cells with misoriented spindles can delay anaphase but eventually progress through mitosis. However, the exact cause and mechanisms for this is not known (Samora *et al.*, 2011; Dunsch *et al.*, 2012). Nevertheless, higher measured spindle angles during metaphase reflect a random orientation of the mitotic spindle upon ANXA1 depletion (Zhu *et al.*, 2013).

In conclusion, ANXA1 regulates mitotic spindle assembly and proper mitotic progression by fostering an orientation of the mitotic spindle parallel to the surface which allows planar cell division in mammary epithelial cells.

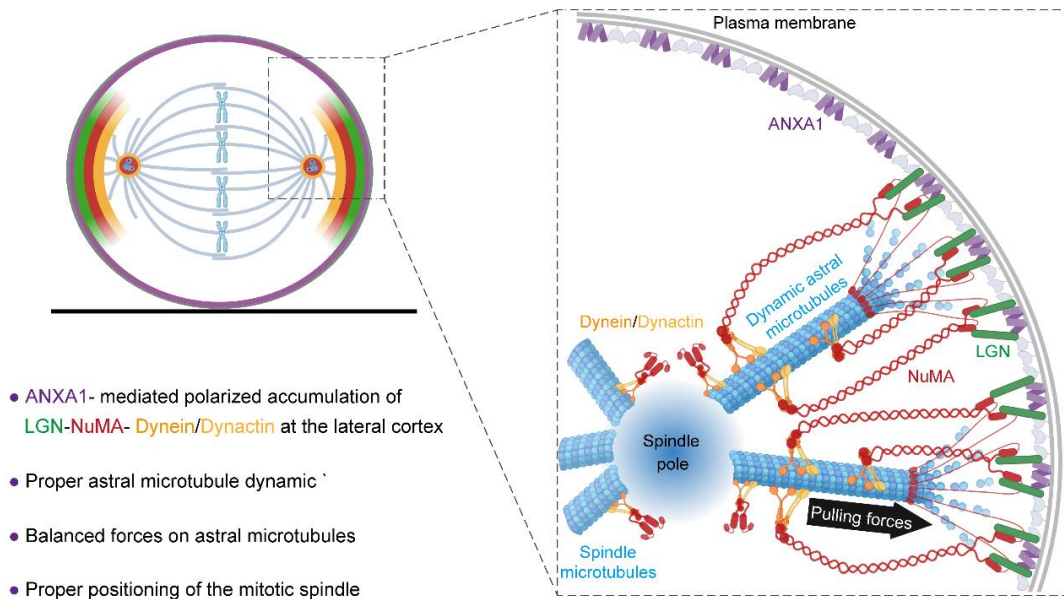
## **Chapter 8    General discussion and future directions**



## 8.1 Summary

Research over the past decades has provided the knowledge that not only correct formation of the mitotic spindle is essential but this must also be coupled to proper positioning of this structure for normal tissue development and function (di Pietro, Echard and Morin, 2016). A variety of mechanisms can regulate spindle orientation and new regulators are constantly discovered. However, clear differences in tissue mechanisms exist which make a complete understanding difficult. Therefore, it is essential to identify specific machineries in distinct cell types which will help to elucidate the effects of disrupted spindle orientation in the tissue of interest (Lechler and Mapelli, 2021). This specific knowledge is also needed for the mammary gland because key regulators are missing. The data presented in this thesis discovered ANXA1 as a novel intrinsic cue of OCDs in mammary epithelial cells that promotes planar spindle orientation. The protein was identified by investigating the cortical LGN interactome during spindle orientation at metaphase in mammary epithelia cells that were engineered to express GFP-LGN. This was the first time that a complete set of proteins was identified that associated with LGN in mammary cells. Within the list of proteins were proteins with previously undescribed functions in mitosis. One of these was ANXA1 which was confirmed as a novel partner of LGN. Characterisation of ANXA1 revealed for the first time a spatiotemporal localisation within the cell during the cell cycle. Specifically, the protein distributed along the cell cortex with exclusion at lateral sites during prometaphase but a uniform localisation during other stages of mitosis. Furthermore, ANXA1 exhibited an accumulation in vesicular structures around the mitotic spindle. Co-localisation with LGN showed that the two proteins displayed a mutual exclusion localisation at the cell cortex during prometaphase but overlap at the lateral cortex during metaphase. Functional characterisation of ANXA1 revealed a precise mechanism for the protein in restricting and polarising LGN to lateral sites during prometaphase and possibly stabilizing this localisation in metaphase which allows recruitment of NuMA and the dynein/dynactin complex to the lateral cortex in a G $\alpha$ i-independent mechanisms. Subsequently, ANXA1 mediates correct spindle assembly and spindle orientation via proper astral MT dynamics. Together, this work described a function of ANXA1 in mitosis and revealed a novel mechanisms of mitotic spindle orientation in mammary epithelial cells (Figure 8.1).

### A Normal mitotic spindle orientation



### B Mitotic spindle orientation without ANXA1

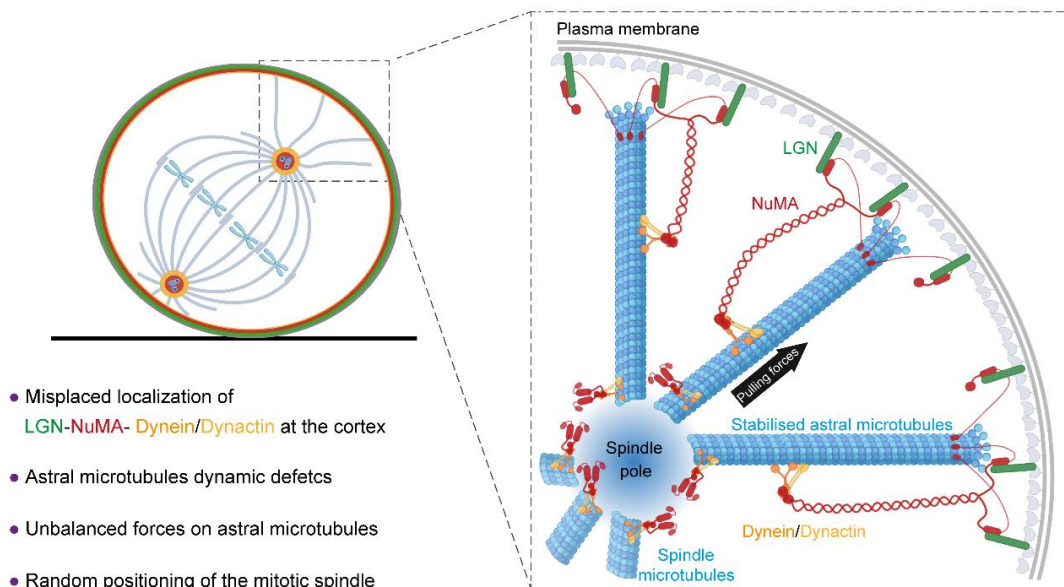


#### Figure 8.1 Proposed model for ANXA1 regulation of planar mitotic spindle orientation

(A) During metaphase, ANXA1 distributes at the cell cortex and associates with LGN to instruct the polarised localisation of the LGN/NuMA/dynein/dynactin complex lateral sites. The dynein/dynactin motor complex in conjunction with NuMA generates balanced pulling forces on astral microtubules to ensue planar orientation of the mitotic spindle. (B) Loss of ANXA1 results in misplacement of LGN/NuMA/dynein/dynactin. This affects the length and stability of astral microtubules leading to unbalanced forces and subsequently to random spindle orientation.

## 8.2 Binding dynamics of ANXA1 and LGN in mitotic and interphase mammary epithelial cells

With the novel findings in this thesis showing that ANXA1 polarizes LGN to the lateral cortex which promotes proper formation of the spindle orientation machinery it remains an open question how this protein recruitment is regulated. ANXA1 binds with its core C-terminal domain to plasma membranes and the N-terminal domain is exposed and free for interactions (Fu *et al.*, 2020). It seems more likely that ANXA1 would modulate LGN dynamics via the N-terminal domain because this comprises the region where binding sites for other interactors have been identified for individual ANXA members whereas the C-terminus is shared by all ANXAs. Therefore, the N-terminal regions constitutes the physiological activity of ANXA1 (Gerke, Creutz and Moss, 2005). Which part of LGN may associate with ANXA1 is more complex. Based on past studies several binding dynamics would be possible. The first but less likely option is an association via the C-terminal domain where Gai subunits bind to the GoLoco motifs of LGN (Willard, Kimple and Siderovski, 2004). These motifs specifically bind G $\alpha$  subunits and no other protein to date has been shown to interact with these domains (Siderovski, Diversé-Pierluissi and De Vries, 1999). Therefore, it seems more favourable if ANXA1 bound to the linker region or TPR domains of LGN. In fact, other LGN regulators have been identified to associate with these parts of the protein. For example, Dlg1 interacts with LGN via its linker region (Saadaoui *et al.*, 2014). If ANXA1 interacted with the same region it would allow simultaneous binding to Gai subunits for anchoring at the cell cortex during metaphase. The last option would be an association with the TPRs. Most studies that identified binding sites of spindle orientation regulators on LGN showed that these proteins interact with TPR regions including NuMA, E-cadherin, Afadin and mINSC (Du and Macara, 2004; Culurgioni *et al.*, 2011; Carminati *et al.*, 2016; Gloerich *et al.*, 2017). Because Afadin and mINSC bind to LGN TPR regions that also interact with NuMA a mutually exclusive association was suggested (Culurgioni *et al.*, 2011; Carminati *et al.*, 2016). ANXA1 binding to TPR regions may also compete with NuMA binding. Therefore, the dynamics of ANXA1 may include a sequential localisation where LGN is localised to the lateral cortex by ANXA1, then LGN binds to Gai and lastly recruits NuMA to the cell cortex (Culurgioni *et al.*, 2011; Carminati *et al.*, 2016). All these hypotheses highlight that several possibilities exist how ANXA1 may act on LGN. In general, protein interactions are highly specific and are determined by structural and physico-chemical properties of the two interacting proteins. Thus, a certain conservation exists in the interaction patterns of proteins and the number of interaction types is limited (Shoemaker and Panchenko, 2007). Thus, it can be speculated that

ANXA1 exerts functions on LGN with similar mechanisms as described for the other LGN regulators. However, these hypotheses can only be tested experimentally. Therefore, mapping the binding sites will be essential in the future to reveal the possible ANXA1-LGN interaction to gain a better knowledge how ANXA1 modulates polarised LGN localisation at the cell cortex. Additionally, this would also provide a better understanding how ANXA1 dynamics work in conjunction with NuMA and Gai subunits. This will ultimately elucidate a similar or new mechanism of recruitment of the LGN complex to the cell cortex during mitosis in mammary epithelial cells.

Besides the novel identified association of ANXA1 and LGN during mitosis another interesting dynamic of the proteins was observed. When analysing close proximity using PLA an association between the proteins was detected in interphase cells. This raises the question whether the proteins only share the same localisation or if this possible association is physiological relevant. Recently, LGN was identified to have additional functions during the cell cycle besides regulating spindle orientation during mitosis. These include a role in cell adhesion and migration of endothelial cells and neutrophils by altering MT dynamics during interphase (Kamakura *et al.*, 2013; Wright *et al.*, 2015). This is interesting because ANXA1 is also involved in endothelial migration (Pin *et al.*, 2012). No specific mechanisms for both of the proteins have been described in this context however, these studies provided a mutual function of LGN and ANXA1. Whether these functions are in conjunction remains unanswered but with the discovery in this thesis, it unfolds an exciting new area of research where this interphase association between the proteins will be an interesting target to further characterise the roles of LGN and ANXA1 during the cell cycle.

### **8.3 Regulation of ANXA1 function in oriented cell divisions**

While possible mechanisms on how ANXA1 regulates LGN localisation and mitotic spindle dynamics have been discussed earlier, it remains open how ANXA1 itself may be controlled to exert its novel discovered function. Several ANXA1 mechanisms have been described in the past that can be an interesting target of how the protein is regulated to act on LGN (Gerke and Moss, 2002; Gerke, Creutz and Moss, 2005). In this context its binding partner S100A11 may be an important protein in facilitating the cortical localization of ANXA1. A complex of these two proteins forms to accumulate at the inner leaflet of plasma membranes in the presence of  $\text{Ca}^{2+}$ . This complex regulates several pathways including epidermal differentiation and cell migration and depletion of the S100A11 binding greatly disrupts normal ANXA1 function (Poeter *et al.*, 2013; Bizzarro *et al.*, 2019). Although more specific mechanisms are not known and the dynamics for this complex

formation has yet to be identified, it is intriguing to speculate that S100A11 may be essential for ANXA1 functions in the context of its spatiotemporally controlled localisation during the cell cycle. Intriguingly, S100A11 was identified in the LGN interaction network in this thesis suggesting an ANXA1/S100A11 complex may have been part of the cortical interactome. However, only further experiments can elucidate the involvement of S100A11 in ANXA1-mediated regulations of the spindle orientation machinery.

Another aspect of the regulation of ANXA1 functions is posttranslational modifications including phosphorylation which has been shown to be essential for its localisation within cells (D'Acunto *et al.*, 2014). Especially, the TRPM7 channel-kinase has been identified to phosphorylate ANXA1 which is crucial for its membrane binding and association with S100A11 (Dorovkov and Ryazanov, 2004; Dorovkov, Kostyukova and Ryazanov, 2011). This shows that ANXA1 phosphorylation is essential for its cortical localisation however, although phosphorylation is accepted as regulatory properties, studies could not provide a detailed understanding of the mechanisms of action so far (D'Acunto *et al.*, 2014). Nevertheless, other LGN regulators are known to be phosphorylated to exert their specific function. For example, MISPL is phosphorylated by PLK1 to accumulate at the cell cortex allowing interaction with dynactin and astral MTs to orient the mitotic spindle (Zhu *et al.*, 2013). Similarly, ERM proteins are activated by phosphorylation to localise at the cell cortex and regulate mitotic spindle orientation (Machicoane *et al.*, 2014). Thus, phosphorylation constitutes a mechanism to control LGN regulators and may be an option to explore how ANXA1 is regulated. In conclusion, how ANXA1 is regulated to accumulate at specific cortical regions during the cell cycle was not answered in this thesis however, the knowledge that the ANXA1/S100A11 complex is essential for ANXA1 dynamics and phosphorylation determines the protein's localisation within cells, it unfolds several options for the regulation of specific ANXA1 mechanisms.

#### **8.4 Regulators of mitotic spindle orientation in the mammary gland and as universal mechanisms in epithelial systems**

Systematic approaches to identify the patterns of protein interactions that underlie complex processes are necessary to understand biological questions (Xing *et al.*, 2016). Such approach was used in this thesis where a broad proteomics experiment identified the LGN interactome in mitotic mammary cells to lay the foundation for understanding the key players of mitotic spindle orientation in the mammary gland. Interestingly, many of the proteins in the LGN subnetwork have been identified as regulators of OCD in other epithelial systems including polarity cues and regulators of the spindle orientation complex (discussed in chapter 4.3.3). Although it has been

shown that tissues regulate OCDs differently and even mechanisms of spindle orientation in distinct cell types may vary, it may be possible that some tissues share the same regulatory mechanisms (Finegan and Bergstralh, 2019; van Leen, di Pietro and Bellaïche, 2020). For example, the long-axis rule applies to multiple systems (O'Connell and Wang, 2000; Minc, Burgess and Chang, 2011; Lázaro-Diéguez, Ispolatov and Müsch, 2015) but not all (Scarpa *et al.*, 2018; Finegan *et al.*, 2019). Similarly, PCP may be essential for spindle orientation in some epithelia (Ségalen *et al.*, 2010) but dispensable in others (Box, Joyce and Devenport, 2019). These examples show that some redundancy in cell geometry and polarity cues exist to regulate OCDs. However, if specific intrinsic cues also promote similar functions in different epithelia is less well understood mainly because studies have been focussing on investigating the protein-of-interest in a specific cell type to dissect its specific function due to the known tissue-specific mechanisms of spindle orientation (Lechler and Mapelli, 2021). Therefore, there is a lack of expansion of the knowledge from one epithelial system to another which left the current view on OCDs with a long list of regulators but no complete understanding of an integrated mechanism of several regulators (di Pietro, Echard and Morin, 2016). Therefore, it might be possible that several intrinsic cues have linked functions that have not been proven by experiments. The proteomics study of this thesis would support this hypothesis. While it cannot be ruled that the known regulators of spindle orientation found in the LGN network were not involved in the regulation of OCD in the context of mammary epithelial cells, their presence at least indicates that they have roles in this tissue. Therefore, they may have further functions in other epithelia than had been previously characterised. This may also be true for ANXA1. Past studies that have tested the protein-of-interest in other epithelial cell types found that for example PLK1 exerts its functions in several human epithelial cell lines (Sana *et al.*, 2018). Similarly, Dlg1 is essential for LGN recruitment in several epithelia including neuroepithelial cells and cultured HeLa cells (Saadaoui *et al.*, 2014). This suggests that ANXA1 may also play similar functions in other epithelia. However, this hypothesis can only be validated with further experiments because a universal mechanism does not exist and previous studies have also proven that some proteins regulate LGN dynamics in certain cell types but not in others. One such regulator is aPKC that promotes lateral accumulation of LGN by exclusion from apical sites in MDCK cells (Hao *et al.*, 2010). However, this lateral localization is aPKC-independent in the chick neuroepithelium (Peyre *et al.*, 2011). This highlights that mechanistic variations, especially regulation of LGN dynamics, are known and every newly identified regulator adds complexity to the understanding of spindle orientation which has to be analysed systematically in various tissues to unfold its functions (Vorhagen and Niessen, 2014; Seldin and Macara, 2017). Since this study constitutes the first description of ANXA1 involvement in mitosis, specifically in mammary epithelial cells but the

protein is expressed in many tissues it will be exciting to investigate ANXA1 dynamics in other epithelial types. This will help to elucidate if ANXA1 exerts mammary epithelia- specific functions or if they can be translated to other systems.

## **8.5 ANXA1 mediates planar spindle orientation in an *in vitro* cell culture model**

Besides translating the investigated mechanism of ANXA1 function to other epithelial cell types, it remains also open if the protein exerts a similar polarisation of LGN to the lateral cortex to promote planar divisions in a tissue setting. In this thesis, the novel function of ANXA1 was identified in an *in vitro* system. When using a 2D culture system cells lack their local environment including interactions with the extracellular environment and other cell types which may be critical for the tested hypothesis (Nestor-Bergmann, Goddard and Woolner, 2014). Especially, when studying OCDs, the tissue environment is important to orient the mitotic spindle. Furthermore, in a culture system cells tend to orient the mitotic spindle within the longest cell axis (Finegan and Bergstralh, 2019). This was also true for MCF-10A cells that oriented their spindle mostly planar to the substratum which was similar to previous studies in MCF-10A (Mitsushima, Toyoshima and Nishida, 2009; Porter *et al.*, 2019). In order to validate that measurements of spindle orientation in the 2D culture system was reliable to screen for mechanism and regulators, a high amount of cells was screened (Decarreau *et al.*, 2014). By using this approach, it was determined that ANXA1 knockdown influences spindle orientation significantly *in vitro*. Furthermore, based on other observed mitotic defects upon ANXA1 depletion the 2D system allowed to identify a possible mechanism of ANXA1-mediated recruitment of LGN/NuMA/dynein/dynactin to the lateral cortex to promote proper contact with astral MTs that promotes mitotic spindle positioning. Therefore, the chosen study system served the purposed of identifying a novel mechanisms of OCD in mammary epithelial cells. However, in future work the gained knowledge may be expanded to *in vivo* systems or models that more closely resemble the physiological environment to overcome the limitation of the 2D culture system. This approach has been used in the past to gain further insight into NuMA dynamics and its involvement in active force generation to orient the mitotic spindle (Seldin, Muroyama and Lechler, 2016). By expanding the novel identified function of NuMA from a cell culture system to an animal model it was shown that NuMA MT binding is essential for spindle orientation in a tissue context (Seldin, Muroyama and Lechler, 2016). Interestingly, investigation of Dlg1 function in cultured cells and in a tissue context revealed a homogenous distribution of the protein at the cell cortex in cultured cells but showed a polarised localisation in a tissue showing

that dynamics of proteins may vary between *in vitro* and *in vivo* systems (Saadaoui *et al.*, 2014). Therefore, testing novel protein functions *in vivo* constitutes an ideal tool to clarify the underlying mechanisms. Applying this approach for ANXA1 would allow to investigate the influence of the tissue environment on the novel mechanisms and the dynamics of the protein. Therefore, using mouse models may help to furtherer dissect ANXA1 dynamics in the mammary gland *in vivo*. Furthermore, ANXA1 knockout mice have been produced in the past that can be an excellent model system to investigate how loss of ANXA1 affects mammary gland development (Hannon *et al.*, 2003). ANXA1 knockout mice are viable and breed normally without obvious physical or behavioural differences indicating that organs function normally. In the past, these mice were mainly used as disease models such as for acute and chronic inflammation, obesity and cancer and it revealed essential biological functions of ANXA1. This highlights that an ANXA1 mouse model might be a valuable tool to study more basic processes such as mitotic spindle orientation (Grewal *et al.*, 2016; Foo *et al.*, 2019). Intriguingly, these *in vivo* models may also allow to investigate the link between cell fate, spindle orientation and tissue architecture. The study of this connection is complex and involves advanced genetic and imaging tools to track the outcome of divisions which could not be analysed with the *in vitro* system used in this thesis (Rizzelli *et al.*, 2020). Therefore, the expansion to *in vivo* models can be the next step to examine how ANXA1 regulates mitotic spindle orientation in a tissue environment and how deregulation of the protein can influence division modes and tissue architecture.

An alternative to animal work, may be the use of 3D culture systems. This could be stem-cell derived organotypic 3D cultures (organoids) that form structures with multiple cell types or spheroid structures that are formed from epithelial cells only (Sakalem *et al.*, 2021). The concept of 3D cultures is widely adapted where structures form various layers which has the advantage that cells can establish proper cell-cell and cell-environment contacts where cells obtain stimuli from the surrounding. Thus, structures are formed that more closely imitate tissues (Kapałczyńska *et al.*, 2018; Jensen and Teng, 2020). Such an approach was used when investigating Afadin (Carminati *et al.*, 2016). The group used a 2D culture system to identify a role of the protein in mitotic spindle orientation and confirmed the functional relevance of Afadin using a 3D culture system. With this approach it was confirmed that the protein is required for planar spindle orientation (Carminati *et al.*, 2016). Similarly MISP function was confirmed in a 3D culture system (Kschonsak and Hoffmann, 2018). Therefore, 3D culture systems are ideal system to investigate the role of ANXA1 in the morphogenesis of polarized mammary epithelia. Growth of mammary epithelial cells in 3D spheroids and organoids is well established where lumen formation is observed that recapitulates mammary morphogenesis *in vivo* (Mailleux, Overholtzer and Brugge, 2008; Jamieson *et al.*, 2017).

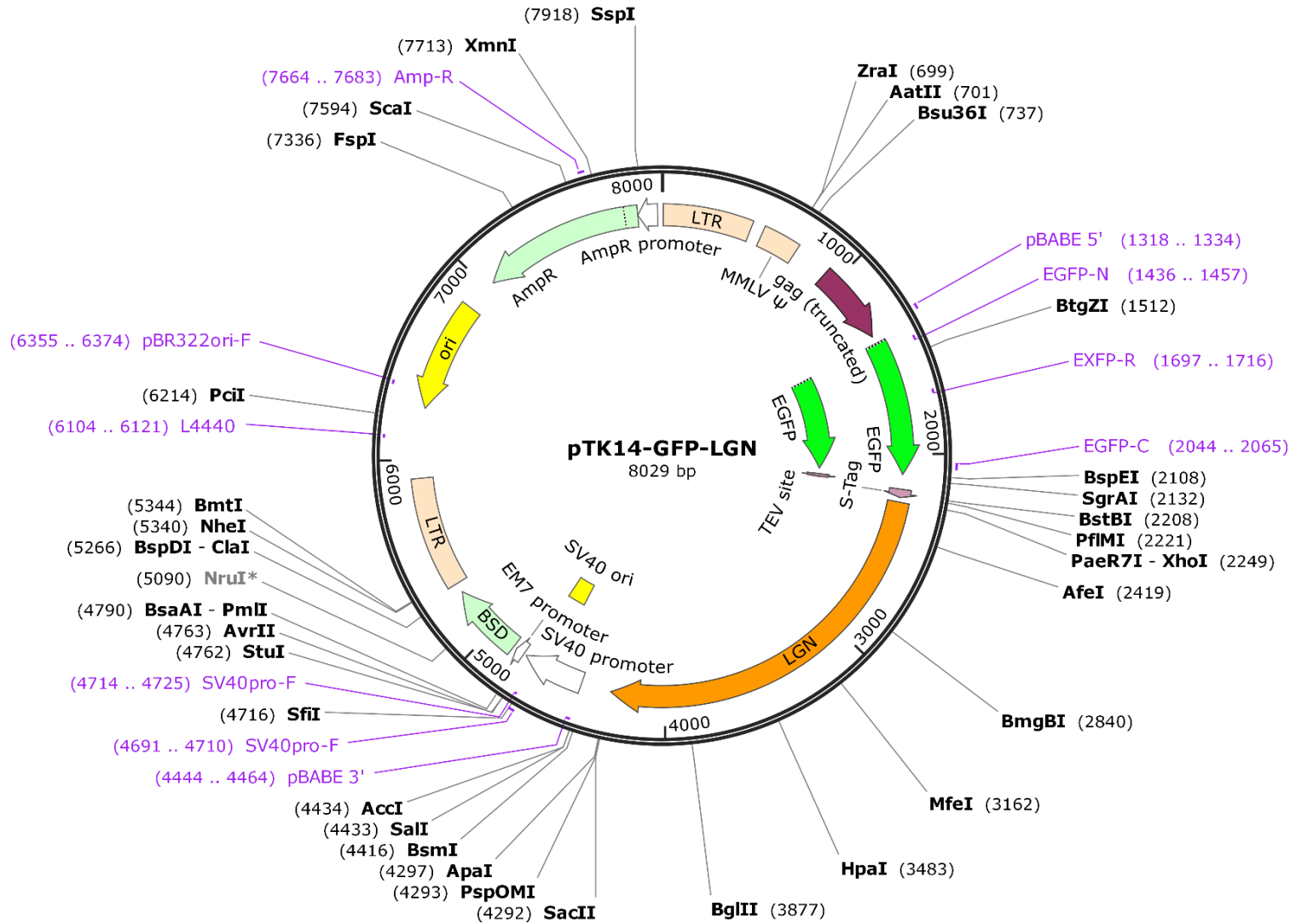
Mammary spheroids have been used in the past to study the link between mitotic spindle orientation and normal development. For example, work investigating the cancer-related protein Stat3 showed that it is needed for correct spindle orientation that allows normal cell division and proper lumen formation in 3D cultures (Morris *et al.*, 2020). Similarly, the protein Connexin 43 is essential for proper apicolateral polarity which ensures proper mitotic spindle orientation and normal epithelial organization in mammary spheroids (Bazzoun *et al.*, 2019). Interestingly, these studies also showed that deregulation of the mechanisms investigated lead to loss of epithelial polarity and multiple lumen formation which was suggested to play a role in cancer progression (Gray, Cheung and Ewald, 2010). Intriguingly, polarity proteins were identified in the proteomics data which suggests that ANXA1 may function in connections with polarity factors. Thus, ANXA1 mechanisms may induce similar epithelia tissue architecture defects and polarity loss when spindle orientation is deregulated as seen in other regulators. Therefore, the use of 3D culture systems will be an excellent model systems to investigate how ANXA1 mechanisms adapt in a more physiological environment under the influence of extracellular stimuli and challenges. This will help to explore ANXA1-regulated mitotic spindle orientation during normal mammary gland morphogenesis but may also contribute to the understanding how deregulation may lead to uncontrolled OCDs and how defective epithelial architecture may progress to cancer.

## Appendix A Plasmid maps of retroviral transfer vectors

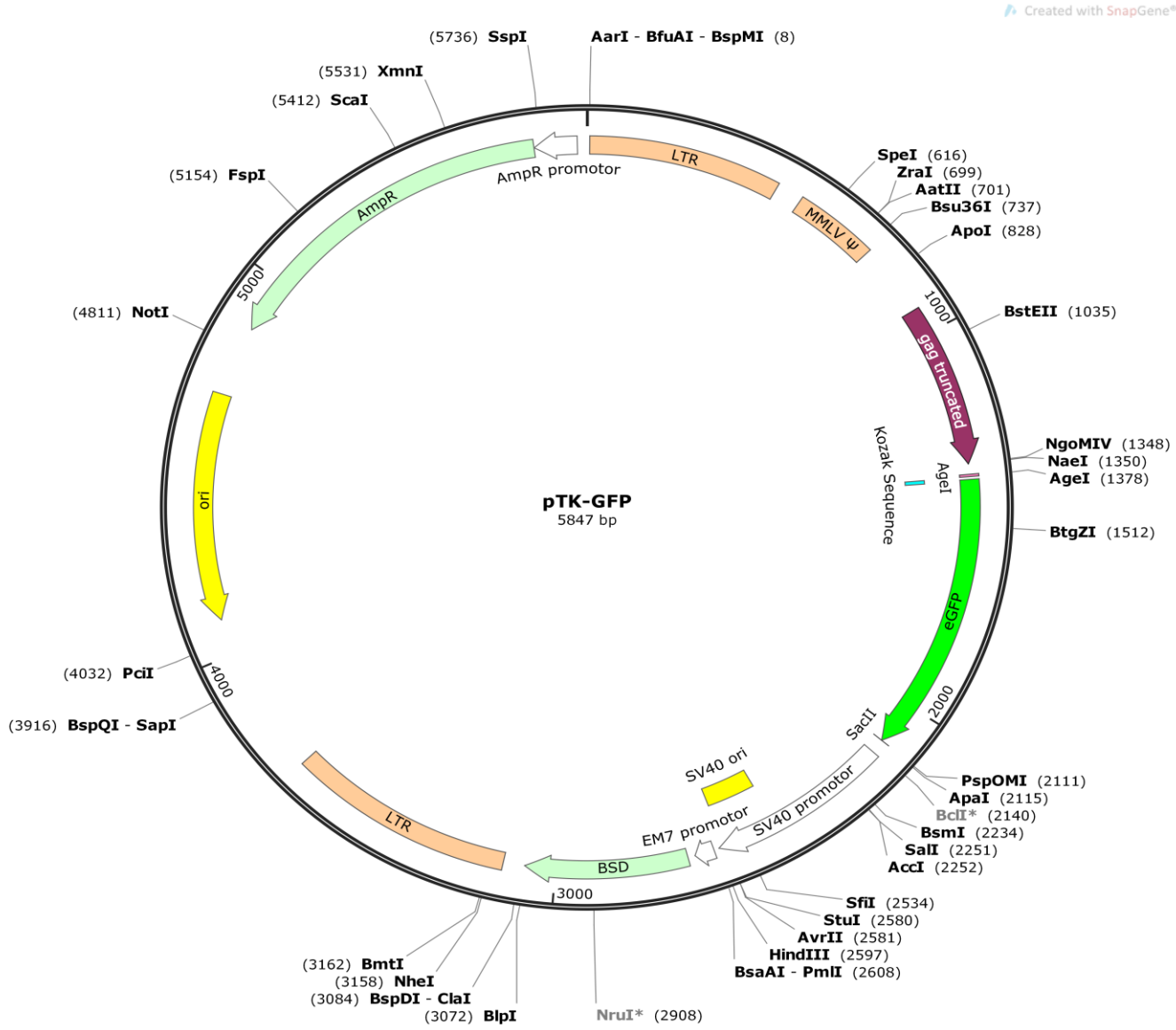
A.1 Plasmid map of pTK14-GFP-LGN .....	203
A.2 Plasmid map of pTK14-GFP .....	204
A.3 Plasmid map of pTK93-ANXA1-mCherry.....	205
A.4 Plasmid map of pTK93-mCherry .....	206
A.5 Plasmid map of pBluescript KS(+).LGN .....	207
A.6 Plasmid map of pTK14-dN-4TPR .....	208
A.7 Plasmid map of pTK14-dN-8TPR .....	209
A.8 Plasmid map of pTK14-dC .....	210

Created with SnapGene®

A.1 Plasmid map of pTK14-GFP-LGN

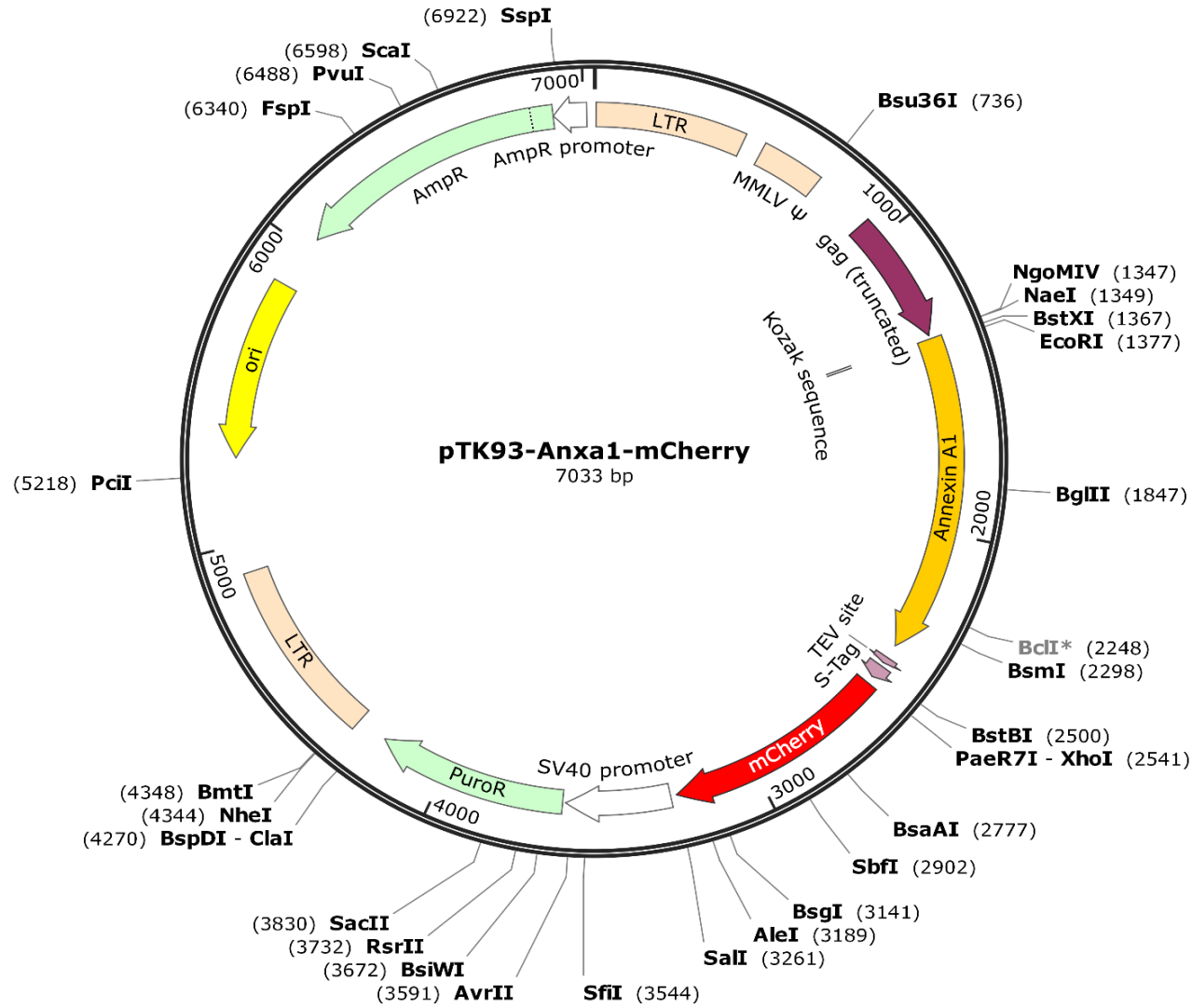


A.2 Plasmid map of pTK14-GFP



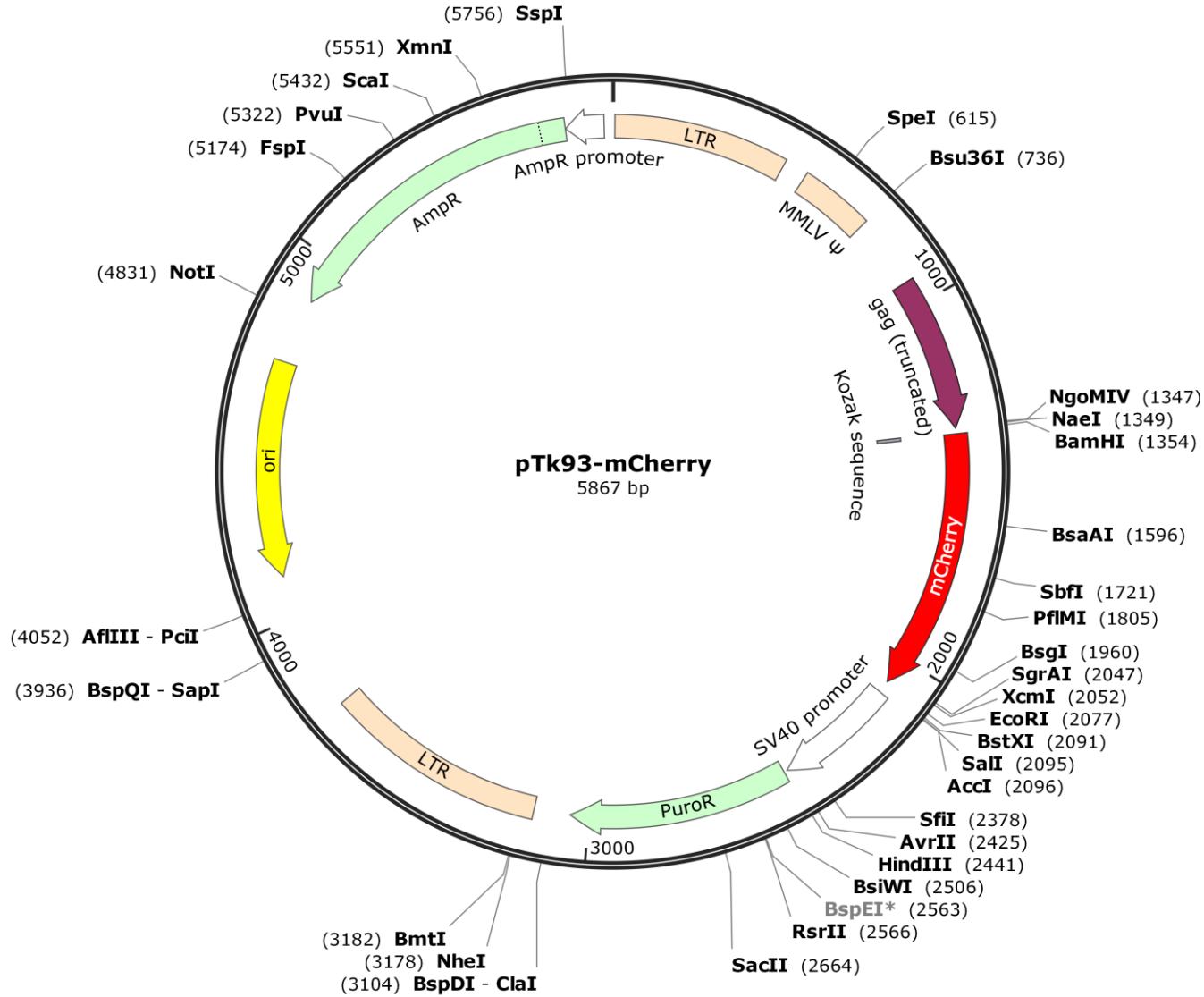
Created with SnapGene®

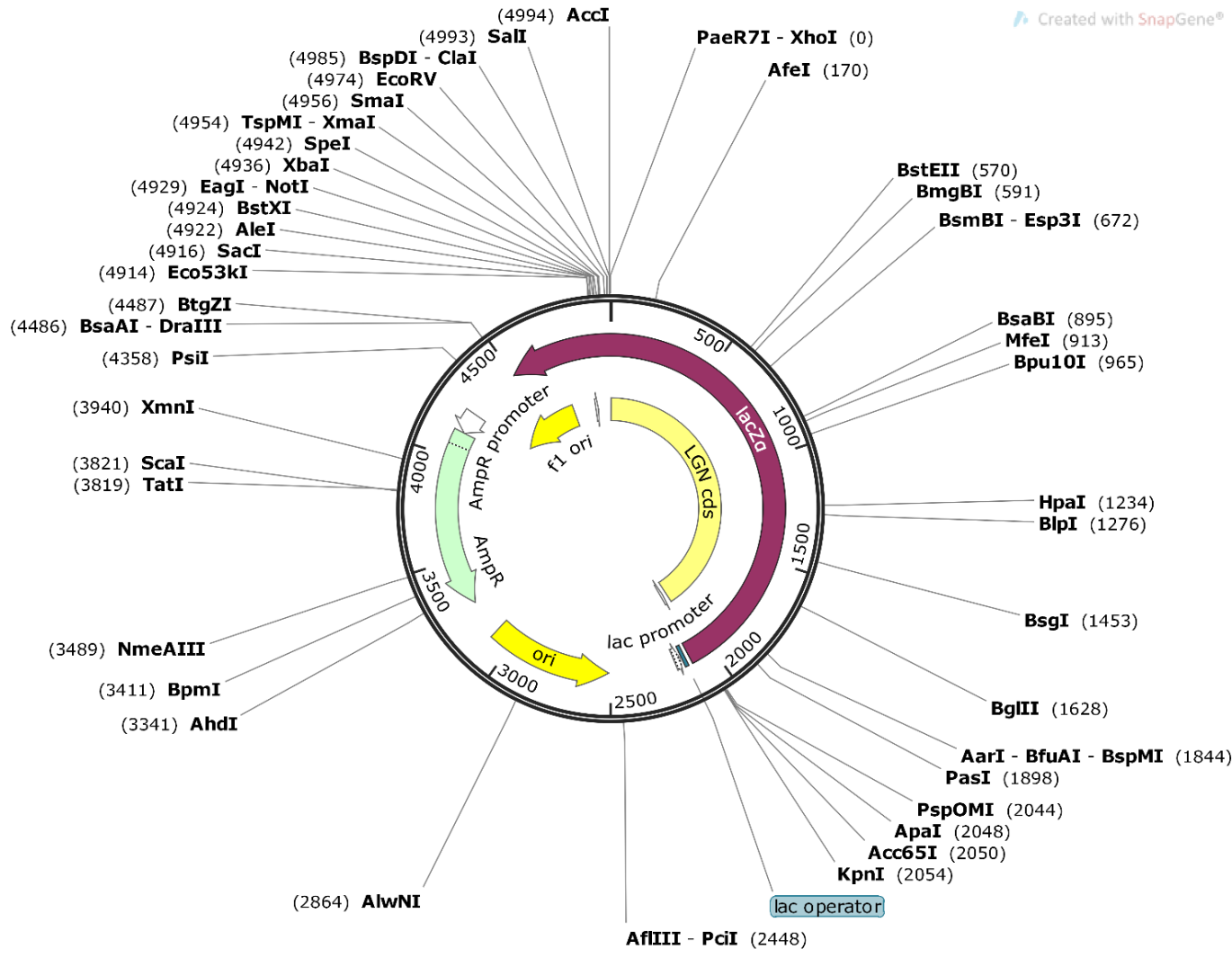
A.3 Plasmid map of pTK93-ANXA1-mCherry



Created with SnapGene®

A.4 Plasmid map of pTK93-mCherry



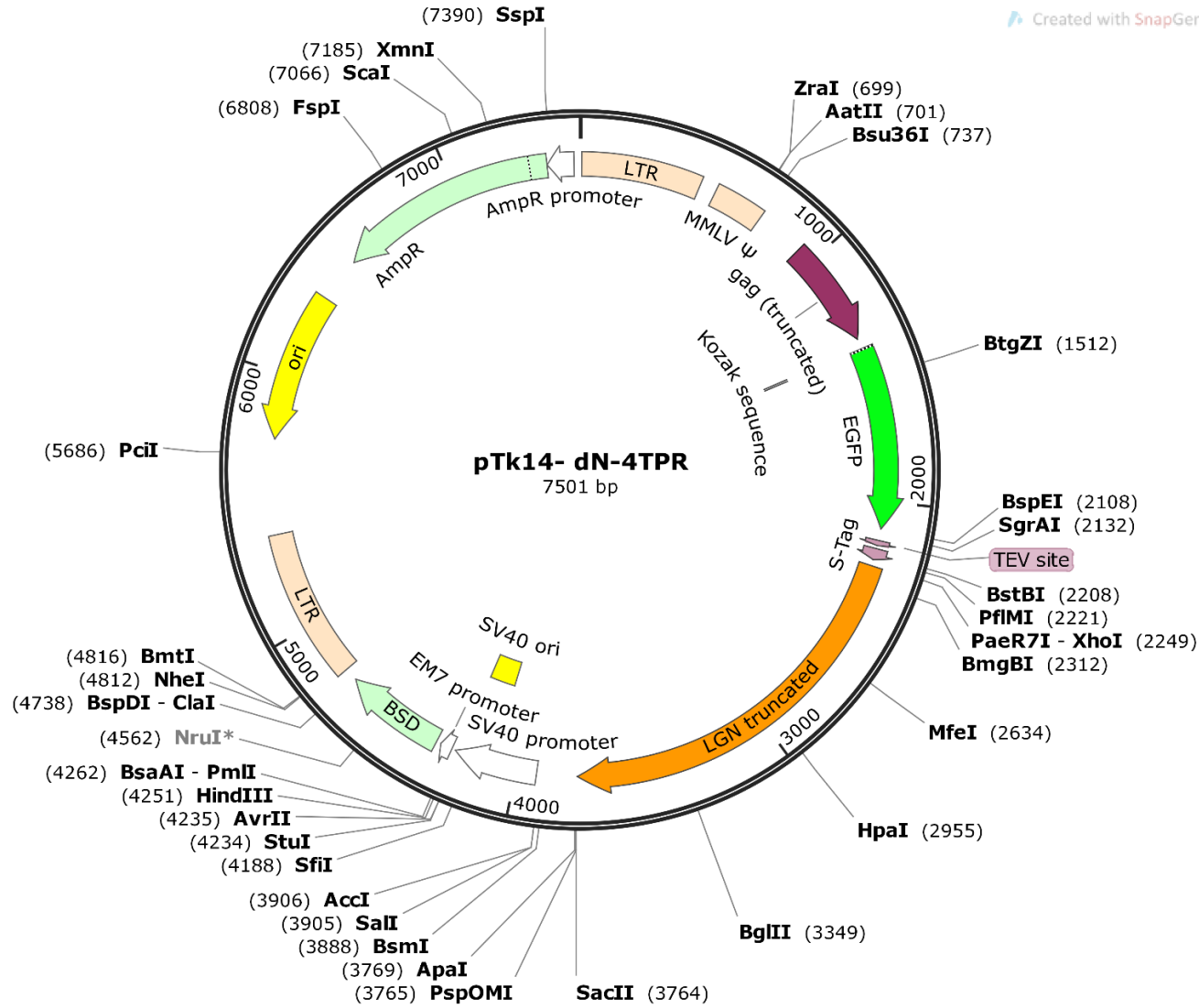


A.5 Plasmid map of pBluescript KS(+).LGN

**pBluescript KS(+).LGN**  
4999 bp

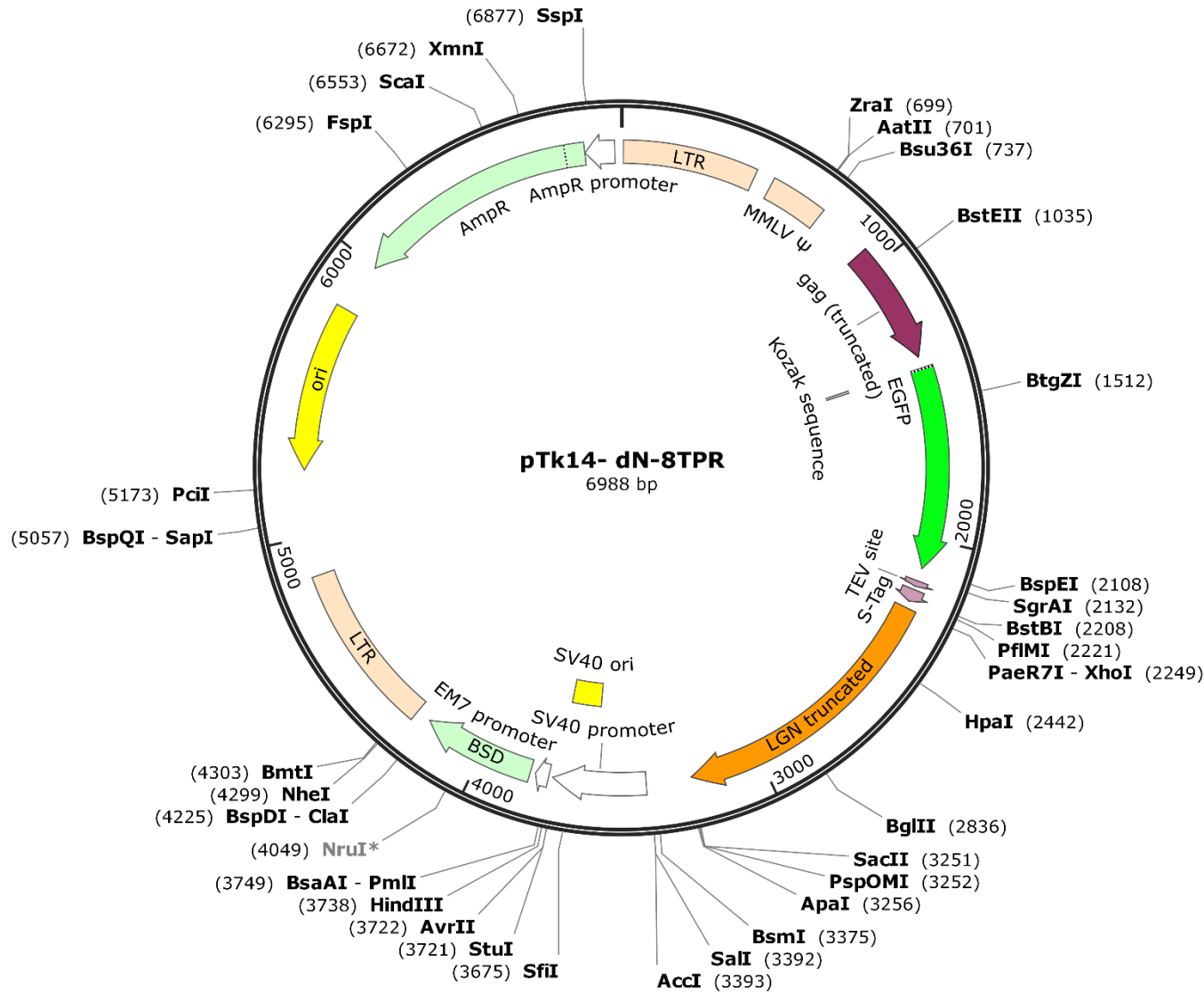
A.6 Plasmid map of pTK14-dN-4TPR

Created with SnapGene®



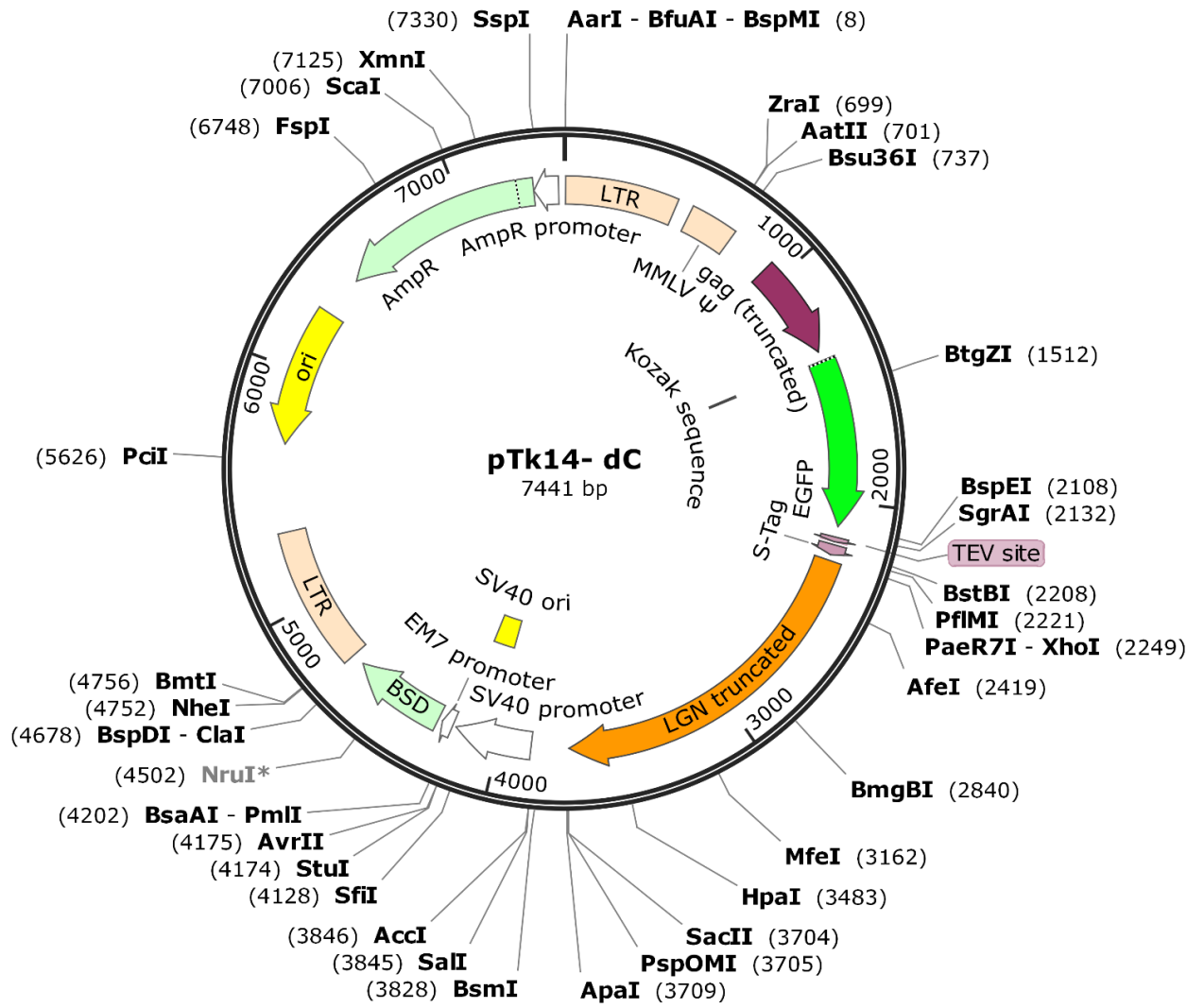
Created with SnapGene®

A.7 Plasmid map of pTk14-dN-8TPR



Created with SnapGene®

A.8 Plasmid map of pTK14-dC



## **Appendix B     Additional proteomics data**

<b>B.1 Peptide coverage of proteins, number of total as well as unique peptides of important proteins identified in co-IP of GFP-LGN using MS.....</b>	<b>212</b>
<b>B.2 STRING interaction scores for proteins in the LGN subnetworks.....</b>	<b>215</b>
<b>B.3 Known and novel interaction partners identified in a STRING interaction network of proteins closest associated with LGN (Exp2) .....</b>	<b>216</b>
<b>B.4 Classification of identified proteins based on their biological function (Exp2) .....</b>	<b>217</b>
<b>B.5 Gene enrichment analysis of significantly enriched biological processes and pathways from proteins in the LGN subnetwork (Exp2) .....</b>	<b>218</b>

**B.1 Peptide coverage of proteins, number of total as well as unique peptides of important proteins identified in co-IP of GFP-LGN using MS**

Gene symbol	Accession Number	Description	Experiment 1 - Mitotic GFP-LGN cells			Experiment 2 - Mitotic GFP-LGN cells		
			% Coverage	# Peptides	# Unique Peptides	% Coverage	# Peptides	# Unique Peptides
<b>Members of the spindle orientation machinery</b>								
GPSM2	P81274	G-protein-signaling modulator 2	65.35087719	46	46	62.28070175	33	30
NUMA1	Q14980	Nuclear mitotic apparatus protein 1	5.673758865	6	6	5.626477541	6	6
GNAI3	P08754	Guanine nucleotide-binding protein G(i) subunit alpha-3				9.604519774	1	1
DYNC1H1	Q14204	Cytoplasmic dynein 1 heavy chain 1	1.248385708	3	3	1.829530779	8	8
DYNLRB1	B1AKR6	Dynein light chain roadblock-type 1	13.51351351	3	3	12.16216216	2	2
DCTN1	Q14203	Dynactin subunit 1	1.095461659	1	1	6.572769953	6	6
DCTN2	Q13561	Dynactin subunit 2	3.49127182	1	1	10.2244389	3	3
ACTR1A	P61163	Alpha-centractin				6.382978723	2	2
<b>Members of the tubulin family</b>								
TUBA1C	F5H5D3	Tubulin alpha chain	33.91136802	14	5	40.65510597	25	17
TUBA1B	F8VVB9	Tubulin alpha-1B chain (Fragment)	56.91056911	9	1			
TUBA4A	P68366	Tubulin alpha-4A chain	34.82142857	12	8	38.83928571	21	13
TUBB	P07437	Tubulin beta chain	78.6036036	26	6	70.72072072	30	7
TUBB2A	Q13885	Tubulin beta-2A chain				52.80898876	20	4
TUBB3	Q13509	Tubulin beta-3 chain	39.33333333	13	4	44.22222222	17	5
TUBB4A	P04350	Tubulin beta-4A chain	64.86486486	23	2			
TUBB4B	P68371	Tubulin beta-4B chain	72.35955056	25	2	70.56179775	30	5
TUBB6	Q9BUF5	Tubulin beta-6 chain	39.23766816	12	5	25.56053812	9	4
TUBB8	Q3ZCM7	Tubulin beta-8 chain	24.0990991	9	1			
TUBG1	P23258	Tubulin gamma-1 chain	1.99556541	1	1			

## B1 Continued

Gene symbol	Accession Number	Description	Experiment 1 - Mitotic GFP-LGN cells			Experiment 2 - Mitotic GFP-LGN cells		
			% Coverage	# Peptides	# Unique Peptides	% Coverage	# Peptides	# Unique Peptides
<b><u>Known regulators of spindle orientation/assembly</u></b>								
ACTR1A	P61163	Alpha-centractin				6.382978723	2	2
CAPZA2	P47755	F-actin-capping protein subunit alpha-2				9.79020979	2	1
CCNB1	P14635	G2/mitotic-specific cyclin-B1	3.266331658	1	1	3.926096998	1	1
CLASP1	Q7Z460	CLIP-associating protein 1	1.430429129	2	2	4.291287386	3	3
EIF3E	P60228	Eukaryotic translation initiation factor 3 subunit E	4.494382022	1	1	16.40449438	6	6
GPSM1	A0A0A0MRC4	G-protein-signaling modulator 1				4.243281471	4	1
HAUS6	Q7Z4H7	HAUS augmin-like complex subunit 6	1.465968586	1	1			
INSC	Q1MX18	Protein inscuteable	12.43523316	3	3	5.18134715	1	1
KPNA2	P52292	Importin subunit alpha-1	5.293005671	3	3	13.42155009	5	5
MAPK3	P27361	Mitogen-activated protein kinase 3				6.068601583	1	1
NUMB	P49757	Protein numb	2.611367127	1	1	1.53609831	1	1
PLK1	P53350	Serine/threonine-protein kinase PLK1	5.970149254	1	1	5.970149254	1	1
RAN	J3KQE5	GTP-binding nuclear protein Ran	17.94871795	5	5	26.4957265	8	8
<b><u>Unknown regulators of mitotic processes</u></b>								
ANXA1	P04083	Annexin A1	12.13872832	2	2	25.72254335	6	6
BRD4	O60885	Bromodomain-containing protein 4				1.54185022	1	1
CACNA1B	H0Y718	Voltage-dependent N-type calcium channel subunit alpha-1B				15.24390244	1	1
CASP3	P42574	Caspase-3				6.859205776	1	1
CASP6	P55212	Caspase-6				6.484641638	1	1
CEP78	A8MST6	Centrosomal protein of 78 kDa				3.262411348	1	1
PTPN11	Q06124	Tyrosine-protein phosphatase non-receptor type 11				3.182579564	1	1
S100A11	P31949	Protein S100-A11	30.47619048	1	1	12.38095238	1	1
SAA1	E9PQD6	Serum amyloid A protein	13.93442623	1	1	41.80327869	3	3

**B1 Continued**

Gene symbol	Accession Number	Description	Experiment 1 - Mitotic GFP-LGN cells			Experiment 2 - Mitotic GFP-LGN cells		
			% Coverage	# Peptides	# Unique Peptides	% Coverage	# Peptides	# Unique Peptides
<b><u>Polarity proteins</u></b>								
PARD3	Q8TEW0	Partitioning defective 3	1.843657817	1	1			
CDH1	A0A087WXI5	Cadherin-1 (E-cadherin)	2.436323367	1	1	2.436323367	1	1
SCRIB	A0A0G2JPP5	Scribble	6.827794562	5	5	5.921450151	4	4

**B.2 STRING interaction scores for proteins in the LGN subnetworks**

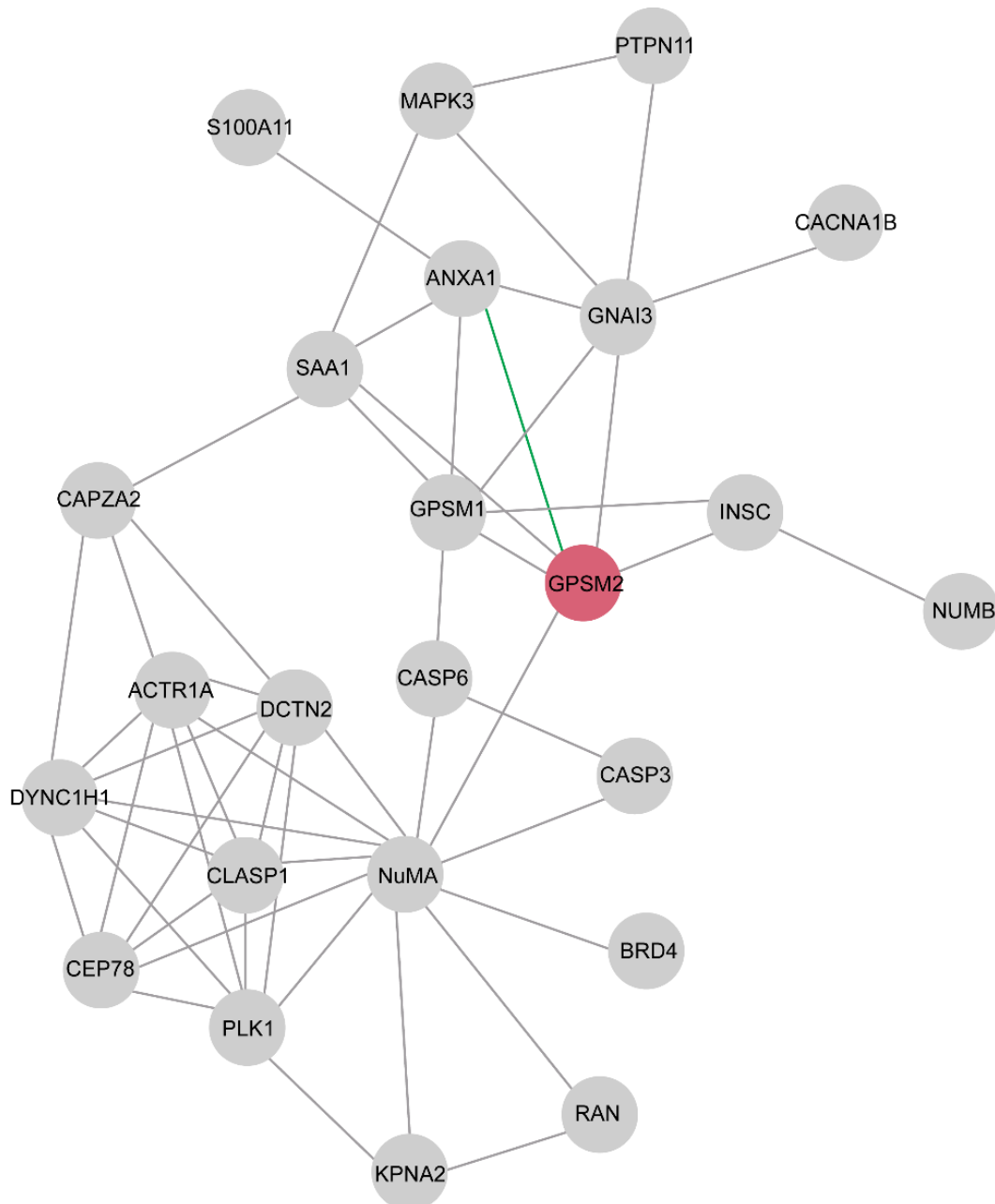
*Edges between two nodes (shared name) and their corresponding confidence score (score) in the LGN interaction network from Experiment 1 and 2. Scores lie between zero and one which represents the probability that the interaction really exists given the available evidence.*

Shared name	Score
NUMA1 (pp) HAUS6	0.902
NUMA1 (pp) EIF3E	0.701
NUMA1 (pp) RAN	0.903
CCNB1 (pp) CLASP1	0.900
NUMA1 (pp) GPSM2	0.729
NUMA1 (pp) DCTN2	0.900
NUMA1 (pp) KPNA2	0.900
CCNB1 (pp) KPNA2	0.945
CLAPS1 (pp) PLK1	0.915
CLASP1 (pp) DCTN2	0.900
CCNB1 (pp) PLK1	0.998
DCTN2 (pp) DYNC1H1	0.991
DCTN2 (pp) PLK1	0.900
DCTN2 (pp) HAUS6	0.900
HAUS6 (pp) PLK1	0.924
RAN (pp) KPNA2	0.954
KPNA2 (pp) PLK1	0.866
HAUS6 (pp) CLASP1	0.904
CLASP1 (pp) DYNC1H1	0.902
CCNB1 (pp) DYNC1H1	0.922
PARD3 (pp) INSC	0.809
TUBG1 (pp) PLK1	0.944
NUMA1 (pp) PLK1	0.903
NUMA1 (pp) DYNC1H1	0.934
NUMA1 (pp) CLASP1	0.901
PLK1 (pp) DYNC1H1	0.900
TUBG1 (pp) DYNC1H1	0.909
TUBG1 (pp) HAUS6	0.913
TUBG1 (pp) NUMA1	0.903
TUBG1 (pp) DCTN2	0.902
ANXA1 (pp) SAA1	0.901
ANXA1 (pp) S100A11	0.634
ANXA1 (pp) GPSM2	0.900
SAA (pp) GPSM2	0.900
DYNC1H1 (pp) HAUS6	0.900
GNAI3 (pp) MAPK3	0.915
GNAI3 (pp) SAA1	0.900
GNAI3 (pp) GPSM1	0.970
GNAI3 (pp) GPSM1	0.970

Shared name	Score
ACTR1A (pp) CLASP1	0.909
ACTR1A (pp) PLK1	0.900
ACTR1A (pp) DYNC1H1	0.994
ACTR1A (pp) NUMA1	0.935
ACTR1A (pp) DCTN2	0.999
ANXA1 (pp) GNAI3	0.902
ANXA1 (pp) GPSM1	0.900
BRD4 (pp) NUMA1	0.857
CAPZA2 (pp) DYNC1H1	0.902
CAPZA2 (pp) SAA1	0.900
CAPZA2 (pp) DCTN2	0.976
CASP3 (pp) CASP6	0.968
CASP3 (pp) NUMA1	0.900
CASP6 (pp) NUMA1	0.900
CEP78 (pp) CLASP1	0.901
CEP78 (pp) PLK1	0.902
CEP78 (pp) DYNC1H1	0.902
CEP78 (pp) NUMA1	0.900
CEP78 (pp) DCTN2	0.901
CLASP1 (pp) DYNC1H1	0.902
MAPK3 (pp) PTPN11	0.975
GNAI3 (pp) PTPN11	0.913
ACTR1A (pp) CAPZA2	0.977
ACTR1A (pp) CEP78	0.902
GPSM1 (pp) INSC	0.804
GPSM1 (pp) NUMA1	0.883
GPSM1 (pp) SAA1	0.900
MAPK3 (pp) SAA1	0.900
CACNA1B (pp) GNAI3	0.608
INSC (pp) GPSM2	0.804
CCNB1 (pp) NUMA1	0.900
NUMB (pp) INSC	0.715
TUBG1 (pp) CLASP1	0.909

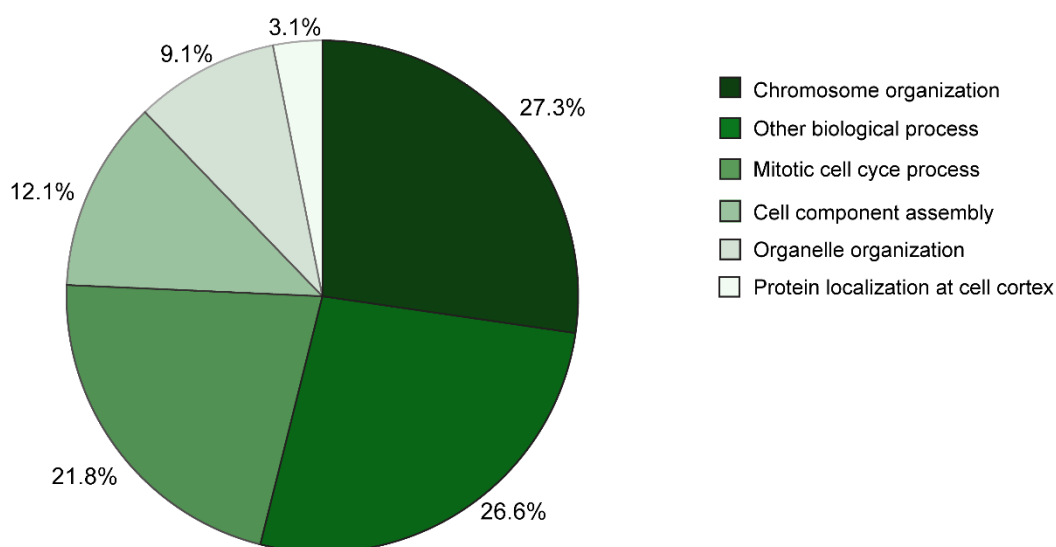
### B.3 Known and novel interaction partners identified in a STRING interaction network of proteins closest associated with LGN (Exp2)

STRING network of LGN (GPSM2, red) and its first neighbours (grey). The green line indicates the validated interaction in this study. To generate this network, subnetworking was performed by selecting LGN and its closest interactors in the entire retrieved STRING network and creation of a new network using Cytoscape software. The network was generated by Dr Farahnaz Sadat Golestan Hashemi and further annotated by the author of this thesis.



**B.4 Classification of identified proteins based on their biological function (Exp2)**

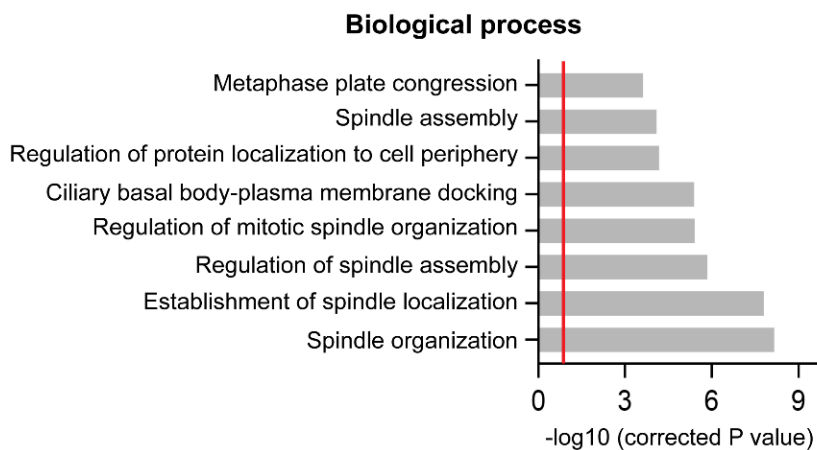
Percentage of proteins involved in enriched Gene Ontology biological processes. Gene enrichment analysis was performed with the entire STRING network of the second MS experiment. Hypergeometric test (Fisher's Exact Test) was used to calculate the statistical significance of the overrepresentation of enriched functional processes with the Bonferroni step-down correction from multiple tests.  $P \leq 0.05$  was considered significant. 100% = 444 proteins. Analysis was performed by Dr Farahnaz Sadat Golestan Hashemi.



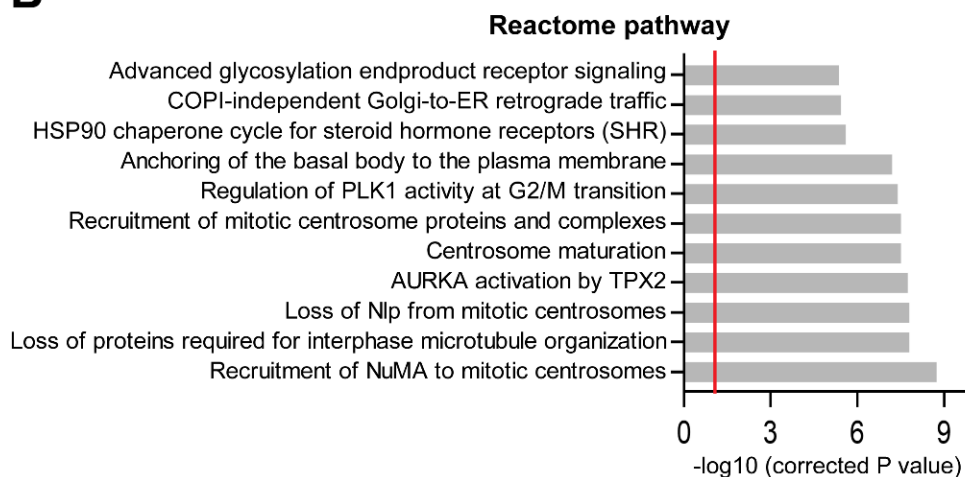
### B.5 Gene enrichment analysis of significantly enriched biological processes and pathways from proteins in the LGN subnetwork (Exp2)

(A) Significantly enriched GO biological processes associated with the proteins in the LGN subnetwork. (B) Significantly enriched Reactome pathways associated with the proteins in the LGN subnetwork.  $P \leq 0.05$  ( $-\log_{10} = 1.3$ , red line) was considered significant for all enrichment analyses. Hypergeometric test (Fisher's Exact Test) was used to calculate the statistical significance of the overrepresentation of enriched genes in functional processes and pathways with the Bonferroni step-down correction method from multiple tests using ClueGO App. Analysis was performed by Dr Farahnaz Sadat Golestan Hashemi.

## A



## B



## Appendix C Fiji macro script

Script used in Figure xx B. Script was written by Dr Xavier Morin.

```

macro elliptic_slicing {
//number of points to measure along the cell perimeter
k=180;
//length (in pixels) of the line for each measure:
px=30;
//starting position of the scan line relative to the ellipses long axis
S=90;
titre=getTitle();
getDimensions(x,y,nb_channel,o,t);
run("Set Measurements...", "area mean standard min bounding fit redirect=None decimal=3");
b=57.29578;
m=nResults;
IJ.deleteRows(0, m-1);
getPixelSize(unit, pw, ph, pd);
P=pd/pw;
run("Properties...", "unit=pixel pixel_width=1.0000 pixel_height=1.0000 voxel_depth="+P)+"
origin=0,0");
    selectWindow(titre);
    run("Set... ", "zoom=150");
    setTool("Freehand");
//message prompting the user to set the ellipse:
    title = "cell center";
    msg = "use the Freehand tool to draw\n the cell's perimeter\n select the best z-level\n
then click \"OK\".";
    waitForUser(title, msg);
//measuring the ellipses center and size:
    run("Fit Ellipse");
    run ("Measure");
    x0=getResult("BX", (0));
    x1=getResult("Width", (0));

```

```

M=getResult("Major", (0));
m=getResult("Minor", (0));
a=getResult("Angle", (0));
E=sqrt(M*M-m*m)/M;

y0=getResult("BY", (0));
y1=getResult("Height", (0));
//center of the ellipse:
X0=x0+x1/2;
Y0=y0+y1/2;

IJ.deleteRows(0, 0);
xx=newArray(k);
yy=newArray(k);
for (i=0; i<k; i++) {
xx[i]=(i);
l=(360*i/k-a+S)/b;
L=(360*i/k+S)/b;
dia=sqrt(m*m/(1-E*E*cos(L)*cos(L)))/2;
n1=dia-px/2;
n2=dia+px/2;
selectWindow(titre);
makeLine(X0+n1*cos(l), Y0+n1*sin(l), X0+n2*cos(l), Y0+n2*sin(l));
run ("Measure");
yy[i]=getResult("Max", (0));
IJ.deleteRows(0, 0);

print(yy[i]);
};
Plot.create("plot1", "X", "Y", xx, yy);
}

```

## Bibliography

(2021) 'The Gene Ontology resource: enriching a GOld mine', *Nucleic Acids Res*, 49(D1), pp. D325-d334.

Abouelasrar Salama, S. *et al.* (2020) 'Serum Amyloid A1 (SAA1) Revisited: Restricted Leukocyte-Activating Properties of Homogeneous SAA1', *Frontiers in Immunology*, 11(843).

Adams, R.J. (1996) 'Metaphase spindles rotate in the neuroepithelium of rat cerebral cortex', *J Neurosci*, 16(23), pp. 7610-8.

Ahn, S.-H. *et al.* (1997) 'Differential expression of annexin I in human mammary ductal epithelial cells in normal and benign and malignant breast tissues', *Clinical & Experimental Metastasis*, 15(2), pp. 151-156.

Alam, M.S. (2018) 'Proximity Ligation Assay (PLA)', *Current protocols in immunology*, 123(1), pp. e58-e58.

Alberts, B., Johnson, A. and Lewis, J. (2002) 'Molecular Biology of the Cell. 4th edition', *New York: Garland Science*.

Aldarmahi, A. and Al-Rabia, M. (2015) 'Optimisation of proteomic approaches to study the maternal interaction with gametes in sow's reproductive tract', *Journal of Microscopy and Ultrastructure*, 3(3), pp. 154-160.

Allan, Victoria J. (2011) 'Cytoplasmic dynein', *Biochemical Society Transactions*, 39(5), pp. 1169-1178.

Alldrige, L.C. and Bryant, C.E. (2003) 'Annexin 1 regulates cell proliferation by disruption of cell morphology and inhibition of cyclin D1 expression through sustained activation of the ERK1/2 MAPK signal', *Experimental Cell Research*, 290(1), pp. 93-107.

Alsemarz, A., Lasko, P. and Fagotto, F. (2018) 'Limited significance of the in situ proximity ligation assay', *bioRxiv*, p. 411355.

Alvarez-Martinez, M.-T. *et al.* (1996) 'Characterization of the Interaction Between Annexin I and Profilin', *European Journal of Biochemistry*, 238(3), pp. 777-784.

Alvarez-Martinez, M.-T. *et al.* (1997) 'Effects of profilin–annexin I association on some properties of both profilin and annexin I: modification of the inhibitory activity of profilin on actin polymerization and inhibition of the self-association of annexin I and its interactions with liposomes', *Biochimica et Biophysica Acta (BBA) - Protein Structure and Molecular Enzymology*, 1339(2), pp. 331-340.

Amin, M.A. and Varma, D. (2017) 'Combining Mitotic Cell Synchronization and High Resolution Confocal Microscopy to Study the Role of Multifunctional Cell Cycle Proteins During Mitosis', *Journal of visualized experiments : JoVE*, (130), p. 56513.

Amos, L.A. (2004) 'Microtubule structure and its stabilisation', *Org Biomol Chem*, 2(15), pp. 2153-60.

Andersen, J.S. *et al.* (2003) 'Proteomic characterization of the human centrosome by protein correlation profiling', *Nature*, 426(6966), pp. 570-574.

- Anson, D.S. (2004) 'The use of retroviral vectors for gene therapy-what are the risks? A review of retroviral pathogenesis and its relevance to retroviral vector-mediated gene delivery', *Genetic Vaccines and Therapy*, 2(1), p. 9.
- Araujo, A.R. *et al.* (2016) 'Positive Feedback Keeps Duration of Mitosis Temporally Insulated from Upstream Cell-Cycle Events', *Mol Cell*, 64(2), pp. 362-375.
- Arur, S. *et al.* (2003) 'Annexin I Is an Endogenous Ligand that Mediates Apoptotic Cell Engulfment', *Developmental Cell*, 4(4), pp. 587-598.
- Ashburner, M. *et al.* (2000) 'Gene ontology: tool for the unification of biology. The Gene Ontology Consortium', *Nat Genet*, 25(1), pp. 25-9.
- Bai, L. and Rohrschneider, L.R. (2010) ' $\beta$ -SHIP promoter expression marks activated stem cells in developing mouse mammary tissue', *Genes & Development*, 24(17), pp. 1882-1892.
- Bajer, A.S. and Mole-Bajer, J. (1972) 'Spindle Dynamics and Chromosome Movements', *Academic, New York*.
- Ballard, M.S. *et al.* (2015) 'Mammary Stem Cell Self-Renewal Is Regulated by Slit2/Robo1 Signaling through SNAI1 and mINSC', *Cell Rep*, 13(2), pp. 290-301.
- BARTON, G.J. *et al.* (1991) 'Amino acid sequence analysis of the annexin super-gene family of proteins', *European Journal of Biochemistry*, 198(3), pp. 749-760.
- Baudoin, N.C. and Cimini, D. (2018) 'A guide to classifying mitotic stages and mitotic defects in fixed cells', *Chromosoma*, 127(2), pp. 215-227.
- Bazzoun, D. *et al.* (2019) 'Connexin 43 maintains tissue polarity and regulates mitotic spindle orientation in the breast epithelium', *Journal of Cell Science*, 132(10).
- Beck, B. *et al.* (2011) 'A vascular niche and a VEGF–Nrp1 loop regulate the initiation and stemness of skin tumours', *Nature*, 478(7369), pp. 399-403.
- Berggård, T., Linse, S. and James, P. (2007) 'Methods for the detection and analysis of protein–protein interactions', *PROTEOMICS*, 7(16), pp. 2833-2842.
- Bergstrahl, D.T., Dawney, N.S. and St Johnston, D. (2017) 'Spindle orientation: a question of complex positioning', *Development*, 144(7), pp. 1137-1145.
- Bhardwaj, A. *et al.* (2015) 'Annexin A1 Preferentially Predicts Poor Prognosis of Basal-Like Breast Cancer Patients by Activating mTOR-S6 Signaling', *PLOS ONE*, 10(5), p. e0127678.
- Bhatarai, S.R. *et al.* (2019) 'The ciliary GTPase Arl3 maintains tissue architecture by directing planar spindle orientation during epidermal morphogenesis', *Development*, 146(9).
- Bindea, G. *et al.* (2009) 'ClueGO: a Cytoscape plug-in to decipher functionally grouped gene ontology and pathway annotation networks', *Bioinformatics*, 25(8), pp. 1091-1093.
- Bird, S.L., Heald, R. and Weis, K. (2013) 'RanGTP and CLASP1 cooperate to position the mitotic spindle', *Molecular Biology of the Cell*, 24(16), pp. 2506-2514.
- Bizzarro, V. *et al.* (2012) 'Annexin A1 induces skeletal muscle cell migration acting through formyl peptide receptors', *PLoS one*, 7(10), pp. e48246-e48246.

- Bizzarro, V. *et al.* (2019) 'Mesoglycan induces keratinocyte activation by triggering syndecan-4 pathway and the formation of the annexin A1/S100A11 complex', *Journal of Cellular Physiology*, 234(11), pp. 20174-20192.
- Bizzarro, V. *et al.* (2010) 'Role of Annexin A1 in mouse myoblast cell differentiation', *Journal of Cellular Physiology*, 224(3), pp. 757-765.
- Blagosklonny, M.V. and Pardee, A.B. (2002) 'The Restriction Point of the Cell Cycle', *Cell Cycle*, 1(2), pp. 102-109.
- Blajeski, A.L. *et al.* (2002) 'G(1) and G(2) cell-cycle arrest following microtubule depolymerization in human breast cancer cells', *The Journal of clinical investigation*, 110(1), pp. 91-99.
- Blanpain, C. *et al.* (2004) 'Self-Renewal, Multipotency, and the Existence of Two Cell Populations within an Epithelial Stem Cell Niche', *Cell*, 118(5), pp. 635-648.
- Blumer, J.B., Chandler, L.J. and Lanier, S.M. (2002) 'Expression Analysis and Subcellular Distribution of the Two G-protein Regulators AGS3 and LGN Indicate Distinct Functionality: LOCALIZATION OF LGN TO THE MIDBODY DURING CYTOKINESIS', *Journal of Biological Chemistry*, 277(18), pp. 15897-15903.
- Bonner, M.K. *et al.* (2011) 'Mitotic spindle proteomics in Chinese hamster ovary cells', *PLoS One*, 6(5), p. e20489.
- Bonner, W.A. *et al.* (1972) 'Fluorescence Activated Cell Sorting', *Review of Scientific Instruments*, 43(3), pp. 404-409.
- Borner, G.H.H. (2020) 'Organellar Maps Through Proteomic Profiling &#x2013; A Conceptual Guide', *Molecular & Cellular Proteomics*, 19(7), pp. 1076-1087.
- Bosveld, F. *et al.* (2016) 'Epithelial tricellular junctions act as interphase cell shape sensors to orient mitosis', *Nature*, 530(7591), pp. 495-498.
- Boudhraa, Z. *et al.* (2016) 'Annexin A1 localization and its relevance to cancer', *Clinical Science*, 130(4), pp. 205-220.
- Boumahdi, S. *et al.* (2014) 'SOX2 controls tumour initiation and cancer stem-cell functions in squamous-cell carcinoma', *Nature*, 511(7508), pp. 246-250.
- Box, K., Joyce, B.W. and Devenport, D. (2019) 'Epithelial geometry regulates spindle orientation and progenitor fate during formation of the mammalian epidermis', *eLife*, 8, p. e47102.
- BROWNSTEIN, C. *et al.* (2001) 'Annexin II', *Annals of the New York Academy of Sciences*, 947(1), pp. 143-156.
- Butler, M.T. and Wallingford, J.B. (2017) 'Planar cell polarity in development and disease', *Nature Reviews Molecular Cell Biology*, 18(6), pp. 375-388.
- Cadart, C. *et al.* (2014) 'Exploring the Function of Cell Shape and Size during Mitosis', *Developmental Cell*, 29(2), pp. 159-169.
- Campos-Gonzalez, R., Kanemitsu, M. and Boynton, A.L. (1990) 'Epidermal growth factor induces the accumulation of calpactin II on the cell surface during membrane ruffling', *Cell Motility*, 15(1), pp. 34-40.

- Cañas, B. *et al.* (2007) 'Trends in sample preparation for classical and second generation proteomics', *Journal of Chromatography A*, 1153(1), pp. 235-258.
- Capalbo, L. *et al.* (2011) 'Rab5 GTPase controls chromosome alignment through Lamin disassembly and relocation of the NuMA-like protein Mud to the poles during mitosis', *Proceedings of the National Academy of Sciences*, 108(42), pp. 17343-17348.
- Cardoza, J.D. *et al.* (2012) 'Mass spectrometry-based proteomics: qualitative identification to activity-based protein profiling', *Wiley interdisciplinary reviews. Systems biology and medicine*, 4(2), pp. 141-162.
- Carminati, M. *et al.* (2016) 'Concomitant binding of Afadin to LGN and F-actin directs planar spindle orientation', *Nat Struct Mol Biol*, 23(2), pp. 155-63.
- Castanon, I. and Gonzalez-Gaitan, M. (2011) 'Oriented cell division in vertebrate embryogenesis', *Curr Opin Cell Biol*, 23(6), pp. 697-704.
- Cepko, C. and Pear, W. (1996) 'Overview of the Retrovirus Transduction System', *Current Protocols in Molecular Biology*, 36(1), pp. 9.9.1-9.9.16.
- Chatterjee, B.E. *et al.* (2005) 'Annexin 1-deficient neutrophils exhibit enhanced transmigration in vivo and increased responsiveness in vitro', *Journal of Leukocyte Biology*, 78(3), pp. 639-646.
- Chepenik, K.P. *et al.* (1995) 'Developmental regulation of various annexins in the embryonic palate of the mouse: dexamethasone affects expression of annexin-1', *Journal of craniofacial genetics and developmental biology*, 15(4), pp. 171-181.
- Chiu, C.W.N. *et al.* (2016) 'SAPCD2 Controls Spindle Orientation and Asymmetric Divisions by Negatively Regulating the Galphai-LGN-NuMA Ternary Complex', *Dev Cell*, 36(1), pp. 50-62.
- Choi, I.L.W. *et al.* (2016) 'Regulation of Airway Inflammation by G-protein Regulatory Motif Peptides of AGS3 protein', *Scientific Reports*, 6(1), p. 27054.
- Chugh, P. and Paluch, E.K. (2018) 'The actin cortex at a glance', *Journal of Cell Science*, 131(14).
- Cicalese, A. *et al.* (2009) 'The tumor suppressor p53 regulates polarity of self-renewing divisions in mammary stem cells', *Cell*, 138(6), pp. 1083-95.
- Clark, I.B. and Meyer, D.I. (1999) 'Overexpression of normal and mutant Arp1alpha (centractin) differentially affects microtubule organization during mitosis and interphase', *J Cell Sci*, 112 ( Pt 20), pp. 3507-18.
- Cleveland, D.W. (1995) 'NuMA: a protein involved in nuclear structure, spindle assembly, and nuclear re-formation', *Trends in Cell Biology*, 5(2), pp. 60-64.
- Compton, D.A., Szilak, I. and Cleveland, D.W. (1992) 'Primary structure of NuMA, an intranuclear protein that defines a novel pathway for segregation of proteins at mitosis', *The Journal of cell biology*, 116(6), pp. 1395-1408.
- Cooper, S. (2003) 'Rethinking synchronization of mammalian cells for cell cycle analysis', *Cellular and Molecular Life Sciences CMLS*, 60(6), pp. 1099-1106.
- Cooper, S. (2019) 'The synchronization manifesto: a critique of whole-culture synchronization', *The FEBS Journal*, 286(23), pp. 4650-4656.

Coquelle, F.M. *et al.* (2002) 'LIS1, CLIP-170's Key to the Dynein/Dynactin Pathway', *Molecular and Cellular Biology*, 22(9), pp. 3089-3102.

Corrigan, A.M. *et al.* (2013) 'Automated tracking of mitotic spindle pole positions shows that LGN is required for spindle rotation but not orientation maintenance', *Cell Cycle*, 12(16), pp. 2643-2655.

Creutz, C.E., Pazoles, C.J. and Pollard, H.B. (1978) 'Identification and purification of an adrenal medullary protein (synexin) that causes calcium-dependent aggregation of isolated chromaffin granules', *Journal of Biological Chemistry*, 253(8), pp. 2858-2866.

Creutz, C.E. *et al.* (1987) 'Identification of chromaffin granule-binding proteins. Relationship of the chromobindins to calelectrin, synhibin, and the tyrosine kinase substrates p35 and p36', *Journal of Biological Chemistry*, 262(4), pp. 1860-8.

Crumpton, M.J. and Dedman, J.R. (1990) 'Protein terminology tangle', *Nature*, 345(6272), pp. 212-212.

Culurgioni, S. *et al.* (2011) 'Inscuteable and NuMA proteins bind competitively to Leu-Gly-Asn repeat-enriched protein (LGN) during asymmetric cell divisions', *Proc Natl Acad Sci U S A*, 108(52), pp. 20998-1003.

D'Acquisto, F. *et al.* (2006) 'Annexin-1 modulates T-cell activation and differentiation', *Blood*, 109(3), pp. 1095-1102.

D'Acunto, C.W. *et al.* (2014) 'The complex understanding of Annexin A1 phosphorylation', *Cellular Signalling*, 26(1), pp. 173-178.

Dana, H. *et al.* (2017) 'Molecular Mechanisms and Biological Functions of siRNA', *International journal of biomedical science : IJBS*, 13(2), pp. 48-57.

Das, S., Hehnlly, H. and Doxsey, S. (2015) 'A new role for Rab GTPases during early mitotic stages', *Small GTPases*, 6(1), pp. 11-15.

David, A.F. *et al.* (2019) 'Augmin accumulation on long-lived microtubules drives amplification and kinetochore-directed growth', *J Cell Biol*, 218(7), pp. 2150-2168.

Davis, P.K., Ho, A. and Dowdy, S.F. (2001) 'Biological methods for cell-cycle synchronization of mammalian cells', *Biotechniques*, 30(6), pp. 1322-6, 1328, 1330-1.

de Jong, R. *et al.* (2017) 'The advantageous role of annexin A1 in cardiovascular disease', *Cell Adhesion & Migration*, 11(3), pp. 261-274.

Decarreau, J. *et al.* (2014) 'Rapid measurement of mitotic spindle orientation in cultured mammalian cells', *Methods in molecular biology (Clifton, N.J.)*, 1136, pp. 31-40.

DeLuca, J.G. *et al.* (2006) 'Kinetochore Microtubule Dynamics and Attachment Stability Are Regulated by Hec1', *Cell*, 127(5), pp. 969-982.

Devenport, D. (2014) 'The cell biology of planar cell polarity', *The Journal of Cell Biology*, 207(2), pp. 171-179.

Devenport, D. (2016) 'Tissue morphodynamics: Translating planar polarity cues into polarized cell behaviors', *Seminars in Cell & Developmental Biology*, 55, pp. 99-110.

- di Pietro, F., Echard, A. and Morin, X. (2016) 'Regulation of mitotic spindle orientation: an integrated view', *EMBO Rep*, 17(8), pp. 1106-30.
- di Pietro, F. *et al.* (2017) 'An RNAi Screen in a Novel Model of Oriented Divisions Identifies the Actin-Capping Protein Z beta as an Essential Regulator of Spindle Orientation', *Curr Biol*, 27(16), pp. 2452-2464 e8.
- Diakonova, M. *et al.* (1997) 'Localization of five annexins in J774 macrophages and on isolated phagosomes', *Journal of Cell Science*, 110(10), pp. 1199-1213.
- Dogterom, M. and Koenderink, G.H. (2019) 'Actin–microtubule crosstalk in cell biology', *Nature Reviews Molecular Cell Biology*, 20(1), pp. 38-54.
- Dong, Y. *et al.* (2016) 'Sample Preparation for Mass Spectrometry Imaging of Plant Tissues: A Review', *Frontiers in Plant Science*, 7(60).
- Dontu, G. *et al.* (2003) 'Stem cells in normal breast development and breast cancer', *Cell Proliferation*, 36(s1), pp. 59-72.
- Dontu, G., Liu, S. and Wicha, M.S. (2005) 'Stem cells in mammary development and carcinogenesis', *Stem Cell Reviews*, 1(3), pp. 207-213.
- Dorovkov, M.V., Kostyukova, A.S. and Ryazanov, A.G. (2011) 'Phosphorylation of Annexin A1 by TRPM7 Kinase: A Switch Regulating the Induction of an  $\alpha$ -Helix', *Biochemistry*, 50(12), pp. 2187-2193.
- Dorovkov, M.V. and Ryazanov, A.G. (2004) 'Phosphorylation of Annexin I by TRPM7 Channel-Kinase \*', *Journal of Biological Chemistry*, 279(49), pp. 50643-50646.
- dos Santos, C.O. *et al.* (2013) 'Molecular hierarchy of mammary differentiation yields refined markers of mammary stem cells', *Proceedings of the National Academy of Sciences*, 110(18), pp. 7123-7130.
- Du, Q. and Macara, I.G. (2004) 'Mammalian Pins is a conformational switch that links NuMA to heterotrimeric G proteins', *Cell*, 119(4), pp. 503-16.
- Du, Q., Stukenberg, P.T. and Macara, G. (2001) 'A mammalian Partner of inscuteable binds NuMA and regulates mitotic spindle organization', *Nature Cell Biology*, 3, pp. 1069-1075.
- Du, Q. *et al.* (2002) 'LGN Blocks the Ability of NuMA to Bind and Stabilize Microtubules: A Mechanism for Mitotic Spindle Assembly Regulation', *Current Biology*, 12, pp. 1928–1933.
- Duarte, S. *et al.* (2019) 'Vimentin filaments interact with the actin cortex in mitosis allowing normal cell division', *Nat Commun*, 10(1), p. 4200.
- Dunsch, A.K. *et al.* (2012) 'Dynein light chain 1 and a spindle-associated adaptor promote dynein asymmetry and spindle orientation', *J Cell Biol*, 198(6), pp. 1039-54.
- Duxbury, M.S. and Whang, E.E. (2004) 'RNA interference: a practical approach', *Journal of Surgical Research*, 117(2), pp. 339-344.
- Eberhard, D.A. *et al.* (2001) 'Control of the nuclear-cytoplasmic partitioning of annexin II by a nuclear export signal and by p11 binding', *Journal of Cell Science*, 114(17), pp. 3155-3166.

- El-Hashash, A.H.K. and Warburton, D. (2012) 'Numb Expression and Asymmetric versus Symmetric Cell Division in Distal Embryonic Lung Epithelium', *Journal of Histochemistry & Cytochemistry*, 60(9), pp. 675-682.
- Elias, S. *et al.* (2014) 'Huntingtin regulates mammary stem cell division and differentiation', *Stem Cell Reports*, 2(4), pp. 491-506.
- Elledge, S.J. (1996) 'Cell Cycle Checkpoints: Preventing an Identity Crisis', *Science*, 274(5293), pp. 1664-1672.
- Elzen, N.d. *et al.* (2009) 'Cadherin Adhesion Receptors Orient the Mitotic Spindle during Symmetric Cell Division in Mammalian Epithelia', *Molecular Biology of the Cell*, 20(16), pp. 3740-3750.
- Fang, Y. *et al.* (2016) 'Knockdown of ANXA1 suppresses the biological behavior of human NSCLC cells in vitro', *Mol Med Rep*, 13(5), pp. 3858-3866.
- Farina, F. *et al.* (2016) 'The centrosome is an actin-organizing centre', *Nature cell biology*, 18(1), pp. 65-75.
- Faulkner, N.E. *et al.* (2000) 'A role for the lissencephaly gene LIS1 in mitosis and cytoplasmic dynein function', *Nature Cell Biology*, 2(11), pp. 784-791.
- Fava, R.A. *et al.* (1993) 'Annexin-1 Localization in Human Skin: Possible Association with Cytoskeletal Elements in Keratinocytes of the Stratum Spinosum', *Journal of Investigative Dermatology*, 101(5), pp. 732-737.
- Fellinger, K. and Rothbauer, U. (2009).
- Ferlazzo, V. *et al.* (2003) 'Anti-inflammatory effects of annexin-1: stimulation of IL-10 release and inhibition of nitric oxide synthesis', *International Immunopharmacology*, 3(10), pp. 1363-1369.
- Finardi, A., Massari, L.F. and Visintin, R. (2020) 'Anaphase Bridges: Not All Natural Fibers Are Healthy', *Genes*, 11(8), p. 902.
- Finegan, T.M. and Bergstralh, D.T. (2019) 'Division orientation: disentangling shape and mechanical forces', *Cell Cycle*, 18(11), pp. 1187-1198.
- Finegan, T.M. *et al.* (2019) 'Tissue tension and not interphase cell shape determines cell division orientation in the Drosophila follicular epithelium', *The EMBO journal*, 38(3), p. e100072.
- Fire, A. *et al.* (1998) 'Potent and specific genetic interference by double-stranded RNA in *Caenorhabditis elegans*', *Nature*, 391(6669), pp. 806-811.
- Flemming, W. (1882) 'Zellsubstanz, Kern und Zellteilung', *FCW Vogel, Leipzig*.
- Flower, R.J. and Blackwell, G.J. (1979) 'Anti-inflammatory steroids induce biosynthesis of a phospholipase A2 inhibitor which prevents prostaglandin generation', *Nature*, 278(5703), pp. 456-459.
- Foo, S.L. *et al.* (2019) 'Annexin-A1 – A Blessing or a Curse in Cancer?', *Trends in Molecular Medicine*, 25(4), pp. 315-327.
- Fox, M.H. (2004) 'Methods for Synchronizing Mammalian Cells', in Lieberman, H.B. (ed.) *Cell Cycle Checkpoint Control Protocols*. Totowa, NJ: Humana Press, pp. 11-16.

- Fredriksson, S. *et al.* (2002) 'Protein detection using proximity-dependent DNA ligation assays', *Nature Biotechnology*, 20(5), pp. 473-477.
- Free, R.B., Hazelwood, L.A. and Sibley, D.R. (2009) 'Identifying Novel Protein-Protein Interactions Using Co-Immunoprecipitation and Mass Spectroscopy', *Current Protocols in Neuroscience*, 46(1), pp. 5.28.1-5.28.14.
- Fu, Z. *et al.* (2020) 'Annexin A1: A double-edged sword as novel cancer biomarker', *Clinica Chimica Acta*, 504, pp. 36-42.
- Fukukawa, C. *et al.* (2010) 'Critical roles of LGN/GPSM2 phosphorylation by PBK/TOPK in cell division of breast cancer cells', *Genes, Chromosomes and Cancer*, 49(10), pp. 861-872.
- Fulcher, L.J. *et al.* (2019) 'FAM83D directs protein kinase CK1 $\alpha$  to the mitotic spindle for proper spindle positioning', *EMBO reports*, 20(9), p. e47495.
- Gallini, S. *et al.* (2016) 'NuMA Phosphorylation by Aurora-A Orchestrates Spindle Orientation', *Current Biology*, 26(4), pp. 458-469.
- Gama, J.B. *et al.* (2017) 'Molecular mechanism of dynein recruitment to kinetochores by the Rod-Zw10-Zwisch complex and Spindly', *Journal of Cell Biology*, 216(4), pp. 943-960.
- Gardner, M.K., Zanic, M. and Howard, J. (2013) 'Microtubule catastrophe and rescue', *Current Opinion in Cell Biology*, 25(1), pp. 14-22.
- Gehmlich, K., Haren, L. and Merdes, A. (2004) 'Cyclin B degradation leads to NuMA release from dynein/dynactin and from spindle poles', *EMBO Rep*, 5(1), pp. 97-103.
- Geisow, M.J. *et al.* (1987) 'Annexins—New family of Ca<sup>2+</sup>-regulated-phospholipid binding protein', *Bioscience Reports*, 7(4), pp. 289-298.
- Gerace, L. and Burke, B. (1988) 'Functional Organization of the Nuclear Envelope', *Annual Review of Cell Biology*, 4(1), pp. 335-374.
- Gerke, V., Creutz, C.E. and Moss, S.E. (2005) 'Annexins: linking Ca<sup>2+</sup> signalling to membrane dynamics', *Nature Reviews Molecular Cell Biology*, 6(6), pp. 449-461.
- Gerke, V. and Moss, S.E. (2002) 'Annexins: From Structure to Function', *Physiological Reviews*, 82(2), pp. 331-371.
- Getting, S.J., Flower, R.J. and Perretti, M. (1997) 'Inhibition of neutrophil and monocyte recruitment by endogenous and exogenous lipocortin 1', *British journal of pharmacology*, 120(6), pp. 1075-1082.
- Glenney, J.R., Jr, Tack, B. and Powell, M.A. (1987) 'Calpactins: two distinct Ca<sup>++</sup>-regulated phospholipid- and actin-binding proteins isolated from lung and placenta', *Journal of Cell Biology*, 104(3), pp. 503-511.
- Gloerich, M. *et al.* (2017) 'Cell division orientation is coupled to cell-cell adhesion by the E-cadherin/LGN complex', *Nat Commun*, 8, p. 13996.
- Godin, J.D. *et al.* (2010) 'Huntingtin Is Required for Mitotic Spindle Orientation and Mammalian Neurogenesis', *Neuron*, 67(3), pp. 392-406.
- Goldstein, B. and Macara, I.G. (2007) 'The PAR Proteins: Fundamental Players in Animal Cell Polarization', *Developmental Cell*, 13(5), pp. 609-622.

- Goldstein, L.S. (1993) 'Functional redundancy in mitotic force generation', *The Journal of Cell Biology*, 120(1), pp. 1-3.
- Gómez-López, S., Lerner, R.G. and Petritsch, C. (2014) 'Asymmetric cell division of stem and progenitor cells during homeostasis and cancer', *Cellular and Molecular Life Sciences*, 71(4), pp. 575-597.
- Goodman, B. and Zheng, Y. (2006) 'Mitotic spindle morphogenesis: Ran on the microtubule cytoskeleton and beyond', *Biochemical Society Transactions*, 34(5), pp. 716-721.
- Goodrich, L.V. and Strutt, D. (2011) 'Principles of planar polarity in animal development', *Development*, 138(10), pp. 1877-1892.
- Goshima, G. and Kimura, A. (2010) 'New look inside the spindle: microtubule-dependent microtubule generation within the spindle', *Curr Opin Cell Biol*, 22(1), pp. 44-9.
- Goshima, G. *et al.* (2008) 'Augmin: a protein complex required for centrosome-independent microtubule generation within the spindle', *J Cell Biol*, 181(3), pp. 421-9.
- Graham, F.L. *et al.* (1977) 'Characteristics of a Human Cell Line Transformed by DNA from Human Adenovirus Type 5', *Journal of General Virology*, 36(1), pp. 59-72.
- Gray, R.S., Cheung, K.J. and Ewald, A.J. (2010) 'Cellular mechanisms regulating epithelial morphogenesis and cancer invasion', *Current Opinion in Cell Biology*, 22(5), pp. 640-650.
- Greenberg, S.R., Tan, W. and Lee, W.-L. (2018) 'Num1 versus NuMA: insights from two functionally homologous proteins', *Biophysical Reviews*, 10(6), pp. 1631-1636.
- Grewal, T. (2017) 'Annexins in cell migration and adhesion', *Cell adhesion & migration*, 11(3), pp. 245-246.
- Grewal, T. *et al.* (2019) 'Annexins in Adipose Tissue: Novel Players in Obesity', *International Journal of Molecular Sciences*, 20(14), p. 3449.
- Grewal, T. *et al.* (2016) 'Annexins – insights from knockout mice', 397(10), p. 1031.
- Gruber, R. *et al.* (2011) 'MCPH1 regulates the neuroprogenitor division mode by coupling the centrosomal cycle with mitotic entry through the Chk1-Cdc25 pathway', *Nat Cell Biol*, 13(11), pp. 1325-34.
- Gulino, A., Di Marcotullio, L. and Screpanti, I. (2010) 'The multiple functions of Numb', *Exp Cell Res*, 316(6), pp. 900-6.
- Gullberg, M. and Andersson, A.-C. (2010) 'Visualization and quantification of protein-protein interactions in cells and tissues', *Nature Methods*, 7(6), pp. v-vi.
- Gundry, R.L. *et al.* (2010) 'Preparation of Proteins and Peptides for Mass Spectrometry Analysis in a Bottom-Up Proteomics Workflow', *Current Protocols in Molecular Biology*, 90(1), pp. 10.25.1-10.25.23.
- Guo, H. *et al.* (2021) 'Importin  $\alpha$  phosphorylation promotes TPX2 activation by GM130 to control astral microtubules and spindle orientation', *Journal of Cell Science*, 134(4).
- Hamers-Casterman, C. *et al.* (1993) 'Naturally occurring antibodies devoid of light chains', *Nature*, 363(6428), pp. 446-448.

- Han, H. (2018) 'RNA Interference to Knock Down Gene Expression', *Methods in molecular biology (Clifton, N.J.)*, 1706, pp. 293-302.
- Han, P.-F. *et al.* (2020) 'Annexin A1 involved in the regulation of inflammation and cell signaling pathways', *Chinese Journal of Traumatology*, 23(2), pp. 96-101.
- Han, X., Aslanian, A. and Yates, J.R. (2008) 'Mass spectrometry for proteomics', *Current Opinion in Chemical Biology*, 12(5), pp. 483-490.
- Hannon, R. *et al.* (2003) 'Aberrant inflammation and resistance to glucocorticoids in Annexin 1-/- Mouse', *The FASEB Journal*, 17(2), pp. 253-255.
- Hao, Y. *et al.* (2010) 'Par3 controls epithelial spindle orientation by aPKC-mediated phosphorylation of apical Pins', *Curr Biol*, 20(20), pp. 1809-18.
- Haren, L. and Merdes, A. (2002) 'Direct binding of NuMA to tubulin is mediated by a novel sequence motif in the tail domain that bundles and stabilizes microtubules', *Journal of Cell Science*, 115(9), pp. 1815-1824.
- Hartsock, A. and Nelson, W.J. (2008) 'Adherens and tight junctions: structure, function and connections to the actin cytoskeleton', *Biochimica et biophysica acta*, 1778(3), pp. 660-669.
- Hayashi, M.T. and Karlseder, J. (2013) 'DNA damage associated with mitosis and cytokinesis failure', *Oncogene*, 32(39), pp. 4593-4601.
- Hayes, M.J. *et al.* (2004) 'Annexin-Actin Interactions', *Traffic*, 5(8), pp. 571-576.
- Hehnlly, H. and Doxsey, S. (2014) 'Rab11 Endosomes Contribute to Mitotic Spindle Organization and Orientation', *Developmental Cell*, 28(5), pp. 497-507.
- Hertwig, O. (1884) *Das Problem der Befruchtung und der Isotropie des Eies, eine Theorie der Vererbung*. Jena.
- Herzenberg, L.A. *et al.* (2002) 'The History and Future of the Fluorescence Activated Cell Sorter and Flow Cytometry: A View from Stanford', *Clinical Chemistry*, 48(10), pp. 1819-1827.
- Holland, A.J., Lan, W. and Cleveland, D.W. (2010) 'Centriole duplication: A lesson in self-control', *Cell cycle (Georgetown, Tex.)*, 9(14), pp. 2731-2736.
- HORLICK, K.R. *et al.* (1991) 'Annexin-I Regulation in Response to Suckling and Rat Mammary Cell Differentiation\*', *Endocrinology*, 128(3), pp. 1574-1579.
- Horvitz, H.R. and Herskowitz, I. (1992) 'Mechanisms of asymmetric cell division: Two Bs or not two Bs, that is the question', *Cell*, 68(2), pp. 237-255.
- Housden, B.E. *et al.* (2017) 'Loss-of-function genetic tools for animal models: cross-species and cross-platform differences', *Nature reviews. Genetics*, 18(1), pp. 24-40.
- Hoyt, M.A. and Geiser, J.R. (1996) 'GENETIC ANALYSIS OF THE MITOTIC SPINDLE', *Annual Review of Genetics*, 30(1), pp. 7-33.
- Huang, L. and Muthuswamy, S.K. (2010) 'Polarity protein alterations in carcinoma: a focus on emerging roles for polarity regulators', *Current Opinion in Genetics & Development*, 20(1), pp. 41-50.

- Hutchins, J.R.A. *et al.* (2010) 'Systematic analysis of human protein complexes identifies chromosome segregation proteins', *Science (New York, N.Y.)*, 328(5978), pp. 593-599.
- Inman, J.L. *et al.* (2015) 'Mammary gland development: cell fate specification, stem cells and the microenvironment', *Development*, 142(6), pp. 1028-42.
- Inoue, D. *et al.* (2019) 'Actin filaments regulate microtubule growth at the centrosome', *The EMBO Journal*, 38(11), p. e99630.
- Isacke, C.M., Lindberg, R.A. and Hunter, T. (1989) 'Synthesis of p36 and p35 is increased when U-937 cells differentiate in culture but expression is not inducible by glucocorticoids', *Molecular and Cellular Biology*, 9(1), pp. 232-240.
- Israels, E.D. and Israels, L.G. (2000) 'The cell cycle', *Oncologist*, 5(6), pp. 510-3.
- Jamieson, P.R. *et al.* (2017) 'Derivation of a robust mouse mammary organoid system for studying tissue dynamics', *Development*, 144(6), pp. 1065-1071.
- Jensen, C. and Teng, Y. (2020) 'Is It Time to Start Transitioning From 2D to 3D Cell Culture?', *Frontiers in Molecular Biosciences*, 7(33).
- Jia, M. *et al.* (2012) 'Crystal Structures of the Scaffolding Protein LGN Reveal the General Mechanism by Which GoLoco Binding Motifs Inhibit the Release of GDP from Gai', *Journal of Biological Chemistry*, 287(44), pp. 36766-36776.
- Jo, Y.-J. *et al.* (2015) 'Actin-capping proteins play essential roles in the asymmetric division of maturing mouse oocytes', *Journal of Cell Science*, 128(1), pp. 160-170.
- Joberty, G. *et al.* (2000) 'The cell-polarity protein Par6 links Par3 and atypical protein kinase C to Cdc42', *Nature Cell Biology*, 2, p. 531.
- Josefsberg, L.B.-Y. *et al.* (2000) 'The Proteasome Is Involved in the First Metaphase-to-Anaphase Transition of Meiosis in Rat Oocytes1', *Biology of Reproduction*, 62(5), pp. 1270-1277.
- Joshi, P.A. *et al.* (2010) 'Progesterone induces adult mammary stem cell expansion', *Nature*, 465, p. 803.
- Kamakura, S. *et al.* (2013) 'The Cell Polarity Protein mInsc Regulates Neutrophil Chemotaxis via a Noncanonical G Protein Signaling Pathway', *Developmental Cell*, 26(3), pp. 292-302.
- Kapałczyńska, M. *et al.* (2018) '2D and 3D cell cultures - a comparison of different types of cancer cell cultures', *Archives of medical science : AMS*, 14(4), pp. 910-919.
- Kardon, J.R. and Vale, R.D. (2009) 'Regulators of the cytoplasmic dynein motor', *Nature Reviews Molecular Cell Biology*, 10(12), pp. 854-865.
- Karsenti, E. and Vernos, I. (2001) 'The Mitotic Spindle: A Self-Made Machine', *Science*, 294(5542), pp. 543-547.
- Kastan, M.B. and Bartek, J. (2004) 'Cell-cycle checkpoints and cancer', *Nature*, 432(7015), pp. 316-323.
- Kaufmann, W.K. and Paules, R.S. (1996) 'DNA damage and cell cycle checkpoints', *The FASEB Journal*, 10(2), pp. 238-247.

- Kaushik, R. *et al.* (2003) 'Subcellular localization of LGN during mitosis: evidence for its cortical localization in mitotic cell culture systems and its requirement for normal cell cycle progression', *Mol Biol Cell*, 14(8), pp. 3144-55.
- Kellogg, D.R., Moritz, M. and Alberts, B.M. (1994) 'THE CENTROSOME AND CELLULAR ORGANIZATION', *Annu. Rev. Biochem*, (63), pp. 639-74.
- Khafizov, K. (2009) 'GoLoco motif proteins binding to Galpha(i1): insights from molecular simulations', *Journal of molecular modeling*, 15(12), pp. 1491-1499.
- Kim, Y.S. *et al.* (2003) 'PKC $\delta$ -dependent cleavage and nuclear translocation of annexin A1 by phorbol 12-myristate 13-acetate', *European Journal of Biochemistry*, 270(20), pp. 4089-4094.
- Kita, A.M. *et al.* (2019) 'Spindle–F-actin interactions in mitotic spindles in an intact vertebrate epithelium', *Molecular Biology of the Cell*, 30(14), pp. 1645-1654.
- Kiyomitsu, T. (2019) 'The cortical force-generating machinery: how cortical spindle-pulling forces are generated', *Current Opinion in Cell Biology*, 60, pp. 1-8.
- Kiyomitsu, T. and Boerner, S. (2021) 'The Nuclear Mitotic Apparatus (NuMA) Protein: A Key Player for Nuclear Formation, Spindle Assembly, and Spindle Positioning', *Frontiers in Cell and Developmental Biology*, 9(728).
- Kiyomitsu, T. and Cheeseman, I.M. (2012) 'Chromosome- and spindle-pole-derived signals generate an intrinsic code for spindle position and orientation', *Nat Cell Biol*, 14(3), pp. 311-7.
- Konno, D. *et al.* (2008) 'Neuroepithelial progenitors undergo LGN-dependent planar divisions to maintain self-renewability during mammalian neurogenesis', *Nat Cell Biol*, 10(1), pp. 93-101.
- Kotak, S. (2019) 'Mechanisms of Spindle Positioning: Lessons from Worms and Mammalian Cells', *Biomolecules*, 9(2), p. 80.
- Kotak, S., Busso, C. and Gonczy, P. (2012) 'Cortical dynein is critical for proper spindle positioning in human cells', *J Cell Biol*, 199(1), pp. 97-110.
- Kotak, S., Busso, C. and Gönczy, P. (2014) 'NuMA interacts with phosphoinositides and links the mitotic spindle with the plasma membrane', *The EMBO journal*, 33(16), pp. 1815-1830.
- Krishnan, K. and Moens, P.D.J. (2009) 'Structure and functions of profilins', *Biophysical reviews*, 1(2), pp. 71-81.
- Kschonsak, Y.T. and Hoffmann, I. (2018) 'Activated Ezrin controls MISP levels to ensure correct NuMA polarization and spindle orientation', *Journal of Cell Science*, p. jcs.214544.
- Kwon, M. *et al.* (2015) 'Direct Microtubule-Binding by Myosin-10 Orients Centrosomes toward Retraction Fibers and Subcortical Actin Clouds', *Dev Cell*, 34(3), pp. 323-37.
- Laan, L. *et al.* (2012) 'Cortical Dynein Controls Microtubule Dynamics to Generate Pulling Forces that Position Microtubule Asters', *Cell*, 148(3), pp. 502-514.
- Laemmli, U.K. (1970) 'Cleavage of Structural Proteins during the Assembly of the Head of Bacteriophage T4', *Nature*, 227(5259), pp. 680-685.
- Lancaster, M.A. and Knoblich, J.A. (2012) 'Spindle orientation in mammalian cerebral cortical development', *Curr Opin Neurobiol*, 22(5), pp. 737-46.

- Lara-Gonzalez, P., Westhorpe, Frederick G. and Taylor, Stephen S. (2012) 'The Spindle Assembly Checkpoint', *Current Biology*, 22(22), pp. R966-R980.
- Larson, M.E. and Bement, W.M. (2017) 'Automated mitotic spindle tracking suggests a link between spindle dynamics, spindle orientation, and anaphase onset in epithelial cells', *Molecular biology of the cell*, 28(6), pp. 746-759.
- Lawo, S. *et al.* (2009) 'HAUS, the 8-Subunit Human Augmin Complex, Regulates Centrosome and Spindle Integrity', *Current Biology*, 19(10), pp. 816-826.
- Lázaro-Diéguez, F., Ispolatov, I. and Müsch, A. (2015) 'Cell shape impacts on the positioning of the mitotic spindle with respect to the substratum', *Mol Biol Cell*, 26(7), pp. 1286-95.
- Le Bras, S. and Le Borgne, R. (2014) 'Epithelial cell division – multiplying without losing touch', *Journal of Cell Science*, 127(24), pp. 5127-5137.
- Lechler, T. and Fuchs, E. (2005) 'Asymmetric cell divisions promote stratification and differentiation of mammalian skin', *Nature*, 437(7056), pp. 275-80.
- Lechler, T. and Mapelli, M. (2021) 'Spindle positioning and its impact on vertebrate tissue architecture and cell fate', *Nature Reviews Molecular Cell Biology*.
- Lee, B.H. *et al.* (2018) 'p37/UBXN2B regulates spindle orientation by limiting cortical NuMA recruitment via PP1/Repo-Man', *J Cell Biol*, 217(2), pp. 483-493.
- Lee, Y.-R.J. and Liu, B. (2019) 'Microtubule nucleation for the assembly of acentrosomal microtubule arrays in plant cells', *New Phytologist*, 222(4), pp. 1705-1718.
- Lénárt, P. *et al.* (2007) 'The Small-Molecule Inhibitor BI 2536 Reveals Novel Insights into Mitotic Roles of Polo-like Kinase 1', *Current Biology*, 17(4), pp. 304-315.
- Li, L. and Clevers, H. (2010) 'Coexistence of Quiescent and Active Adult Stem Cells in Mammals', *Science*, 327(5965), pp. 542-545.
- Lim, L.H.K. and Pervaiz, S. (2007) 'Annexin 1: the new face of an old molecule', *The FASEB Journal*, 21(4), pp. 968-975.
- Lim, S. and Kaldis, P. (2013) 'Cdks, cyclins and CKIs: roles beyond cell cycle regulation', *Development*, 140(15), pp. 3079-3093.
- Liu, H., Sadygov, R.G. and Yates, J.R., 3rd (2004) 'A model for random sampling and estimation of relative protein abundance in shotgun proteomics', *Anal Chem*, 76(14), pp. 4193-201.
- Lloyd-Lewis, B. *et al.* (2017) 'Mammary Stem Cells: Premise, Properties, and Perspectives', *Trends Cell Biol*, 27(8), pp. 556-567.
- Lu, M.S. and Johnston, C.A. (2013) 'Molecular pathways regulating mitotic spindle orientation in animal cells', *Development*, 140(9), pp. 1843-56.
- Lukinavičius, G. *et al.* (2014) 'Fluorogenic probes for live-cell imaging of the cytoskeleton', *Nature Methods*, 11(7), pp. 731-733.
- Lydersen, B.K. and Pettijohn, D.E. (1980) 'Human-specific nuclear protein that associates with the polar region of the mitotic apparatus: Distribution in a human/hamster hybrid cell', *Cell*, 22(2), pp. 489-499.

- Macara, I.G. (2004) 'Parsing the Polarity Code', *Nature Reviews Molecular Cell Biology*, 5(3), pp. 220-231.
- Machicoane, M. *et al.* (2014) 'SLK-dependent activation of ERMs controls LGN-NuMA localization and spindle orientation', *J Cell Biol*, 205(6), pp. 791-9.
- Mack, G.J. and Compton, D.A. (2001) 'Analysis of mitotic microtubule-associated proteins using mass spectrometry identifies astrin, a spindle-associated protein', *Proceedings of the National Academy of Sciences*, 98(25), pp. 14434-14439.
- Maiato, H. and Logarinho, E. (2014) 'Mitotic spindle multipolarity without centrosome amplification', *Nature Cell Biology*, 16(5), pp. 386-394.
- Maier, B. *et al.* (2013) 'The novel actin/focal adhesion-associated protein MISP is involved in mitotic spindle positioning in human cells', *Cell Cycle*, 12(9), pp. 1457-1471.
- Mailleux, A.A., Overholtzer, M. and Brugge, J.S. (2008) 'Lumen formation during mammary epithelial morphogenesis: insights from in vitro and in vivo models', *Cell Cycle*, 7(1), pp. 57-62.
- Malik, R. *et al.* (2009) 'Quantitative Analysis of the Human Spindle Phosphoproteome at Distinct Mitotic Stages', *Journal of Proteome Research*, 8(10), pp. 4553-4563.
- Malumbres, M. and Barbacid, M. (2001) 'To cycle or not to cycle: a critical decision in cancer', *Nature Reviews Cancer*, 1, p. 222.
- Manning, A.L. *et al.* (2010) 'CLASP1, astrin and Kif2b form a molecular switch that regulates kinetochore-microtubule dynamics to promote mitotic progression and fidelity', *The EMBO Journal*, 29(20), pp. 3531-3543.
- Martin-Belmonte, F. and Mostov, K. (2008) 'Regulation of cell polarity during epithelial morphogenesis', *Current Opinion in Cell Biology*, 20(2), pp. 227-234.
- Martin, D.D. *et al.* (2015) 'Autophagy in Huntington disease and huntingtin in autophagy', *Trends Neurosci*, 38(1), pp. 26-35.
- Maschler, S. *et al.* (2010) 'Annexin A1 attenuates EMT and metastatic potential in breast cancer', *EMBO Mol Med*, 2(10), pp. 401-14.
- Matsumura, S. *et al.* (2012) 'ABL1 regulates spindle orientation in adherent cells and mammalian skin', *Nature communications*, 3, pp. 626-626.
- McArthur, S. *et al.* (2015) 'Definition of a Novel Pathway Centered on Lysophosphatidic Acid To Recruit Monocytes during the Resolution Phase of Tissue Inflammation', *The Journal of Immunology*, 195(3), pp. 1139-1151.
- McCaffrey, L.M. and Macara, I.G. (2009) 'The Par3/aPKC interaction is essential for end bud remodeling and progenitor differentiation during mammary gland morphogenesis', *Genes & Development*, 23(12), pp. 1450-1460.
- McCudden, C.R. *et al.* (2005a) 'G-protein signaling: back to the future', *Cellular and Molecular Life Sciences*, 62(5), pp. 551-577.
- McCudden, C.R. *et al.* (2005b) 'Gα selectivity and inhibitor function of the multiple GoLoco motif protein GPSM2/LGN', *Biochimica et Biophysica Acta (BBA) - Molecular Cell Research*, 1745(2), pp. 254-264.

- McEwen, B.F. *et al.* (1997) 'Kinetochore fiber maturation in PtK1 cells and its implications for the mechanisms of chromosome congression and anaphase onset', *J Cell Biol*, 137(7), pp. 1567-80.
- McIntosh, J.R. and Euteneuer, U. (1984) 'Tubulin hooks as probes for microtubule polarity: an analysis of the method and an evaluation of data on microtubule polarity in the mitotic spindle', *The Journal of Cell Biology*, 98(2), pp. 525-533.
- McIntosh, J.R. *et al.* (2010) 'Tubulin depolymerization may be an ancient biological motor', *Journal of Cell Science*, 123(20), pp. 3425-3434.
- Meijering, E. *et al.* (2008) 'Chapter 15 - Time-Lapse Imaging', in Wu, Q., Merchant, F.A. and Castleman, K.R. (eds.) *Microscope Image Processing*. Burlington: Academic Press, pp. 401-440.
- Mellacheruvu, D. *et al.* (2013) 'The CRAPome: a contaminant repository for affinity purification–mass spectrometry data', *Nature Methods*, 10(8), pp. 730-736.
- Meraldi, P., Draviam, V.M. and Sorger, P.K. (2004) 'Timing and Checkpoints in the Regulation of Mitotic Progression', *Developmental Cell*, 7(1), pp. 45-60.
- Merdes, A. *et al.* (1996) 'A Complex of NuMA and Cytoplasmic Dynein Is Essential for Mitotic Spindle Assembly', *Cell*, 87, pp. 447-458.
- Minc, N., Burgess, D. and Chang, F. (2011) 'Influence of Cell Geometry on Division-Plane Positioning', *Cell*, 144(3), pp. 414-426.
- Minghetti, L. *et al.* (1999) 'Down-regulation of microglial cyclo-oxygenase-2 and inducible nitric oxide synthase expression by lipocortin 1', *British journal of pharmacology*, 126(6), pp. 1307-1314.
- Mirsaiedi, M. *et al.* (2016) 'Annexins family: insights into their functions and potential role in pathogenesis of sarcoidosis', *Journal of Translational Medicine*, 14(1), p. 89.
- Miserey-Lenkei, S. and Colombo, M.I. (2016) 'Small RAB GTPases Regulate Multiple Steps of Mitosis', *Frontiers in Cell and Developmental Biology*, 4(2).
- Mitchison, T.J. and Salmon, E.D. (2001) 'Mitosis: a history of division', *Nature Cell Biology*, 3, p. E17.
- Miteva, Y.V., Budayeva, H.G. and Cristea, I.M. (2013) 'Proteomics-Based Methods for Discovery, Quantification, and Validation of Protein–Protein Interactions', *Analytical Chemistry*, 85(2), pp. 749-768.
- Mitsushima, M., Toyoshima, F. and Nishida, E. (2009) 'Dual role of Cdc42 in spindle orientation control of adherent cells', *Mol Cell Biol*, 29(10), pp. 2816-27.
- Miwa, N., Uebi, T. and Kawamura, S. (2008) 'S100–annexin complexes – biology of conditional association', *The FEBS Journal*, 275(20), pp. 4945-4955.
- Mlecnik, B., Galon, J. and Bindea, G. (2018) 'Comprehensive functional analysis of large lists of genes and proteins', *Journal of Proteomics*, 171, pp. 2-10.
- Mocellin, S. and Provenzano, M. (2004) 'RNA interference: learning gene knock-down from cell physiology', *Journal of translational medicine*, 2(1), pp. 39-39.
- Mochizuki, N. *et al.* (1996) 'Identification and cDNA cloning of a novel human mosaic protein, LGN, based on interaction with Gai2', *Gene*, 181(1), pp. 39-43.

- Molina-Calavita, M. *et al.* (2014) 'Mutant Huntingtin Affects Cortical Progenitor Cell Division and Development of the Mouse Neocortex', *The Journal of Neuroscience*, 34(30), pp. 10034-10040.
- Moon, H.M. *et al.* (2013) 'LIS1 controls mitosis and mitotic spindle organization via the LIS1–NDEL1–dynein complex', *Human Molecular Genetics*, 23(2), pp. 449-466.
- Moore, J.K., Li, J. and Cooper, J.A. (2008) 'Dynactin Function in Mitotic Spindle Positioning', *Traffic*, 9(4), pp. 510-527.
- Moresco, J.J., Carvalho, P.C. and Yates, J.R. (2010) 'Identifying components of protein complexes in *C. elegans* using co-immunoprecipitation and mass spectrometry', *Journal of Proteomics*, 73(11), pp. 2198-2204.
- Morgan, R.O. *et al.* (1998) 'Genomic Locations of ANX11 and ANX13 and the Evolutionary Genetics of Human Annexins', *Genomics*, 48(1), pp. 100-110.
- Morgenstern, J.P. and Land, H. (1990) 'Advanced mammalian gene transfer: high titre retroviral vectors with multiple drug selection markers and a complementary helper-free packaging cell line', *Nucleic Acids Research*, 18(12), pp. 3587-3596.
- Morin, X. and Bellaïche, Y. (2011) 'Mitotic spindle orientation in asymmetric and symmetric cell divisions during animal development', *Dev Cell*, 21(1), pp. 102-19.
- Morin, X., Jaouen, F. and Durbec, P. (2007) 'Control of planar divisions by the G-protein regulator LGN maintains progenitors in the chick neuroepithelium', *Nat Neurosci*, 10(11), pp. 1440-8.
- Morris, C. and Jalinot, P. (2005) 'Silencing of human Int-6 impairs mitosis progression and inhibits cyclin B–Cdk1 activation', *Oncogene*, 24(7), pp. 1203-1211.
- Morris, E.J. *et al.* (2020) 'A Model of Differential Mammary Growth Initiation by Stat3 and Asymmetric Integrin- $\alpha$ 6 Inheritance', *Cell Reports*, 30(11), pp. 3605-3615.e5.
- Morrison, S.J. and Kimble, J. (2006) 'Asymmetric and symmetric stem-cell divisions in development and cancer', *Nature*, 441(7097), pp. 1068-1074.
- Moss, S.E. and Morgan, R.O. (2004) 'The annexins', *Genome Biology*, 5(4), p. 219.
- Mullis, K.B. and Faloona, F.A. (1987) '[21] Specific synthesis of DNA in vitro via a polymerase-catalyzed chain reaction', in *Methods in Enzymology*. Academic Press, pp. 335-350.
- Musacchio, A. and Salmon, E.D. (2007) 'The spindle-assembly checkpoint in space and time', *Nature Reviews Molecular Cell Biology*, 8(5), pp. 379-393.
- Nadella, R. *et al.* (2010) 'Activator of G protein signaling 3 promotes epithelial cell proliferation in PKD', *Journal of the American Society of Nephrology : JASN*, 21(8), pp. 1275-1280.
- Nakajima, Y.-i. (2018) 'Mitotic spindle orientation in epithelial homeostasis and plasticity', *The Journal of Biochemistry*, 164(4), pp. 277-284.
- Nelson, W.J. (2003) 'Adaptation of core mechanisms to generate cell polarity', *Nature*, 422, p. 766.
- Nestor-Bergmann, A., Goddard, G. and Woolner, S. (2014) 'Force and the spindle: mechanical cues in mitotic spindle orientation', *Seminars in cell & developmental biology*, 34, pp. 133-139.
- Neumuller, R.A. and Knoblich, J.A. (2009) 'Dividing cellular asymmetry: asymmetric cell division and its implications for stem cells and cancer', *Genes Dev*, 23(23), pp. 2675-99.

- Noatynska, A., Gotta, M. and Meraldi, P. (2012) 'Mitotic spindle (DIS)orientation and DISease: cause or consequence?', *The Journal of cell biology*, 199(7), pp. 1025-1035.
- Noctor, S.C. *et al.* (2004) 'Cortical neurons arise in symmetric and asymmetric division zones and migrate through specific phases', *Nature Neuroscience*, 7(2), pp. 136-144.
- Norbury, C. and Nurse, P. (1992) 'Animal Cell Cycles and Their Control', *Annual Review of Biochemistry*, 61(1), pp. 441-468.
- Nousiainen, M. *et al.* (2006) 'Phosphoproteome analysis of the human mitotic spindle', *Proceedings of the National Academy of Sciences*, 103(14), pp. 5391-5396.
- O'Connell, C.B. and Wang, Y.-I. (2000) 'Mammalian Spindle Orientation and Position Respond to Changes in Cell Shape in a Dynein-dependent Fashion', *Molecular Biology of the Cell*, 11(5), pp. 1765-1774.
- Obaya, A.J. and Sedivy, J.M. (2002) 'Regulation of cyclin-Cdk activity in mammalian cells', *Cell Mol Life Sci*, 59(1), pp. 126-42.
- Okumura, M. *et al.* (2018) 'Dynein–Dynactin–NuMA clusters generate cortical spindle-pulling forces as a multi-arm ensemble', *eLife*, 7, p. e36559.
- Olziersky, A.-M. *et al.* (2018) 'Chapter 1 - Mitotic live-cell imaging at different timescales', in Maiato, H. and Schuh, M. (eds.) *Methods in Cell Biology*. Academic Press, pp. 1-27.
- Ong, S.E. and Mann, M. (2005) 'Mass spectrometry-based proteomics turns quantitative', *Nat Chem Biol*, 1(5), pp. 252-62.
- Oozer, F. *et al.* (2017) 'A role for core planar polarity proteins in cell contact-mediated orientation of planar cell division across the mammalian embryonic skin', *Scientific Reports*, 7(1), p. 1880.
- ÖSTERGREN, G. (1951) 'THE MECHANISM OF CO-ORIENTATION IN BIVALENTS AND MULTIVALENTS', *Hereditas*, 37(1-2), pp. 85-156.
- Pampalona, J. *et al.* (2016) 'Chromosome Bridges Maintain Kinetochore-Microtubule Attachment throughout Mitosis and Rarely Break during Anaphase', *PLOS ONE*, 11(1), p. e0147420.
- Pan, X. *et al.* (2021) 'Identification of Protein Subcellular Localization With Network and Functional Embeddings', *Frontiers in Genetics*, 11(1800).
- Pan, Z. *et al.* (2013) 'An Autoinhibited Conformation of LGN Reveals a Distinct Interaction Mode between GoLoco Motifs and TPR Motifs', *Structure*, 21(6), pp. 1007-1017.
- Pandey, A. and Mann, M. (2000) 'Proteomics to study genes and genomes', *Nature*, 405(6788), pp. 837-846.
- Panousopoulou, E. and Green, J.B.A. (2014) 'Spindle orientation processes in epithelial growth and organisation', *Seminars in Cell & Developmental Biology*, 34, pp. 124-132.
- Pardee, A.B. (1974) 'A restriction point for control of normal animal cell proliferation', *Proceedings of the National Academy of Sciences of the United States of America*, 71(4), pp. 1286-1290.
- Pease, J.C. and Tirnauer, J.S. (2011) 'Mitotic spindle misorientation in cancer – out of alignment and into the fire', *Journal of Cell Science*, 124(7), pp. 1007-1016.

- Pereira, A.L. *et al.* (2006) 'Mammalian CLASP1 and CLASP2 Cooperate to Ensure Mitotic Fidelity by Regulating Spindle and Kinetochore Function', *Molecular Biology of the Cell*, 17(10), pp. 4526-4542.
- Perez-Riba, A. and Itzhaki, L.S. (2019) 'The tetratricopeptide-repeat motif is a versatile platform that enables diverse modes of molecular recognition', *Current Opinion in Structural Biology*, 54, pp. 43-49.
- Perez-Riverol, Y. *et al.* (2019) 'The PRIDE database and related tools and resources in 2019: improving support for quantification data', *Nucleic Acids Res*, 47(D1), pp. D442-d450.
- Petry, S. (2016) 'Mechanisms of Mitotic Spindle Assembly', *Annual Review of Biochemistry*, 85(1), pp. 659-683.
- Peyre, E. *et al.* (2011) 'A lateral belt of cortical LGN and NuMA guides mitotic spindle movements and planar division in neuroepithelial cells', *Journal of Cell Biology*, 193(1), pp. 141-154.
- Phizicky, E.M. and Fields, S. (1995) 'Protein-protein interactions: methods for detection and analysis', *Microbiological reviews*, 59(1), pp. 94-123.
- Pieczynski, J. and Margolis, B. (2011) 'Protein complexes that control renal epithelial polarity', *American Journal of Physiology-Renal Physiology*, 300(3), pp. F589-F601.
- Pin, A.-L. *et al.* (2012) 'Annexin-1-mediated Endothelial Cell Migration and Angiogenesis Are Regulated by Vascular Endothelial Growth Factor (VEGF)-induced Inhibition of miR-196a Expression \*<sup><sup></sup>', *Journal of Biological Chemistry*, 287(36), pp. 30541-30551.</sup>
- Pirovano, L. *et al.* (2019) 'Hexameric NuMA:LGN structures promote multivalent interactions required for planar epithelial divisions', *Nature Communications*, 10(1), p. 2208.
- Poeter, M. *et al.* (2013) 'Disruption of the annexin A1/S100A11 complex increases the migration and clonogenic growth by dysregulating epithelial growth factor (EGF) signaling', *Biochimica et Biophysica Acta (BBA) - Molecular Cell Research*, 1833(7), pp. 1700-1711.
- Porter, A.P. *et al.* (2019) 'The interaction between CASK and the tumour suppressor Dlg1 regulates mitotic spindle orientation in mammalian epithelia', *J Cell Sci*, 132(14).
- Prosser, S.L. and Pelletier, L. (2017) 'Mitotic spindle assembly in animal cells: a fine balancing act', *Nat Rev Mol Cell Biol*, 18(3), pp. 187-201.
- Pupjalis, D. *et al.* (2011) 'Annexin A1 released from apoptotic cells acts through formyl peptide receptors to dampen inflammatory monocyte activation via JAK/STAT/SOCS signalling', *EMBO Molecular Medicine*, 3(2), pp. 102-114.
- Purvis, G.S.D., Solito, E. and Thiemermann, C. (2019) 'Annexin-A1: Therapeutic Potential in Microvascular Disease', *Frontiers in immunology*, 10, pp. 938-938.
- Qin, J.Y. *et al.* (2010) 'Systematic Comparison of Constitutive Promoters and the Doxycycline-Inducible Promoter', *PLOS ONE*, 5(5), p. e10611.
- Quyn, A.J. *et al.* (2010) 'Spindle Orientation Bias in Gut Epithelial Stem Cell Compartments Is Lost in Precancerous Tissue', *Cell Stem Cell*, 6(2), pp. 175-181.
- Radke, S. *et al.* (2004) 'Specific association of annexin 1 with plasma membrane-resident and internalized EGF receptors mediated through the protein core domain', *FEBS Letters*, 578(1), pp. 95-98.

- Ragkousi, K. and Gibson, M.C. (2014) 'Cell division and the maintenance of epithelial order', *J Cell Biol*, 207(2), pp. 181-8.
- Rao, S.R. *et al.* (2016) 'The Clathrin-dependent Spindle Proteome', *Molecular & Cellular Proteomics*, 15(8), pp. 2537-2553.
- Ray, S. and Lechler, T. (2011) 'Regulation of asymmetric cell division in the epidermis', *Cell Div*, 6(1), p. 12.
- Regan, J.L. *et al.* (2013) 'Aurora A kinase regulates mammary epithelial cell fate by determining mitotic spindle orientation in a Notch-dependent manner', *Cell Rep*, 4(1), pp. 110-23.
- Renna, C. *et al.* (2020) 'Organizational Principles of the NuMA-Dynein Interaction Interface and Implications for Mitotic Spindle Functions', *Structure*, 28(7), pp. 820-829.e6.
- Rentero, C. *et al.* (2018) 'Annexins-Coordinators of Cholesterol Homeostasis in Endocytic Pathways', *International journal of molecular sciences*, 19(5), p. 1444.
- Rescher, U., Zobiack, N. and Gerke, V. (2000) 'Intact Ca(2+)-binding sites are required for targeting of annexin 1 to endosomal membranes in living HeLa cells', *Journal of Cell Science*, 113(22), pp. 3931-3938.
- Rieder, C. and Salmon, E. (1994) 'Motile kinetochores and polar ejection forces dictate chromosome position on the vertebrate mitotic spindle', *The Journal of Cell Biology*, 124(3), pp. 223-233.
- Rintala-Dempsey, A.C., Rezvanpour, A. and Shaw, G.S. (2008) 'S100-annexin complexes – structural insights', *The FEBS Journal*, 275(20), pp. 4956-4966.
- Rizzelli, F. *et al.* (2020) 'The crosstalk between microtubules, actin and membranes shapes cell division', *Open Biol*, 10(3), p. 190314.
- Roberts, A.J. *et al.* (2013) 'Functions and mechanics of dynein motor proteins', *Nature Reviews Molecular Cell Biology*, 14(11), pp. 713-726.
- Rodriguez-Boulan, E. and Macara, I.G. (2014) 'Organization and execution of the epithelial polarity programme', *Nature Reviews Molecular Cell Biology*, 15(4), pp. 225-242.
- Roth, A. *et al.* (2016) 'The STRING database in 2017: quality-controlled protein–protein association networks, made broadly accessible', *Nucleic Acids Research*, 45(D1), pp. D362-D368.
- Rothbauer, U. *et al.* (2008) 'A Versatile Nanotrap for Biochemical and Functional Studies with Fluorescent Fusion Proteins', *Molecular & Cellular Proteomics*, 7(2), pp. 282-289.
- Saadaoui, M. *et al.* (2017) 'Loss of the canonical spindle orientation function in the Pins/LGN homolog AGS3', *EMBO reports*, 18(9), pp. 1509-1520.
- Saadaoui, M. *et al.* (2014) 'Dlg1 controls planar spindle orientation in the neuroepithelium through direct interaction with LGN', *J Cell Biol*, 206(6), pp. 707-17.
- Sakalem, M.E. *et al.* (2021) 'Historical evolution of spheroids and organoids, and possibilities of use in life sciences and medicine', *Biotechnology Journal*, 16(5), p. 2000463.
- Salmon, E.D. (1989) 'Cytokinesis in animal cells', *Current Opinion in Cell Biology*, (1), pp. 541-547.

- Samora, C.P. *et al.* (2011) 'MAP4 and CLASP1 operate as a safety mechanism to maintain a stable spindle position in mitosis', *Nature Cell Biology*, 13, p. 1040.
- Sana, S. *et al.* (2018) 'Plk1 regulates spindle orientation by phosphorylating NuMA in human cells', *Life Science Alliance*, 1(6), p. e201800223.
- Sanada, K. and Tsai, L.-H. (2005) 'G Protein  $\beta\gamma$  Subunits and AGS3 Control Spindle Orientation and Asymmetric Cell Fate of Cerebral Cortical Progenitors', *Cell*, 122(1), pp. 119-131.
- Santoro, A. *et al.* (2016) 'Molecular mechanisms of asymmetric divisions in mammary stem cells', *EMBO Rep*, 17(12), pp. 1700-1720.
- Sauer, G. *et al.* (2005) 'Proteome analysis of the human mitotic spindle', *Mol Cell Proteomics*, 4(1), pp. 35-43.
- Scarpa, E. *et al.* (2018) 'Actomyosin-Driven Tension at Compartmental Boundaries Orients Cell Division Independently of Cell Geometry In Vivo', *Developmental Cell*, 47(6), pp. 727-740.e6.
- Schindelin, J. *et al.* (2012) 'Fiji: an open-source platform for biological-image analysis', *Nature Methods*, 9(7), pp. 676-682.
- Schlaepfer, D.D. and Haigler, H.T. (1987) 'Characterization of Ca<sup>2+</sup>-dependent phospholipid binding and phosphorylation of lipocortin I', *Journal of Biological Chemistry*, 262(14), pp. 6931-6937.
- Schlaepfer, D.D. and Haigler, H.T. (1990) 'Expression of annexins as a function of cellular growth state', *Journal of Cell Biology*, 111(1), pp. 229-238.
- Schrader, F. (1953) 'Mitosis, the Movements of Chromosomes in Cell Division', *Columbia Univ. Press, New York*, 2.
- Schroer, T.A. (2004) 'DYNAMACTIN', *Annual Review of Cell and Developmental Biology*, 20(1), pp. 759-779.
- Schwartz-Albiez, R. *et al.* (1993) 'Differential expression of annexins I and II in normal and malignant human mammary epithelial cells', *Differentiation*, 52(3), pp. 229-237.
- Seemann, J. *et al.* (1996) 'The association of annexin I with early endosomes is regulated by Ca<sup>2+</sup> and requires an intact N-terminal domain', *Mol Biol Cell*, 7(9), pp. 1359-74.
- Ségalen, M. *et al.* (2010) 'The Fz-Dsh Planar Cell Polarity Pathway Induces Oriented Cell Division via Mud/NuMA in Drosophila and Zebrafish', *Developmental Cell*, 19(5), pp. 740-752.
- Segatto, I. *et al.* (2019) 'Stathmin Is Required for Normal Mouse Mammary Gland Development and  $\Delta$ 16HER2-Driven Tumorigenesis', *Cancer Research*, 79(2), pp. 397-409.
- Segurado, M. and Tercero, J.A. (2009) 'The S-phase checkpoint: targeting the replication fork', *Biology of the Cell*, 101(11), pp. 617-627.
- Seldin, L. and Macara, I. (2017) 'Epithelial spindle orientation diversities and uncertainties: recent developments and lingering questions', *F1000Res*, 6, p. 984.
- Seldin, L., Muroyama, A. and Lechler, T. (2016) 'NuMA-microtubule interactions are critical for spindle orientation and the morphogenesis of diverse epidermal structures', *Elife*, 5.

- Seldin, L. *et al.* (2013) 'NuMA localization, stability, and function in spindle orientation involve 4.1 and Cdk1 interactions', *Mol Biol Cell*, 24(23), pp. 3651-62.
- Sena-Esteves, M. *et al.* (2002) 'Generation of stable retrovirus packaging cell lines after transduction with herpes simplex virus hybrid amplicon vectors', *The Journal of Gene Medicine*, 4(3), pp. 229-239.
- Serres, M.P. *et al.* (2020) 'F-Actin Interactome Reveals Vimentin as a Key Regulator of Actin Organization and Cell Mechanics in Mitosis', *Dev Cell*, 52(2), pp. 210-222 e7.
- Shannon, P. *et al.* (2003) 'Cytoscape: A Software Environment for Integrated Models of Biomolecular Interaction Networks', *Genome Research*, 13(11), pp. 2498-2504.
- Shao, G. *et al.* (2019) 'Advancements of Annexin A1 in inflammation and tumorigenesis', *OncoTargets and therapy*, 12, pp. 3245-3254.
- Sharp, D.J., Rogers, G.C. and Scholey, J.M. (2000) 'Microtubule motors in mitosis', *Nature*, 407, p. 41.
- Sheikh, M.H. and Solito, E. (2018) 'Annexin A1: Uncovering the Many Talents of an Old Protein', *International journal of molecular sciences*, 19(4), p. 1045.
- Shen, D. *et al.* (2006) 'Decreased expression of annexin A1 is correlated with breast cancer development and progression as determined by a tissue microarray analysis', *Human Pathology*, 37(12), pp. 1583-1591.
- Shoemaker, B.A. and Panchenko, A.R. (2007) 'Deciphering Protein–Protein Interactions. Part I. Experimental Techniques and Databases', *PLOS Computational Biology*, 3(3), p. e42.
- Shu, H.B. and Joshi, H.C. (1995) 'Gamma-tubulin can both nucleate microtubule assembly and self-assemble into novel tubular structures in mammalian cells', *The Journal of cell biology*, 130(5), pp. 1137-1147.
- Siderovski, D.P., Diversé-Pierluissi, M.a.A. and De Vries, L. (1999) 'The GoLoco motif: a G-binding motif and potential guanine-nucleotide exchange factor', *Trends in Biochemical Sciences*, 24(9), pp. 340-341.
- Sikorski, R.S. *et al.* (1990) 'A repeating amino acid motif in CDC23 defines a family of proteins and a new relationship among genes required for mitosis and RNA synthesis', *Cell*, 60(2), pp. 307-317.
- Siller, K.H. and Doe, C.Q. (2009) 'Spindle orientation during asymmetric cell division', *Nature Cell Biology*, 11, p. 365.
- Singh, D. *et al.* (2021) 'Destabilization of Long Astral Microtubules via Cdk1-Dependent Removal of GTSE1 from Their Plus Ends Facilitates Prometaphase Spindle Orientation', *Current Biology*, 31(4), pp. 766-781.e8.
- Sluder, G. and Nordberg, J.J. (2004) 'The good, the bad and the ugly: the practical consequences of centrosome amplification', *Current Opinion in Cell Biology*, 16(1), pp. 49-54.
- Smith, P.K. *et al.* (1985) 'Measurement of protein using bicinchoninic acid', *Analytical Biochemistry*, 150(1), pp. 76-85.
- Smits, A.H. *et al.* (2013) 'Stoichiometry of chromatin-associated protein complexes revealed by label-free quantitative mass spectrometry-based proteomics', *Nucleic acids research*, 41(1), pp. e28-e28.

- Snider, J. *et al.* (2015) 'Fundamentals of protein interaction network mapping', *Molecular systems biology*, 11(12), pp. 848-848.
- Solito, E. *et al.* (2001) 'Transfection of annexin 1 in monocytic cells produces a high degree of spontaneous and stimulated apoptosis associated with caspase-3 activation', *British Journal of Pharmacology*, 133(2), pp. 217-228.
- Solito, E. *et al.* (1998) 'Human annexin 1 is highly expressed during the differentiation of the epithelial cell line A 549: involvement of nuclear factor interleukin 6 in phorbol ester induction of annexin 1', *Cell growth & differentiation : the molecular biology journal of the American Association for Cancer Research*, 9(4), pp. 327-336.
- SOLITO, E. *et al.* (2003) 'A novel calcium-dependent proapoptotic effect of annexin 1 on human neutrophils', *The FASEB Journal*, 17(11), pp. 1544-1546.
- Solito, E., Nuti, S. and Parente, L. (1994) 'Dexamethasone-induced translocation of lipocortin (annexin) 1 to the cell membrane of U-937 cells', *British Journal of Pharmacology*, 112(2), pp. 347-348.
- Soule, H.D. *et al.* (1990) 'Isolation and Characterization of a Spontaneously Immortalized Human Breast Epithelial Cell Line, MCF-10', *Cancer Research*, 50(18), pp. 6075-6086.
- St Johnston, D. and Sanson, B. (2011) 'Epithelial polarity and morphogenesis', *Current Opinion in Cell Biology*, 23(5), pp. 540-546.
- Sternberg (1983) 'Biomedical Image Processing', *Computer*, 16(1), pp. 22-34.
- Strutt, D. (2008) 'The planar polarity pathway', *Current Biology*, 18(19).
- Su, W.-H. *et al.* (2012) 'Polarity protein complex Scribble/Lgl/Dlg and epithelial cell barriers', *Advances in experimental medicine and biology*, 763, pp. 149-170.
- Sumara, I. *et al.* (2004) 'Roles of Polo-like Kinase 1 in the Assembly of Functional Mitotic Spindles', *Current Biology*, 14(19), pp. 1712-1722.
- Sun, Q. and Schatten, H. (2006) 'Role of NuMA in vertebrate cells: review of an intriguing multifunctional protein', *Frontiers in Bioscience*, 11, pp. 1137-1146.
- Syrovatkina, V. *et al.* (2016) 'Regulation, Signaling, and Physiological Functions of G-Proteins', *Journal of molecular biology*, 428(19), pp. 3850-3868.
- Szklarczyk, D. *et al.* (2018) 'STRING v11: protein–protein association networks with increased coverage, supporting functional discovery in genome-wide experimental datasets', *Nucleic Acids Research*, 47(D1), pp. D607-D613.
- Szklarczyk, D. *et al.* (2019) 'STRING v11: protein-protein association networks with increased coverage, supporting functional discovery in genome-wide experimental datasets', *Nucleic acids research*, 47(D1), pp. D607-D613.
- Szklarczyk, D. *et al.* (2020) 'The STRING database in 2021: customizable protein–protein networks, and functional characterization of user-uploaded gene/measurement sets', *Nucleic Acids Research*, 49(D1), pp. D605-D612.
- Tabb, D.L. *et al.* (2010) 'Repeatability and reproducibility in proteomic identifications by liquid chromatography-tandem mass spectrometry', *Journal of proteome research*, 9(2), pp. 761-776.

- Takatsu, H. *et al.* (2013) 'Mitosis-Coupled, Microtubule-Dependent Clustering of Endosomal Vesicles around Centrosomes', *Cell Structure and Function*, 38(1), pp. 31-41.
- Takayanagi, H. *et al.* (2019) 'Intramolecular interaction in LGN, an adaptor protein that regulates mitotic spindle orientation', *Journal of Biological Chemistry*, 294(51), pp. 19655-19666.
- Tame, M.A. *et al.* (2016) 'Chromosome misalignments induce spindle-positioning defects', *EMBO reports*, 17(3), pp. 317-325.
- Tang, N. *et al.* (2011) 'Control of mitotic spindle angle by the RAS-regulated ERK1/2 pathway determines lung tube shape', *Science*, 333(6040), pp. 342-345.
- They, M. *et al.* (2007) 'Experimental and theoretical study of mitotic spindle orientation', *Nature*, 447(7143), pp. 493-6.
- Théry, M. *et al.* (2007) 'Experimental and theoretical study of mitotic spindle orientation', *Nature*, 447(7143), pp. 493-496.
- Tolić, I.M. (2018) 'Mitotic spindle: kinetochore fibers hold on tight to interpolar bundles', *European Biophysics Journal*, 47(3), pp. 191-203.
- Tomas, A., Futter, C. and Moss, S.E. (2004) 'Annexin 11 is required for midbody formation and completion of the terminal phase of cytokinesis', *The Journal of cell biology*, 165(6), pp. 813-822.
- Tomas, A. and Moss, S.E. (2003) 'Calcium- and Cell Cycle-dependent Association of Annexin 11 with the Nuclear Envelope', *Journal of Biological Chemistry*, 278(22), pp. 20210-20216.
- Tosoni, D. *et al.* (2015) 'The Numb/p53 circuitry couples replicative self-renewal and tumor suppression in mammary epithelial cells', *J Cell Biol*, 211(4), pp. 845-62.
- Tovey, Corinne A. and Conduit, Paul T. (2018) 'Microtubule nucleation by  $\gamma$ -tubulin complexes and beyond', *Essays in Biochemistry*, 62(6), pp. 765-780.
- Toyoshima, F. and Nishida, E. (2007) 'Integrin-mediated adhesion orients the spindle parallel to the substratum in an EB1- and myosin X-dependent manner', *The EMBO Journal*, 26(6), pp. 1487-1498.
- Tuncay, H. and Ebnet, K. (2016) 'Cell adhesion molecule control of planar spindle orientation', *Cellular and Molecular Life Sciences*, 73(6), pp. 1195-1207.
- Tyers, M. and Mann, M. (2003) 'From genomics to proteomics', *Nature*, 422(6928), pp. 193-197.
- Uchiyama, S. *et al.* (2004) 'Protein composition of human metaphase chromosomes analyzed by two-dimensional electrophoreses', *Cytogenetic and Genome Research*, 107(1-2), pp. 49-54.
- Uehara, R. *et al.* (2009) 'The augmin complex plays a critical role in spindle microtubule generation for mitotic progression and cytokinesis in human cells', *Proceedings of the National Academy of Sciences*, 106(17), pp. 6998-7003.
- Urnavicius, L. *et al.* (2015) 'The structure of the dynactin complex and its interaction with dynein', *Science*, 347(6229), pp. 1441-1446.
- van Leen, E.V., di Pietro, F. and Bellaïche, Y. (2020) 'Oriented cell divisions in epithelia: from force generation to force anisotropy by tension, shape and vertices', *Current Opinion in Cell Biology*, 62, pp. 9-16.

- Vassilev, L.T. *et al.* (2006) 'Selective small-molecule inhibitor reveals critical mitotic functions of human CDK1', *Proceedings of the National Academy of Sciences*, 103(28), pp. 10660-10665.
- Villegas, E. *et al.* (2014) 'Plk2 regulates mitotic spindle orientation and mammary gland development', *Development*, 141(7), pp. 1562-71.
- Visconti, R., Della Monica, R. and Grieco, D. (2016) 'Cell cycle checkpoint in cancer: a therapeutically targetable double-edged sword', *Journal of Experimental & Clinical Cancer Research*, 35(1), p. 153.
- Visvader, J.E. and Stingl, J. (2014) 'Mammary stem cells and the differentiation hierarchy: current status and perspectives', *Genes Dev*, 28(11), pp. 1143-58.
- Vorhagen, S. and Niessen, C.M. (2014) 'Mammalian aPKC/Par polarity complex mediated regulation of epithelial division orientation and cell fate', *Exp Cell Res*, 328(2), pp. 296-302.
- Walczak, C.E. and Heald, R. (2008) 'Mechanisms of Mitotic Spindle Assembly and Function', in *A Survey of Cell Biology*. pp. 111-158.
- Wang, X. *et al.* (2018) 'E-cadherin bridges cell polarity and spindle orientation to ensure prostate epithelial integrity and prevent carcinogenesis in vivo', *PLOS Genetics*, 14(8), p. e1007609.
- Wang, Z. *et al.* (2009) 'Numb regulates cell-cell adhesion and polarity in response to tyrosine kinase signalling', *The EMBO Journal*, 28(16), pp. 2360-2373.
- Wei, L. *et al.* (2021) 'Knockdown of Annexin-A1 Inhibits Growth, Migration and Invasion of Glioma Cells by Suppressing the PI3K/Akt Signaling Pathway', *ASN Neuro*, 13, p. 17590914211001218.
- Weibrecht, I. *et al.* (2010) 'Proximity ligation assays: a recent addition to the proteomics toolbox', *Expert Review of Proteomics*, 7(3), pp. 401-409.
- Whitfield, M.L. *et al.* (2002) 'Identification of genes periodically expressed in the human cell cycle and their expression in tumors', *Mol Biol Cell*, 13(6), pp. 1977-2000.
- Wilkins, M.R. *et al.* (1996) 'From Proteins to Proteomes: Large Scale Protein Identification by Two-Dimensional Electrophoresis and Amino Acid Analysis', *Bio/Technology*, 14(1), pp. 61-65.
- Willard, F.S., Kimple, R.J. and Siderovski, D.P. (2004) 'Return of the GDI: the GoLoco motif in cell division', *Annu Rev Biochem*, 73, pp. 925-51.
- William, F. *et al.* (1988) 'Differentiation of HL-60 cells is associated with an increase in the 35-kDa protein lipocortin I', *Journal of Cellular Physiology*, 137(3), pp. 402-410.
- Williams, G.H. and Stoeber, K. (2012) 'The cell cycle and cancer', *The Journal of Pathology*, 226(2), pp. 352-364.
- Williams, S.E. *et al.* (2011) 'Asymmetric cell divisions promote Notch-dependent epidermal differentiation', *Nature*, 470(7334), pp. 353-358.
- Williams, S.E. and Fuchs, E. (2013) 'Oriented divisions, fate decisions', *Curr Opin Cell Biol*, 25(6), pp. 749-58.
- Wilson, A., Laurenti, E. and Trumpp, A. (2009) 'Balancing dormant and self-renewing hematopoietic stem cells', *Current Opinion in Genetics & Development*, 19(5), pp. 461-468.
- Wilson, E.B. (1928) 'The Cell in Development and Heredity', *Macmillan, New York*, 3.

- Wittmann, T., Hyman, A. and Desai, A. (2001) 'The spindle: a dynamic assembly of microtubules and motors', *Nature Cell Biology*, 3(1), pp. E28-E34.
- Woodard, G.E. *et al.* (2010) 'Ric-8A and Gi alpha recruit LGN, NuMA, and dynein to the cell cortex to help orient the mitotic spindle', *Mol Cell Biol*, 30(14), pp. 3519-30.
- Woodward, W.A. *et al.* (2005) 'On mammary stem cells', *J Cell Sci*, 118(Pt 16), pp. 3585-94.
- Wright, C.E. *et al.* (2015) 'LGN Directs Interphase Endothelial Cell Behavior via the Microtubule Network', *PLOS ONE*, 10(9), p. e0138763.
- Wu, X., Hasan, M.A. and Chen, J.Y. (2014) 'Pathway and network analysis in proteomics', *Journal of theoretical biology*, 362, pp. 44-52.
- Xiao, Y. *et al.* (2017) 'Annexin A1 can inhibit the in vitro invasive ability of nasopharyngeal carcinoma cells possibly through Annexin A1/S100A9/Vimentin interaction', *PLoS One*, 12(3), p. e0174383.
- Xing, S. *et al.* (2016) 'Techniques for the Analysis of Protein-Protein Interactions in Vivo', *Plant Physiol*, 171(2), pp. 727-58.
- Yanagida, M. (2014) 'The role of model organisms in the history of mitosis research', *Cold Spring Harb Perspect Biol*, 6(9), p. a015768.
- Yasumi, M. *et al.* (2005) 'Direct binding of Lgl2 to LGN during mitosis and its requirement for normal cell division', *J Biol Chem*, 280(8), pp. 6761-5.
- Yazid, S. *et al.* (2009) 'Cromoglycate drugs suppress eicosanoid generation in U937 cells by promoting the release of Anx-A1', *Biochemical Pharmacology*, 77(12), pp. 1814-1826.
- Yoshii, K. *et al.* (2000) 'Purification, identification and phosphorylation of annexin I from rat liver mitochondria', *Acta Med Okayama*, 54(2), pp. 57-65.
- Yu, H. and Yao, X. (2008) 'Cyclin B1: conductor of mitotic symphony orchestra', *Cell Research*, 18(2), pp. 218-220.
- Zhang, Y. *et al.* (2013) 'Protein analysis by shotgun/bottom-up proteomics', *Chemical reviews*, 113(4), pp. 2343-2394.
- Zheng, C. and Baum, B.J. (2005) 'Evaluation of Viral and Mammalian Promoters for Use in Gene Delivery to Salivary Glands', *Molecular Therapy*, 12(3), pp. 528-536.
- Zheng, Z. *et al.* (2013) 'Evidence for dynein and astral microtubule-mediated cortical release and transport of Galphai/LGN/NuMA complex in mitotic cells', *Mol Biol Cell*, 24(7), pp. 901-13.
- Zheng, Z. *et al.* (2010) 'LGN regulates mitotic spindle orientation during epithelial morphogenesis', *The Journal of cell biology*, 189(2), pp. 275-288.
- Zhu, H. *et al.* (2008) 'FAM29A promotes microtubule amplification via recruitment of the NEDD1-gamma-tubulin complex to the mitotic spindle', *J Cell Biol*, 183(5), pp. 835-48.
- Zhu, J. *et al.* (2011a) 'Guanylate kinase domains of the MAGUK family scaffold proteins as specific phospho-protein-binding modules', *The EMBO journal*, 30(24), pp. 4986-4997.

- Zhu, J. *et al.* (2011b) 'LGN/mInsc and LGN/NuMA complex structures suggest distinct functions in asymmetric cell division for the Par3/mInsc/LGN and Galphai/LGN/NuMA pathways', *Mol Cell*, 43(3), pp. 418-31.
- Zhu, M. *et al.* (2013) 'MISP is a novel Plk1 substrate required for proper spindle orientation and mitotic progression', *J Cell Biol*, 200(6), pp. 773-87.
- Zigman, M. *et al.* (2005) 'Mammalian inscuteable regulates spindle orientation and cell fate in the developing retina', *Neuron*, 48(4), pp. 539-45.
- Zimmer, A.M. *et al.* (2019) 'Loss-of-function approaches in comparative physiology: is there a future for knockdown experiments in the era of genome editing?', *Journal of Experimental Biology*, 222(7).
- Zimmer, M. (2002) 'Green Fluorescent Protein (GFP): Applications, Structure, and Related Photophysical Behavior', *Chemical Reviews*, 102(3), pp. 759-782.
- Zulkipli, I. *et al.* (2018) 'Spindle rotation in human cells is reliant on a MARK2-mediated equatorial spindle-centering mechanism', *Journal of Cell Biology*, 217(9), pp. 3057-3070.
- Zupa, E. *et al.* (2021) 'The structure of the  $\gamma$ -TuRC: a 25-years-old molecular puzzle', *Current Opinion in Structural Biology*, 66, pp. 15-21.



